Searching for the "next big thing" – Examining the potential for new feeder zone mineralisation in the western Navan area, County Meath, Ireland

Michael Convery

Submitted for the degree

of

Masters by Research

Scottish Universities Environmental Research Centre

College of Science and Engineering

University of Glasgow

DECLARATION

The material presented in this thesis is the result of research carried out between September 2015 and May 2016 at the Scottish Universities Environmental Research Centre College of Science and Engineering, University of Glasgow.

Under the supervision of

Professor Adrian Boyce

and

Dr Jason Newton

This thesis is based on my own independent research and any published or unpublished material used here is given full acknowledgment.

Michael T. Convery

Adrian J. Boyce

Jason Newton

Abstract

This study focuses on the Navan Deposit, County Meath, Ireland – a carbonate-hosted Zn-Pb sulphide deposit originally comprising 110Mt @ 8% Zn and 2% Pb, prior to depletion by mining. Navan belongs to the "Irish-type" deposit group – Zn-Pb deposits hosted in the Irish Ore Field that have characteristics of both MVT and SEDEX-style deposits, though cannot be easily be categorised as either. The Irish-types formed from mixing of two fluids – a metalliferous hydrothermal fluid, and a bacteriogenic-sulphide enriched brine. The hydrothermal fluid from Irish-types in the southern Irish Midlands yield a respective hydrothermal fluid homogenisation temperature and salinity range of 170-280^{o}C and 12-18 wt.% NaCl. The Navan hydrothermal fluid was notably lower temperature at 100-140^{o}C and had a salinity of 5-10 wt.% NaCl. Mixing of this moderate temperature fluid with a high salinity bacteriogenic-sulphur enriched brine (70-100^{o}C, 20-25 wt.% NaCl) allowed high-grade Zn-Pb ore to precipitate along a shallow, extending sea basin at approximately 345 Ma (Lower Carboniferous).

Navan ore has an average Zn/Pb ratio of 4, though low-grade, low Zn/Pb below 3 is observed in the hangingwall of the Randalstown Fault 200 metres west of the mine site – an end-Variscan reverse fault of at least several hundred metres throw and one kilometre dextral displacement. Low Zn/Pb has been previously noted in Navan and other Irish-type deposits as an indication of a nearby "feeder zone" – early-forming normal faults that allowed hydrothermal fluid upwelling. Hydrothermal fluids then mixed with downwelling bacteriogenic sulphide-enriched brines on, or close to the seafloor to produce high-grade Zn-Pb sulphide ore. Low Zn/Pb in western Navan, therefore, is of particular interest and may point to a new, unidentified feeder. In addition, Cpy-Qtz(-barite) veining has been identified in drillcore for the first time in the Navan area approximately 850 metres west of the Randalstown Fault, coinciding with the low Zn/Pb area. Notable chalcopyrite has been identified close to feeder-zone faults in other Irish-type deposits, though is absent at Navan – until this discovery.

Mineralised samples were selected along four drillhole transects – The "A1 Transect" was selected trending southeast along the hangingwall of the Randalstown Fault, while the "A2 Transect" trends southeast along the Randalstown Fault footwall. The "B and C Transects" trend perpendicular and parallel to the Main Orebody, respectively. Sulphides from the Main Orebody and western Navan share a similar paragenesis, suggesting that both may have derived from the same hydrothermal fluid event. Sulphur isotope analysis constrains a δ^{34}S range of -1.5 to 12.5‰ for Zn-Pb sulphides west of the Randalstown Fault. This range coincides with previous studies that

have constrained the $\delta^{34}S$ range for the hydrothermal fluid (-4 to 16‰) that supplied Zn-Pb to the Navan Main Orebody and is interpreted to represent hydrothermal fluid that migrated westward during early normal faulting. Fluid inclusion analyses constrain a mineralisation temperature and salinity range of 87-136.5^{o}C, and 6.8-22.7 wt.% NaCl, respectively. This is broadly coincident with the hydrothermal fluid temperature and salinity range. Higher fluid salinity is interpreted to reflect mixing with limited downwelling seawater and/or in-situ pore water.

Cpy-Qtz(-barite) veining in western Navan is hosted in a 10.5 metre thick stratal dolomite and formed from a separate mineralising fluid to the Navan Deposit. $\delta^{34}S$ analysis of three chalcopyrites yield a range of 0.8-3.3‰, results consistent with a hydrothermal fluid origin. Fluid inclusion analysis of two-phase quartz-hosted inclusions yield a temperature range of 191-223^{o}C, while monophase inclusions constrained a salinity range of 10.2-22.8 wt.% NaCl. The assemblage is both distinct from Navan and closer to higher temperature systems in the southern Irish Midlands – an observation supported by a mineralisation temperature range that is closer to the southern Irish-type deposit systems. The mineralising fluids were both higher temperature and more saline than the Navan hydrothermal fluid, potentially pointing to the feeder zone of a new, unidentified system.

Table of contents

Table of contents

Figures

Tables

Acknowledgements

Chapter 1

1. Introduction, aims and approach……1
   1.1. Introduction……1
      1.1.1. Aims……4
   1.2. Rational……6
   1.3. Approach……8
      1.3.1. Petrography to assess and compare hangingwall, footwall and Main Mine paragenesis……8
      1.3.2. Stable isotope geochemistry……9
         1.3.2.1. Sulphur isotope analysis to determine mineralising fluid, origin, flow and mixing……9
         1.3.2.2. Carbon-oxygen isotopes to assess fluid-rock interaction, relationship to Rizzi's Dolomite Plume and to distinguish separate hydrothermal events……9
      1.3.3. Fluid inclusion analysis to assess and compare hangingwall, footwall and Main Mine mineralisation temperature……10

Chapter 2

2. Introduction……11
   2.1. Sedimentary-exhalative deposits……15
      2.1.1. Geology……15
      2.1.2. Ore……16
   2.2. Mississippi Valley-Type Deposits……18
      2.2.1. Geology……18
      2.2.2. Ore……20
   2.3. Irish-Type Deposits……20
      2.3.1. Geology……20
      2.3.2. Ore……20

2.3.3. Mineralisation temperature……..23
2.3.4. Dolomitisation……..25

Chapter 3

3. Geology of Navan……28
3.1. Regional geology……29
3.1.1. Lower Palaeozoic Basement……29
3.1.1.1. Longford Down Northern Belt……30
3.1.1.2. Longford Down Central Belt……30
3.1.1.3. Grengegeeth Terrane……30
3.1.2. Red Beds (Baronstown Formation)……31
3.1.3. Laminated Beds (Portandogh Member – Liscartan Formation)……31
3.1.4. Muddy Limestone (Bishopscourt Member – Liscartan Formation)……31
3.1.5. Pale Beds (Navan Formation)……31
3.1.6. Shaley Pales (Moathill Formation)……33
3.1.7. Argillaceous Bioclastic Limestone (Slane Castle Formation)……33
3.1.8. Waulsortian Reef Limestones (Feltrim Formation)……34
3.1.9. Erosion Surface and the Boulder Conglomerate……34
3.1.10. Tober Colleen Formation……34
3.1.11. Upper Dark Limestone (Lucan Formation)……34
3.1.12. Permian-Tertiary……35
3.2. Deposit geometry……36
3.2.1. Structural geology of the Navan area……36
3.2.1.1. The Caledonian Orogeny……36
3.2.1.2. Regional-scale basinal extension……36
3.2.1.3. Variscan compression……37
3.3. Navan ore……38
3.3.1. 5 Lens……39
3.3.2. 4 Lens……39
3.3.3. 3 Lens……39
3.3.4. 2 Lens……39
3.3.5. 1 Lens……40
3.3.6. 0 Lens……40
3.3.7. U Lens……40
3.3.8. Conglomerate Group Ore (CGO)……40
3.4. Dolomitisation……42

Chapter 4

4. Methodology……44
4.1. Geological logging and sampling……44
4.2. Thin and polished section microscopy……46
4.3. Sulphur isotope analysis……47
4.4. Carbon-oxygen isotope analysis……47
4.5. Fluid inclusion thermometry……48

Chapter 5

5. Geological, petrographic and Zn/Pb studies of the A-C Transects……57
5.1. Geological logging……57
5.1.1. Results along the B-C Transects……58
5.1.2. Zn/Pb ratios along the B-C Transects……58
5.1.3. Geology along the A1 and A2 Transects……65
5.1.4. Zn/Pb ratios along the A1 and A2 Transects……66
5.2. Gross sulphide textures……73
5.2.1. Vein/veinlet……74
5.2.2. Vuggy……76
5.2.3. Layered……77
5.2.4. Chaotic……78
5.2.5. Disseminated……79
5.2.6. Breccia/replacement……79
5.2.7. Coarsely-crystalline, blocky sulphide mineralisation……81
5.2.8. Cpy-Qtz(-bar) and late-stage calcite-saddle dolomite – Drillhole N02230……81
5.3. Petrography and sulphide paragenesis of the A-C Transects……83
5.3.1. C Transect……83
5.3.2. A1 Transect……84
5.3.3. Chalcopyrite in drillhole N02230……87
5.3.4. A2 Transect……90

Chapter 6

6. Isotopic and fluid inclusion studies of the Navan transects……93
6.1. Sulphur isotopes……93
6.1.1. B Transect……94
6.1.2. C Transect……95

6.1.3. A1-A2 Transects ……97
6.1.4. A1 Transect……97
6.1.5. A2 transect……99
6.2. Fluid inclusion analysis……101
6.2.1. C Transect……104
6.2.2. A1 Transect……106
6.2.3. A2 Transect……109
6.3. Carbon-oxygen isotopes……113
6.3.1. B-B' Transect……115
6.3.2. C-C' Transect……115
6.3.3. A1 Transect……115
6.3.4. A2 Transect……116

Chapter 7

7. Discussion……121
7.1. Geology and Zn/Pb ratios of the western Navan area……124
7.1.1. Zn/Pb ratios along the A-C Transects……124
7.2. Thin section microscopy……126
7.3. Sulphur isotopes……130
7.4. Fluid inclusion thermometry……133
7.5. Carbon-oxygen isotopes……136

Chapter 8

8. Conclusion/Closing remarks……142
8.1. Implications for exploration……144

Chapter 9

9. References……147
10. Appendix……164
10.1. Sample locations and descriptions……164
10.2. Zn+Pb core assays……167
10.3. Thin section petrography……176
10.4. $\delta^{34}S$ values……226
10.5. Fluid inclusion homogenisation temperatures and salinity values……228
10.6. C-O values……231

Figures

Figure 1.1. Geological map of the Ireland with locations of Irish-type deposits and notable copper occurrences

Fig 1.2. Geological map of the Navan area with orebody overlay, satellite deposits, low Zn/Pb areas, and intersection point of cpy-Qtz(-barite)

Figure 1.3. Resource discovery map of Navan through mining history

Figure 1.4. Zn/Pb ratio map of the Main Mine 5 Lens

Figure 2.1. Regional map of the Navan area with orebody outline over surficial geology

Figure 2.2. World map showing main locations of SEDEX, MVT and Irish-type Deposits

Figure 2.3. Genetic model for Sedimentary-Exhalative deposits

Figure 2.4. Genetic model for Mississippi Valley-Type Deposits

Figure 2.5. Genetic model for Irish-type Deposits

Figure 2.6. Aggregated fluid inclusion homogenisation temperature and salinity data from the Irish-type deposits

Fig 3.1. Stratigraphic table of the Navan area

Fig 3.2. Diagram showing chronological development of majoRandalstown Fault systems at Navan

Fig 4.1. Adapted geological map of the Navan area showing locations of the A-C transects overlaid on 5 Lens outline and surficial geology

Fig 4.2. Plan view of A1 and A2 transects

Fig 4.3. Cross section of A1-A2 transects, looking north-northwest

Fig 4.4. Plan view of the B Transect

Fig 4.5. Cross section of the B Transect, looking north-northwest

Fig 4.6. Plan view of the C Transect

Fig 4.7. Oblique view of the C Transect

Fig 5.1. Adapted geological map of the Navan area showing locations of the A-C transects overlaid on 5 Lens outline and surficial geology

Fig 5.2. Correlation panel along the B Transect

Fig 5.3. Correlation panel along the C Transect

Fig 5.4. Generalised vertical stratigraphy of the B, C and A1 Transects

Fig 5.5. Zn/Pb ratios of the drillholes along the B Transect

Fig 5.6. Zn/Pb ratios of the drillholes along the C Transect

Fig 5.7. Marker horizon table for the A-C Transects

Fig 5.8. Correlation panel of the A1 and A2 Transects

Fig 5.9. Generalised vertical stratigraphy of Western Navan

Fig 5.10. Zn/Pb ratio of drillholes along the A1 Transect

Fig 5.11. Zn/Pb ratio of drillholes along the A2 Transect

Fig 5.12. Geological map of the Navan area

Fig 5.13. Vein/veinlet textures in core

Fig 5.14. Granular/vuggy textures in core

Fig 5.15. Layered/banded textures in core

Fig 5.16. Chaotic textures in core

Fig 5.17. Disseminated sulphide textures in core

Fig 5.18. Breccia/Vein breccia textures in core

Fig 5.19. Blocky sulphide textures in core

Fig 5.20. Cpy-Qtz(-barite) core textures in drillhole N02230

Fig 5.21. Photomicrographs of C Transect sulphides

Fig 5.22. C Transect paragenesis chart

Fig 5.23. Photomicrographs of A1 Zn-Pb sulphides

Fig 5.24. A1 Transect paragenesis chart

Fig 5.25. Photomicrographs of cpy-Qtz(-barite) in drillhole N02230

Fig 5.26. N02230 cpy-Qtz(-barite) paragenesis chart

Fig 5.27. Photomicrographs of A2 Transect sulphides

Fig 5.28. A2 Transect paragenesis chart

Fig 6.1. Adapted geological map of the Navan area showing locations of the A-C transects overlaid on 5 Lens outline and surficial geology

Fig 6.2. B Transect $\delta^{34}S$ histogram

Fig 6.3. B Transect $\delta^{34}S$ scatterplot over distance

Fig 6.4. C Transect $\delta^{34}S$ scatterplot over distance

Fig 6.5. C Transect $\delta^{34}S$ histogram

Fig 6.6. A1 $\delta^{34}S$ histogram

Fig 6.7. A2 $\delta^{34}S$ histogram

Fig 6.8. A1-A2 $\delta^{34}S$ scatterplot over distance

Fig 6.9. Example photomicrograph of cleavage-parallel, monophase inclusions in sample N02045-3

Fig 6.10. Example photomicrographs of two-phase inclusions in sample N01056-1

Fig 6.11. Adapted geological map of the Navan area showing locations of the A-C transects overlaid on 5 Lens outline and surficial geology

Fig 6.12. T_h vs salinity (wt.% NaCl) scatterplot for C Transect fluid inclusions

Fig 6.13. Histogram of C Transect fluid inclusion salinities

Fig 6.14. Histogram of C Transect fluid inclusion homogenisation temperature

Fig 6.15. T_h vs salinity (wt.% NaCl) scatterplot for A1 Transect fluid inclusions

Fig 6.16. Histogram of A1 Transect fluid inclusion salinities

Fig 6.17. Histogram of A2 Transect fluid inclusion homogenisation temperature

Fig 6.18. T_h vs salinity (wt.% NaCl) scatterplot for A2 Transect fluid inclusions

Fig 6.19. Histogram of A2 Transect fluid inclusion salinities

Fig 6.20. Histogram of A2 Transect fluid inclusion homogenisation temperature

Fig 6.21. Aggregated fluid inclusion homogenisation temperature and salinity plot

Fig 6.22. Adapted geological map of the Navan area showing locations of the A-C transects overlaid on 5 Lens outline and surficial geology

Fig 6.23. Carbon-oxygen plot for A-C Transect 5 Lens Dolomite, stratal dolomite, and calcite-saddle dolomite veining

Fig 7.1. Geology at the base of the Boulder Conglomerate with interpreted hydrothermal fluid flow directions at end-Chadian

Fig 7.2. Adapted geological map of the Navan area showing locations of the A-C transects overlaid on 5 Lens outline and surficial geology

Fig 7.3. Aggregated fluid inclusion homogenisation temperature/salinity from previous inclusion studies of the Navan Orebody and this report

Fig 7.4. ^{13}C-^{18}O fluid evolution plot modified from Hitzman and Beaty (1996)

Fig 7.5. $\delta^{18}O$ over $\delta^{13}C$ evolution plot for A-C Transect carbonates at 0-250^{o}C

Fig 7.6. $\delta^{18}O$ over $\delta^{13}C$ evolution plot for C Transect carbonates at 0-250^{o}C

Fig 8.1. Genetic model for Randalstown Fault hangingwall sulphides

Fig 8.2. Expanded geological model for hangingwall sulphides and cpy-Qtz(-barite) mineralisation in western Navan

Tables

Table 2.1. Characteristics of the major Irish-type deposits

Table 2.2. Characteristics of SEDEX, MVT and Irish-type deposits

Table 3.1. Mineralisation textures and geological characteristics of the Navan ore lenses and Conglomerate Group Ore

Table 6.1. $\delta^{34}S$ values from B Transect sulphides

Table 6.2. $\delta^{34}S$ values from C Transect sulphides

Table 6.3. $\delta^{34}S$ values from A1 Transect sulphides

Table 6.4. $\delta^{34}S$ values from A2 Transect sulphides

Table 6.5. Homogenisation temperature and salinity values for A1 Transect calcites

Table 6.6. Homogenisation temperature and salinity values for A2 Transect calcites

Table 6.7. Homogenisation temperature and salinity values for C Transect calcites

Table 6.8. $\delta^{18}O$ – $\delta^{13}C$ values from A-C Transect carbonates

Table 10.1. Sample collection depths and descriptions

Table 10.2. A-C Transect core assay data

Table 10.3. A-C Transect $\delta^{34}S$ values

Table 10.4. Fluid inclusion values

Table 10.5. A-C Transect $\delta^{13}C$ – $\delta^{18}O$ values

Acknowledgements and thanks:

This project developed from a combination of factors – A desire to keep going with academia after finishing my undergraduate degree at Leicester University, craving geological fieldwork and gaining industry work, and the "graduate blues" – a natural response to just finishing the best four years of my life with the best possible friends. Firstly, I'd like to thank my sponsors – The Mining Institute of Scotland and the Institute of Materials, Minerals and Mining – both of whom provided financial support that made this project possible from the beginning. The University of Glasgow has my immense gratitude for providing a tuition fee waiver, thus allowing me to study without the worry of additional student debt!

Firstly, Professor Adrian Boyce, the man himself. I first contacted Adrian in Summer 2014 with a vague interest in pursuing a project on Navan. Thankfully, Adrian, with his established connections at Boliden Tara Mines, was able to help establish contact with the Exploration Department for me and rapidly a new project. After that, he has provided regular (albeit brutally direct) advice on where to take the project and what angles to pursue. He has been a fountain of advice and knowledge throughout the whole endeavour, and was crucial in securing the funding necessary to get this project off the ground. He's also introduced me to the word "mince" in the context of feedback, so that's basically ruined that word for me.

The Exploration Department at Boliden Tara Mines' Exploration Office has my enormous gratitude. John Ashton and Robert Blakeman were key in helping to develop this project, secure funding and provide project and editing advice throughout the year. Johnny Harrington and Brian Cosgrove were true champs in securing what had to be the dirtiest and most inconvenient core, not just on-site but probably in the history of mining. Throughout the relatively short time of one year, I had the opportunity to interact with a wide range of Navan experts. Special thanks go to Tony Fallick and Andrew Caulfield for their expert advice at different times throughout the project. Brett Davidheiser-Kroll and Freya Marks deserve my thanks for helping me get set up and get to grips with structuring my sampling program. Jamie Wilkinson's input at the Natural History Museum was hugely beneficial, helping me with the fundamentals of fluid inclusion thermometry. His insight and expert knowledge on Navan and fluid inclusion thermometry made the data collection, analysis and discussion process a mostly smooth ride, and provided me with an extremely generous time slot to get the most possible work done at the Museum's fluid inclusion stage.

My three months with Tara Mine coincided with that of several students. In a small town in a small country, boredom is often not far away, even if you're lucky enough to be working on the

world-class Navan Zn-Pb Deposit (110Mt @ 10% Zn+Pb etc). Thankfully, Rob Marshall, Ally Barrow, Nicola McBarron (a truly bizarre girl, probably one of the weirdest I've ever met), Hayley Blyth, Tasha Finnegan and Caoimhe Moriarty made the whole experience smooth sailing

Jason Newton also deserves a big round of applause for giving me as detailed feedback as possible, even though Navan wasn't his exact expertise. All of the staff at SUERC, especially Alison McDonald, Terry Donnelly, Andrew Tait, Caroline Donnelly, and Valerie Olive all deserve my gratitude for helping me at different stages with data collection and getting established, particularly Alison though for having to show me more than once how to run the sulphur line or the ICP-MS! I have to thank Professor Robert Ellam, Professor Fin Stuart, Dr Darren Mark, and Kerry Kier, all of whom helped me to navigate a challenging second half of my project.

Finally, my mum, as always, deserves special thanks for her ability to temper my sometimes excessive ambitions and keep things a little more grounded. Getting this project going in its early days wasn't a certainty by any means, and mum helped to remind me of that when I needed it. Hard-headed advice from a Northern Irish mum can sometimes be helpful if you're getting ahead of yourself.

Chapter 1

Introduction, Aims and Approach

This chapter provides an overview of the context of this study within the Navan Deposit, the aims, and the approaches used to deliver the aims.

1.1. Introduction:

The Navan Deposit, Ireland, is a world-class Zn-Pb deposit and by far the largest discovered in the Irish Ore Field and Europe, comprising 110Mt of ore @ 8% Zn and 2% Pb before depletion by mining. Located ~40km northwest of Dublin (Figure 1.1), the mine is currently operated by Boliden Tara Mines Limited, producing 2.5Mt of ore per annum, and has produced 87.7Mt ore @ 8.1% Zn and 1.9% Pb (Ashton, 2016 – pers comm). The deposit was first discovered in 1970 through exploration drilling, then delineating an initial resource of 69.9Mt @ 10.1% Zn and 2.6 Pb. The discovery of the Southwest Extension in the 1990s added an additional 25Mt to the total resource, while drilling on Nevinstown, the Liscartan License and Rathaldron on the northern edge of the Main Mine site have further expanded the mine lifespan. Recent efforts to expand the resource have focused on delineating the Southwest-Extension South ("Gainstown") prospect to the southeast of the deposit, and characterising an area of low Zn/Pb mineralisation one kilometre west of the deposit in the hangingwall of the Randalstown Fault ("Randalstown Fault") - a dextral reverse fault measuring a respective displacement and throw of at least several hundred metres and one kilometre dextral displacement interpreted to form at end-Variscan (Figure 1.2). Low Zn/Pb has been previously observed in other Irish Midlands Zn-Pb deposits, especially the Silvermines deposit, as a good indicator for "feeder zones" (Taylor, 1984) – early-forming normal faults that acted as conduits for upwelling, metalliferous hydrothermal fluids. While the Main Mine site has been intensively drilled and has accumulated over 27,000 drillholes since Tara Mine began operations in 1977, drilling in the Randalstown Fault hangingwall is sparse and the area lacks geologic resolution.

Additionally, Cpy-quartz(-barite) veining - previously unobserved at Navan - has been intersected in drillcore approximately one kilometre west of the Main Mine, coinciding with the low Zn/Pb mineralisation area. Chalcopyrite has been identified close to feeder zones at other Irish Zn-Pb deposits including Silvermines and Lisheen, though only as a minor mineral phase and has been

recognised as higher temperature (E.g. Taylor, 1984, Boyce, 1990, Hitzman and Beaty, 1996, Banks and et al, 2002). Cpy-quartz vein arrays have been identified in the south of Ireland, particularly in the Munster Basin in County Cork, becoming less common in the Irish Midlands where Zn-Pb mineralisation dominates (e.g. Wen, 1996). This study seeks to constrain the provenance of low Zn-Pb mineralisation and chalcopyrite in the western Navan area and determine whether both are an expression of an unidentified feeder.

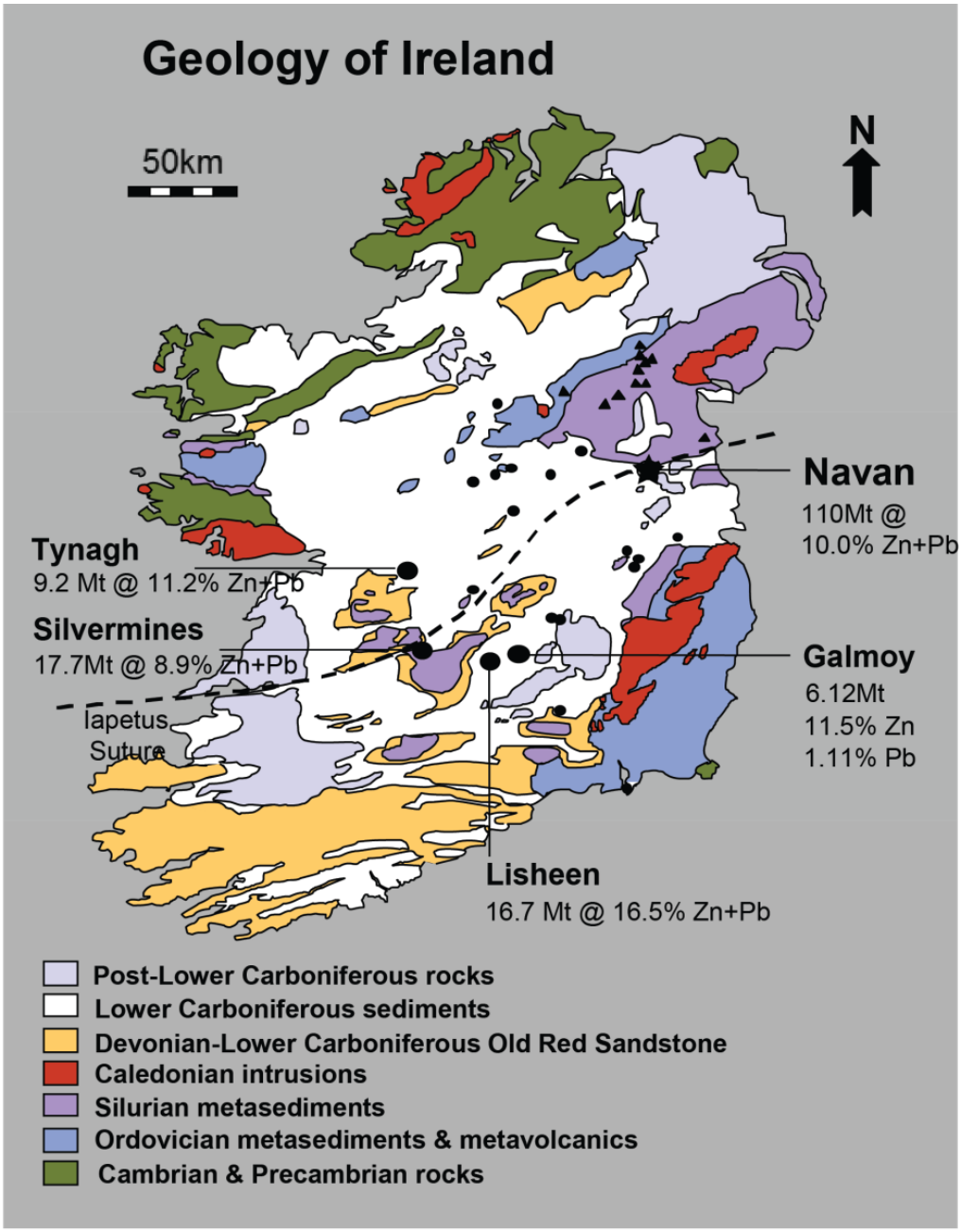

Figure 1.1 – Geological map of Ireland with major Zn-Pb ore deposits and respective grades and tonnages

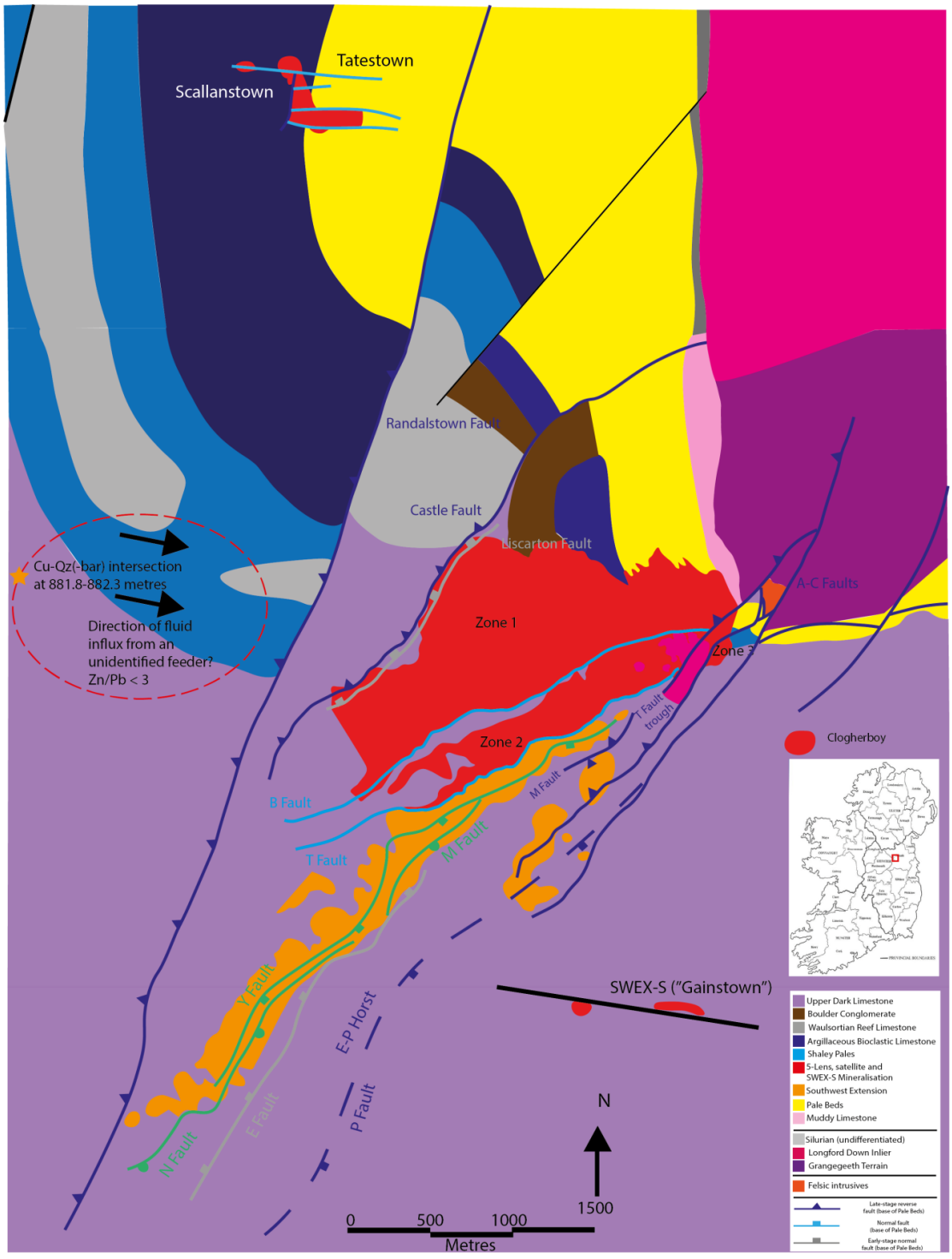

Figure 1.2 – Geology of the Navan area with 5 Lens, satellite deposits and SWEX-S outlines overlying surficial geology (red) and SWEX in orange. Chalcopyrite intersection point west of the Randalstown Fault is represented by orange star.

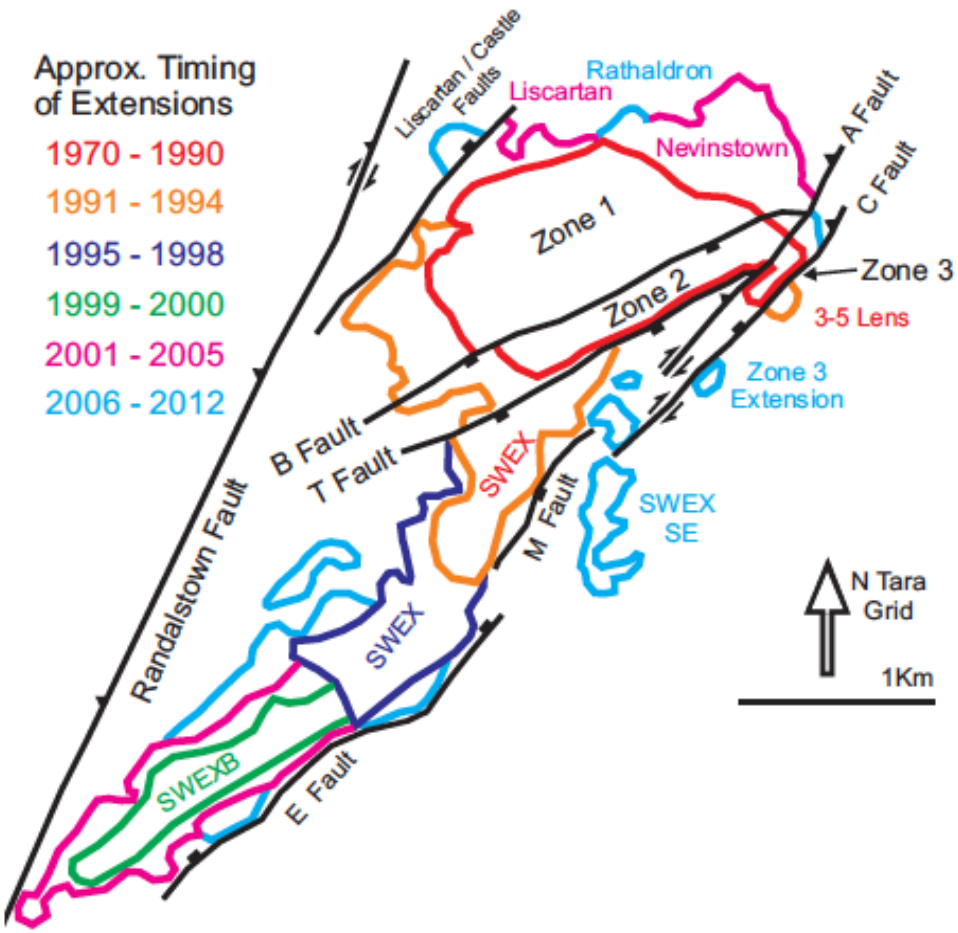

Figure 1.3 - Diagrammatic representation of resource expansion at Tara Mine since Main Orebody discovery in 1970 (Ashton et al, 2015)

1.1.1. Aims:

This study addresses a number questions, using geochemical and petrographic analyses to characterise Randalstown Fault hangingwall Zn-Pb sulphide and cpy-Qtz(-barite) which appears to be paragenetically separate:

1) Why is mineralisation in the hangingwall of the Randalstown Fault low Zn/Pb? Could Zn/Pb mineralisation west of the Navan Deposit represent a displaced continuation of the Main Mine 5 Lens, or an expression of an unidentified feeder zone?

   1A) Using mineralised 5 Lens samples obtained from the hangingwall and footwall of the Randalstown Fault, and from the Main Mine, assess the sulphide paragenesis in the upthrown and downthrown blocks of the Randalstown Fault. Does the accessory mineral

assemblage point to feeder zone input? Can sulphur isotope analyses of Randalstown Fault hangingwall sulphides help to fingerprint a mineralising fluid?

1B) Using sulphur isotope analysis for galena and sphalerite west of the Randalstown Fault, fingerprint the original mineralising fluid. Was the ore fluid of high or low $\delta^{34}S$? If so, what are the implications for feeder-zone potential and exploration?

1C) Using C-O isotope analysis, can hydrothermal dolomites hosted in the hangingwall be linked to paragenetically early hydrothermal dolomites in the Main Mine (e.g. Rizzi, 1992, Braithwaite and Rizzi, 1997, Everett and Wilkinson, 2001)?

1D) Using fluid inclusion thermometry, determine whether low-grade mineralisation in the Randalstown Fault hangingwall precipitated from fluids responsible for Main Mine mineralisation (e.g. Peace, 1999, Everett and Wilkinson, 2001, Wilkinson, 2010). Alternatively, were the mineralising fluids of a higher temperature, and thus possibly with a deeper/feeder affinity?

2) Can light be shed on the provenance of the Cpy-quartz(-barite) veining? Is copper veining an expression of a distinct mineralisation style not observed in the Main Mine, or feeder zone related?

2A) Assess the paragenesis of Cpy-quartz(-barite) veining using thin section microscopy.

2B) Using sulphur isotope analysis, characterise the original mineralising fluid and compare with that of the Randalstown Fault hangingwall, footwall and Main Mine sulphides to assess a paragenetic relationship.

2B) Using fluid inclusion thermometry, constrain the mineralising temperature of copper-bearing veins, and compare against existing literature detailing similar Cpy-veining elsewhere in Ireland.

1.2. Rationale

Observations that low Zn/Pb ratios may be useful for constraining "feeder" zones in Irish Midlands Zn-Pb deposits were made by Taylor and Andrew (1978) and Taylor (1984) in Silvermines (County Tipperary), and Andrew and Ashton (1982) at Navan. These studies identified very low Zn/Pb in proximity to early-forming faults and increasing with distance, exhibiting a strongly zoned, lateral Zn/Pb ratio distribution. This relationship was interpreted to represent steadily decreasing temperature with fluid migration, where galena precipitated at higher temperatures and became depleted in the mineralising fluid, while sphalerite was precipitated as fluid temperature decreased.

Detailed interrogation of Navan's assay dataset by Davidheiser-Kroll (2014) identified two distinct Zn/Pb populations in the 5 Lens – Zn/Pb below 2.75 is observed in the southwest Main Mine 5 Lens, while Zn/Pb above 2.75 is observed to the northeast (figure 1.4). Davidheiser-Kroll (2014) suggested that this distribution could occur from two scenarios: 1) Heterogeneity in the Lower Palaeozoic basement producing ore fluids with distinct Zn/Pb characters, or 2) thermodynamic regime changes which affected an ore fluid of evolving Zn/Pb ratio as it laterally migrated northeast. Marks (2015) investigated the epigenetic "halo" of the Navan deposit – a weakly mineralised low Zn/Pb "skirt" of the Main Mine. Marks (2015) concluded that low Zn/Pb in the northwest Navan area resulted from mineralisation deriving from a laterally migrating hydrothermal fluid coeval with Main Mine mineralisation. This fluid was interpreted to not have undergone mixing with bacteriogenic sulphur – critical to fixing metalliferous fluids at Navan to produce high-grade ore (Fallick et al, 2001).

Chalcopyrite mineralisation is relatively rare in the Irish base-metal orefield (Hitzman and Beaty, 1996). Chalcopyrite has been observed as an accessory mineral in proximity to normal faults in Lisheen (County Tipperary) and Silvermines (e.g. Taylor, 1984, Hitzman and Beaty, 1996, Wilkinson et al, 2005A), though is rare at Navan, and is found as a trace, later-stage that overprins Zn-Pb sulphide, and in the underlying Lower Palaeozoic Basement (Boyce et al, 1994).

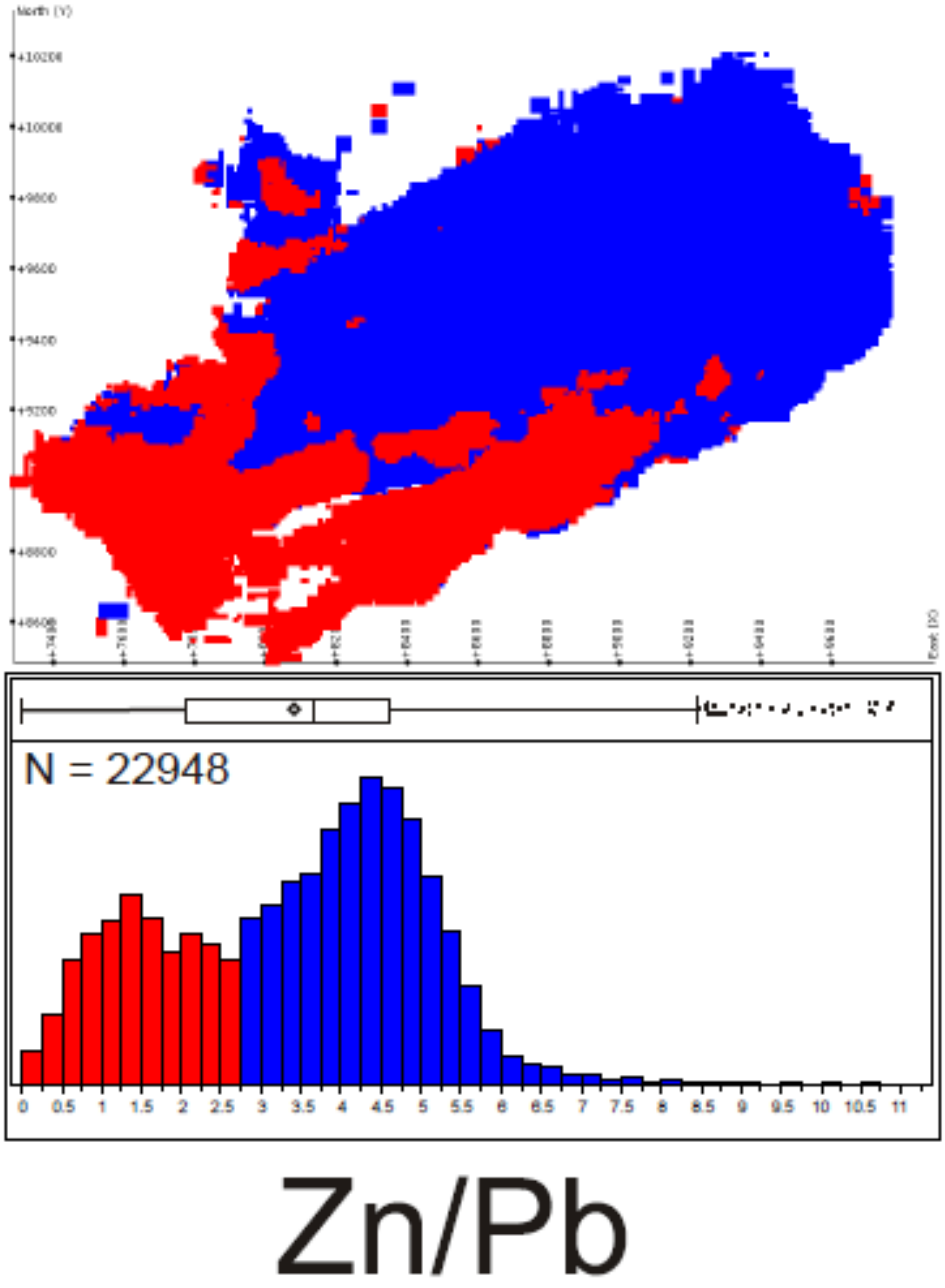

Figure 1.4 – Zn/Pb ratio map of the Main Mine 5 Lens (Davidheiser-Kroll, 2014)

1.3. Approach:

1.3.1. Petrography to assess and compare hangingwall, footwall and Main Mine paragenesis:

Navan ore comprises high-grade Zn-Pb sulphide produced by mixing of metal-rich hydrothermal fluids and surface brines (e.g. Coomer and Robinson, 1976; Fallick et al, 2001; Blakeman et al, 2002). Everett and Wilkinson (2001), and Altinok (2005) constrain a five-stage paragenesis for Navan and other Irish Midlands Zn-Pb deposits:

1) Pre-sulphide calcite cementation followed by hydrothermal dolomitisation. Host rock dolomitisation precedes sulphide mineralisation and is believed to be associated with interpreted "feeder zones" in Irish-type deposits. In the case of Navan, dolomitisation is interpreted to be temporally related to early-forming normal faults (e.g. Braithwaite and Rizzi, 1997, Anderson et al, 1998, Everett and Wilkinson, 2001)

2) Fe-sulphide replacement of carbonates - Fe sulphides are the paragenetically earliest sulphides, and precipitate with sphalerite bands in colloform pyrites.

3) Carbonate replacement by sphalerite

4) Sulphide mineralisation – sphalerite, galena, Fe-sulphides and sulfosalts. Sphalerites contain discontinuous bands of dolomite and become increasingly coarse-grained with further deposition. Colloform, coarsely-grained sphalerites are intergrown by pyrite, galena and sulfosalts.

5) Late carbonate precipitation – this phase comprises calcite with subordinate dolomite, galena and sphalerite.

Ag-Sb-Cu sulfosalt assemblages and colloform marcasite-pyrites have been observed close to feeder zones in other Irish-type deposits. Additionally, early iron-sulphides are often cross-cut and overprinted by later Zn-Pb sulphides (Hitzman and Beaty, 1996). By examining Zn-Pb sulphide paragenesis in the hangingwall and footwall of the Randalstown Fault, and samples from the Main Mine this study seeks to identify potential "feeder-type" mineralisation assemblages and a paragenesis sequence that can help fingerprint an unidentified feeder system in western Navan.

1.3.2. Stable isotope geochemistry:

1.3.2.1. Sulphur isotope analysis to determine mineralising fluid, origin, flow and mixing

Sulphur isotope studies of Navan mineralisation have helped to characterise and vector in on feeder zones (Blakeman et al, 2002). Sulphides within 3 metres of early-forming faults have a high $\delta^{34}S$ signal signal. The ratio of ^{34}S and ^{32}S is measured in permil (‰) and determined using the equation:

$$\delta^{34}S_{sample} = [(R_{sample}/R_{std}) - 1)] \times 1000]$$

Where "R" refers to the $^{34}S/^{32}S$ ratio, and "std" is an international standard - the Canyon Diablo Troilite.

High $\delta^{34}S$ (1-18‰) values are interpreted to reflect hydrothermal fluid through the normal faults (Blakeman et al, 2002). In contrast, the $\delta^{34}S$ of sphalerite and galena greater than 3 metres away from interpreted feeders in the Main Orebody are clearly bacteriogenic, constraining a range of -1 to 26‰. High $\delta^{34}S$ in sulphides may thus provide a useful fingerprinting method for finding areas of hydrothermal fluid influx and thus new feeder zones at Navan.

1.3.2.2. Carbon-oxygen isotopes to assess fluid-rock interaction, relationship to Rizzi's Dolomite Plume and to distinguish separate hydrothermal events

The 5 Lens Dolomite – a six to twelve metre thick hydrothermal dolomite that replaced a pre-existing calcarenite sequence in the 5 Lens – was an important aquitard that focused mineralising fluids and has been interpreted to form from high-temperature Carboniferous seawater downwelling along early-forming normal faults and interacting with the Pale Beds sequence (e.g. Rizzi, 1992; Braithwaite & Rizzi, 1997). Isotopic analyses of 5 Lens Dolomites in the Randalstown Fault hangingwall dolomites show a $\delta^{13}C$ and $\delta^{18}O$ broadly coincident with the Main Mine 5 Lens Dolomite array (Braithwaite & Rizzi, 1997, Ashton et al, 2015), suggesting that hangingwall dolomitisation are likely temporally related to a so called Dolomite Plume (Rizzi, 1992, Braithwaite and Rizzi, 1997). Hangingwall 5 Lens Dolomites are rare though are identified in two of this study's drillholes, and these have been analysed to determine relationship, if any, to the Dolomite Plume.

In addition, Cpy-Qtz(-barite) mineralisation is hosted in a 10.5 metre thick stratal dolomite approximately one kilometre from the Randalstown Fault. This study used C-O isotope analysis to assess the provenance of 5 Lens and stratal dolomites, and late-stage calcite-dolomite veining that that cross-cuts Cpy-Qtz(-barite) west of the Randalstown Faultand determine if they are temporally related to the Dolomite Plume at the Main Mine site. If so, is this indication of a nearby feeder?

1.3.3. Fluid inclusion analysis to assess and compare hangingwall, footwall and Main Mine mineralisation temperature:

Fluid inclusion analyses of Navan ore and hydrothermal carbonates has constrained a fluid-mixing model involving two fluids – a moderate temperature, moderate salinity metalliferous hydrothermal fluid (100-140^{o}C, 5-10 wt.% NaCl) and a low temperature, high salinity (70-100^{o}C, 20-25 wt.% NaCl) bacteriogenic sulphide-enriched brine (e.g. Peace, 1999, Everett & Wilkinson, 2001, Yardley et al, 2005, Wilkinson, 2010). Fluid inclusion analyses of primary inclusions from calcites in Zn-Pb sulphide-calcite veins in the Randalstown Fault hangingwall is used to constrain the homogenisation temperature and salinity of the fluid responsible for low Zn/Pb mineralisation. Analysis was completed to assess whether A) a high temperature fluid could be identified in the Randalstown Fault hangingwall that may indicate feeder zone potential (e.g. Samson and Russell, 1987, Banks et al, 2002), and B) a low temperature, high salinity fluid could be constrained that may indicate fluid mixing necessary for producing ore (e.g. Anderson et al, 1998, Everett et al, 2001, Fallick et al, 2001, Wilkinson et al, 2003, 2005, Wilkinson, 2010).

Chapter 2

Brief Summary of Irish Ores and genetic models for the Irish-type base-metal deposits

This chapter examines the geology, mineralogy and provenance of Sedimentary-Exhalative, Mississippi Valley-Type and Irish-type deposits. The chapter discusses the genetic similarities of the three deposit-types, and the difficulties in categorising Irish-types.

2. Introduction:

Ireland, despite its small geographical size, is geologically diverse and contains several high-grade, high-tonnage base-metal and gold ore deposit-types. Ireland hosts several operating mines and actively explored mineral prospects, including mesothermal Au (Curraghinalt, Cavanacaw and Omagh) in County Tyrone in Northern Ireland, Volcanic Massive Sulphides (Avoca) in County Wicklow, County Wexford, Cpy-Ba veining in west County Cork, coal in County Tipperary and Kilkenny, and Gypsum in County Cavan (E.g. Wen et al, 1996, Hollis et al, 2014, Geological Survey of Ireland). Of special interest is the Irish Ore Field in the Irish Midlands.

By far the most abundant metallic resource discovered in Ireland, to date, is the Lower Carboniferous carbonate-hosted base-metal ore field in the Central Irish Midlands. Comprising 8000 km^2, the Irish Ore Field hosts the world-class Navan Zn-Pb Deposit in addition to smaller orebodies including former mines: Lisheen, Silvermines, Tynagh, and Galmoy (Fig 1.1). Zn-Pb orebodies in the Irish Midlands are commonly referred to as “Irish-type”, exhibiting characteristics of both Sedimentary Exhalative (SEDEX) and Mississippi Valley-Type (MVT) deposits and are widely considered to be either a sub-type of both deposit-types, or a separate deposit system. Irish-type deposits share characteristics best summarised by Hitzman & Beaty (1996), Anderson et al (1998), Davidheiser-Kroll (2014), and Ashton et al (2015):

1) The deposits are hosted in non-argillaceous, shallow marine Lower Carboniferous carbonate shelf sequences. Lisheen, Galmoy, Tynagh, Silvermines, Pallas Green and

Garrynalick deposits are hosted in the Waulsortian Limestone sequence, while Navan occurs in the stratigraphically lower Pale Beds sequence (Navan Group).

2) The Irish-type deposits show a clear spatial and temporal relationship with and are structurally controlled by steeply dipping, extensional normal faults, with ore oftern occurring in breccia form. The relationship between mineralisation at Navan is complicated by several generations of normal faulting and eventual basin inversion, though there is a clear spatial and temporal relationship between faulting and ore formation, reflected in the complexity of ore textures in the mine. Normal fault networks are extensively interpreted as conduits for hydrothermal fluids. Many of these fault systems are considered to be reactivated from pre-existing Caledonian structures (I.e. are synthetic faults).

3) Irish-type ore have a generally simple sphalerite-galena-pyrite assemblage with lesser marcasite, and accessory Pb-Cpy-Ag-As sulfosalts. Gangue commonly comprises calcite, dolomite, barite (varies from a minor to major constituent between deposits) and quartz. Minor chalcopyrite is observed in interpreted feeder zone-proximal settings in Lisheen and Silvermines and is observed as a minor accessory mineral in Navan ore.

4) Ore in Irish-type deposits can be purely epigenetic (e.g. vein-type), and/or stratabound syngenetic to penecontemporaneous, to fully replacive, resulting in significant variation in ore formats, from fine-grained, anhedral massive sulphides, to replacive, open space, cavity fill, vein, pod and layered textures.

5) Deposits formed from mixing of two fluids – A moderate temperature, moderate salinity metalliferous fluid, and a low temperature, high salinity brine. Low temperature fluids are interpreted as hypersaline brines enriched in sulphur bacterially reduced from seawater sulphate, while the moderate temperature fluids (considered the principal ore (metal-bearing) fluid) were derived from circulating seawater that scavenged base metals from the underlying Lower Palaeozoic basement.

The Navan Deposit is hosted in a Lower Carboniferous (Tournaisian) carbonate sequence, referred to as the Pale Beds (the “Navan Formation”) - deposited during a marine transgressive episode along a Laurasian continental shelf (Anderson, 1990, Wilkinson, 2005, Ashton et al, 2015). The Pale Beds are a series medium-grained micrites, dolomites, oolitic and bioclastic limestones, and clean-silty calcarenites and calcisiltites (see Chapter 5). The remaining large base-metal deposits - Tynagh, Galmoy, Silvermines, and Lisheen - are hosted in late Courceyan-Chadian Waulsortian

limestones and dolomites (Boyce et al, 1983; Hitzman & Large, 1986; Hizman & Beaty, 2002). 97% of Navan ore is hosted in the Pale Beds, while the remaining 3%, comprising iron sulphide with sub-ordinate sphalerite and galena, occurs in the overlying Conglomerate Group Ore of the Boulder Conglomerate - a mega-conglomerate succession associated with catastrophic slope collapse during basinal extension that heavily downcuts through the Pale Beds succession to the southeast. The Main Orebody is hosted within the lower section of the Pale Beds while the Southwest Extension occurs in the upper section of the sequence (Ashton et al, 2003, 2015).

Similarities between Navan and other sediment-hosted Zn-Pb deposit-types complicate categorisation. Zn-Pb deposits in the Irish Midlands are often referred to in literature as “Irish-type”, and are often considered to be either a sub-category of sedimentary-exhalative-style (“SEDEX”) (e.g. Fallick et al, 2001, Blakeman et al, 2002, Lee & Wilkinson, 2002, Wilkinson, 2003, 2005, Wilkinson, 2010, Davidheiser-Kroll, 2014, Ashton et al, 2015), and Mississippi Valley-Type-style (“MVT”) (e.g. Peace, 1999, Peace et al, 2003, Hitzman, 1999, Leach et al, 2001, Leach et al, 2005, Leach et al, 2010), or a separate deposit type (e.g. Wilkinson et al, 2003). Recent discoveries in Limerick identify a spatial association with diatreme volcanism - an association atypical of extant Irish-type deposits (Blaney & Redmond, 2010, Elliot et al, 2013).

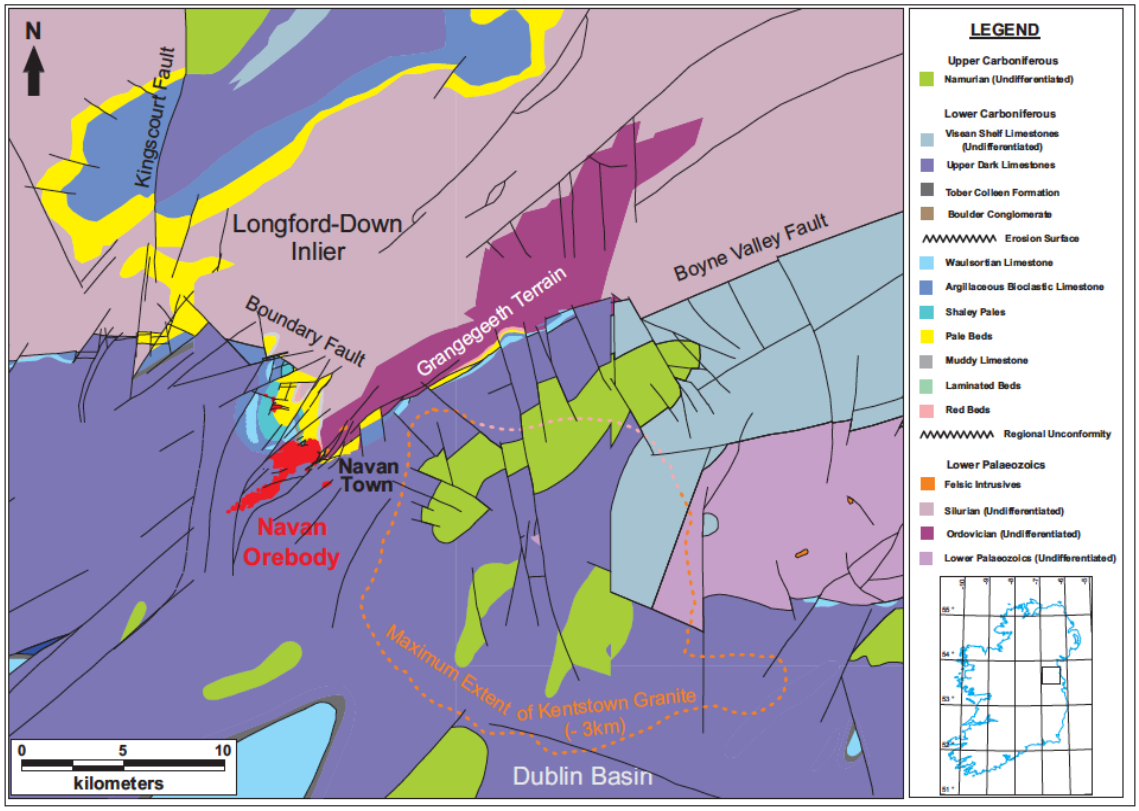

Figure 2.1 - Regional geology of the Navan area. The Navan Orebody (in red overlying surficial geology) is located southwest of the Longford Down Massif - A faulted lower Ordovician-Silurian sedimentary and volcaniclastic package sub-divided into the Longford-Down Inlier and the Grangegeeth Terrane that continues under the Navan Deposit. (Ashton et al, 2015)

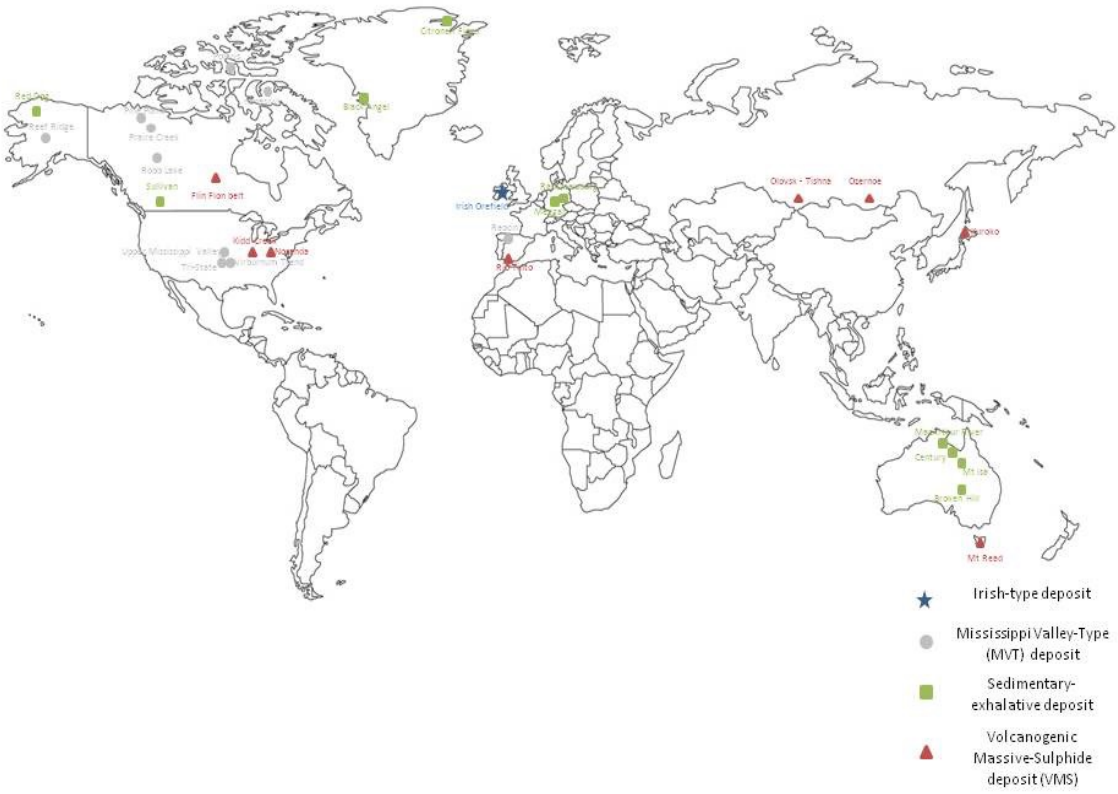

Figure 2.2 - Global distribution of major SEDEX, MVT, VMS and Irish-Type deposits

Sedimentary-Exhalative Deposits

2.1. Sedimentary-exhalative deposits:

As of 2004, SEDimentary-EXhalative - SEDEX - deposits comprise 40% and 65% of Zn and Pb production in the western world, respectively (Goodfellow & Lydon, 2007). The term "SEDEX" was developed by Carne & Cathro (1982), the term stemming from the observation that sulphides in this deposit-type are fine-grained, stratified and often appear synsedimentary. SEDEX deposits occur in first-order intracratonic and epigenetic sag basins (fig 2.3) and are dominantly mid-Proterozoic–Present in age with rare Archean occurrences. Two spikes in SEDEX occurrence are observed in the Proterozoic in Australia (Mt Isa amongst others), Canada (Sullivan), South Africa (Gamsburg), while Phanerozoic deposits include Red Dog in Western Canada and Meggen and Rammelsburg in Western Europe. The distribution of SEDEX deposits through geological time is interpreted to be related to supercontinent breakup during extensional tectonic regimes, and the abundance of seawater sulphate that supplied sulphur to the system (E.g. Goodfellow et al, 1993, Lyons et al, 2006).

2.1.1. Geology

Sedimentary-exhalative-style deposits are hosted in oxygen-deficient sedimentary basin successions deposited as intracratonic and epigenetic basin fill, or distal back-arcs (Goodfellow & Lydon, 2007). Host lithologies include carbonaceous shales, sands, siltstones (typically dolomitised), cherts, sedimentary breccias, and rare volcaniclastic deposits (Anderson, 1990, Leach et al, 2010). Turbidites, slump debris deposits, volcaniclastics and tuffs are less typical host rocks. SEDEX-style systems are thought to be associated with regional-scale extensional events, occurring within extensional, first-order sedimentary basins, typically hundreds of kilometres long. Second-order basins are smaller scale at tens of km's long and are identified in the stratigraphic column by an abrupt transition to submarine debris flows and breccias, where extensional basin formation generates between 4-15km of turbidites, conglomerates, sandstones and red beds. SEDEX mineralisation occurs within the first 1-4km of the sedimentary pile. Occasional interbedded volcanic ashes and tuffs (e.g. Rammelsburg), suggest regional volcanism (Emsbo, 2009, Large and Walcher, 1999). Regional-scale faulting provides a "plumbing system" for hydrothermal fluids to upwell. Sedimentary-exhalative deposits often share a distal spatial relationship with bedded barites, sedimentary manganese and phosphates, and Mississippi

Valley-Type deposits (Kelly et al, 1987, USGS, 2010). SEDEX-style deposits do not share an obvious spatial or temporal association with igneous centres

2.1.2 Ore:

SEDEX deposits consist of laterally continuous (up to kilometres long), tablular and finely grained sulphide ore lenses, typically intercalated by chemical sediments and locally bound by sub-basin faults (Kelly et al. 1986, Goodfellow & Lydon, 2007, Emsbo, 2009). Ore lenses exhibit an average height-width ratio of 1:20 (Goodfellow & Lydon, 2007). The main sulphide is pyrite (though pyrrohtites are described in Sullivan and Mt. Isa), sphalerite, galena and Ag-sulfosalts, though some may also contain economic copper sulphides. Disseminated, stockwork and vein mineralisation is observed to underlie many SEDEX deposits, which are interpreted as feeder zones contributing to mineralisation. Deposits which occur close to "feeder zones" (interpreted from vein stockworks) are described as "vent-proximal", while those which share a weaker spatial relationship with feeder zones are termed "vent-distal" (Sangster and Hillary, 2000, Goodfellow & Lydon, 2007). Vent-proximal deposit mineralisation can be broadly divided into four zones: 1) Bedded sulphide, 2) Vent complexes, 3) Sulphide stringers and, 4) distally hydrothermally altered sediments and disseminated sulphide (Goodfellow & Lydon, 2007). Vent-distal deposits have weak zonation and well-developed bedding (Goodfellow & Lydon, 2007). Highest-grade mineralisation occurs at the boundary between the vent complex and overlying ore lenses, interpreted as leaching from the stockwork and deposition in the overlying sediments (Goodenough & Lydon, 2007). Feeder zones contain elevated gold, silver, barium, cadmium, antimony and arsenic and comprise sulphides, carbonates, quartz veining and alteration of the adjacent deposit footwall. Manganese alteration halos are often observed (Kelly et al, 1986, Goodfellow & Lydon, 2007, Emsbo, 2009).

SEDEX deposits are interpreted to form from ore precipitation via exhalation of low temperature metalliferous fluids onto a sea floor followed by mixing and cooling with seawater in an extending basin (fig 2.3). Initial basin extension produces horst and graben structures, while subsequent post-rift and sag promoted hydrothermal fluid convection capable of mobilising Zn and Pb hosted in rift sediments. Re-activation of regional scale fault systems provides the "plumbing system" for basinal hydrothermal fluids to ascend and exhale onto the seafloor. The orefluids are initially oxidising and carry Pb and Zn as chloride complexes, before reacting with H_2S in the seawater. Geothermal heating facilitated by the overlying sedimentary pile, combined with downwelling of cold, dense seawater enables a free hydrothermal convective system to scavenge, transport and deposit metals on the seafloor via exhalation. Seafloor topography exhibits a strong control on

deposit geometry (Goodfellow, 1987, Goodfellow & Lydon, 2007). Absolute dating of SEDEX deposits is difficult due to a lack of dateable minerals.

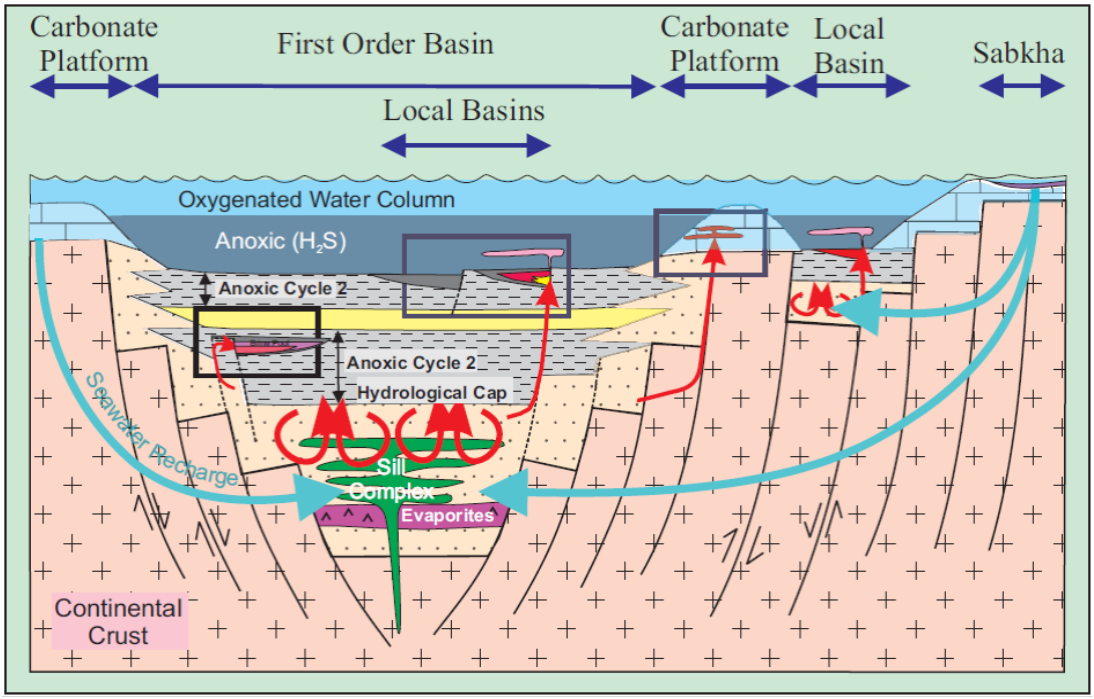

Figure 2.3 - SEDEX genetic model (Goodfellow & Lydon, 2007). Secondary porosity (regional-scale fracture system) of the continental crust is produced by extensional rifting, enabling down-welling of cold seawater, heating by a distal magmatic source and circulation along a large-scale hydrothermal convective system.

Mississippi Valley-Type Deposits

2.2. Mississippi Valley-Type (MVT):

Mississippi Valley-Type deposits contain approximately 27% of global Zn-Pb resources and are encountered worldwide, though particularly in the Southern United States. MVT systems contribute 25 and 26% of global Pb and Zn production, respectively (Paradis et al, 2007). Ore tonnage is variable, ranging between 1-100Mt, while orefields also vary significantly in size (e.g. Orsk Orefield at 350,000km^2, USGS, 2009). MVT deposits are believed to form from a low temperature, high salinity hydrological system scavenging metals from large-scale sedimentary basins via regional-scale fluid flow (Anderson, 1975, Leach et al, 2010). MVT systems share an affinity for carbonate sequences, are considered to be related to major compressional thrusting events, and differ from skarns in that they do not exhibit a temporal or spatial relationship with igneous intrusions (Leach et al, 2005, 2010, USGS, 2010).

2.2.1 Geology

MVT deposits are hosted in coarse-grained limestones, dolostones and sandstones in underformed carbonate shelf sequences, passive margins, back arcs and orogenic thrust terranes (Leach et al, 2010 – Fig 2.4). MVTs are dominantly Phanerozoic (80%), comprising 94% of total Zn-Pb in all MVT systems, while the remaining 20% of deposits are Proterozoic and contribute the remaining 6%. MVT deposits are believed to form from regional-scale groundwater migration, where compressional thrusting, topographic head and high rainfall provide the mechanisms for regional-scale fluid-flow. MVT deposits are typically small (<15Mt), though normally form clusters which may extend to form districts (Piranjo, 2009). Leach et al (2010) interpret the temporal relationship between MVT systems and large-scale thrust terranes to be related to supercontinent breakup and collision cycle. There is consistent evidence for large-scale dissolution of the host rock in the form of collapse structures, solution breccias and karsting, which provide lithological traps for the orefluids (Sangster, 1983, Pijarno, 2009).
MVT ore fluids are low temperature, high salinity ranging between 90-150 ^{o}C and 10-30 wt.% NaCl, respectively (Leach et al, 2005, Piranjo, 2009, USGS, 2009). Metals are interpreted to be leached by fluids in large sedimentary basins and transported in the orefluid as chloride complexes. Given that the orefluid is oxidised, this means that sulphate is the dominant sulphur species and, therefore has to be mixed prior to ore precipitation or reduced at the deposition site (Anderson, 1975, Leach et al, 2010). Host rocks with reducing hydrocarbons are seen as

preferable (Leach et al, 2010). MVT ore fluids are considered to be analogous with oil-field brines in deep sedimentary piles. Absolute dating of MVT deposits is difficult due to a lack of dateable minerals.

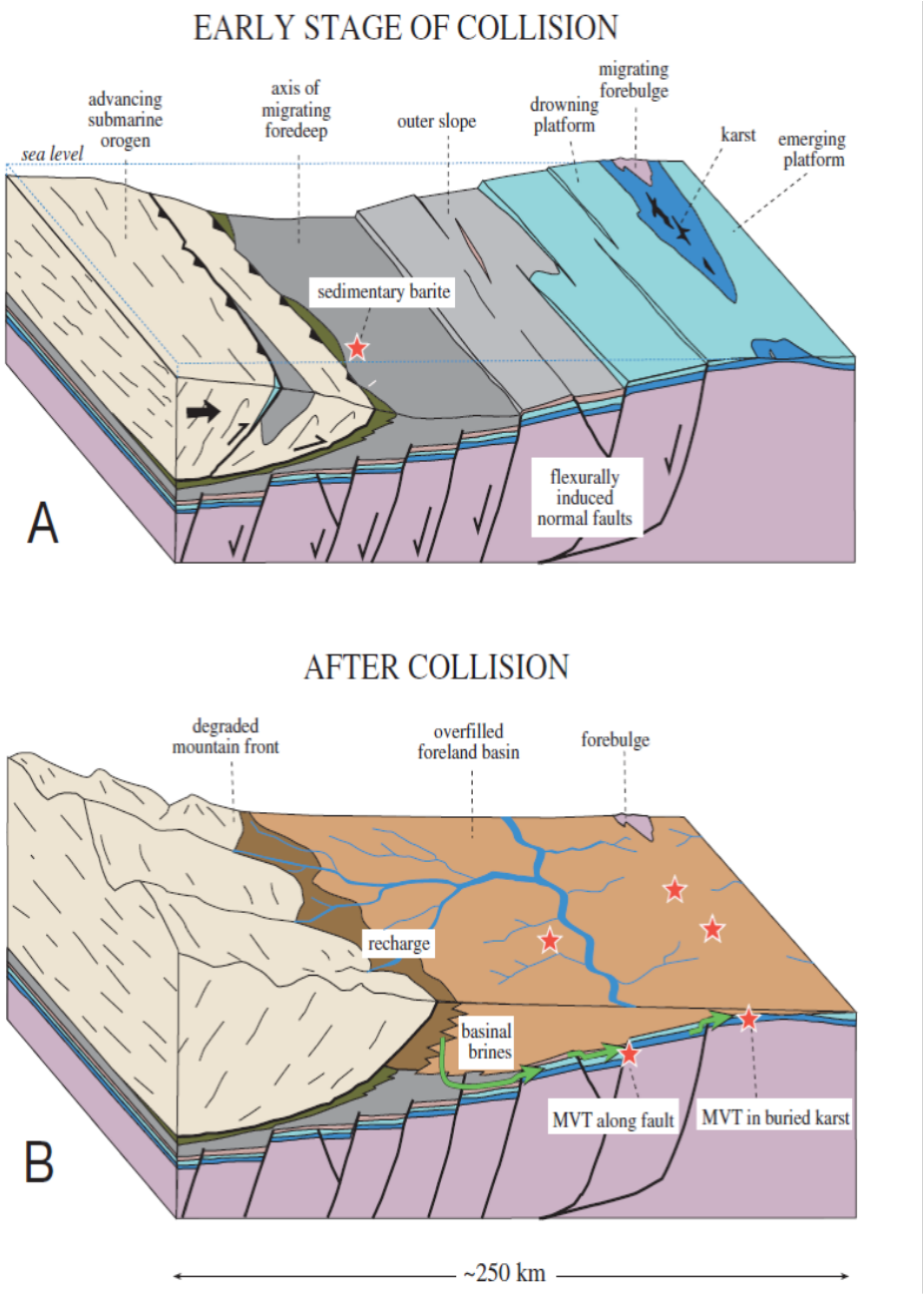

Figure 2.4 - Geological setting for the formation of foreland basins. In diagram A, the foreland basin forms during plate convergence, where the submarine plate loads the passive margin, producing an emerging platform and migrating foreland basin, extensional normal faulting and foreland bulge. In Diagram B, tectonism has ceased, and the foreland basin is overfilled by sediment. Sediment overfill is interpreted to create the ideal hydrological conditions to form MVTs (Leach et al, 2010)

2.2.2. Ore

MVTs typically have a simple mineralogy, comprising galena-sphalerite, barite ± Fluorite, iron-sulphides, and dolomite, calcite, ankerite, siderite, and gypsum gangue (Leach et al, 2001, 2010, Paradis et al, 2007, USGS, 2010). Copper sulphides are low, though Cornwallis district in Canada (Randell and Anderson, 1996) and the Viburnum Trend of the Southeast Missouri district (Sangster, 1990) contain economic Cu. More exotic Cu, Co, Ni, Ag, As and Sb sulfosalts have been recovered from MVT systems in the Viburnum Trend (Leach et al, 2005, Pijarno, 2009).
A principle characteristic of MVT systems is that mineralisation is epigenetic, meaning that mineralisation occurs after deposition of the host rock (Leach & Sangster, 1993). MVT deposits are broadly stratiform on a regional scale, though may be locally discordant and cross-cut stratigraphies. Systems may occur as several massive replacement zones, while secondary porosity is a principle control on ore morphology. Examples include mineralisation in dissolution breccias (e.g. Pine Point) and interconnected karst systems (East Tennessee). Breccia zone mineralisation may be broadly tabular or conical (Paradis et al, 2007).

Irish-type deposits

2.3. Irish-Type Deposits:

The phrase “Irish-Type” refers to Lower Carboniferous, carbonate-hosted Zn-Pb deposits hosted in the Irish Midlands in the Republic of Ireland. Navan – by far the largest discovered Irish-type ore deposit - occurs approximately twenty kilometres northwest of the northern margin of the Dublin Basin (Fig 1.1, 2.1, 3.1). Irish-type deposits share similarities with SEDEX and MVT systems (Table 2.2) in that they show a clear affinity for carbonate stratigraphy and simple Zn-Pb mineralogy, are spacially and temporally related to regional-scale faulting and first order basins, and formed by mixing of two fluids (e.g. Anderson et al, 1998, Everett et al, 2001, Fallick et al, 2001, Wilkinson et al, 2003, 2005, Wilkinson, 2010) (Fig 2.5). This hybridisation of characteristics has led to Irish-type mineralisation being described as a subset of SEDEX and MVT deposits, or as a separate deposit-type in its own right.

2.3.1. Geology:

Irish-type base-metal deposits in Ireland are hosted in Lower Carboniferous (Courceyan-Arundian) marine transgressive carbonates. Navan is hosted in the shallow marine carbonate Pale Beds sequence (Navan Group – Fig 3.1), while Tynagh, Silvermines, Galmoy, and Lisheen occur in

stratigraphically higher (though sometimes older, given the S-N Tournaisian transgression, Andrews, 1986) Waulsortian mudbank limestones (Russell et al, 1981, Hitzman & Large, 1996, Hitzman & Beaty, 2003, Wilkinson et al, 2005, Ashton et al, 2015). Deposits occur adjacent to regional scale, Chadian-Arundian ENE trending normal faults interpreted as conduits for hydrothermal fluid upwelling from the Lower Palaeozoic Basement. These upwelling fluids are widely interpreted to mix with an evaporated seawater brine enriched in bacteriogenic sulphur close to normal faults, and in zones of carbonate dissolution with enhanced second porosity (e.g. Russell, 1978, Samson and Russell, 1987, Everett et al, 2001, Lee, 2002, Wilkinson, 2010, Ashton et al, 2015). Mixing of these two fluids at salinities >15 wt.% NaCl and 200^{o}C promoted ore formation. Hydrothermal dolomite horizons are interpreted as important aquitards that focused mineralising fluids (e.g. Hitzman & Large, 1986, Hitzman & Beaty, 2003, Wilkinson, 2010, Ashton et al, 2015). Spatial association with first-order basin faulting indicates a strong structural control on mineralisation (Russell et al, 1981, Taylor, 1984, Hitzman et al, 2002, Ashton et al, 2015). He analysis of fluid inclusions by Davidheiser-Kroll (2014) on the Navan deposit advocates a mantle heat component produced by decompressional partial melting of the lower crust during basinal extension.

2.3.2. Ore

Irish-type deposits have a similar mineralogy to MVT systems, comprising Zn-Pb-Fe sulphides, Ag-Sb-Cu sulfosalts, and dolomite, siderite and calcite gangue. Irish-type mineralisation is texturally complex, comprising soft-sediment replacement and preservation of cross-bedding (Anderson, 1990, Redmond, 1991), cavity and geopetal-infills (Hitzman et al, 1996), cross-cutting veining and breccia matrix infills (Mills, 1987, Hitzman et al, 2002). Mineralisation is variously described as syngenetic, syn-diagenetic, to epigenetic, though hydrothermal chimneys and vent biota at Silvermines and the Ballynoe barite deposit suggests that at least a small component of Irish-type ore formation formed with the host rock (Boyce et al, 1983b, Boyce et al, 2003). Irish-type deposits are noted to contain higher Cu, Fe, and Ag than most MVT deposits (Hitzman & Beaty, 1996) and may contain significant Fe-sulphides (particularly at Navan in the Conglomerate Group Ore), though this is normally a minor component of mineralisation. The paragenesis of the Irish-type mineralisation has been constrained to a five-stage process by Hitzman and Beaty (1996):

1) Pre-sulphide deposition of dolomite – Host rock dolomitisation preceded sulphide mineralisation and is strongly spatially associated with interpreted “feeder zones” at Lisheen, Galmoy, and Silvermines. Spatial association at Navan is less obvious. Barites at Lisheen and Silvermines are overprinted by sulphides, though occur post-mineralisation Navan.

2) Iron-sulphide replacement of carbonates - Fe sulphides are paragenetically earliest and form with minor banded sphalerite.

3) Replacement of carbonates by sphalerite

4) Mainstage sulphide mineralisation – Sphalerite, galena, iron-sulphides and sulfosalts co-precipitate. Sphalerites contain discontinuous bands of dolomite. Colloform, coarsely-grained sphalerites are intergrown by pyrite, galena and sulfosalts. Barites and Cpy-sulphides are present in mixed assemblages.

5) Late carbonate precipitation – Phase comprises calcites with sub-ordiante dolomite, galena and sphalerite.

Ambiguity surrounding the formational conditions of the Irish-type deposits splits academic opinion into those who advocate a SEDEX-style formation (e.g. Andrew & Ashton, 1985, Fallick et al, 2001, Blakeman et al, 2002, Lee & Wilkinson, 2002, Wilkinson, 2003, 2005, Wilkinson, 2010 Davidheiser-Kroll, 2014, Ashton et al, 2015), and others who suggest Irish-type deposits are MVT-style (e.g. Peace, 1999, Peace et al, 2003, Leach et al, 2005, 201, Hitzman, 1999, Leach et al, 2001, Leach et al, 2005, Leach et al, 2010) Others, including Wilkinson et al (2003) see classification as either deposit-type as inadequate in underlining hybrid features that distinguish Irish-type deposits.

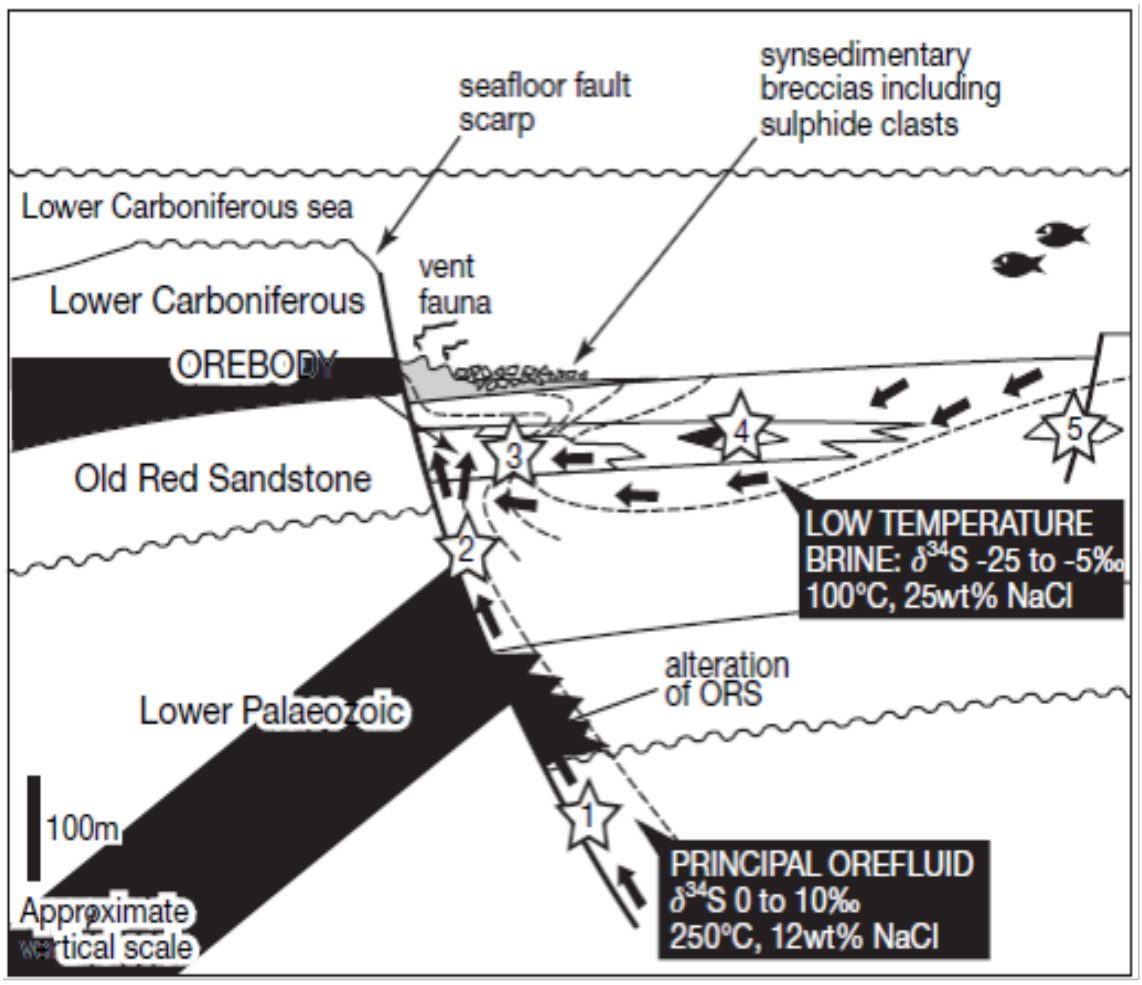

Figure 2.5 - Cartoon genetic model for Irish-type deposits hosted in the Courceyan and Waulsortian limestones. The model advocates hydrothermal fluid convection by heating of cold, down-welling seawater, and mixing of fluids at hydrothermal chimneys close to early-forming normal faults (Wilkinson et al, 2005A)

2.3.3. Mineralisation temperature

Accurate fluid inclusion readings are difficult to obtain from Irish-type deposits due to the small size of many fluid inclusions (e.g. Hitzman & Beaty, 2003, Ashton et al, 2015, Wilkinson, 2015 – Pers comm). Coarsely-crystalline minerals are typically selected for fluid inclusion studies, though fine-grained mineralisation studies have also been conducted at Tynagh (Banks and Russell, 1992) and Lisheen (Thompson et al, 1992). Analysis of fluid inclusions in calcites and barite carries the risk of low accuracy, due to the risk of re-equilibration of the ore fluid under lower internal overpressures if the host crystal undergoes post-mineralisation deformation (Wilkinson, 2010). Calcite, dolomite, barite, and sphalerite inclusions have been analysed to constrain Irish-type mineralisation

temperature (e.g. Samson and Russell, 1987, Everett and Wilkinson, 2001, Knight, 2012, Peace, 1999, Wilkinson et al, 2002, Peace et al, 2003, 2005a, 2005b, Wilkinson, 2010, Treloar, 2014, Marks, 2015), though the sheer volume of study dedicated to fluid inclusion microthermometry is difficult to concisely summarise. Table 2.1 compiles the results of several studies providing mineralisation temperatures for the major Irish-type deposits.

Wilkinson (2010) identifies a broad homogenisation temperature range of 70-280°C and 7-29 wt.% salinity for the Irish-type deposits. At Navan, two fluids were involved in mineralisation - a high temperature, low salinity (100-140°C, 5-10 wt.% eq. NaCl) metalliferous, hydrothermal fluid, and a low temperature, high salinity (70-100°C, 20-25 wt% eq. NaCl) bacteriogenic sulphide-enriched brine (Fig 2.5, 2.6). The hydrothermal fluid transported metals as chloride complexes from Lower Palaeozoic basement volcanic and volcaniclastics, while the latter is interpreted to be a cold, down-welling residual brine enriched in bacteriogenically reduced sulphur. Mixing of these two fluids via exhalation close to the seafloor promotes metal precipitation via reduction in temperature and pH (Anderson, 1975, Russell, 1978). Homogenisation temperatures exceeding 280°C have been recorded in the Waulsortian and are associated with elevated Cu and Ni (Wilkinson, 2010 and pers comm), while apparent boiling in SWEX-S barite inclusions at Navan may constrain fluid exhalation to less than 100 metres below sea level (Treloar, 2014).

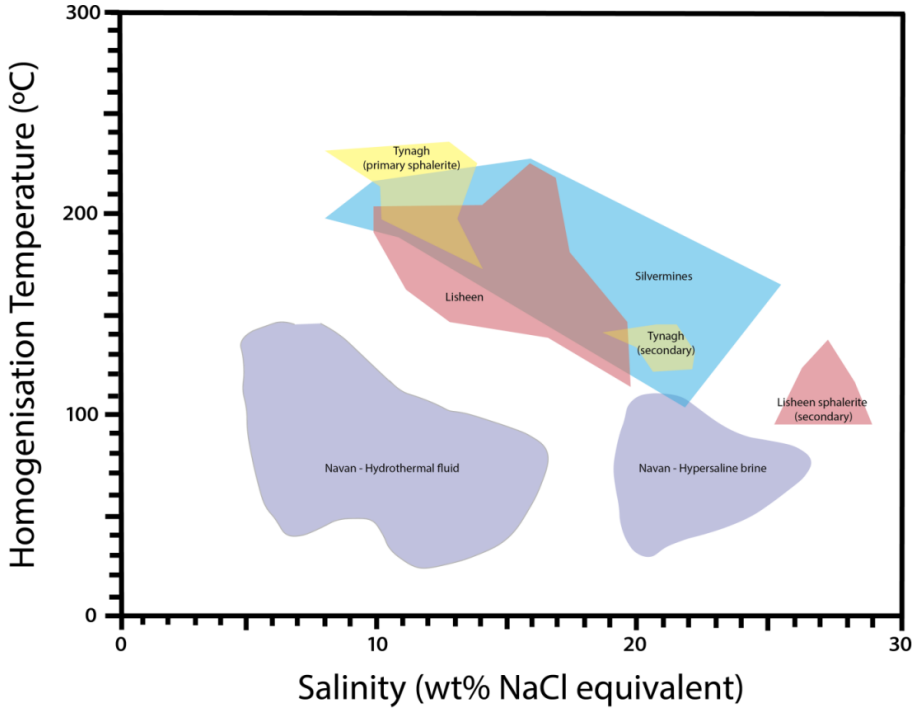

Figure 2.6 - T_h and fluid inclusion salinity fields obtained from Navan, Tynagh and Lisheen. Original diagram adapted from Davidheiser-Kroll (2014) and fluid inclusion data compiled from Everett et al (1999), Everett and Wilkinson (2001), and Treloar (2014)

	Host geology	Mainstage homogenisation temperature (T_h)/salinity wt %	Mineralisation	Mineralisation textures
Navan	Courceyan micrites, dolomites, limestones, calcarenites and sandstones (U-Lens)	100-140 °C, 5-10 wt %	Zn-Pb-Fe sulphides. Calcite, barite and dolomite gangue. Antimony and arsenic-sulfosalts may occur as boulangerite lamellae, particularly at Silvermines	High grade massive lenses, pods, breccia fills, clast and fine-grained replacement, geo-petal infills, veins, disseminated, laminated - massively banded, chaotic
Lisheen	Waulsortian limestones and dolomite breccias	87-240 °C, 7-20 wt %		Massives lenses, pods, breccia matrix fill, sulphide-dolomite veins and veinlets, Banded, layered, colloform
Silvermines		140-220 °C, 8-28 wt %		Stratiform lenses, layered sulphides, vein-veinlets, rare silicified breccias in higher temperature mineralisation
Galmoy		160-170 °C, 13-14 wt %		Stacked stratiform lenses and mineralized breccias
Tynagh		70-243 °C, 8-21 wt %		Soft-sediment replacement. Banded, cavity and geopetal-infills. Capped by banded ironstone formation. Sulphides do not occur more than 100 metres from regional extensional faults

Table 2.1 - Summary of Irish-type deposit characteristics. T_h is lower in Navan than other Irish-type deposits. T_h and salinity wt % values obtained from Riedel (1980), Samson and Russell (1987), Hitzman and Beaty (1996), Wilkinson et al (2005A), Wilkinson (2010), Ashton et al (2015)

2.3.4. Dolomitisation

Dolomitisation is widely observed in the Lower Carboniferous carbonate stratigraphy of the Irish Midlands and has been interpreted to be temporally related to mineralisation (Anderson, 1990, Boast et al, 1981, Braithwaite & Rizzi, 1997, Everett & Wilkinson, 2001, Hitzman & Beaty, 2003, Mulhall & Sevastopulo, 2004, Reed & Wallace, 2004, Wilkinson et

al, 2005). Dolomitisation in Waulsortian-hosted deposits precedes ore formation and was produced by interaction of heated Carboniferous seawater with the carbonate host rocks during early normal faulting (e.g. Wilkinson, 2003). The wide variability in dolomitisation textures and lithostratigraphy complicates correlating dolomite events across the Irish Ore Field (Hitzman & Beaty, 2003, Wilkinson, 2003).

Early-stage dolomite is generally coarsely-crystalline and planar, while those that cross-cut and replace sulphide mineralisation are fine-grained (Wilkinson, 2003). Dolomites destroy primary porosity and variably cross-cut sulphide mineralisation at Navan, though enhance secondary porosity in Waulsortian limestones (Hitzman et al, 2002, Wilkinson, 2003, Wilkinson, 2015 – Pers comm). Dolomitisation is best developed in the southern Irish Midlands close to the Leinster Massif, becoming less developed in Navan and Silvermines. Late-stage dolomite replacement spatially related to faulting at Galmoy, Lisheen and Tynagh has been widely observed (Hitzman & Beaty, 2003, Wilkinson, 2003). Complex dolomite zoning is well-described, suggesting a multi-stage paragenesis (e.g. Anderson, 1990, Rizzi, 1992, Braithwaite & Rizzi, 1997)

	Sedimentary-exhalative (SEDEX)	**Mississippi Valley-Type (MVT)**	**Irish-Type**
Geographical distribution	Worldwide – Canada, Australia, Germany, Alaska	Worldwide. Mainly North America, especially the Southern United States. Other occurrences in China, Iran, Mongolia, Russia, Canada and Australia	Irish Midlands
Geological setting	Extensional first and second-order basins	Carbonate platform sequences and thrust belt terranes	Regional-scale, extensional sedimentary basins.
Geological age	Mid Proterozoic-present - Strong association with extensional breakup of Pangaea. Rare occurrences in Archean	80% of deposits are Phanerozoic, 20% are Precambrian. Individual deposits are difficult to provide an age for, due to a lack of dateable minerals.	Lower Carboniferous (Lower Courceyan – Arundian)
Tonnage	Variable – 2 – 130 Mt	Extremely variable – Median tonnage of 7Mt @ 7.9% Zn+Pb	Navan – 110MT @ 8% Zn and 2% Pb. Lisheen – 23Mt @ 11.5% Zn & 1.9 Pb Silvermines – 17.7Mt @ 6.4% Zn & 2.5% Pb Galmoy – 6.9Mt @12.8% Zn & 1.3% Pb Tynagh – 9.2Mt @ 5% Zn & 6.2% Pb
Host-rock	Varied – Includes sandstones, siltstones, limestones, dolomites, cherts, and turbidites.	Limestones, dolostones and rare micrites	Limestones, dolomites and micrites
Mineralisation	Zn-Pb-Ba (Cu). Ag, Sb and As may occur in sulfosalts	PbS, ZnS, FeS_x, $BaSO_4$. Ag may occur in sulfosalts	Dominantly PbS-ZnS. Minor Ag sulfosalts. Pyrite is prevalent in the CGO at Navan
Timing of mineralisation	Syngenetic – early diagenetic	Epigenetic	Epigenetic, though exhibits characteristics which suggest a clear syngenetic component

Mineralisation temperature	Low – 100-200°C	Low – typically 75-200°C	100-240°C
Ore geometry	Stratiform, fine-grained and laminated to bedded sulphides. Pyrites may exhibit colloform-framboidal sub-micron textures. Low-grade metamorphism may produce porphyroblastic pyrites	Typically stratiform on a regional scale (tens of km's), though show local discordance, particularly in fault-controlled deposits. Ore morphology is strongly controlled by secondary porosity features (e.g. dissolution and collapse breccias, karst networks and open cavities).	Regionally stratform lenses, replacement of soft-sediment textures, crackle breccias, veins, pods, lenses, fine-grained replacement textures and disseminated sulphides
Examples	Mt Isa, Red Dog, Sullivan, MacArthur River, Broken Hill	Tri-State District, Pine Point, Viburnum Trend, Eastern Tennessee, Silesia, Jinding, Ozark	Navan, Lisheen, Galmoy, Silvermines, Tynagh

Table 2.2 - Geological characteristics of SEDEX, MVT, VMS, and Irish-Type Deposits. Adapted from Anderson (1975, 1982), Kelley et al (1986), Hitzman & Beaty (1996), Johnston (1999), Menzie & Moseir (1986), Wilkinson et al (2003), Leach et al (2010), USGS (2010), Wilkinson (2010) and Ashton et al (2015)

Chapter 3

Geology of Navan

This chapter focuses on the geological history of the Navan area, the mineralogy of the Navan Deposit and geological controls on Navan ore.

3. Introduction

The Navan ore deposit is underlain by the Lower Palaeozoic Basement – an Ordovician lithological package consisting of Ordovician-Silurian shales, greywackes, volcaniclastics and syenite intrusives. The basement is unconformably overlain by immature fluviatiles and mudstones. Immersion is marked by the deposition of the Laminated Beds (LB) – a 40 metre thick succession of thick mudstones withintercalating siltaceous intervals. The sequence develops as a prograding, shallow marine carbonate shelf sequence, transitioning into oolitic limestones, dolomites and micrites, becoming increasingly sandy up-stratigraphy. The Navan Deposit, - divided into five lenses (termed the 5-1), the U Lens and Southwest Extension - occurs exclusively in the Pale Beds (fig 3.1). The lowermost 5 Lens is the most laterally continuous and highest grade, while the overlying lenses are smaller and less laterally continuous up-stratigraphy. The Pale Beds are conformably overlain by the Shaley Pales (SP) and Argillaceous Bioclastic Limestone (ABL).

The sequence is eroded by the Boulder Conglomerate – a mega-conglomerate sequence that increasingly downcuts to the southeast and erodes to the Lower Palaeozoic Basement at its deepest. The conglomerate is interpreted to have formed from catastrophic slope collapse produced by basinal extension into the Chadian. The unconformable contact produced by erosion is referred to as the “Erosion Surface” (“ES”), while the overlying slump debris and mega-conglomerate pile is named the “Boulder Conglomerate” (“BC”). The Boulder Conglomerate hosts the Conglomerate Group Ore, comprising 3% of total ore, comprising iron-sulphide (pyrite and marcasite) and sub-ordinate sphalerite and galena. The Boulder Conglomerate is overlain by the Tober Collen Mudstone and the Upper Dark Limestones (UDL). The sequence underwent later

reverse/wrench faulting and basin inversion, interpreted to be end-Variscan (Ashton et al, 2015). The Navan area is bound by the Longford Down Inlier and Gangareenth Terrane to the north and northeast. Dolomitisation in Navan is less pervasive than that in the Waulsortian-hosted deposits (Rizzi, 1992, Rizzi & Braithwaite, 1997, Ashton et al, 2015) and is restricted to the lower Pale Beds. Dolomitisation and faulting were key lithological and structural controls on the grade and distribution of mineralisation at Navan (e.g. Wilkinson, 2003, Ashton et al, 2015)

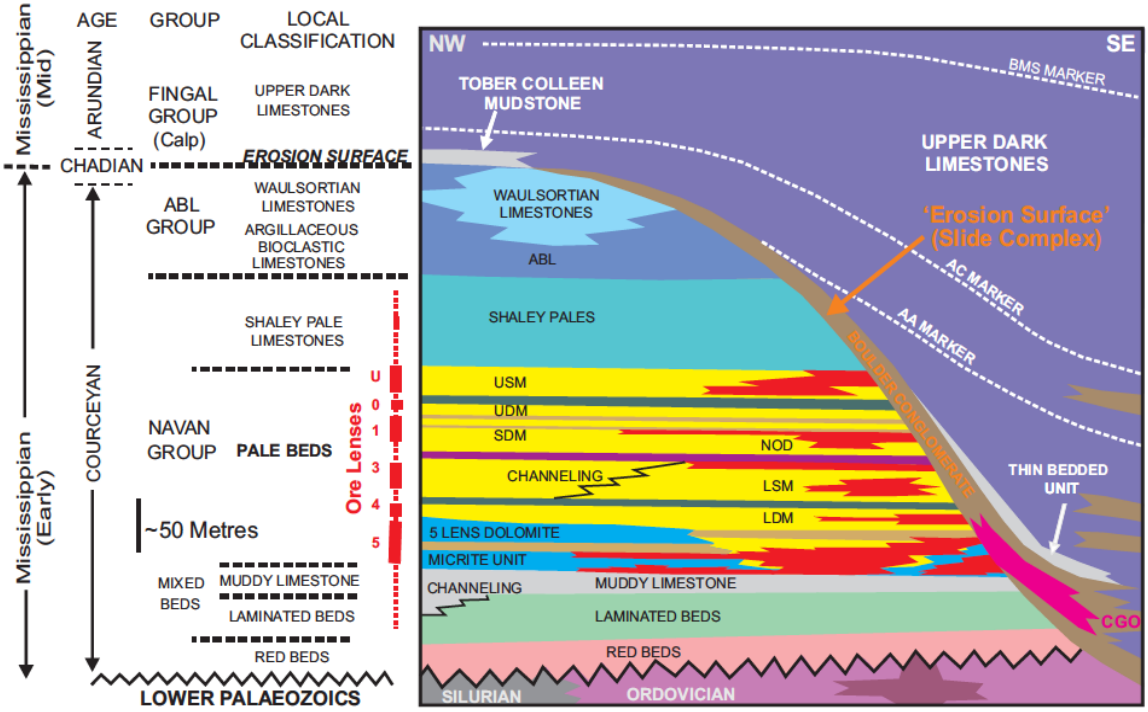

Figure 3.1 – Stratigraphic table of the Navan area. The Erosion Surface increasingly downcuts the Pale Beds sequence further southeast and bisects the Navan Orebody (shown in red) (Blakeman et al, 2002, Ashton et al, 2015)

3.1. Regional geology:

3.1.1. Lower Palaeozoic Basment:

The Lower Palaeozoic basement underlies the Navan Deposit and outcrops to the northeast. The basement consists of a complexly sheared, folded and grenschist metamorphosed series of shales, greywackes, volcaniclastics and Ordovician intrusive sequence metamorphosed to greenschist facies (Anderson, 1990). The basement underlying the Navan Deposit is considered to be the southwest continuation of the Gangareenth Terrane, which intruded as an island arc in Ordovician-Silurian (Romano, 1980, Vaughan, 1991, Vaughan and Johnston, 1992, Geraghty and McConnell, 1999,

McConnell et al, 2001). Syenite intrusives outcrop over several square kilometres in proximity to Navan, though there is no obvious temporal relationship with ore. The Grangegeeth Terrane belongs to the Longford Down Inlier - an uplifted horst of the Lower Palaeozoic divided into the Longford Down Northern Belt, The Longford Down Central Belt, and the Grangegeeth Terrane, respectively.

3.1.1.1. Longford Down Northern Belt

The Longford Down Northern Belt consists of Ordovician greywackes and interbedded shales, cherts, metabentonites. arenites, and cobble conglomerates (Murphy et al, 1991). Murphy et al (1991) interpreted the sequence to represent a volcanic arc that intruded to the southeast, while the felsic and metamorphic members originated from continental sediments to the northwest.

3.1.1.2. Longford Down Central Belt

The Longford Down Central Belt consists of mafic-intermediate volcanics, epiclastics, and interbedded carbonaceous shales, the latter becoming increasingly prevalent along the southeast. Pelagic lithologies consist of carbonaceous shales, mudstones, metabentonites and cherts (Murphy et al, 1991). Llandovery and Wenlock age greywacke sandstones and metabentonites overlie the pelagics (Murphy et al, 1991).

3.1.1.3. The Grangegeeth Terrane:

The Grangageeth comprises Ordovician-Silurian volcaniclastics, Llanvirn sediments and Slane group mugearite flows, outcropping between Navan and Clogher Head in County Louth (Murphy et al, 1991). The package is unconformably overlain by the Grangegeeth Group, interpreted to be Llandeilo to lower Caradoc and consists of volcanic conglomerates and sediments (Romano, 1980, Murphy et al, 1991). The Grangegeeth is overlain by Mellifont Abbey Group black shales and succeeded by mudstones and volcaniclastic sandstones (Murphy et al, 1991).

3.1.2. Red Beds (Baronstown Formation):

The Devonian Red Beds sequences unconformably overlies the Lower Palaeozoic basement and consists of a heavily hematised sequence of immature fluviatiles and pebble conglomerates. Initial marine transgression is represented by a 0.5 metre green reduction zone at the top of the formation and the overlying Laminated Beds (Anderson, 1990).

3.1.3. Laminated Beds (Portandogh Member – Liscartan Formation)

The Laminated Beds (LB) overlie the Red Beds and consist of a forty metre thick succession of thinly interbedded siltstones, sandstones, calcarenites and mudstones. The Formation is sub-divided by Philcox (1984) into six units – CG-CB, where CG-CE comprise sandstones and silty shales, CD-CC consist of calcareous siltstones and mudstones, and CB contains bioclastic grainstones (Philcox, 1984, Rizzi, 1992). The Laminated Beds are interpreted to mark the beginning of marine transgression. (Ashton et al, 1986, Rizzi, 1992).

3.1.4. Muddy Limestone (Bishopscourt Member – Liscartan Formation)

The Muddy Limestones overlie the Laminated Beds and consist of a 10-25 metre thick, varying sequence of microconglomerates, calcirudites, and bioclastic argillites. The lower section of the formation comprises poorly sorted, bioclastic microconglomerates and calcirudites, while the upper section consists of dark, well-bedded argillites (Philcox, 1984, Anderson, 1990, Rizzi, 1992). The Muddy Limestone grades into the Muddy Limestone Transition - a thinly bedded sequence of oncolitic, mud-abundant micrites that transitions into the 5 Lens Micrite at the base of the Pale Beds sequence.

3.1.5. Pale Beds (Meath Formation)

The Pale Beds contain ninety-seven percent of the Navan ore and consist of a sequence of deeper water limestones, micrites, dolomites, calcarenites, and argillites (Anderson, 1990, Strogen et al, 1990, Rizzi, 1992). The basal unit of the Lower Pale Beds comprises a 60 metre thick succession of clean, bird’s eye and styolitic micrites. The Pale Beds

sequence becomes increasingly argillaceous and sand and silt-rich up-stratigraphy. Calcisiltite sequences (referred to as “Marker Horizons”) denote the upper and lower limits of the ore lenses and are often intensely dolomitised (Andrew & Ashton, 1985, Blakeman et al, 2002, Ashton et al, 2015):

- The 5 Lens Dolomite is a 6-12 metre thick hydrothermal dolomite that replaced a pre-existing calcarenite succession that interbeds the 5 Lens Micrite. The 5 Lens Dolomite marks the 5 Lens hangingwall and is interpreted as an important control on ore, while a thin, green shale horizon denotes the maximum extent along the base of the 5 Lens (I.e. the footwall). The dolomite is interpreted as forming a lithological cap and aquitard to migrating ore fluids and can occur up to ten metres thick in the western mine area (Andrew & Ashton, 1985). The 5 Lens Dolomite is not a marker horizon, though it is clearly distinguishable from the enclosing 5 Lens Micrite and is interpreted to be a major aquitard for hydrothermal fluids.

- The top of the 5 Lens is defined by the Lower Dark Marker (LDM), a sequence of thickly bedded, bioturbated calcisiltites.

- The 4-Lens hanging wall is denoted by the Lower Sandstone Member (LSM), a massively bedded, clean calcareous sandstone.

- The 2/3 Lens is defined by the Nodular marker - a nodular, crinoidal calcisiltite which denotes the hanging wall.

- The hanging wall of the 1-Lens is marked by the Upper Dark Member (UDM), a thickly bedded sequence of dark shales and intercalating calcisiltites. The base of the 1-Lens is observed by pale grey, fossiliferous calcarenites. The Lower Bryozoan Marker (LBM) is identified by an increase in finger bryozoan, though it is not always well-developed, especially west of the mine.

- The Upper Sandstone Member (USM) - a massively bedded, pale grey sandstone - denotes the base of the U-Lens.

3.1.6. Shaley Pales (Moathill Formation)

The Shaley Pale Limestones (SP) comprise a 110 metre thick succession of interbedded limestones (packstones and wackstones), shales and calcisiltites (Philcox, 1984, Anderson, 1990, Strogen et al, 1990, Rizzi, 1992). Bedding profiles vary between irregular to planar, while contacts can be either gradational or sharp. Limestone bedding varies between a few cm's to up to 70cm thick. The SP are heavily faulted and truncated by the down-cutting Chadian Erosion Surface, which restrains efforts to correlate the sequence (Anderson, 1990).

Philcox (1984, 1990) divides the Shaley Pales into three sub-groups – the Lower, Middle, and Upper Shaley Pales. The Lower Shaley Pales is at least 25 metres thick and contains at least three interbedded calcareous sandstones. The Middle Shaley Pales Limestones is up to 50 metres thick and consists of interbedded calcarenites, sandstones, siltstones, and calcareous, argillaceous sandstones. The uppermost bed of the Middle Shaley Pales consists of a finely grained sandstone approximately 3 metres thick. The Upper Shaley Pales sequence is approximately 35 metres thick and consists of interbedded crinoidal calcarenites and shales, with calcareous sandstones and silty calcarenites towards the base of the succession (Philcox, 1984, Rizzi, 1992).

3.1.7. Argillaceous Bioclastic Limestone (Slane Castle Formation)

The Argillaceous Bioclastic Limestone (ABL) is a 130 metre thick series of argillaceous limestones, thick, interbedded shales and muddy calcarenites that conformably overlies the Shaley Pales and becomes increasingly argillaceous up-stratigraphy (Philcox, 1984, Anderson, 1990, Rizzi, 1992). The stratigraphy is regularly thinly interbedded by dark argillaceous bands and crinoidal banding. The top of the formation transitions into chert and is marked by a contact with the overlying Waulsortian Reef Limestones (Philcox, 1984, Rizzi, 1992). Philcox (1984) identifies a progression from relatively clean succession of sandy/silty limestones at the base of the ABL, through increasingly argillaceous limestones thinly interbedded by shales, to fine-grained argillaceous limestones thickly interbedded by calcareous shales.

3.1.8. Waulsortian Reef Limestones (Feltrim Formation)

The ABL grades diachronously into the Waulsortian Reef Limestones (Waulsortian), which only occurs in the northwest Navan area. The Waulsortian sequence comprises pale grey, fenestrate bryozoan-rich biomicrites, containing crinoid-rich facies. The Waulsortian is well-developed in Limerick Province, occurring for up to several hundred metres above the underlying Argillaceous Bioclastic Limestone (Boyce et al, 1983A, Philcox, 1984, Anderson, 1990, Ashton et al, 2015).

3.1.9. Erosion Surface and the Boulder Conglomerate:

The Boulder Conglomerate comprises a mega-conglomerate sequence formed from catastrophic slope collapse via low-angle gravity sliding along the later-forming normal B and T Faults (discussed in section 3.2.1). This produced a northwest-southeast trending truncation into the Pale Beds sequence that down-cuts as deep as 700 metres into the underlying Lower Palaeozoic basement (Anderson, 1990). The Erosion surface has long been considered a submarine debris flow surface, related to the onset of major subsidence in the Dublin Basin (Boyce et al, 1983A). The Boulder Conglomerate contains mineralised clasts of Pale Beds debris and hosts the Conglomerate Group ore, suggesting that mineralisation likely continued well into the Chadian. The Erosion Surface and Boulder Conglomerate are well-developed in the eastern mine area, becoming less pervasive further west.

3.1.10. Tober Colleen Formation:

Where the Boulder Conglomerate is absent, the Tober Colleen Formation (TCF) is well developed and consists of bioturbated mudstones and thinly interbedded argillaceous micrites and calcarenites (Ashton et al, 2015).

3.1.11. Upper Dark Limestone (Lucan Formation)

The Upper Dark Limestones is a 400 metre thick succession of Chadian limestone and shales, where the lowermost unit - the Thin Bedded Unit (“TBU”) - overlies the Boulder Conglomerate and consists of a 20 metre thick sequence of interbedded, turbiditic

limestones and shales (Ford, 1996, Philcox, 1989, Rizzi, 1992). The TBU grades into the Boudin Mudstone Unit, comprising graded calcarenites (Philcox, 1989, Altinok, 2005), grading into a 160 metre thick succession of limestones, shales and poorly sorted conglomerates and becoming increasingly argillaceous up-stratigraphy (Anderson, 1990). Thinly bedded and discontinuous pyrites and sub-ordinate galena and sphalerite hosted in dark argillites within 50 metres of the base of the UDL indicate that exhalative mineralisation may have continued well into the Chadian (Anderson, 1990, Blakeman, 2002). The sequence overlying the TBU is interpreted by Philcox (1989) to represent a deepening succession and provides the main sedimentary fill of the Dublin Basin (Ashton et al, 2015)

3.1.12. Permian – Tertiary:

End of Palaeozoic-Tertiary deposition was restricted to small half-grabens in Kingscourt and Wexford northeast of the Navan area. Extensive flood basalt volcanism occurred in NE Ireland (especially in Northern Ireland), with associated basic dyking (Anderson, 1990).

3.2. Deposit geometry

The Main Orebody and Southwest Extension is a broadly elliptical (1.5 x 5 km), heavily faulted and dislocated series of stacked stratiform ore lenses trending NE-SW (Fig 3.1 and Fig 3.2). The deposit runs parallel to and shares a spatial affinity with early-forming normal faults and late-stage reverse and wrench faulting, suggesting a structural control on mineralisation (Fig 3.2). The Main Orebody is bounded to the west by the Liscartan and Castle Faults to the west, and the A, C, D, and E Faults to the east and southeast. The orebody is cross-cut by the B and A/T Faults sub-dividing the deposit into Zones 1-3. Zone 1 comprises the orebody northwest of the B Fault, Zone 2 is bounded by the B and T Faults and Zone 3 lies southeast of the T fault and comprises the northeastern section of the deposit located east of the A Fault (Fig 3.2). The Navan orebody has three satellite deposits: Clogherboy to the west and Tatestown and Scallenstown to the northwest.

3.2.1. Structural geology of the Navan area:

The geology of the Navan area is dominated by an asymmetric, southwest-plunging anticline located along the western margin of the Longford Down Inlier (fig 2.1). The Navan area has undergone multiple stages of faulting in the form of normal, wrench and reverse faulting and later basin inversion (Anderson, 1998, Ashton et al, 2015). The deposit and adjacent geology are bounded and cross-cut by several normal fault systems, interpreted to follow the structural grain of the underlying Iapetus Suture (Phillips & Sevastopulo, 1986, Blakeman, 2002, Ashton et al, 2015). The structural history of the Navan area can be divided into three stages:

3.2.1.1 The Caledonian Orogeny:

The Caledonian Orogeny (440-360 Ma) occurred during the collision of Avalonia and Laurentia (Vaughan & Johnson, 1992, Rao et al, 2007). The collision culminated in the closure of the Iapetus Ocean and development of the Caledonian Mountains in Scotland, Wales, and Ireland via Benioff-type subduction (Beamish & Smyth, 1986). The Iapetus Suture Zone represents the point of contact between the two continental blocks formed in the early-Devonian (Rao et al, 2007). Tracing the Iapetus Suture Zone across Ireland is difficult due to a thick sedimentary cover and lack of deep-penetrating seismic surveys, although it is believed to directly underlie the Navan area and the structural grain was likely a control on the orientation of normal faults (I.e. synthetic faulting) (Andrew & Ashton, 1985, Vaughan & Johnston, 1992, Rao et al, 2007)

3.2.1.2. Regional-scale basinal extension:

The Navan area underwent extensional faulting related to rifting in the Dublin and Shannon Basins in the Tournasian-Visean, where Navan is interpreted as the uplifted margin to the northwest of the Dublin Basin. Ashton et al (2015) interpret the NE-SW trending extensional faults in the Navan area to result from the reactivation of pre-existing Caledonian structures underlying Navan. Extensional faulting is prevalent between pre-rift to post-rift sag phase (Tournasian-Visean). The L and E Faults have an estimated throw and dip greater than 100 metres and 50-60^{o}, while the F1-F27 branch

dip at 50-70^{o} and have smaller throws of approximately 30 metres. The L Fault defines the northern extent of the Main Orebody, while the E Fault bounds the southeast margin of the Southwest Extension and northwest section of the Lower Palaeozoic E-P Fault Horst. Ashton et al (2015) interpret a thickening of the Waulsortian in the hangingwall of the L Fault to result from increased sedimentation during faulting. No significant displacement in the overlying Boulder Conglomerate and Upper Dark Limestone has been observed, suggesting the E Fault is an early structure. An extensive fault-fracture zone crosscuts the Main Orebody and is located between the L and E Faults, suggested to be a possible relay ramp structure (Ashton et al, 2015). The system comprises the minor F1, F2, F3 and branch, F20, F22, F25, F26, and F27 faults, where mineralisation is locally observed to increase towards fault structures.

The B Fault exhibits a throw of 70 metres while the T Fault displaces the Lower Carboniferous by approximately 200 metres. The B and T Faults are interpreted as late Courceyan-early Chadian, given that they are down-cut by the Erosion Surface and do not displace the overlying Upper Dark Limestone (Anderson et al, 1998). The Y, M, and N Faults occur southeast of the B and T Faults and are interpreted to have developed during the transition of the B and T Fault profiles from planar to listric (Ashton et al, 2015) profiles, and have dips of 15-70^{o}.

3.2.1.3. Variscan compression:

The Variscan Orogeny resulted from obduction-collision of Gondwana and Laurasia during the formation of Pangaea (Warr, 2012). E-W striking compression in Ireland is most intense in the south, decreasing further north. Variscan reactivation caused reverse and wrench motion along the A-C, D, Randalstown and Castle faults, causing basin inversion at approximately 300 Ma (Hitzman, 1999, Ashton et al, 2015) The A, C, and D Faults underwent inversion during compression, where the A Fault demonstrates strike-slip displacement of at least 180 metres and reverse movement of approximately 80 metres. The Randalstown Fault - approximately 200 metres west of the Main Orebody - steeply dips at 70-90^{o} and has a throw of at least several hundred metres. Davidheiser-Kroll (2015) obtained $^{40}Ar/^{39}Ar$ isotope data from feldspar grains to constrain Variscan compression to 293 ± 3 Ma, coinciding with emplacement of the Cornubian batholith.

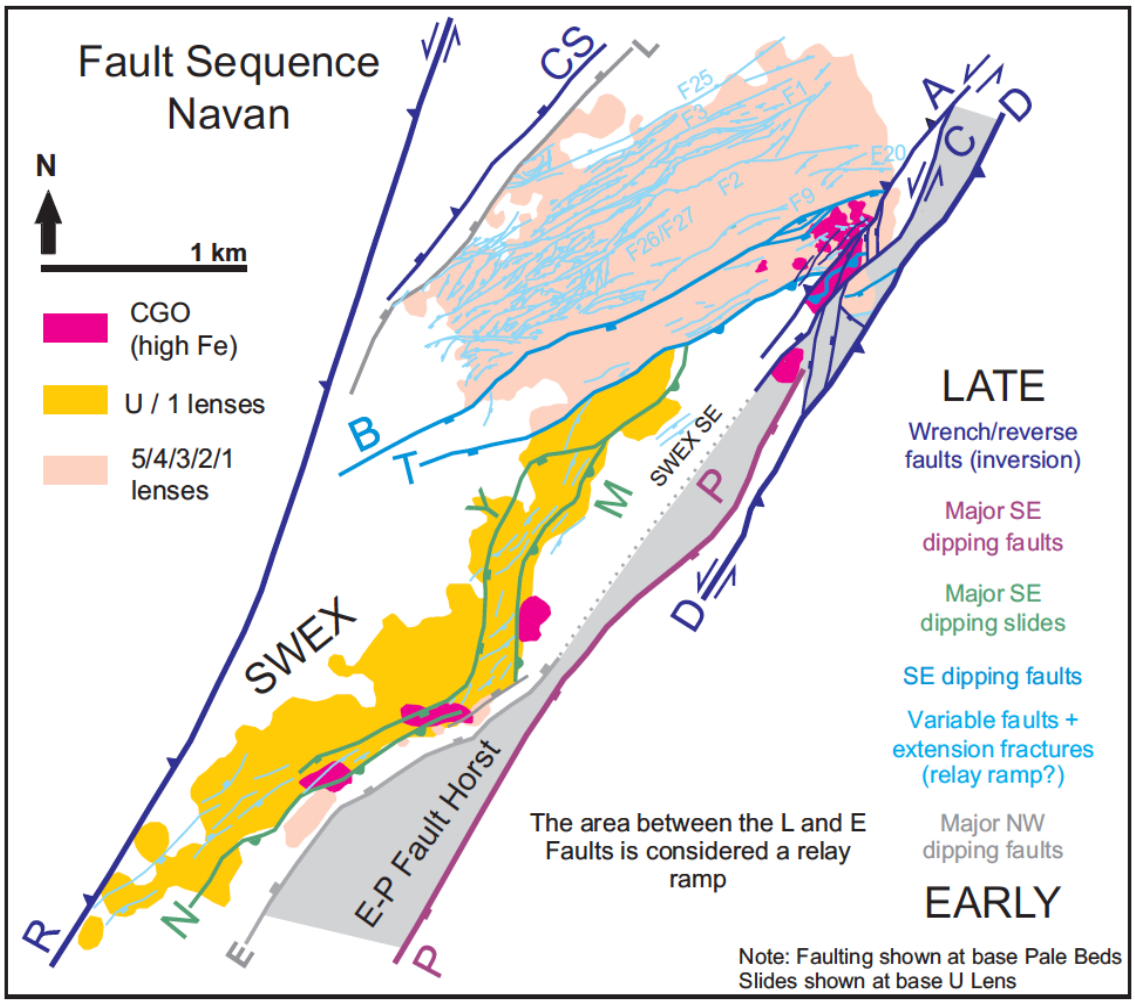

Fig 3.2 - Chronological fault development at Navan (Ashton et al, 2015). The Main Orebody (pink) is bounded by the L, B and T Faults, and extensively cross-cut by the minor F1-F27 normal fault array

3.3. Navan ore:

Navan ore has a simple mineralogy, comprising sphalerite-galena-pyrite, minor sulfosalts, and calcite, barite and dolomite gangue. Freibergite and pyraygerite are the deposit's silver-bearing mineral phases and occur as inclusions in galena (Ashton et al, 2015). The Navan deposit consists of five lenses (termed 5 to 1 depending on stratigraphic level, 5 being the stratigraphically lowest, 1 the highest), the U-Lens, and Conglomerate Group Ore, respectively (Fig 3.1, table 3.1). The lenses and Southwest Extension are hosted in the Pale Beds, while the Conglomerate Group Ore occurs in Chadian debris flow deposits of the overlying Boulder Conglomerate. The upper and lower contacts of the lenses are defined by "Marker Horizons" – weakly bedded, often dolomitized calcisiltite successions. As the Main Orebody can be sub-divided into three zones (Zones 1-3 – Fig 1.3) by the

cross-cutting B and A/T Faults, the lenses are appropriately sub-divided into their respective zones. For example, the 5 Lens in the 1 Zone would be termed the “1-5 Lens”.

3.3.1. 5 Lens

The 5 Lens is hosted in the Micrite Unite and comprises the highest-tonnage and most continuous ore lens, containing 70% of Navan ore. 5 Lens sulphides exhibit a complex series of textures, including breccia, vein, pod, replacement and stratiform lenses (Anderson et al, 1998, Ashton et al, 2015). Mineralisation often underlies dolomitic and silty horizons in the Micrite Unit, interpreted as important aquitards that focused migrating ore-fluids (e.g. Anderson et al, 1998, Ashton et al, 2015). Stratiform mineralisation is noted to occur below the Bottom Dark Member (“BDM”), Lower Dark Member (“LDM”) siltstones and the 5 Lens Dolomite. The 5 Lens Dolomite comprises at least ten metres of oolitic sandstones and calcarenites that have undergone complete dolomitisation, occluding primary porosity and acting as a “cap” on mineralising fluids (Ashton et al, 2015).

3.3.2. 4 Lens

4-Lens mineralisation is well developed in the central and eastern extent of the mine site and preferentially occurs in sandy grainstones. 4-Lens is less laterally continuous than the underlying 5 Lens.

3.3.3. 3 Lens

3-Lens mineralisation occurs in sandy grainstones and is best observed in the eastern extent of the mine and Zone 2 East, where 3-Lens comprises a major resource. Both 3 and 4-Lens terminate down-dip at approximately the same depth.

3.3.4. 2 Lens

2-Lens comprises a single, high-grade stratiform sulphide band, varying between several cm to several metres thick and occurring immediately beneath the Nodular Marker (NOD).

3.3.5. 1 Lens

The 1-Lens is well developed in Zone 2 (I.e. the 2-1 Lens) and comprises a single, tabular ore lens approximately 750 x 300 metres in length and bounded by the B and T Faults. The base of the 1-Lens is marked by the Nodular Marker, a muddy, nodular calcarenite containing abundant biodebris, while the top is defined by the Upper Dark Marker. The Sub-Dark Marker may be observed beneath the Upper Dark Marker.

3.3.6. 0 Lens

0-Lens mineralisation is restricted to silty grainstones between the Upper Sandstone Marker and Upper Dark Marker and occurs exclusively in the SWEX. Mineralisation is almost barren.

3.3.7. U Lens

U Lens mineralisation is hosted in calcarenite and grainstone sequences. The U-Lens is not developed in the eastern part of the mine as the upper section of the Pale Beds is truncated by the Erosion Surface. In proximity to the Y, M, and N Faults, mineralisation grade and thickness increases, and occurs as host rock-replacement and cavity fill textures.

3.3.8. Conglomerate Group Ore (CGO):

The Conglomerate Group Ore comprised 3% of the total Navan tonnage prior to mining. CGO ore comprises massively-bedded iron-sulphides interlayered with and cross-cut by sphalerite and galena, suggesting that Zn-Pb sulphide mineralisation continued post-CGO mineralisation. CGO pyrite varies in texture, ranging from fine-grained framboidal pyrites, argillite-interbedded laminae and laminate to massive with medium-crystalline calcites. Where pyrite bedding is most massive, accessory sphalerite and galena is often most abundant (Ashton et al, 2015).

Ore Lens	Host lithology	Mineralisation	Mineralisation textures	Structural/lithological controls
Conglomerate Group Ore (CGO)	Boulder Conglomerate – mega-conglomerate and slope debris deposits	Principally iron-sulphide (pyrite and marcasite), with sub-ordinate sphalerite and galena	Typically fine-grained FeS_2, though may be bedding-parallel or massive. Sub-ordinate PbS and ZnS	Erosion Surface is a topographical control on deposition. Occurs above early-forming southeast-dipping fault systems and slide complexes. Occurs northwest of the E, P, and D Faults in topographic lows of irregular grabens.
0-Lens	Calcarenites	Rare sulphide, mostly barren		Occurs in central SWEX, northwest of the Y Fault
1-Lens	Calcarenites and interbedded bioclastic bands	2-1 comprises high-grade, tabular mineralisation	Single, tabular ore lens. Becomes more discontinuous and comprises thin stratiform, pods, replacement and small veinlets towards Zone 2 West	2-1 bounded by the B and T Faults to the northwest and southeast, respectively. Terminates above Zone 2 West.
2/3-Lens	Calcarenites and interbedded microconglomerates	Dominantly Zn-Pb.	Stratiform – few cm's to several metres thick	Thin, stratiform sulphides occur immediately below Nodular Marker in 2-Lens. 3-Lens comprises major resource in eastern part of mine and terminates down-dip at same depth as 2-4 Lens.
4-Lens	Oolitic and bioclastic calcarenites		Bedding-parallel, massive, vein, and fabric replacive sulphides	Often occurs above well-developed 4-Lens and neaRandalstown Faults. Well-developed in eastern and central mine
5 Lens	Micrite Unit (MU) – Bird's Eye Micrites and oolitic grainstones		Lenses, sub-lenses, high-grade pods, mineralised breccias and veins. Sharp, planar contact shared with argillites and dolomites	Occurs only in proximity to E and L Faults – Both interpreted as major feeder zones
U-Lens	Calcarenites and quartzose sandstones		Lenses, pods, veins and disseminated ZnS and minor PbS and FeS_2. Cavity infills close to Y, M, and N Faults.	Mineralisation grade and thickness increases in proximity to the Y, M, and N Faults

Table 3.1 - Summary of lens characteristics in the Navan orebody (Andrew & Ashton, 1985, Anderson, 1998, Ashton et al, 2015)

3.4. **Dolomite**:

Dolomitisation is restricted to the Pale Beds and occurs in 0.5 – 40 metre thick successions, often exhibiting a higher silt/sand content than undolomitised limestone facies (Anderson, 1998). Rizzi (1992) and Braithwaite & Rizzi (1997). Rizzi (1992) completed a detailed cathodoluminescence study of dolomite samples from the "dolomite plume" - a pervasive, semi-linear zone of dolomitisation trending east-northeast through the axis of the 5 Lens of the Main Orebody. Dolomitisation preferentially occurs in silt and mud-rich sandy/oolitic horizons, described as stratal "fingers" and is typically destructive of pre-existing sedimentary textures and features (e.g. grains, ooliths, shell debris - Rizzi, 1997). Rizzi (1992) describes a three-stage dolomite paragenesis for the Navan area:

Stage 1 is the most volumetric dolomite stage. Stage 1 comprises a brown, dully luminescent "mosaic" replacement of allochems. Dolomite rhombs typically display three (can occasionally reach six) zonations, while rhomb crystal edges may be corroded. Some rhombs exhibit bright orange sub-zones. Rizzi describes a dully brown luminescence as evidence for an Fe content of between 10,000-15,000 ppm, while zonation points towards varying redox conditions as Fe^{2+} is substituted for Ca^{2+} and Mg^{2+}.Corrosion of dolomite rhombs is interpreted by Rizzi to represent a dissolution event that increased secondary porosity and promoted fracturing through concentric zones.

Stage 2 is subdivided into three sub-stages:

1) Initial Stage 2 dolomite comprises a bright red dolomite that overgrows individual corroded rhombs which form composite crystals as well as developing in holes developed during Stage 1. The first dolomite stage of Stage 2 also develops in Stage 1 fractures and replaces bioclasts. A bright orange-yellow colouration denotes a Fe^{2+} and Mn^{2+} concentration of near 10^5 and 100-1000 ppm, respectively.

2) The second sub-stage comprises a bright red-orange yellow couplet dolomite that occurs at the centre of the "plume". The second stage occurs only at the

centre of most intense dolomitisation and disappears along the “stratal fingers”, being uncommon in the 5 Lens Dolomite (“DOL”). Rizzi interprets the geographical distribution of this stage as a function of regional fluid-flow.

3) The final sub-stage comprises a non-luminescent dolomite that overprints the red/orange-yellow dolomites. Where Stage 2 is absent, the dull dolomite directly overprints dull, Stage 1 dolomite. A similar non-luminescent, dull dolomite infills remaining pore space and replace remaining biodebris, and is interpreted to belong to the same paragenetic event. Non-luminescence suggests a Fe^{2+} content greater than 10.5^{5} ppm.

Stage 3 comprises saddle dolomite lining vugs. Dolomites are generally dull though seven faint, concentric sub-zones can be observed. Cores are dark crimson brown and overprinted by a thin crimson brown dolomite.

Rizzi (1992) identifies dolomitisation at Navan as a late-stage, deep-burial feature and the final porosity infill stage, observing that saddle dolomites overprint late-stage blocky calcite cements and infill relic porosity. Rizzi (1992) advocates that stylolites develop between 200-1000 metres and that dolomites are observed to cross-cut early calcite cements and infill stylolites.

Chapter 4

Methodology

This chapter focuses on the methods applied to characterise and interrogate low Zn/Pb and cpy-Qtz(-barite) mineralisation west of the Randalstown Fault and the rationale behind each approach.

4.1. **Sampling:**

Geological logging of the Pale Beds sequence was completed for twenty-one drillholes along four transects. This was carried out in order to gain familiarity with the lithology and mineralisation styles in the Main Orebody, footwall and hangingwall, and to determine how the geology develops west of the Randalstown Fault when compared with that of the Main Mine. This was carried out with the aim to determine if the area presents features characteristics of feeder zones, offering a potential vector to either the existing deposit, or to new ore occurrences. The four transects are termed A1, A2, B and C. The A1 and A2 transects span a complete section across the Randalstown Fault. Transect C was selected to offer a view of near Main Orebody ore and geology, and to provide context for the Randalstown transects. Transect C was selected because of its occurrence in the relatively anomalous low Zn/Pb area identified by Davidheiser-Kroll (2014):

- The A1 Transect comprises five drillholes that traverses the hangingwall (west-northwest of the fault plane) of the Randalstown Fault along a low Zn/Pb mineralisation area. In this transect, Drillhole N02230 – the western-most drillhole – intersects cpy-qtz vein mineralisation at 881.8-882.3 metres, being one of the foci of this research. This transect was studied to assess sphalerite-galena paragenesis in the Randalstown Fault hangingwall, with a view to assess whether an identical paragenesis could be developed from samples along the A2, B and C Transect (I.e. Southwest of, and the Main Orebody). Specifically, this study aimed to assess if “typical” feeder zone textures and mineral assemblages could be identified in the Randalstown Fault hangingwall such as late-stage

replacive pyrite, sulfosalts and copper sulphide assemblages (Hitzman and Beaty, 1996). Secondly, cpy-Qtz(-barite) samples were selected from drillhole N02230 – the western most drillhole along the A1 Transect. Samples were obtained to determine the paragenesis, that could then be compared with both Zn-Pb sulphides in the Randalstown Fault hangingwall and low Zn/Pb population in the Main Mine 5 Lens. Again, this was carried out to determine if "typical" feeder zone mineralisation and textures could be observed.

- The A2 Transect comprises seven drillholes that trend southwest of the 5 Lens cut-off in the Randalstown Fault footwall (southeast of the fault plane). Samples were collected from the A2 Transect to assess if a common paragenesis could be tied together between the Main Mine 5 Lens, the Randalstown Fault hangingwall, and southwest of the Main Mine 5 Lens.

- The B-B' Transect comprises four drillholes previously selected by Braithwaite and Rizzi (1997) for detailed cathodoluminescence and carbon-oxygen isotope analyses of Main Mine dolomites. B-B' runs perpendicular to the 5 Lens axis and trends to the southeast, beginning approximately 200 metres southeast of the L Fault and terminating 250 metres southeast of the T Fault. This transect was selected to compare sulphide paragenesis and the C-O isotope composition of the 5 Lens Dolomite in the Main Mine with those in the hangingwall.

- The C-C' Transect consists of five drillholes that coincide with the low Zn/Pb area in the southwest Main Mine area identified by Davidheiser-Kroll (2014) – interpreted to be the upwelling point for unmodified, low Zn/Pb fluids that then migrated northeast. This allowed comparison of sulphide paragenesis of samples from the low Zn/Pb population in the southwest mine area with that of low Zn/Pb samples from the Randalstown Fault hangingwall. This was carried out to try and distinguish paragenetic differences, if any, between sulphides taken form low Zn/Pb areas from the Main Mine 5 Lens, those southwest of the Main Mine, and from northwest of the Randalstown Fault. Additionally, this provided the author with the opportunity to determine if hangingwall sulphides are coeval with the Main Orebody and resulted from hydrothermal fluid flow away from the mine site.

Eighty-three samples were selected from core for standard petrography, including reflected and transmitted light microscopy, and SEM petrographic work – 21 of which were 5 Lens Dolomite

samples while the remaining 62 were mineralised micrites. For the purpose of fluid inclusion studies, coarsely-crystalline samples were selected for microthermometric analyses of fluid inclusions. Coarsely-crystalline calcite and sphalerite-bearing samples were selected for fluid inclusion work. Emphasis was placed, where possible, on collecting mineralisation that exhibited clear cross-cutting relations, multiple mineralisation styles and disseminated/weakly mineralised sulphide. Core assay data was obtained from Boliden Tara Mines. Sample label is derived from the drillhole collar, followed by the order of collection from core. For example, the third sample obtained from drillhole N01001 will be labelled "N01001-3"

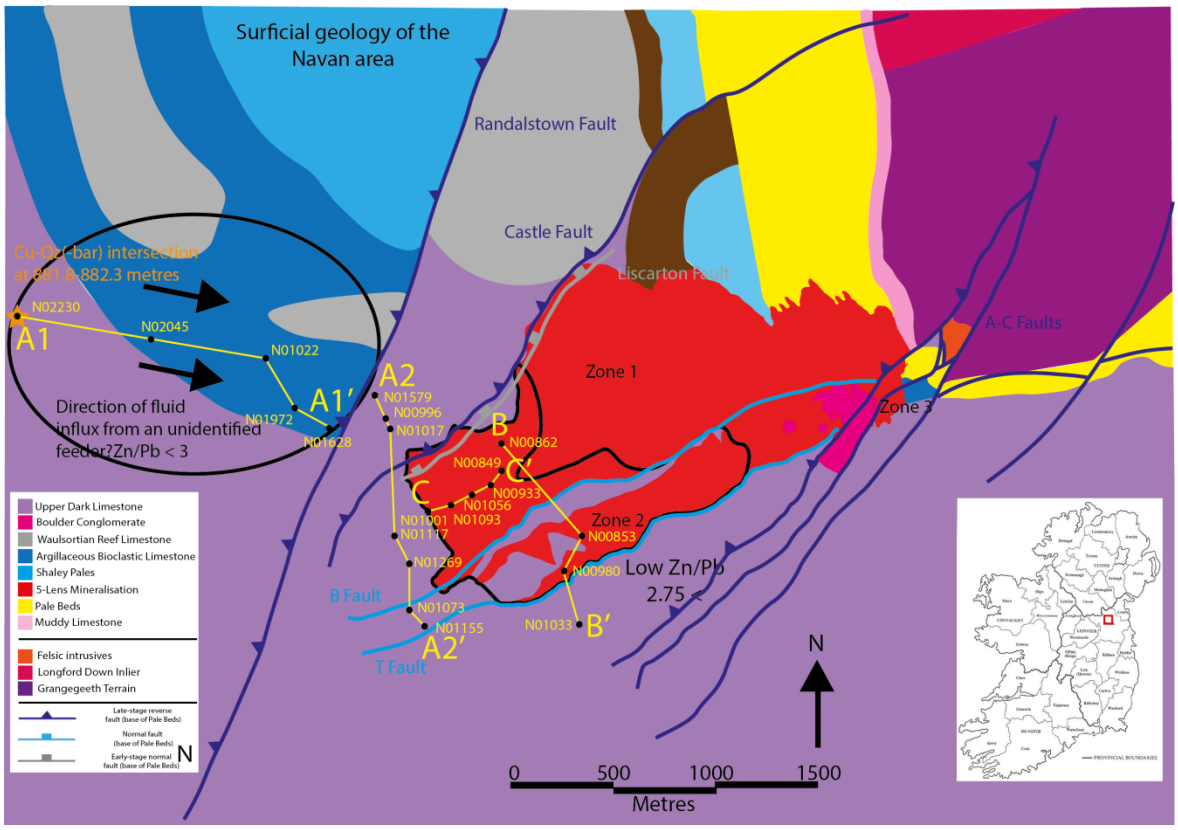

Figure 4.1 – Geological map of Navan area with Main Mine 5 Lens outline (red), low Zn/Pb populations (circled black) and A-C Transects (yellow). For a more detailed Zn/Pb map of the Main Mine, refer to Figure 1.4

4.2. Thin and polished section microscopy:

Thirty-eight core samples were selected for thin section microscopy. Samples were cut to 10mm blocks using a rock saw, cleaned in acetone and dried for 30 minutes. These were cut to 30 µm, mounted on glass slides with resin, and polished using aluminium oxide paste. Transmitted and reflected light microscopy was completed using a Carl Zeiss Axio Microscope and photomicrographs obtained using an AxioCam IOC3. Samples analysed by SEM for sulphide composition were carbon coated and analysed using a Carl Zeiss Sigma Variable Pressure Analytical SEM. A breakdown of core sample locations, and their stratigraphic depth collected is

provided in Appendix 10.1 (Table 10.1). Individual thin section petrography and descriptions are provided in Appendix 10.3.

Mineralisation west of the Randalstown Fault is concentrated in the 5 Lens (Fig 8.1, Fig 8.2). Therefore, in order to assess whether this is an expression of an unidentified feeder, or from hydrothermal fluids migrating west of the Main Orebody (I.e. a continuation of the 5 Lens displaced by dextral reverse faulting), mineralised samples were selected from the 5 Lens Micrite along the A-C Transects. Where 5 Lens mineralisation was not available or absent from core, samples were taken from the overlying 4 Lens (Appendix 10.1).

4.3. Sulphur isotope analysis:

Seventy-nine samples were obtained for sulphur isotope analysis. Sufficiently coarsely-crystalline sulphides were sampled using a dental drill, mixed with Cu_2O in excess, and oxidised in a 950^{o}C furnace for twenty-five minutes. SO_2 was collected via a distillation trap at -196^{o}C with a n-pentane jacket frozen by liquid N_2. Non-condensible gases were removed via vacuum tap. Liquid nitrogen was removed and CO_2 driven off via distillation for three minutes. The CO_2 was removed via vacuum trap, and purified sulphur dioxide gas then collected via a second distillation trap and analysed using a MAT 253 dual source source mass spectrometer. This method follows Robinson and Kusakabe (1975). Finely-crystalline sulphide on polished slabs that could not be sampled by dental drill were laser combusted as described in Fallick et al (1992) and Wagner et al (2002). The resultant sulphur dioxide gas was purified using the same process as above and analysed, on-line, using a VG Sira II dual-inlet gas source mass spectrometer. Raw outputted $\delta^{66}SO_2$ values were corrected to $\delta^{34}S$ using NBS-123 (+17.1‰) and IAEA-S-3 (-31‰) standards, as well as an internal lab chalcopyrite CP-1 (-4.6‰) standard. Results were reported relative to Vienna-Canyon Diablo Troilite (V-CDT). Error of reproducibility is based on repeat analyses of international standards, providing a 1σ error of ± 0.1‰.

4.4. Carbon-oxygen isotope analysis:

Calcite and dolomite samples were sampled using a dental drill. 10 to 15 mg of calcite dolomite powder were sampled. Phosphoric acid – a viscous acid that often contains trapped air -was initially heated to drive off any remaining air. Phosphoric acid was then heated for 30 minutes, either in a water bath at 25^{o}C for calcite, or on a hot plate at 100^{o}C for dolomite. Phosphoric acid

was then reacted with carbonate powders and returned to either the water bath or hot plate for eighteen hours. Carbon dioxide gas was purified using an in-house vacuum line in the following manner. Water was retained in a "slush trap" (carbon dioxide ice and acetone) and the reacted carbon dioxide gas separated from non-condensible gases and analysed using a VG Sira II dual-inlet gas source mass spectrometer. $\delta^{13}C$ results were reported relative to Vienna-Pee Dee Belemnite, while $\delta^{18}O$ was reported relative to Pee Dee Belemnite and Vienna-Standard Mean Oceanic Water. Error of reproducibility is based on repeat analyses of international standards, providing a 1σ error of ± 0.1‰.

4.5. Fluid inclusion analysis:

Fourteen fluid inclusion wafers were used for fluid inclusion analysis. Six, three and five wafers were prepared from samples selected along the A1, A2 and C Transects, respectively. The intention of selecting fluid inclusion wafer samples from along the A1 and A2 Transects was to compare the mineralisation temperature of Zn-Pb-calcite in the Randalstown Fault hanging wall west of the Navan deposit, and southwest of the 5-Lens in the foot wall of the fault, respectively. Additionally, samples were selected from each transect to determine whether a westward decrease in the assumed mineralisation temperature could be observed and, therefore, provide evidence for a westward migration of mineralising fluid contemporaneous with the deposit. Fluid inclusion wafers prepared from C Transect drillholes coincide with a low Zn/Pb 5-Lens zone identified by Davidheiser-Kroll (2014). The intention of preparing samples from the C Transect for fluid inclusion analysis was to determine whether mineralisation in the low Zn/Pb 5 Lens zone developed at a similar temperature to that of low Zn/Pb identified along the A1 Transect (Randalstown Fault hanging wall). It was determined that, for the specific purposes of this study, samples selected from along the B Transect (trending perpendicular to the 5-Lens axis – approximate Zn/Pb ratio of 4) would not best serve this aim. Navan fluid inclusions are difficult to observe due to their rarity, small size, and the highrefractive index of calcite, dolomite and sphalerite where two-stage fluid inclusions may be hosted, making direct observation a challenge. Given this, multiple cycles of sample freezing and subsequent heating (as discussed below) were conducted to determine the fluid inclusion properties where results were in doubt or uncertain.

Fluid inclusion wafers were cut to 200 µm and polished on both sides with an aluminium oxide paste. The wafers were then broken up, mounted, and analysed using a Nikon Ophinot microscope with fitted fluid inclusion stage. The homogenisation temperature (T_h) was measured

by observing when the vapour bubble of a two-phase fluid inclusion is completely resorbed on heating (for example of two-phase inclusion, see Fig 6.10), forming a single aqueous phase. This temperature is interpreted to represent the minimum temperature at which mineralisation would have occurred (the "trapping temperature" of the fluid along the proto-crystal). In order to determine the salinity of a fluid inclusion, the sample was cooled with liquid nitrogen until completely solid (T_{FREEZE}). Slow heating of the inclusion and careful observation can yield a final melting temperature ($T_{M\text{-}ICE}$), which may be observed by, A) absorption of ice into the liquid phase, B) the sudden re-nucleation of a vapour bubble occurring simultaneously with ice melting, or C) by observing the motion of a nucleated vapour bubble become increasingly exaggerated with continued melting before return to a state of low motion.

One of the initial challenges of fluid inclusion analysis is to determine the salinity of the trapped fluid, which can be inferred from direct observation of the freezing and subsequent melting behaviour of the inclusion, which is controlled by its' dissolved solutes. Where a trapped fluid contains less than 23.2 wt.% NaCl (I.e. below NaCl supersaturation), a fluid inclusion will freeze to form water ice and hydrohalite ($NaCl.2H_2O$) (Bodnar & Vityk, 1994, Bodnar, 2003, Wilkinson, 2016 – pers comm). Hydrohalite has a melting temperature of -21.2°C, referred to as the "eutectic temperature" (T_E). However, other dissolved solutes, including KCl (sylvite) and $CaCl_2$ further lower the T_E and complicate attempts to accurately characterise the solute content of an inclusion at -22.9°C and -52°C, respectively. Therefore, after determining what fluid inclusion species represented the primary (I.e. mineralising) event, suitably large inclusions (at least > 5 μm) were then chosen selected to observe for "typical" freezing and subsequent melting temperatures on heating to determine the inclusion solute content. Almost all fluid inclusions observed exhibited a T_E ranging from -50 to -60°C, suggesting that inclusions hosted both in calcite, and in quartz from drillhole N02230 lie within a H_2O-NaCl-$CaCl_2$ field (Wilkinson, 2001)

Given that fluid inclusions were dominantly observed in calcites, accurate measurement of metastable freezing, first melt, and final melting was compromised by the high relief of calcite in transmitted light. Additionally, an ideal fluid inclusion size for clear observation is typically between 5-20μm (Wilkinson, 2002). Fluid inclusions observed in samples from along the Randalstown Fault hangingwall (A1 Transect) were typically less than 2μm, Additionally, subtle (or unsubtle where particularly rapid) changes in pleochroism that can be used to identify freezing, first and final melting, are difficult to observe in small inclusions. Where T_{FREEZE} or $T_{M\text{-}ICE}$ were in doubt, the sample was re-heated to room temperature, subsequently cooled at 50°C/min until T_{FREEZE} (observed as a "snap" change in inclusion colour) was observed, and re-heated at 2-5°C/min so that eutectic melting (T_E) could be observed. Additionally, only primary fluid inclusions in calcite – those that are cleavage-parallel and,

therefore assumed to have formed with the mineral – were analysed for the purposes of this study. Given that cleavages represent a plane of weakness in any mineral, only cleavage-parallel inclusions were selected for analysis, given the risk for potential leakage when an inclusion overlays a cleavage plane, giving a T_{FREEZE} and $T_{M\text{-}ICE}$ unrepresentative of the original mineralising fluid.

Monophase inclusions (for example, see Fig 6.9) were dominantly observed in quartz from drillhole N02230 along the A1 Transect. These are "metastable", meaning that they comprise one phase and are under an effective negative pressure (Roedder, 1971,Roedder & Belkin, 1988, Wilkinson, 2016 – pers comm). Due to the general absence of a vapour bubble, the homogenisation temperature could not be determined for most quartz-hosted inclusions. However, fluid inclusions in Irish-type from Irish-type Zn-Pb deposits exhibit a strong linear and predictable correlation between T_{FREEZE} and $T_{M\text{-}ICE}$ of 0.968. Therefore, we can still yield salinity by determining T_{FREEZE} and calculating $T_{M\text{-}ICE}$, using the following MX+C equation (Wilkinson, 2016 – pers comm, Wilkinson, 2016), assuming that there is a strong, linear correlation between T_{FREEZE} and $T_{M\text{-}ICE}$:

TM-ICE = 0.5535 x TFREEZE + 22.2

Salinity (wt.% NaCl equivalent)

Where 0.5535 is the intercept (M) of a line intersecting the Y Axis in $T_{FREEZE} – T_{M\text{-}ICE}$ space assuming a coefficient R of 0.963, T_{FREEZE} is the freezing temperature (X) of the inclusion (I.e. entirely becomes solid ice and metastable) and 22.2 (C) is the eutectic melting point (T_E – The melting temperature of water ice). By determining $T_{M\text{-}ICE}$, an approximate fluid inclusion salinity can be constrained as previously described.

One hundred and thirty three fluid inclusions, hosted in calcite, quartz and dolomite were observed (Table 6.5-6.7, 10.4). Of these, 115 were two-phase inclusions, while 18 were classified as monophase and occurred exclusively in quartz from drillhole N02230. No solids were observed in any inclusions analysed. Where neither $T_{M\text{-}ICE}$ not T_E could not be determined, either due to or a vapour bubble not re-nucleating or small inclusion size preventing accurate observation, only T_{FREEZE} was recorded.

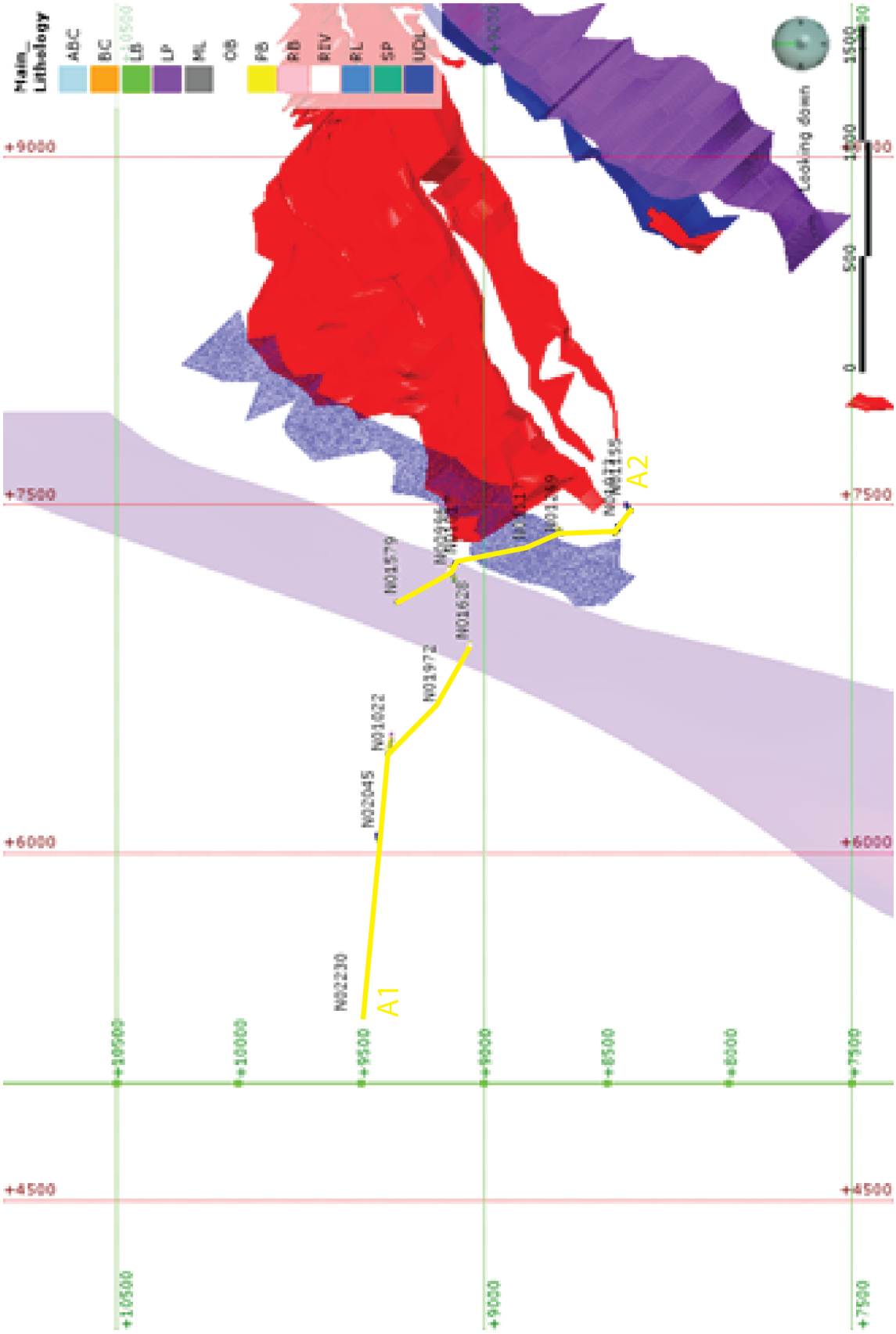

Figure 4.2 - Plan-view of A1 and A2 Transects. N0XXXX number (black) represents drillhole collar number, while N0XXXX-X number (blue) represents sample points. Section line in yellow. From west to east along the A1 Transect, the drillhole collars are as follow – N02230, N02045, N01022, N01972, N01628. From northwest to southeast along te A2 Transect, the drillhole collars are as follow – N01579, N00996, N01017, N01117, N01269, N01073, and N01155

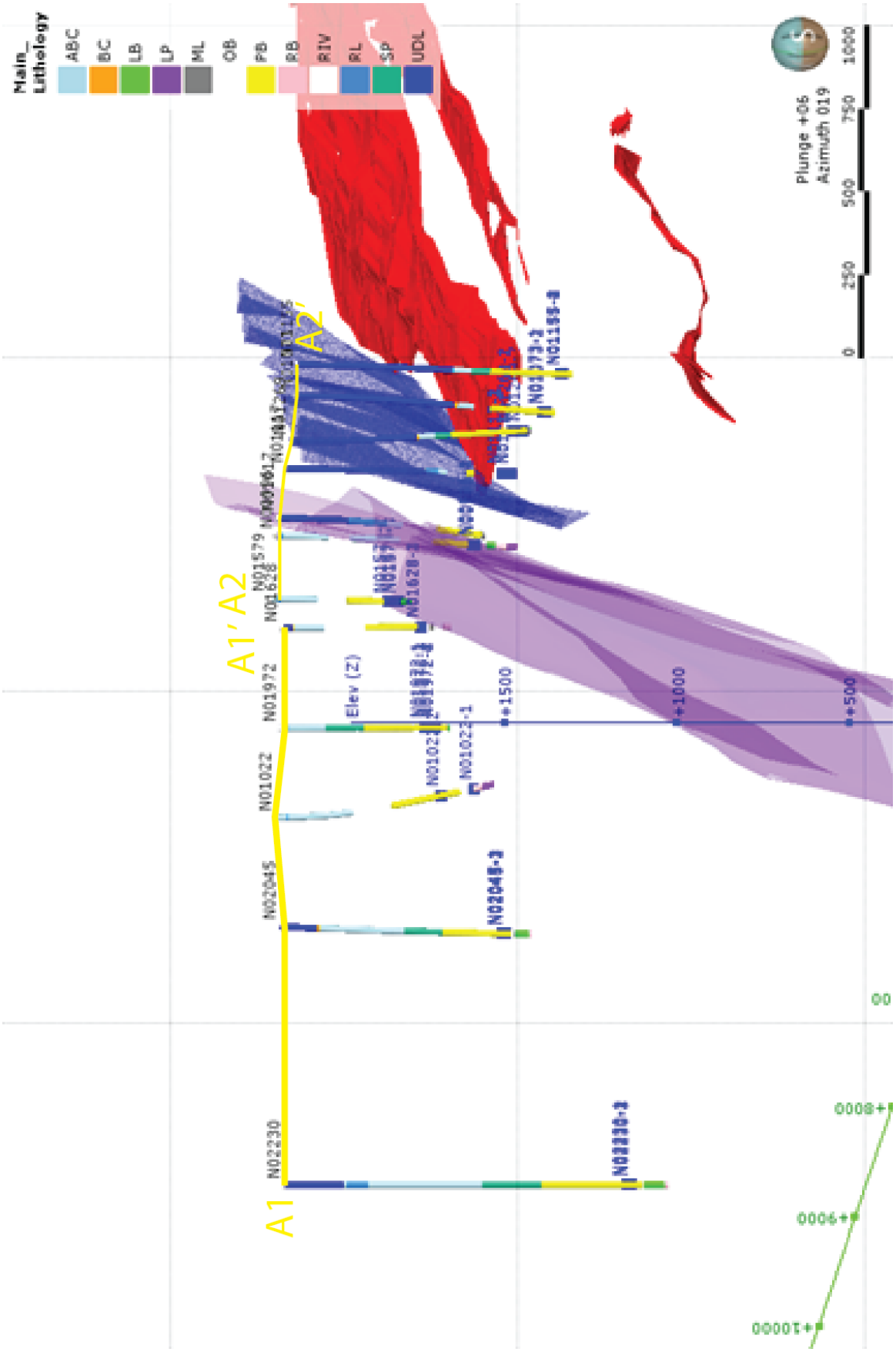

Figure 4.3 - Cross-section of A1 and A2 Transects. N0XXXX number (black) represents drillhole collar number, while N0XXXX-X number (blue) represents sample points. Section line in yellow.

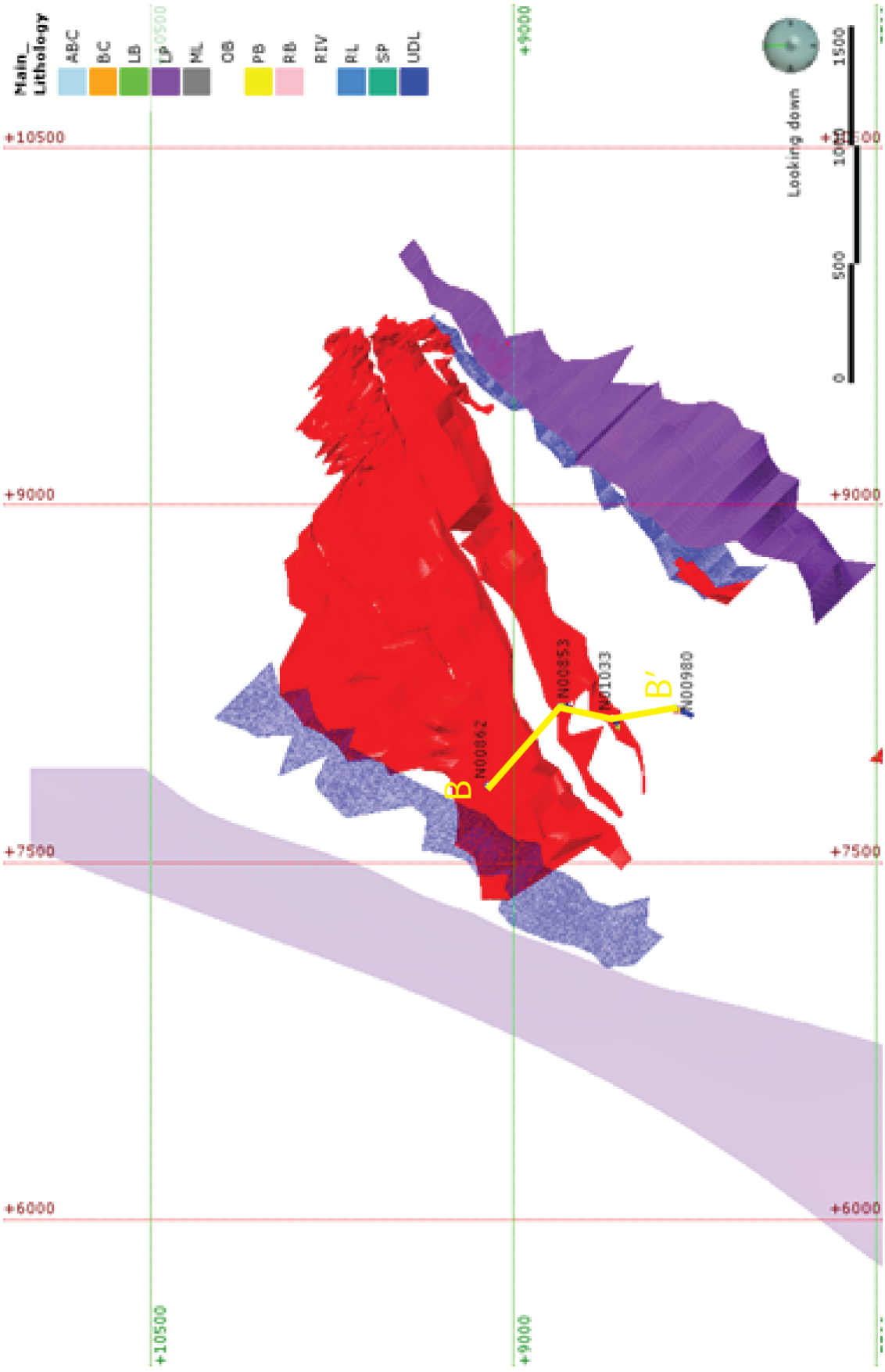

Figure 4.2 - Plan-view of B Transect. N0XXXX number (black) represents drillhole collar number, while N0XXXX-X number (blue) represents sample points. Section line in yellow. From south to north/northwest, the drillhole collars are as follow – N00980, N01033, N00853, and N00862

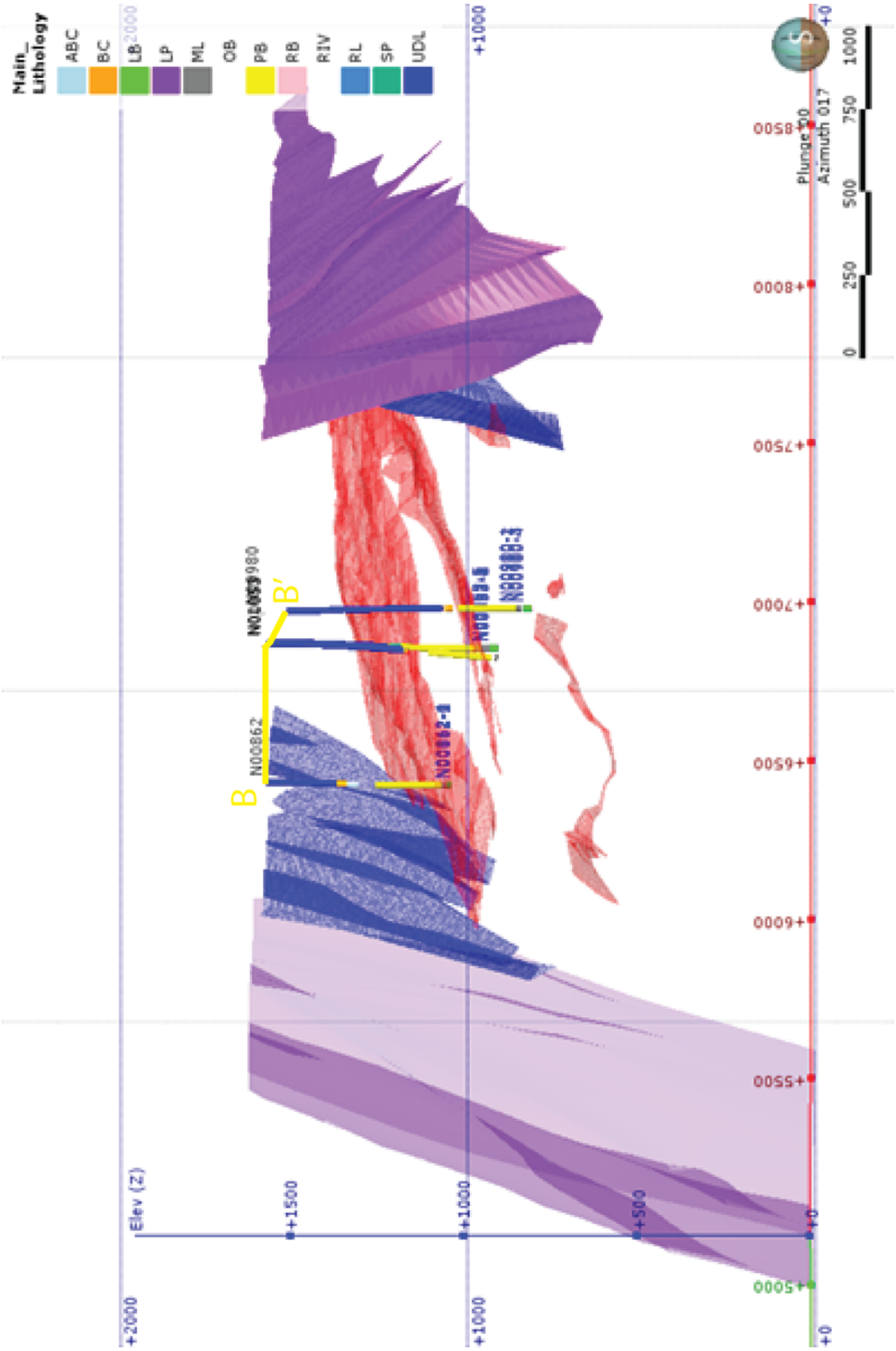

Figure 4.5 - Cross-section of B-B' Transect. N0XXXX number (black) represents drillhole collar number, while N0XXXX-X number (light blue-green) represents sample points.

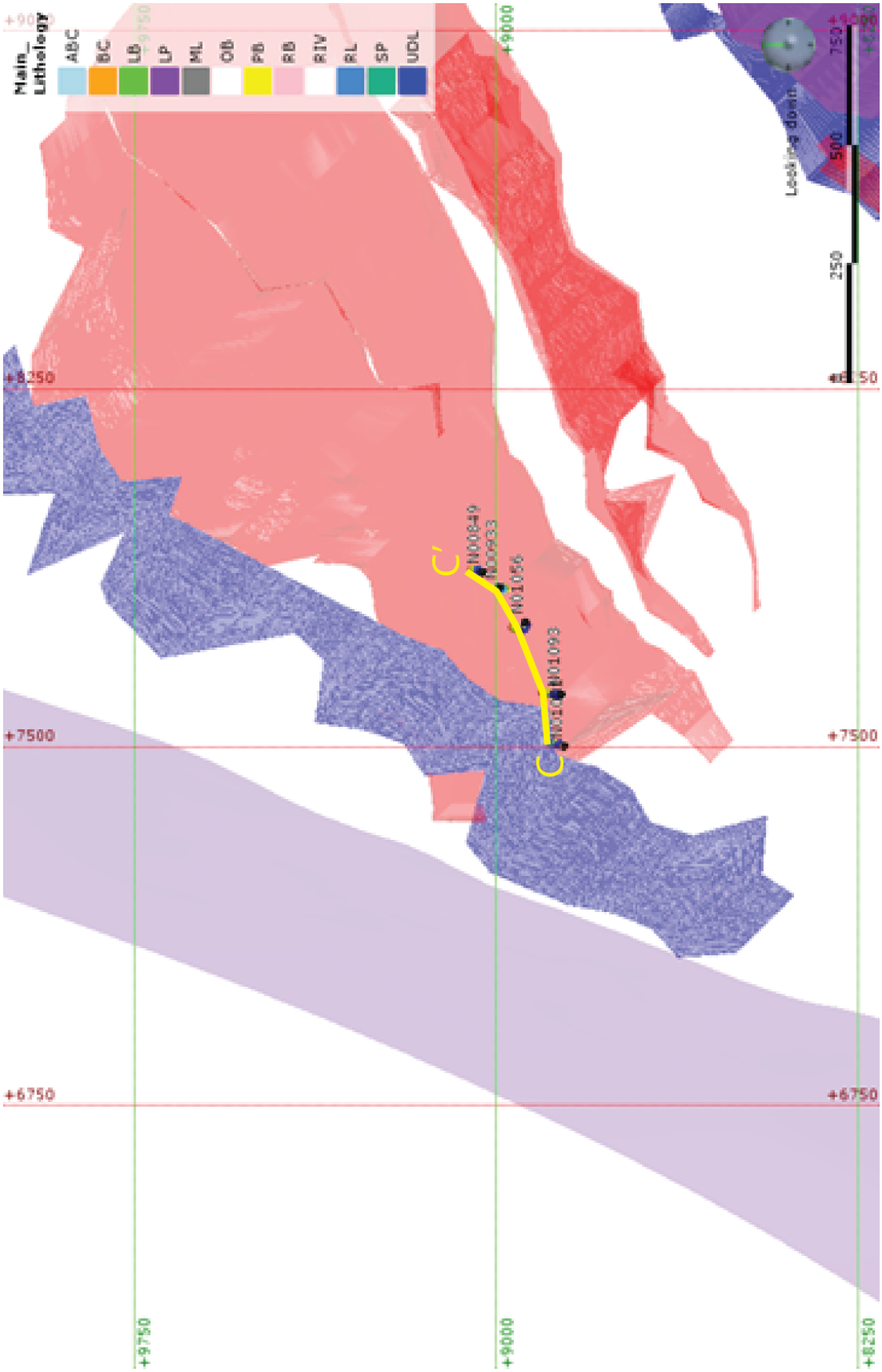

Figure 4.6 - Plan-view of C-C' Transect. N0XXXX number (black) represents drillhole collar. N0XXXX-X number (blue) represents sample points. Section line in yellow. From southwest to northeast, the drillhole collars are as follow – N01001, N01093, N01056, N00933, and N00849

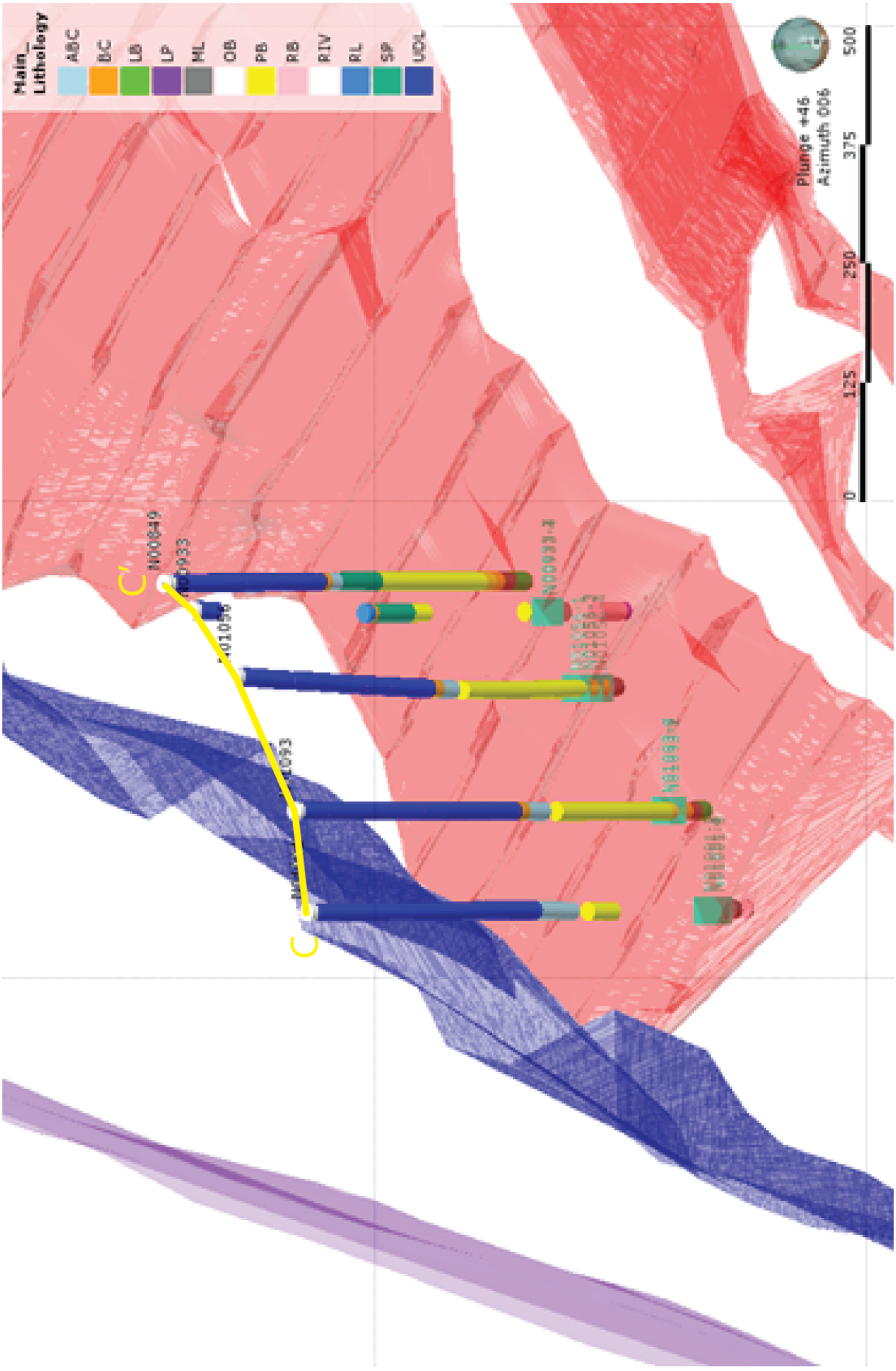

Figure 4.7 -Oblique view of C-C' Transect. N0XXXX number (black) represents drillhole collar. N0XXXX-X number (turquoise) represents sample points. Section line in yellow

Chapter 5

This chapter focuses on results from the geological and Zn/Pb ratio development along the A-C Transects, sulphide and carbonate paragenesis, sulphur isotope distribution and its' relationship to gross sulphide texture, and fluid inclusion microthermometry

Geological, petrographic and Zn/Pb studies of the A-C Transects.

5.1. Geology and Zn/Pb ratios along the A-C Transects:

The Pale Beds stratigraphic sequence in western Navan (I.e. west of the Randalstown Fault) is very similar to that of the Main Mine and footwall of the Randalstown Fault, though has very poor marker horizon development. The B and C Transects are definitive of the Main Mine sequence, comprising thickly interbedded micrites, oolites, calcarenites and massively bedded micro-conglomerates (3-Lens), interbedded with calcarenite, calcisiltite and shaley marker horizons that define the upper and lower limits of each lens (Fig 5.2-5.4). The stratigraphy becomes notably sandier and more argillaceous up-stratigraphy. Unbedded stratal dolomites - hydrothermal dolomite horizons replacing calcarenites (particularly in intensely silty horizons), micro-conglomerate-rudite sequences and oolitic grainstones – are well-developed in the 1 to 3 Lenses of the B-C Transects (Fig 5.2-5.4). The A1 and A2 Transects have slightly different geological sequences, where A1 (hangingwall) drillholes exhibit a westward transition from broadly typical Main Mine geology to massively bedded calcarenites, oolites and micro-conglomerates with poor to absent marker horizon development, while stratigraphy in A2 is well-correlated and very similar to the B-B' and C-C' Transects (Fig 5.2-5.4, Fig 5.8). Stratal dolomite is absent in the A1 Transect until drillhole N02230 (Fig 5.7, 5.8)

Zn/Pb ratios along the A-C Transects can be divided into two groups – Those in the underlying 5 Lens have the lowest Zn/Pb population, while the Zn/Pb ratio of the 1-4 Lenses is much higher. The B and C Transects have average respective average 1-4 Lens of 6.4 and 3.4, while 5 Lens Zn/Pb ratios are lower at 1.2 and 0.5. The A1 and A2 Transects have markedly different respective average 1-4 Lens and 5 Lens Zn/Pb ratios – The A1 1-4 Lens equivalent sequence has an average Zn/Pb ratio of 1.8, while the 5 Lens Zn/Pb average is 1.1. This average increases to 1.8 when factoring out assay data from drillhole N01628, which contains blocky sph-gal (fig 5.19). The A2

Transect 1-4 Lens has a markedly high Zn/Pb ratio of 40, while the 5 Lens Zn/Pb ratio is significantly lower at 5.2.

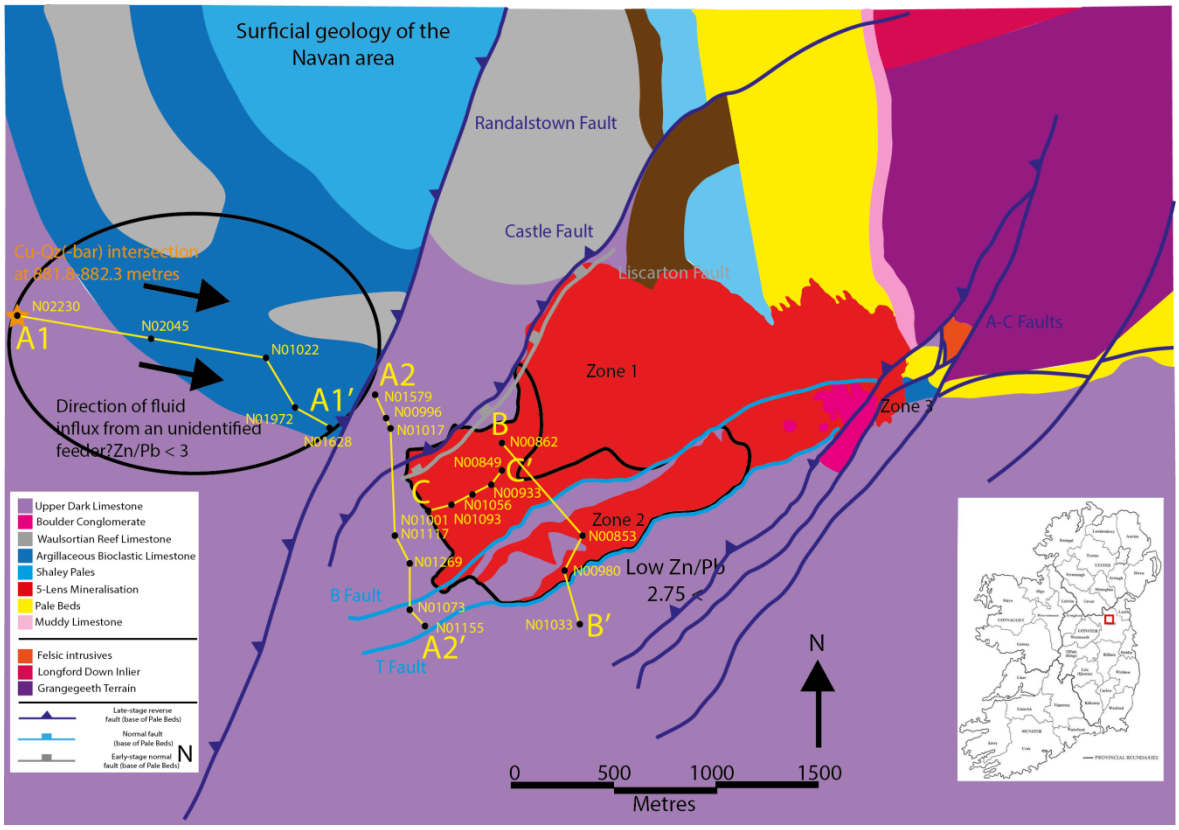

Figure 5.1 – Geological map of Navan area with Main Mine 5 Lens outline (red), low Zn/Pb populations (circled black) and A-C Transects (yellow). For a more detailed Zn/Pb map of the Main Mine, refer to Figure 1.4

5.1.1. Geology along the B-B' and C-C' Transects:

The geology of the B-B' and C-C' Transects are typical of the Main Mine Pale Beds stratigraphy, comprising well-developed calcarenites, oolites, micro-conglomerates and micrites (Fig 3.1, 5.2-5.4). Marker horizons and the 5 Lens Dolomite are well-developed, and correlated.

5.1.2. Zn/Pb ratios along the B and C Transects:

The Zn/Pb ratio of assayed core identifies two distinct groups – core samples obtained from the B-B' Transect 5 Lens have a low average Zn/Pb ratio of 1.2, while those in the overlying 1-4 Lenses register a higher average Zn/Pb ratio of 6.4 (Fig 5.5). Zn/Pb ratios sampled along the C-C' Transect in the low Zn/Pb zone in the southwest 5 Lens identified by Davidheiser-Kroll (2014) demonstrate a similar, though more irregular behaviour across the transect. 5 Lens core samples have a mean

Zn/Pb ratio of 3.4, while overlying 1-4 Lenses exhibit an average of 3.4 (Fig 5.6). 5 Lens Zn/Pb ratios are notably low in drillhole N00862 at 1.44, while those in N00853, N01033 and N00980 are notably higher, ranging from 2.8 to 3.9 with no geographical correlation. This behaviour is produced by both lower Zn, and increasing Pb.

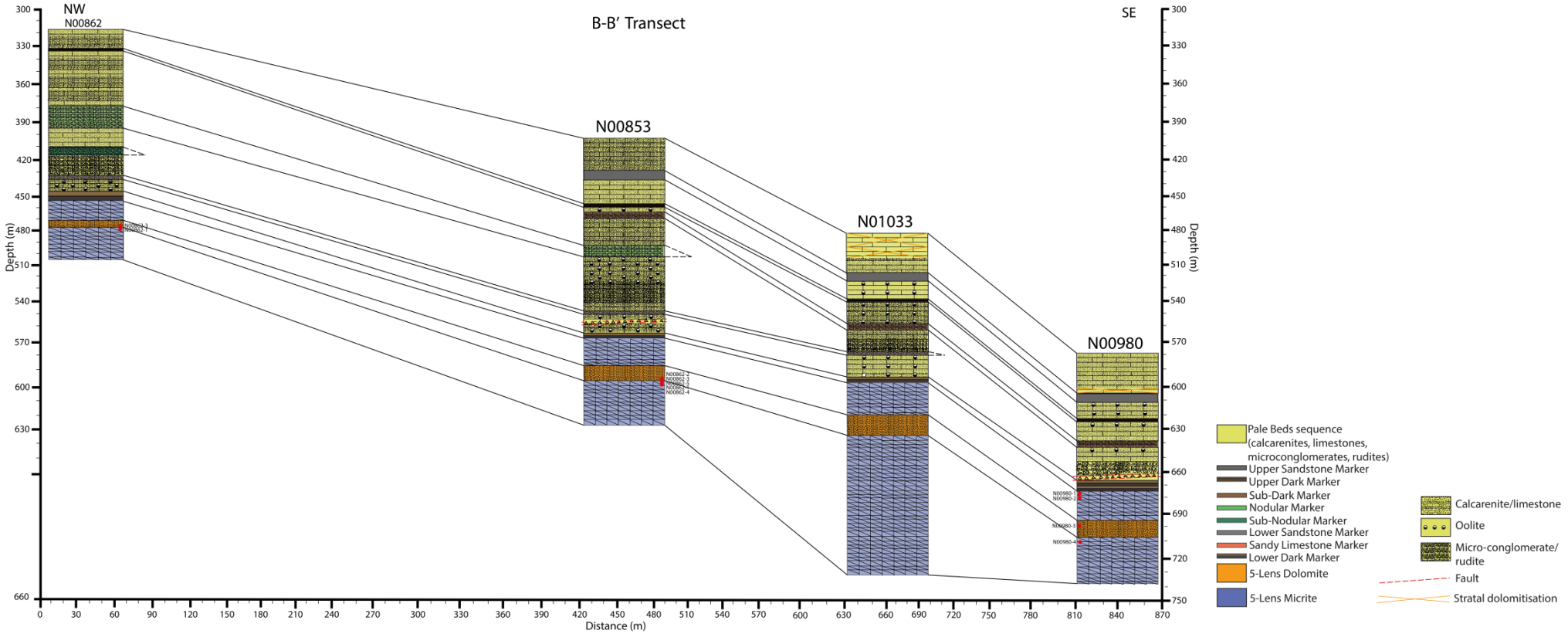

Figure 5.2 - Stratigraphic correlation panel of the B-B’ Transect

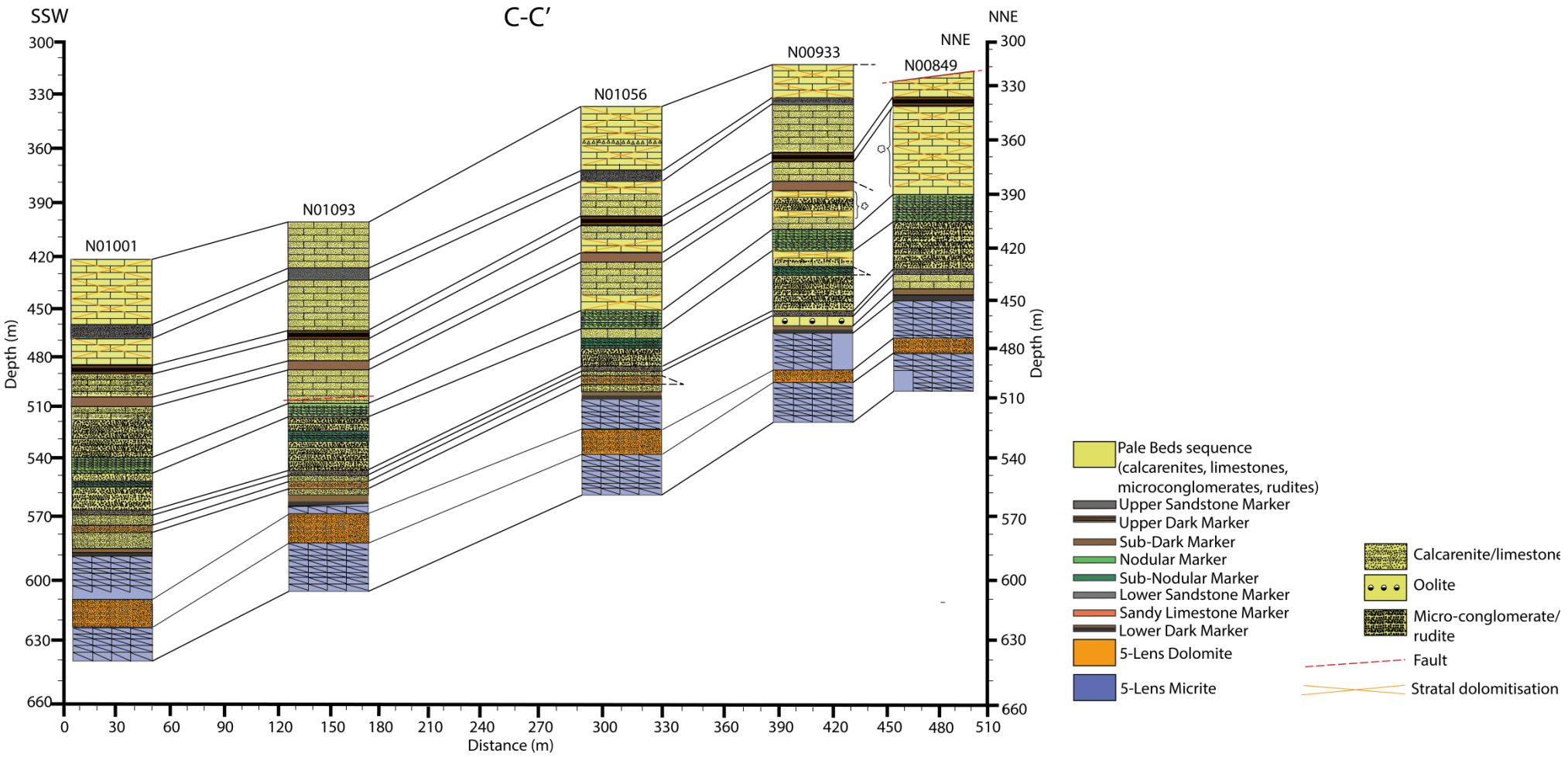

Figure 5.3 - Stratigraphic correlation panel of the C-C' Transect

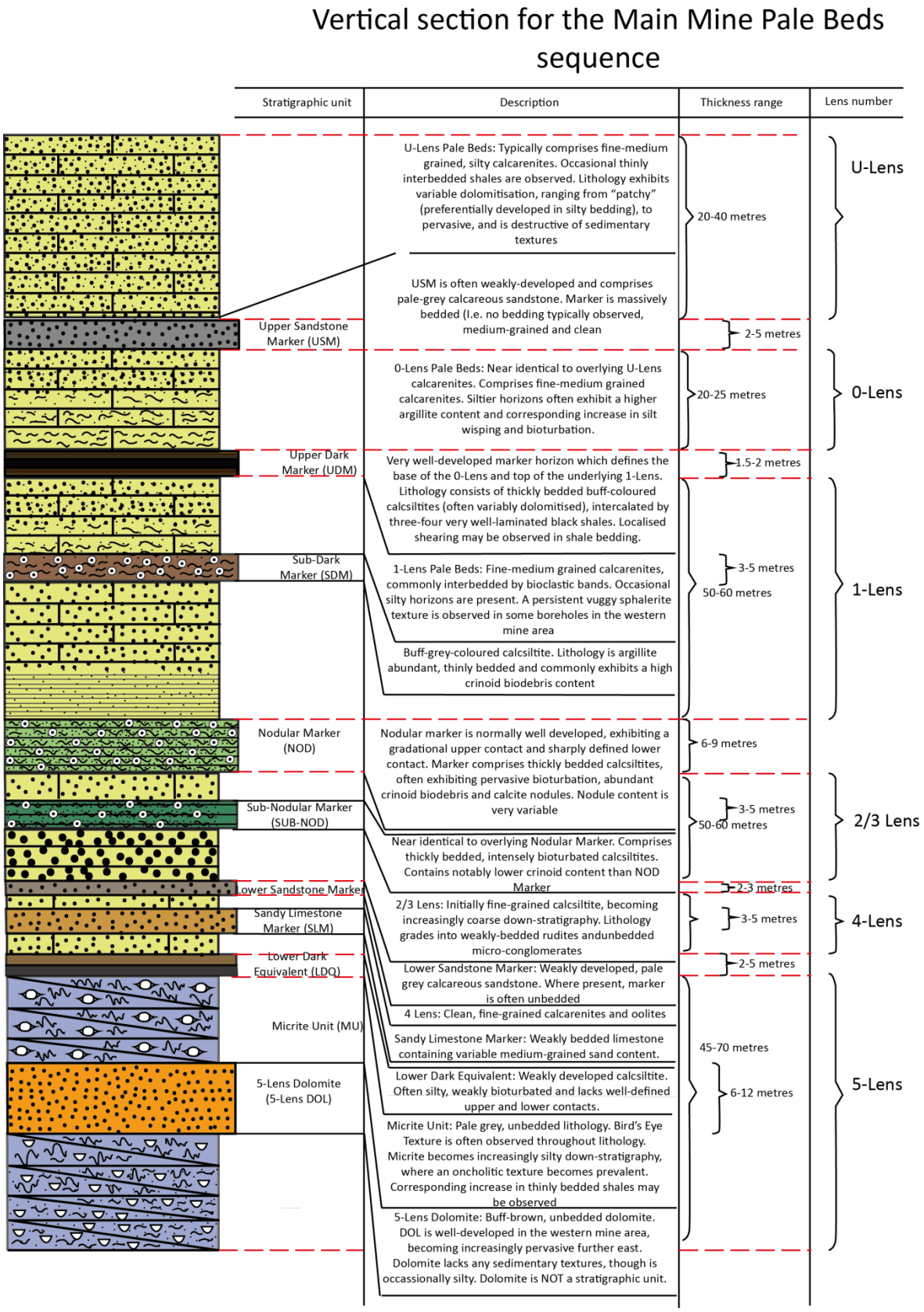

Figure 5.4 - Generalised Vertical Stratigraphy of the geology of the Navan Main Mine (B-C Transects) and A2 Transect

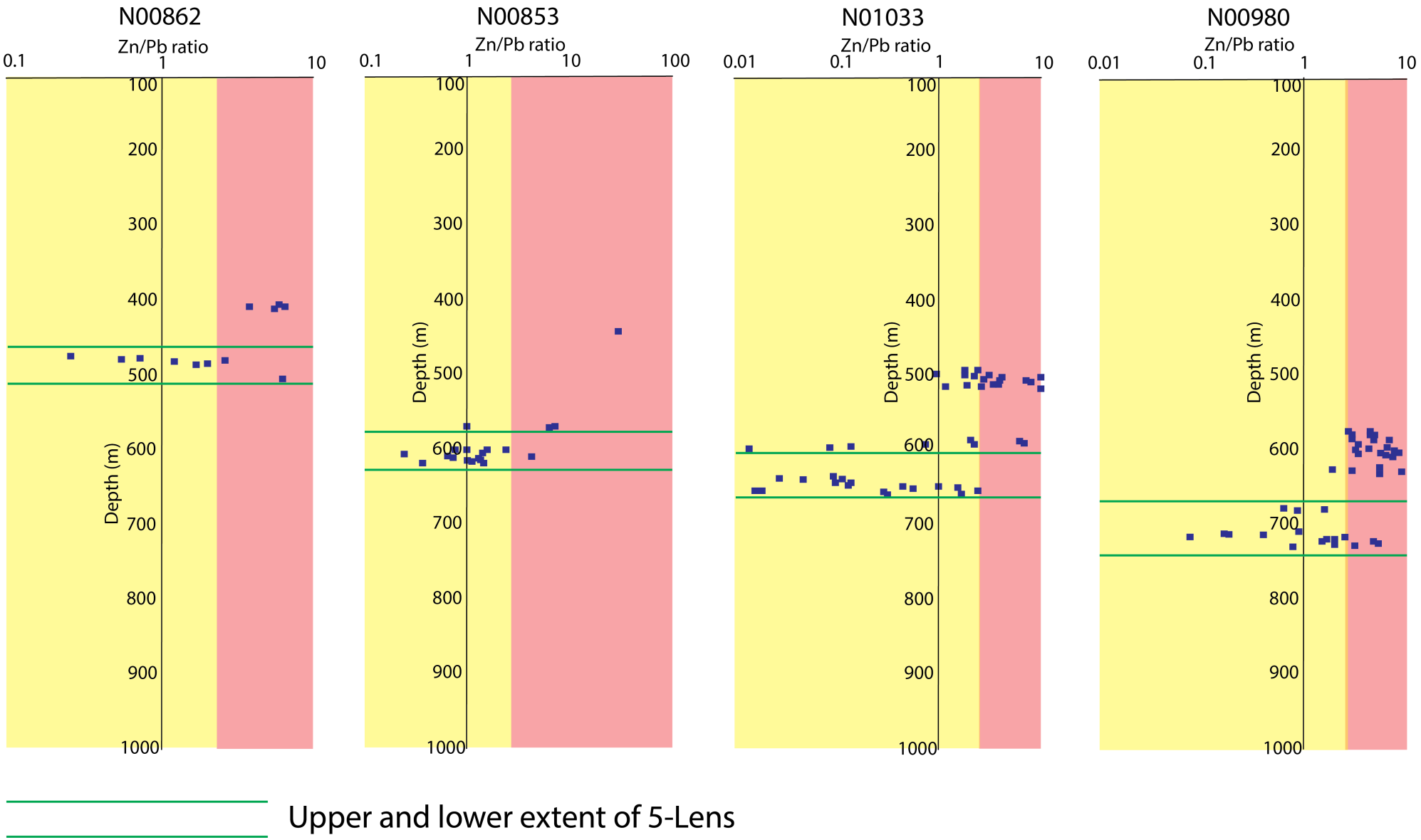

Figure 5.5 – Core assay data from the B-B' Transect drillholes. Pink represents an average Zn/Pb ratio of 4 or more (average Main Mine ratio), while yellow denotes ratios below 4

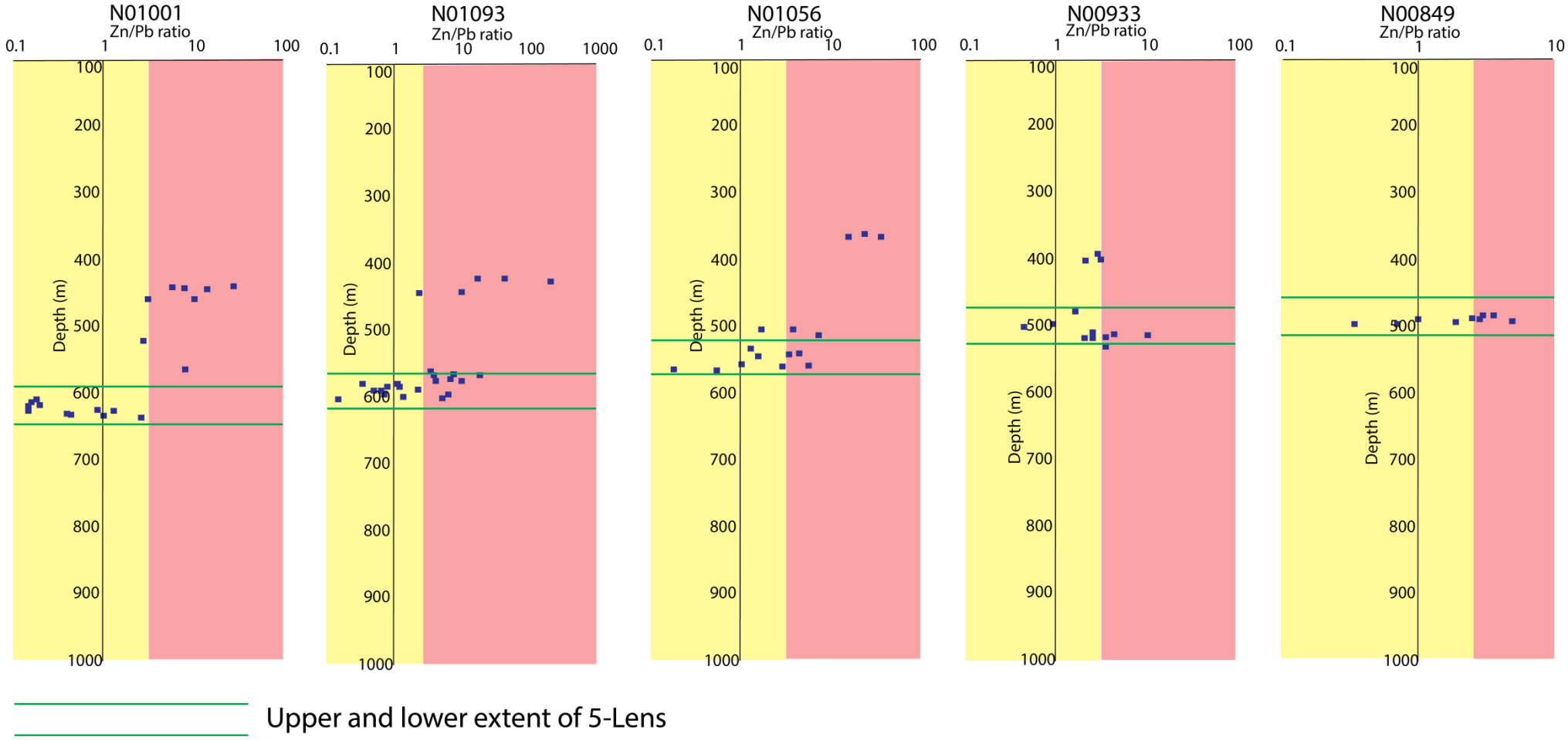

Figure 5.6 – Core assay data from the C-C' Transect drillholes. Pink represents an average Zn/Pb ratio of 4 or more (average Main Mine ratio), while yellow denotes ratios below 4

5.1.3. Geology along the A1 and A2 Transects:

The stratigraphic sequences of the A1 and A2 are rather similar, with the exception of poor marker horizon development in the distal hangingwall of the Randalstown Fault, (Fig 5.7-5.9). The geology along the A2 Transect southeast of the Randalstown Fault is mostly typical of the Main Mine, comprising thickly bedded calcarenites, oolites, microconglomerates and well-developed marker horizons. Stratal calcarenite dolomitisation in the 1-3 Lenses is discontinuous (Fig 5.8). The geology along the A1 Transect northwest of the hangingwall shows gradual evolution from thickly bedded calcarenites, oolites and interbedded micro-conglomerates, to repetitive, fine-grained calcarenite sequences and unbedded micro-conglomerates observed in borehole N02230 approximately 850 metres west of the fault (Fig 5.8). 1-3 Lens stratal dolomitisation is mostly absent along the A1 Transect, though is observed in drillhole N02230 at 880.5-890.8 which hosts Cpy-quartz(-barite) in later-stage calcite-saddle dolomite veins. The 5 Lens Micrite is observed in all A1 Transect drillholes, though the 5 Lens Dolomite only occurs in drillholes N02045 and N01628. The 5 Lens micrite in drillhole N02230 lacks styolitic and oncholitic textures observed in the Main Mine 5 Lens Micrite along the B and C Transects.

A1 Transect drillholes have poor marker development, while marker horizon development in the A2 Transect is similar to that of the Main Mine (Fig 5.4, Fig 5.7-5.9). The Nodular and Sub-Nodular Markers (3-Lens and mid 3-Lens) - comprising crinoid debris-rich pale brown calcisiltites - are absent in the A1 Transect, while the USM, UDM and LDM are poorly developed (Fig 5.7). The Pale Bed stratigraphy of drillhole N02230 is distinct from other hangingwall drillholes. Marker horizons are almost entirely absent (excluding possible USM), and the stratigraphic sequence comprises repetitive calcarenite sequences, poorly-bedded oolites and unbedded micro-conglomerates down-stratigraphy (Fig 5.8). The A2 Transect geology is mostly typical of the Main Mine, though the Sub-Nodular Marker is absent. Stratal dolomitisation in the 1-3 Lenses is common, though may be irregularly developed and is absent from drillholes N01017 and N01269. Unbedded to weakly-bedded micro-conglomerates, which typify 3-Lens stratigraphy below the Sub-Dark Marker are well developed and observed in all drillholes.

5.1.4. Zn/Pb ratios along the A1 and A2 Transects

The Zn/Pb ratios of the 1-4 and 5 Lens sequences of the A1 and A2 are distinct. The A1 1-4 Lens sequence has an average Zn/Pb ratio of 1.8, while the 5 Lens Zn/Pb average is higher at 4. This average decreases to 1.1 drillhole N01628 assay data is factored out. The A2 Transect 1-4 Lens has a markedly high Zn/Pb ratio of 40, while the 5 Lens Zn/Pb ratio is significantly lower at 5.2.

Marker horizon and dolomite occurrences in the A1 Transect

Marker Horizon/dolomite	A1 Transect (hanging-wall)	A2 Transect (foot-wall)	B Transect	C Transect (low Zn/Pb Main Mine)
Upper Sandstone Marker	All drillholes - Very poorly developed	N00996-N01017, N01269-N01155, faulted out of succession in N01579 and N01117	N00853-N00980	N01001-N00933
Upper Dark Marker	N01972 to N02230 (faulted out of succession in N01628	N00996-N01017, N01269-N01155	All drillholes	All drillholes
Nodular Marker	Absent	N01579, N01117-N01155, faulted out of succession in N00996 and N01017	N00862-N00853	All drillholes
Sub-Nodular Marker	Absent	N01579, faulted out of succession in N00996-N01117	N00862	N01001-N00933
Sub-Dark Marker	N01628 to N02045	N01073-N01155	N00853-N00980	N01001-N00933
Lower Sandstone Marker	N01972 to N01022 - Often poorly developed	N01269-N01155, faulted out of succession in N00996-N001117	N00862-N01033	N01001-N00849
Sandy Limestone Marker	Absent	N01155	Absent	N01001-N01056
Lower Dark Marker	N01628 to N02045	N01579-N01017, N01269-N01155, faulted out of succession in N01117	All drillholes	All drillholes
5-Lens Dolomite	N02045 and N01628	N00996-N01269-N01155, faulted out of succession in N01073 by B Fault	All drillholes	All drillholes
Stratal dolomite	N02230	N00996, N01117-N01155	N01033-N00980	N01001, N01056-N00849

Figure 5.7 – Table denoting marker occurrence in the A-C Transects

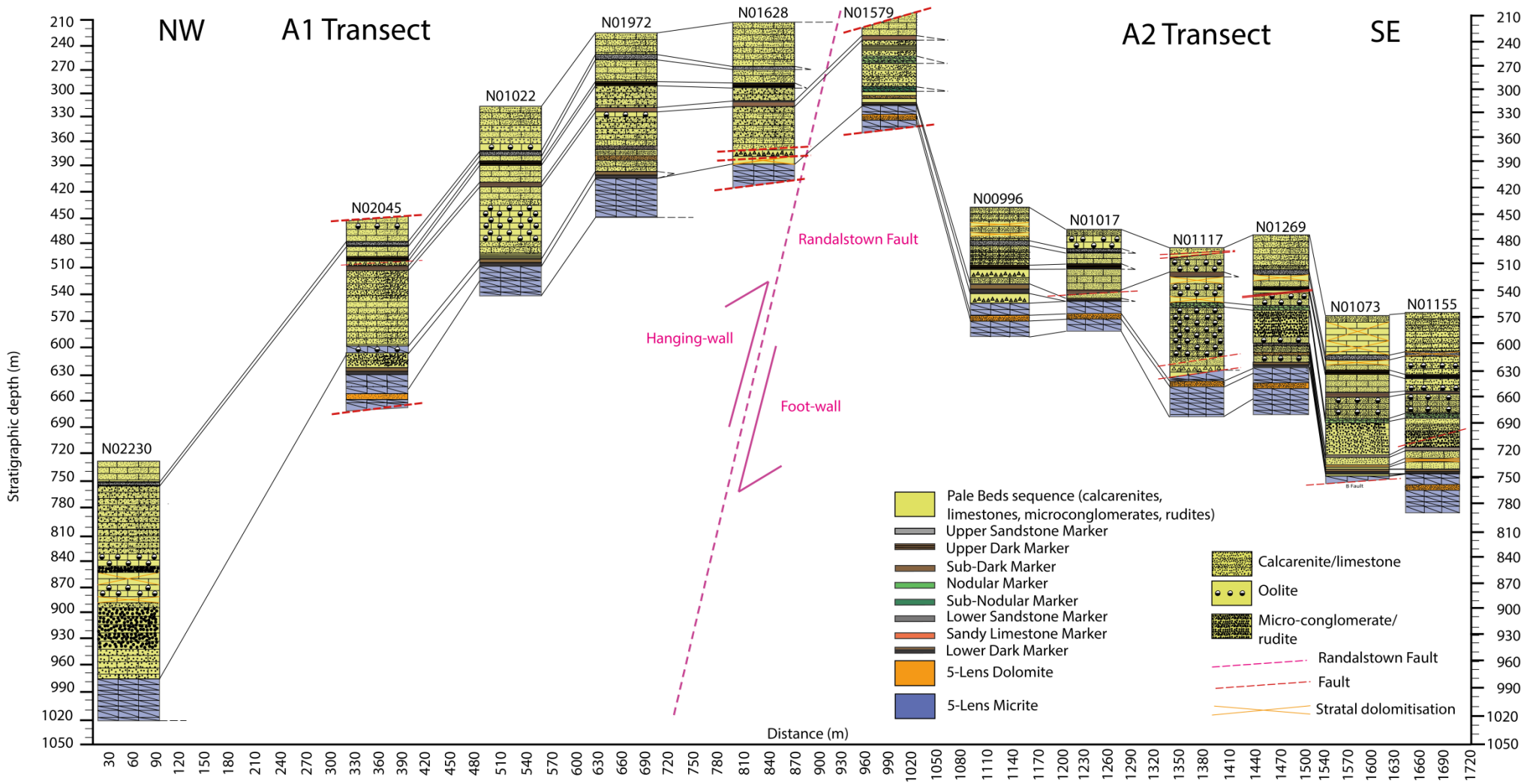

Figure 5.8 - Stratigraphic correlation panel of the A1-A2 Transects

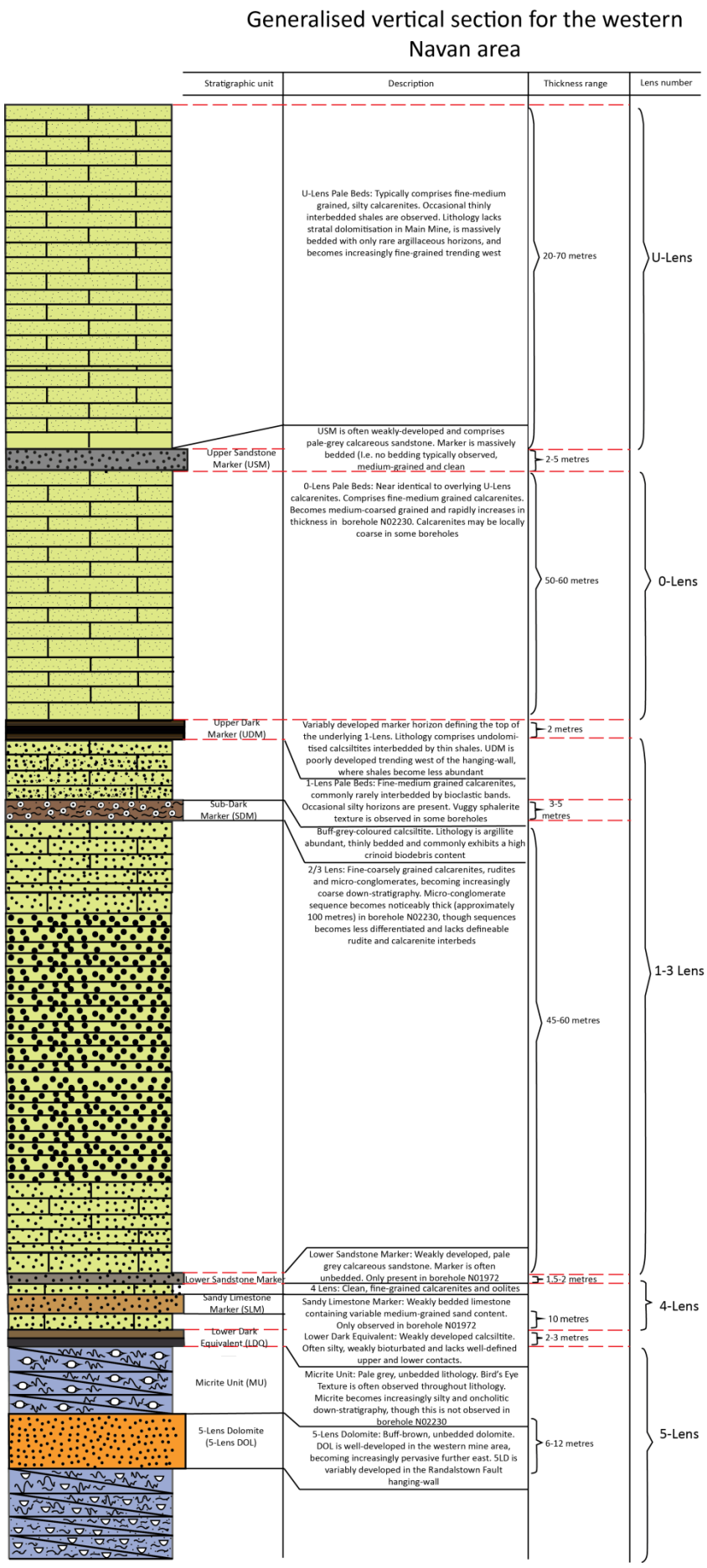

Figure 5.9 - Generalised Vertical Section of the geology of the A1 Transect

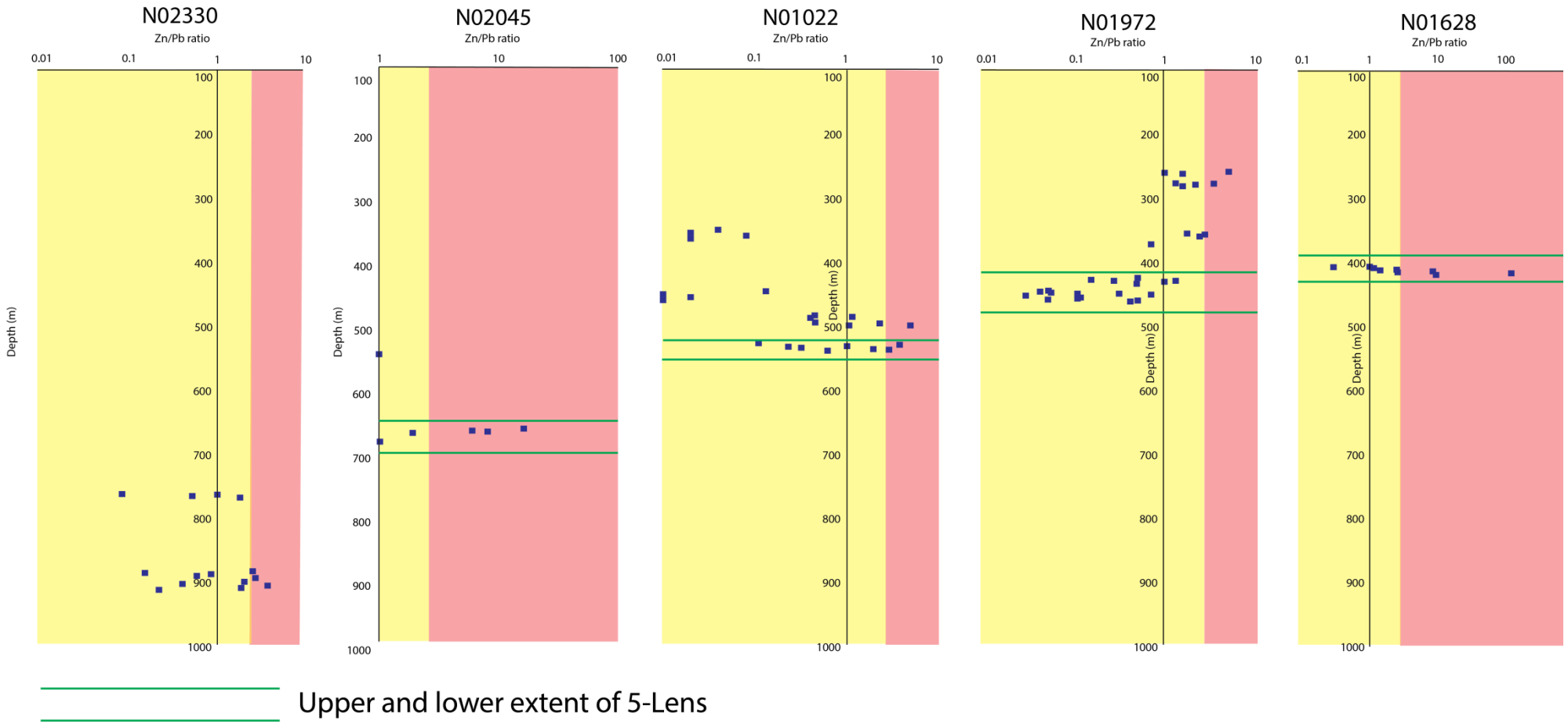

Figure 5.10 – Core assay data from the A1-A1' Transect drillholes

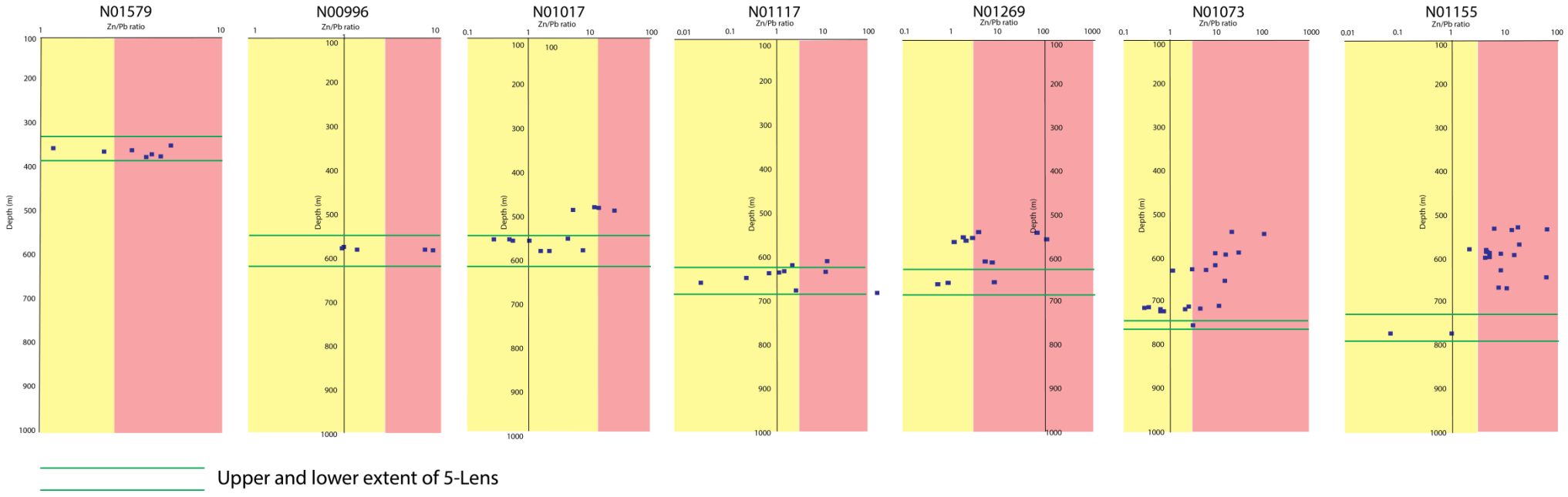

Figure 5.11 – Core assay data from the A2-A2' Transect drillholes

This section identifies three takeaway points from the geological development of the Navan area:

- The A2, B, and C Transects represent the “typical” Navan geology. The geology comprises calcarenites, oolitic grainstones, and micro-conglomerate-rudite sequences, which often show pervasive “stratal” dolomitisation. These sequences are often interbedded by silty and argillaceous horizons, which are more prone to dolomitisation – an observation made by Rizzi (1992) and Braithwaite and Rizzi (1997).

- In drillholes N01628 and N01972 along the A1 Transect (west of the Randalstown Fault in the hanging-wall), the geological sequence is largely similar to that of the A2, B, and C Transects. N01628 shows the greatest level of normal faulting, which removes the Lower Dark Marker, the 5 Lens Dolomite, and most of the 5 Lens Micrite out of sequence. West of drillhole N01972, marker horizon development is very poor and the sequence becomes increasingly clean and less argillaceous than the Main Mine Pale Beds sequence. Dolomitisation is near absent, albeit for two 5 Lens Dolomite occurrences in N02045.

- The geological sequence of drillhole N02230 along the A1 Transect is distinct from those further east, comprising repetitive calcarenite and micro-conglomerate – rudite sequences. Only the Upper Sandstone Marker and poorly developed Upper Dark Marker are observed. The sequence is notable for one stratal dolomite at 882-832.5 metres, that appears to act as a “cap” on cpy-qtz veining. This is discussed in sections X, Y, and Z.

Petrography and mineral paragenesis of the A-C Transects

5.2. Gross sulphide textures:

Summary descriptions of all examined polished thin sections are given in Appendix 10.3. Navan ore sulphides consists of sphalerite and galena with accessory sulfosalts. Non-ore sulphides consist of pyrite-maracasite. Chalcopyrite is rarely observed at Navan. Despite relatively simple mineralogy, the Navan ore is complex, consisting of multiple textures and multiple cross-cutting relations, suggesting that mineralisation was a sustained and multi-episodic process (Ashton et al, 2015). Astonishingly high-grade (with vertical intersection of up to 15 m @ >40 percent Zn + Pb, Anderson et al, 1998) stratabound mineralisation in the Main Mine 5 Lens occurs along the lower contact of the 5 Lens Dolomite, interpreted as an aquitard that ponded mineralising fluids.

This section looks at the distribution of sulphides textures along the A-C Transects, providing an examination of gross sulphide textures *in-core* (section 5.2), and sulphide paragenesis along the A-C Transects in reflected light. Paragenesis findings are provided in section 5.3, and discussed in section 7.2.

Mineralisation along the B-C Transects comprise multiple stages of cross-cutting veins (Fig 5.13), chaotic sulphide-calcite (Fig 5.16), and breccia and replacement sulphides (Fig 5.18). Those from the A1 Transect northwest of the Randalstown Fault comprise gal-sph-cal veins and veinlets, often developed against argillite bands or styloites (e.g. Fig 5.13.C) – visible in thin section), interpreted as local aquitards. Zn-Pb sulphides along the A1 and A2 Transects often occur in paragenetically simple formats, such as single stage vein/veinlet and disseminated galena-sphalerite (e.g. Fig 5.13 D-F, 5.17). Mineralisation in drillhole N01628 (proximal to fault plane in hangingwall) comprises blocky galena-sphalerite-calcite with weakly mineralised micrite clasts (Fig 5.19). Cpy-Qtz(-barite) veining is observed in drillhole N02230, approximately 850 metres west of the Randalstown Fault (Fig 5.12, 5.20), comprising medium-coarsely crystalline quartz with chalcopyrite often following “foliations” in vein core. Sulphides from the A2 Transect in the foot-wall of the Randalstown Fault occur as vein/veinlets, fabric replacive and banded sulphide forms.

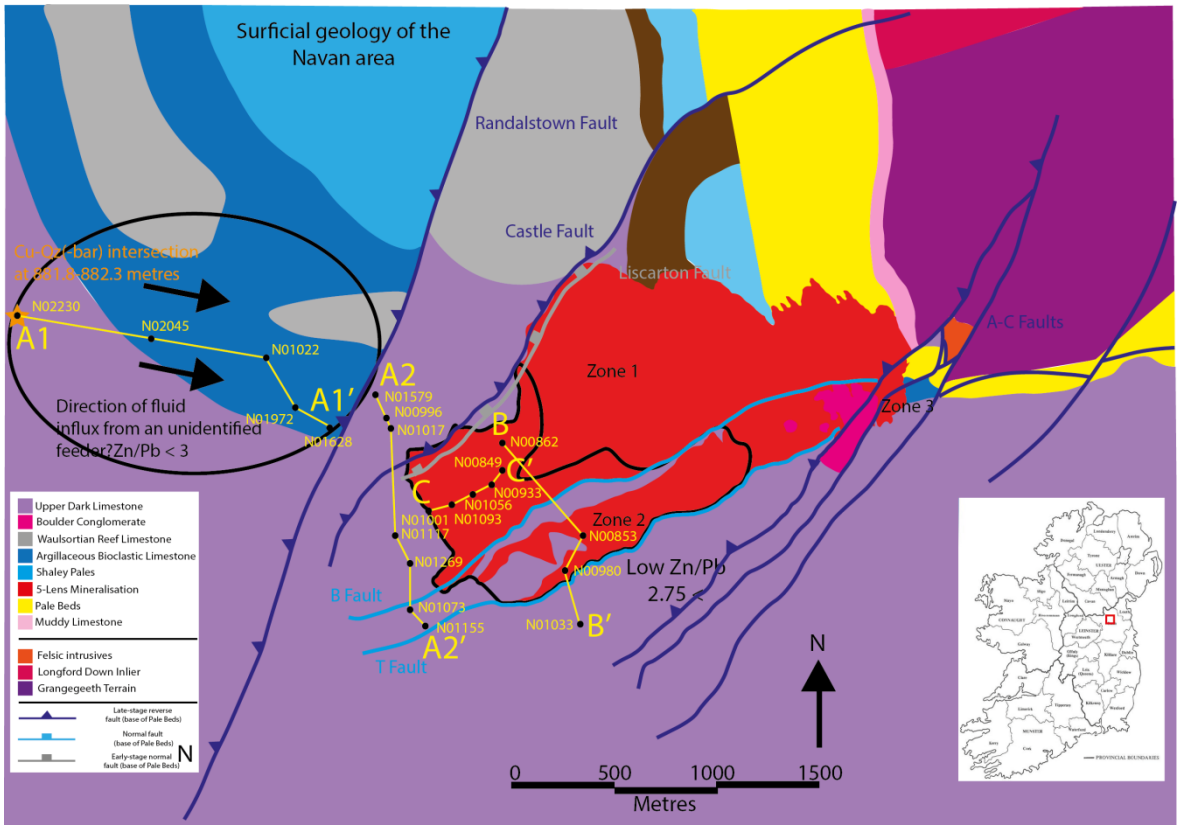

Figure 5.12 – Geological map of Navan area with Main Mine 5 Lens outline (red), low Zn/Pb populations (circled black) and A-C Transects (yellow). For a more detailed Zn/Pb map of the Main Mine, refer to Figure 1.4

5.2.1. Vein/veinlet mineralisation

Vein/veinlet mineralisation comprises gal-(sph)-cal mineralisation, which is often single-stage along the A1 and A2 Transects, though exhibits cross-cutting textures in Main Mine sulphides along the B and C Transects. Veins often follow the profiles of prominent stylolites and thin argillite bands (Fig 5.13C for gross sulphide texture) – a behaviour observed in thin section (Appendix 10.3 - Fig G1). Vein sulphides along the A1 and A2 Transects are concentrated in the 5 Lens Micrite, though are also observed in the 5 Lens Dolomite (Fig 5.13 A). Veins observed along the A1 Transect in the 5 Lens Micrite comprise gal-sph-cal, though vein sulphides from N02045 comprises galena-calcite.


A
Gal


B
Gal

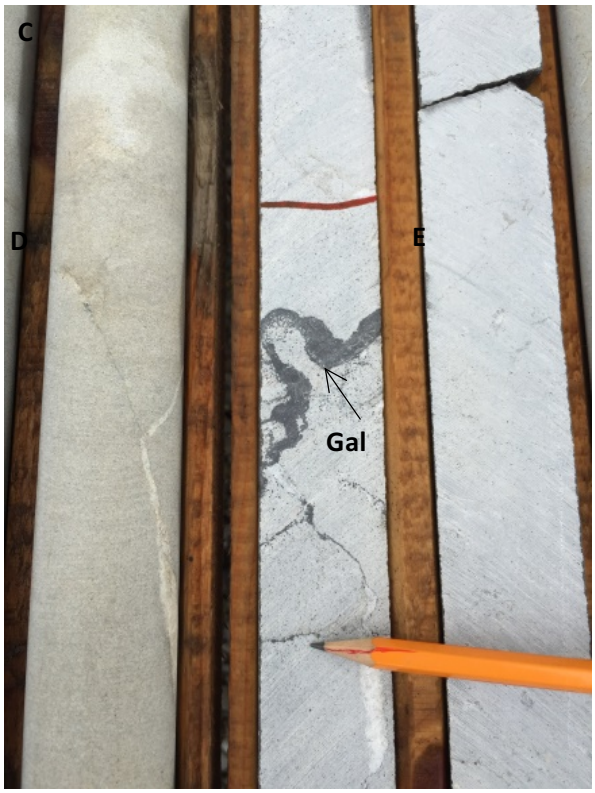
C
D
E
Gal

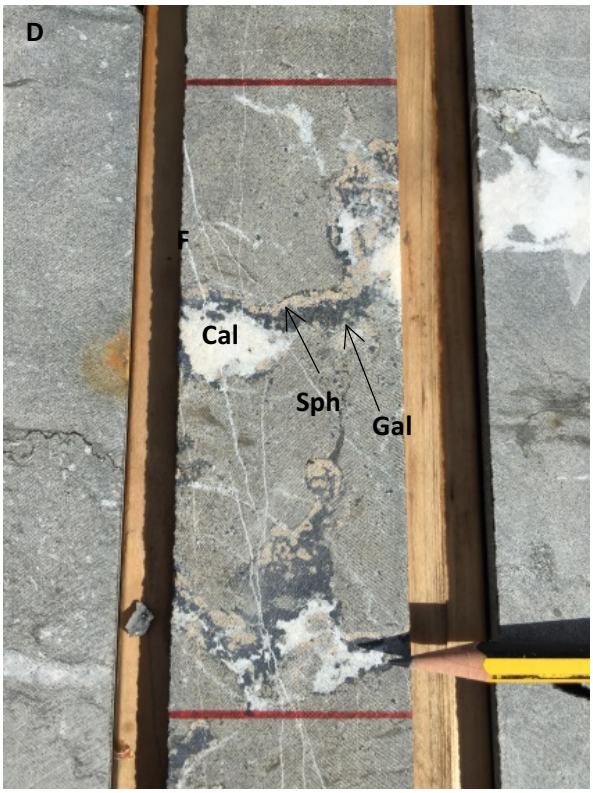
D
F
Cal
Sph
Gal

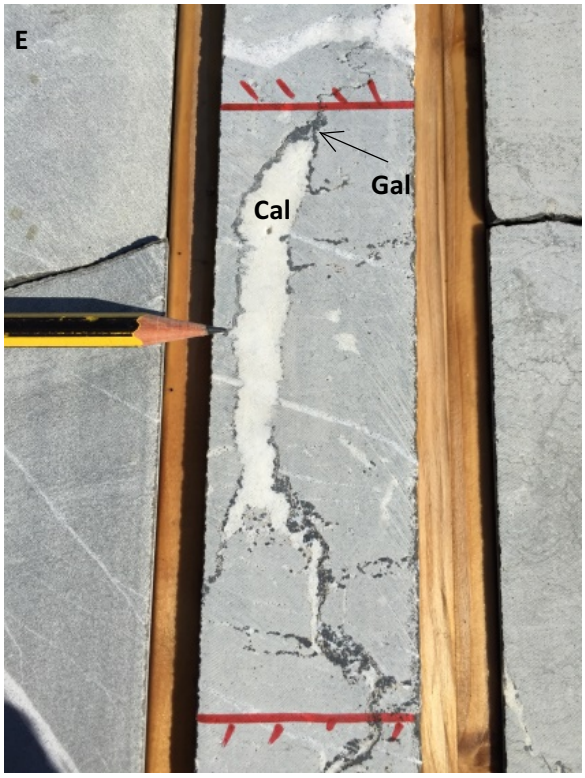

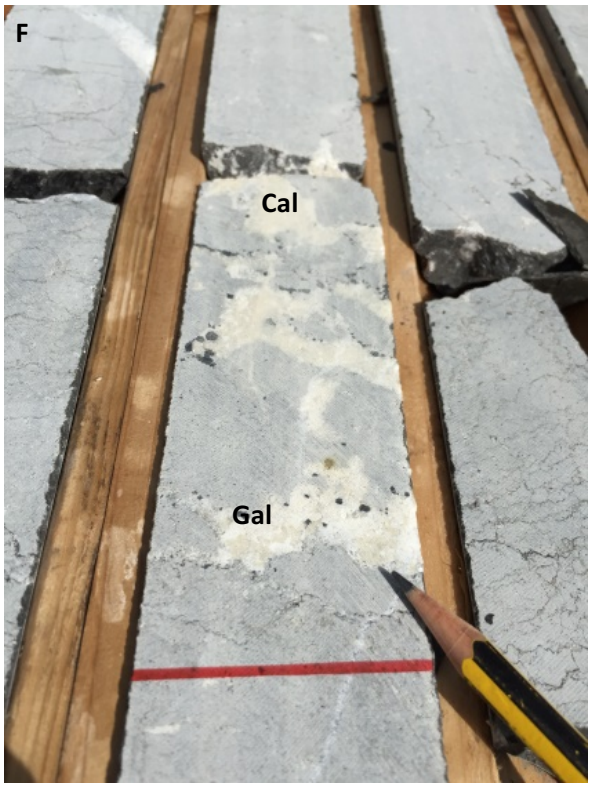

Figure 5.13 – Vein sulphide textures in core

Figure A- Gal-cal vein with sub-ordinate sphalerite - Sample N01001-3

Figure B – Cross-cutting gal-sph-cal veins - Sample N01001-4

Figure C – Galena vein following stylolite - Sample N01117-4

Figure D – Coarsely-crystalline galena-sphalerite-calcite veining- Sample N01972-2

5.2.2. Vuggy-style mineralisation

Vuggy mineralisation is rare in the 5 Lens Micrite though normally comprises open-space granular sphalerite, accessory galena and bladed calcites (Fig 5.14A and 5.14B). Vuggy, granular sphalerite is observed in the 5 Lens of drillhole N01093 in the B-B' Transect, though is significantly more common in the overlying 1-4 Lenses, particularly in stratal dolomite horizons in drillholes N00862 and N00853 along the B-B' Transect.

Figure 5.14 – Vuggy sulphides in core

Figure A – Vuggy, granular sphalerite containing partial calcite – Sample N01093-5

5.2.3. Layered/banded mineralisation

Layered/banded mineralisation comprises thinly interlayered/intercalating, finely-crystalline sphalerite-pyrite and minor euhedral galenas. Layered sulphide often contain interlayered medium-crystalline calcite and weakly mineralised host micrite. Layered sulphides also often exhibit weak brecciation and displacement, or discontinuous inter-banding and veinlet splaying (Fig 5.15A and 5.15B). Layered and banded sulphides are encountered in drillhole N01022 along the A1 Transect, and drillholes N00933 and N00849 along the C-C' Transect

Figure 5.15 – Layered/banded sulphides in core

Figure A - Discontinuous banded sphalerite-pyrite and sub-ordinate galena - Sample N00933-5.

5.2.4. Chaotic mineralisation:

Chaotic style mineralisation is rare and only observed in Main Mine drillholes. Chaotic mineralisation is multi-cyclic, exhibiting multiple cross-cutting relations and is often veined by or contains medium-crystalline calcite (Fig 5.16).

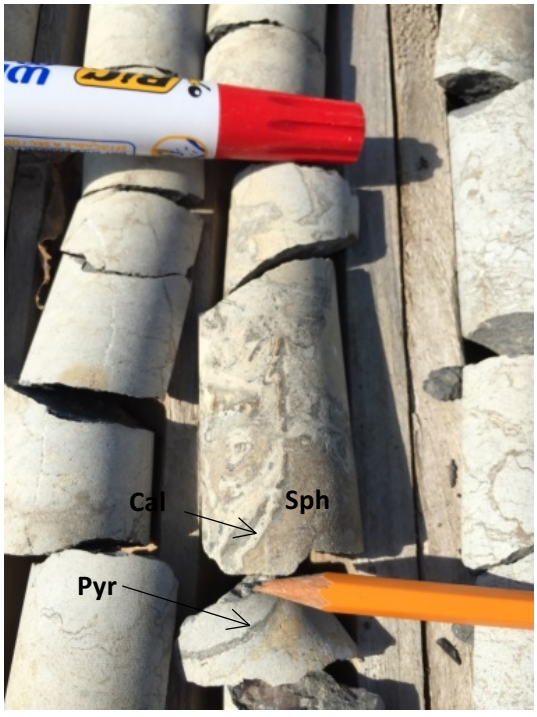

5.2.5. Disseminated mineralisation:

Disseminated mineralisation comprises subhedral-euhedral galena between drillholes N02230 to N01022, and N01155 in the A2 Transect (Fig 5.17). Disseminated sphalerite is prevalent throughout the Pale Beds sequence along the A-C Transects, though disseminated galena is dominant in drillholes N02230-N01022 along the A1 Transect.

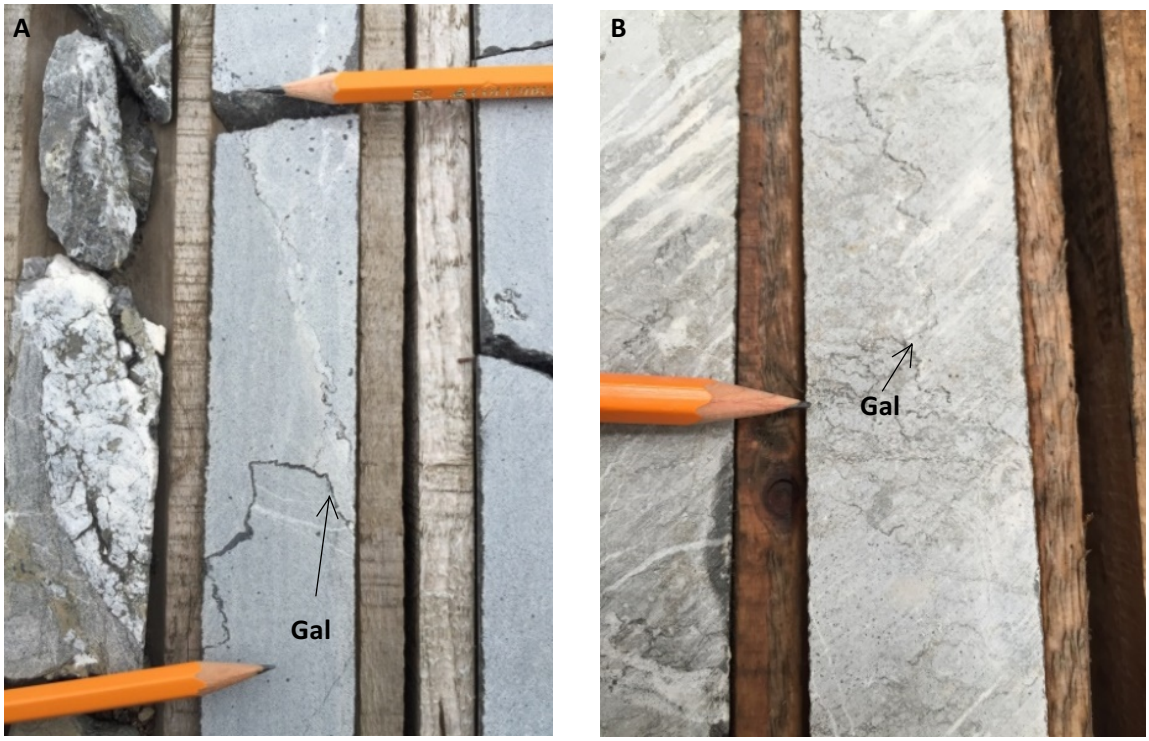

Figure 5.17 – Disseminated mineralisation

Figure A – Disseminated and veinlet galena mineralisation - Sample N01022-2

Fig B – Disseminated mineralisation – Sample N01155-3

5.2.6. Breccia/replacement mineralisation:

Replacement mineralisation comprises fine-grained sphalerite and sub-ordinate euhedral galenas in a fine-grained dolomite matrix, inter-veined by coarsely-crystalline, barren calcites. Breccia-style mineralisation is only observed in drillhole N00996 (Randalstown Fault footwall) and consists of coarsely-crystalline sphalerite-dolomite hosted in a coarsely-crystalline calcite-dolomite vein breccia (Fig 5.18).

Figure 5.18 – Breccia/replacement mineralisation textures in core

Figure A - N00996-2 – Sphalerite-calcite-(dolomite) breccia

Figure B – N00996-3 – Sphalerite-calcite-(dolomite) breccia

Figure C – N01017-3 – Sphalerite replacement following thin argillite bands

5.2.7. Coarsely-crystalline, blocky sulphide mineralisation:

Blocky sulphide mineralisation is only observed in drillhole N01628 (50 metres west-northwest of the Randalstown Fault), consisting of coarsely-crystalline sphalerite, galena, and calcite containing weakly mineralised fossiliferous micrite clasts (Fig 5.19).

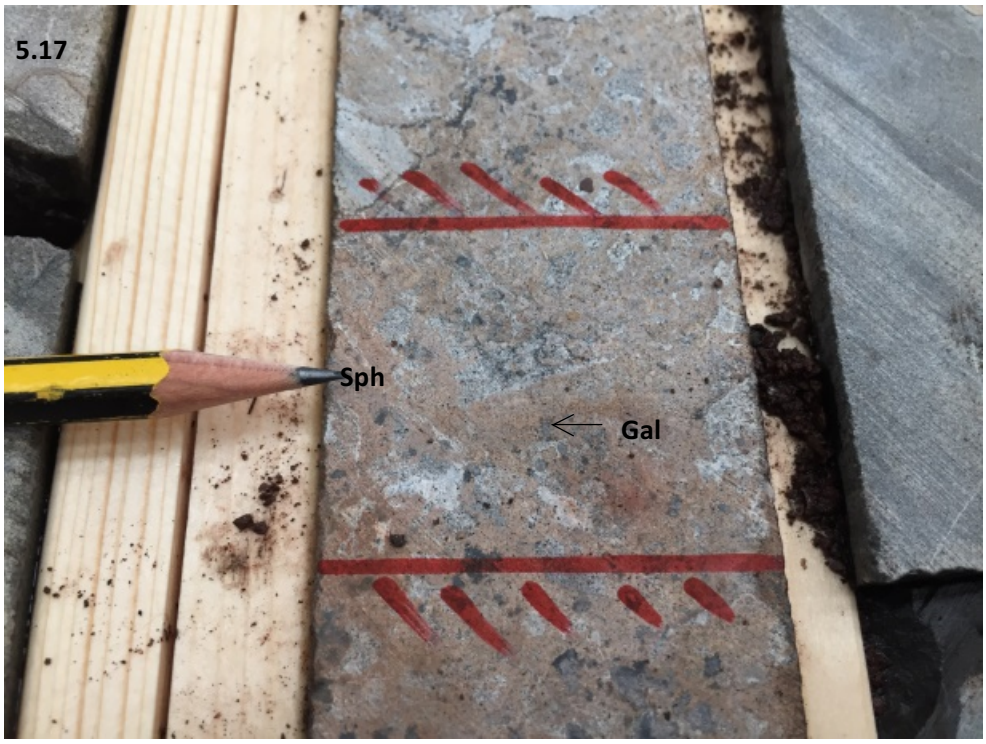

Fig 5.19 – Blocky sphalerite and galena-calcite containing remnant weakly mineralised micrite clasts – Sample N01628-1

5.2.8. Chalcopyrite-Quartz(-baryte) and late-stage calcite-saddle dolomite – Drillhole N02230

Mineralisation in drillhole N02230 comprises fine-medium crystalline Cpy-Qtz(-barite) “clasts” hosted in coarsely-crystalline calcite-saddle dolomite veining (Fig 20 A-C). Chalcopyrite exhibits a strong “foliation”, occurring along the intercrystalline boundaries of coarsely-crystalline quartz textures (discussed in section 5.3.3). Mineralisation is hosted in a 10.5 metre thick stratal dolomite (originally a calcarenite – discussed in section 5.3.3). Mineralisation is hosted in what is interpreted to be the 3-Lens equivalent, based on the presence of micro-conglomerate sequences.

Fig 5.20 – Gross sulphide and gangue textures in core from drillhole N02230

Figure A – Chalcopyrite hosted in medium-crystalline quartz. Pencil indicates quartz "foliation" and preferred chalcopyrite growth direction. Minor calcite cross-cuts at centre bottom - Sample N02230-4

Figure B – Coarsely crystalline chalcopyrite hosted in brecciated quartz-barite clasts – Sample N02230-5

5.3. Petrography and sulphide paragenesis of the A-C Transects

5.3.1. C Transect:

Mineralised C Transect samples comprise sphalerite-galena-(pyrite) and carbonates deposited in multiple stages. A detailed paragenesis has been determined as follows (also see fig 5.21):

1) Early calcite cementation followed by planar/non-planar dolomite replacement.

2) Framboidal pyrite is paragenetically earliest, preferentially developing in siltier matrix and intensely dolomitised horizons, followed by later, finely-crystalline subhedral-euhedral pyrites (very rarely cross-cutting).

3) Fine-coarsely crystalline sphalerite and galena post-date pyrite, often as a replacive or mantling phase. Sphalerite and galena are often observed to mutually intergrow or replace each other. Sphalerite and galena often contain co-precipitated euhedral dolomite rhombs (E.g. Fig 5.22 C). Sulfosalt may form in solid state with galena as very finely-crystalline laths.

4) Sulphides are cross-cut and overprinted by rare, finely-crystalline anhedral chalcopyrite and thin chalcopyrite veinlets (e.g. Fig 5.22 A, B and D).

5) All stages are variably cross-cut by finely-crystalline, fibrous calcite veins (Fig 5.22 D). Veins may co-precipitate with galena.

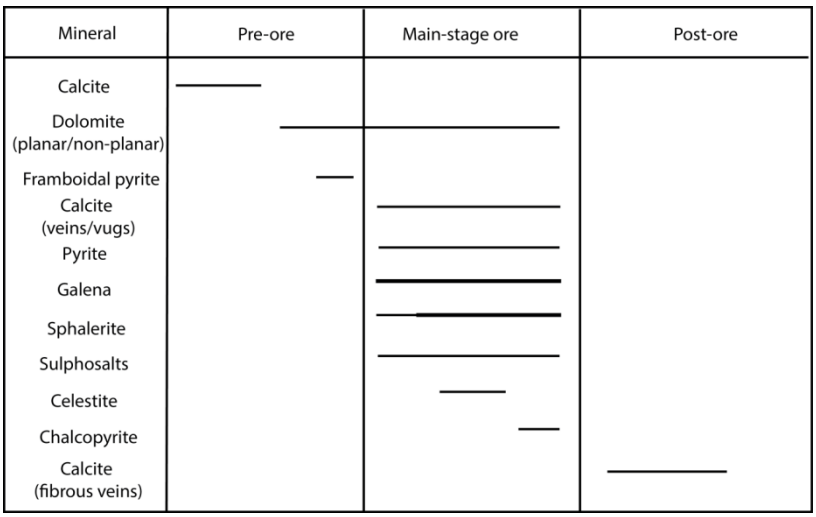

Figure 5.21 – Paragenesis of C transect sulphides

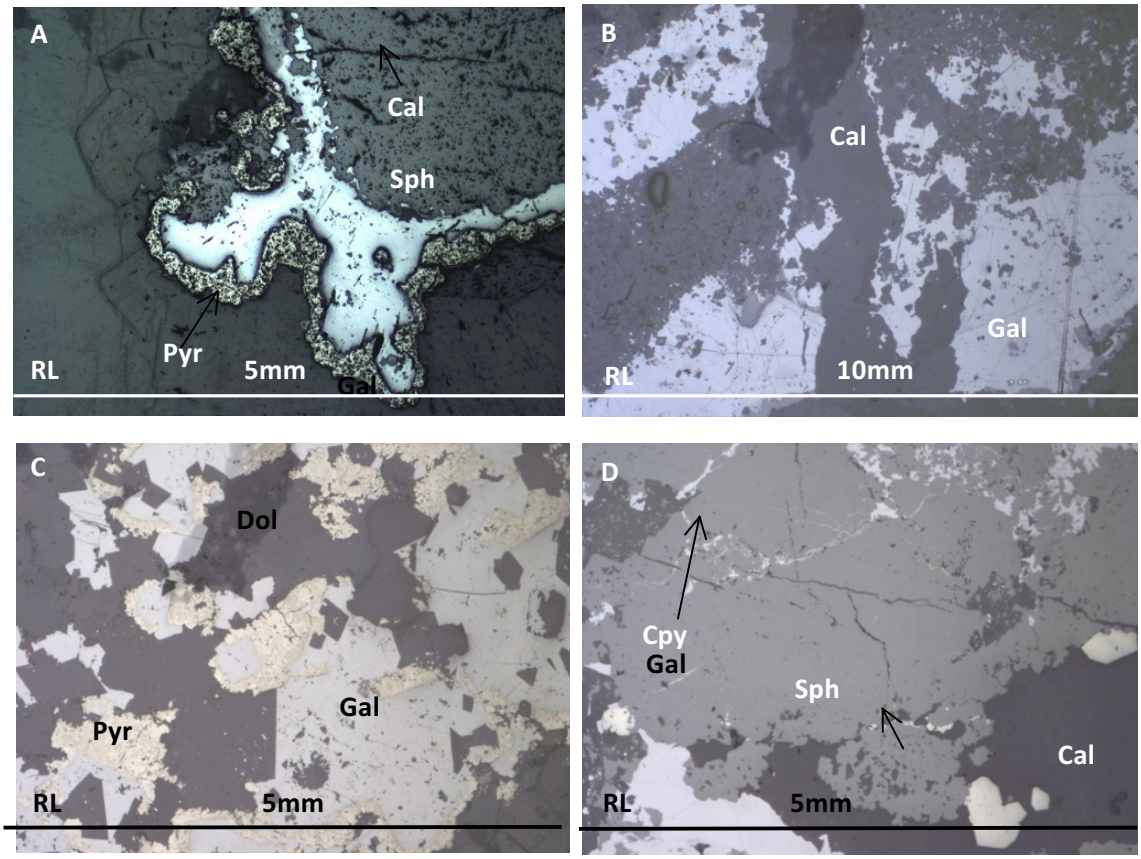

Figure 5.22. – Photomicrographs of sulphides from the C Transect

Figure A – N00849-1 – Banded py-gal-sph, cross-cut by minor late-stage veins

Figure B – N01001-1 – Gal-cal vein cross-cut by late-stage calcite veinlet

Figure C – N01001-2 – Pyrite developing in between pore space of galena and co-precipitated. planar dolomites. Minor replacement of dolomite by pyrite observed.

Figure D – N01001-2 – Sphalerite cross-cut by thin chalcopyrite veinlets, in turn cross-cut by late-stage calcite veinlets.

5.3.2. A1-A1' Transect:

Hangingwall sulphide paragenesis is comparable with that of Main Mine sulphides (Fig 5.21 and 5.23), and the paragenesis defined by Rizzi (1992), Braithwaite & Rizzi (1997), Peace (1999), Everett & Wilkinson (2001), Hitzman and Beaty (2003), and Yardley et al (2005)

1) Early calcite cementation followed by planar/non-planar dolomite replacement.

2) Framboidal pyrite is paragenetically earliest, followed by later, finely-crystalline subhedral-euhedral pyrites. Framboidal pyrite is rare in hangingwall samples and only observed in samples N02230-1 and N01022-1.

3) Fine-medium crystalline sphalerite and galena succeeds pyrite. Sphalerite and galena often exhibit intergrown textures or mutual replacement. Disseminated, medium-crystalline galenas often exhibit relict ooid/bioclast textures (e.g. fig 5.24 B). Galena-sphalerite often contain co-precipitated, anhedral dolomite (E.g. Fig 5.24 A). Galenas from drillholes N01628 and N01972 contain abundant co-precipitated tennantite and boulangerite that form perpendicularly aligned laths in galenas, or intergrowths (e.g. Fig 5.24 D). Sulfosalt abundance in galenas decreases rapidly from N01628 and are a trace assemblage in N01972 and N01022 galenas.

4) Sulphides are overprinted by rare chalcopyrite (e.g. Fig 5.24 E). However, this is only observed in sample N01628-1

5) Sulphides are cross-cut by finely-crystalline, fibrous calcite veins. Veins may co-precipitate with rare galena (e.g. Fig 5.24 G), which may be in turn overprinted by rare, late-stage galena (e.g. Fig 5.24 F)

Hangingwall sulphide mineralisation is often single-stage and does not demonstrate sulphide cross-cutting relations which are common in C Transect sulphides. The only evidence for multi-stage mineralisation is in samples N01972-1, where late-stage pyrite-marcasite overprints galena, and in N01628-1, where aggregate sphalerite grains exhibit well-developed oscillatory zoning and cross-cutting relations with late-stage galenas (Appendix 10.3 - Fig L1). Sulfosalt inclusions in galena are rare in hangingwall sulphides, though are abundant in drillhole N01628 and comprise an accessory mineral phase in galenas in N01972. Late-stage chalcopyrite is not observed west of drillhole N01628, while Cpy-Qtz in N02230 is paragenetically separate.

Mineral	Pre-mineralisation	Main-stage mineralisation	Post-mineralisation
Calcite			
Dolomite (planar/non-planar)			
Framboidal pyrite			
Calcite (veins/vugs)			
Pyrite			
Galena			
Sphalerite			
Sulphosalts			
Chalcopyrite			
Calcite (fibrous veins)			

Figure 5.23 – Paragenesis of A1 Transect Zn-Pb sulphides

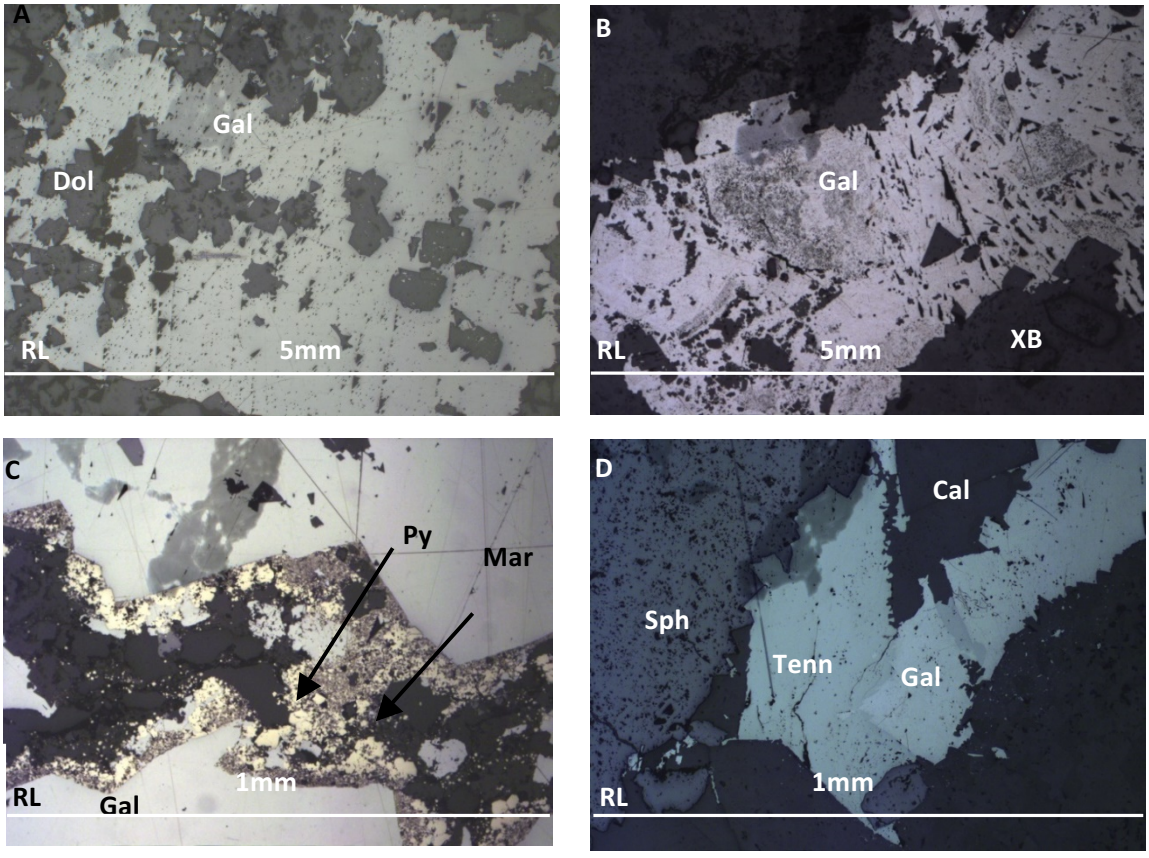

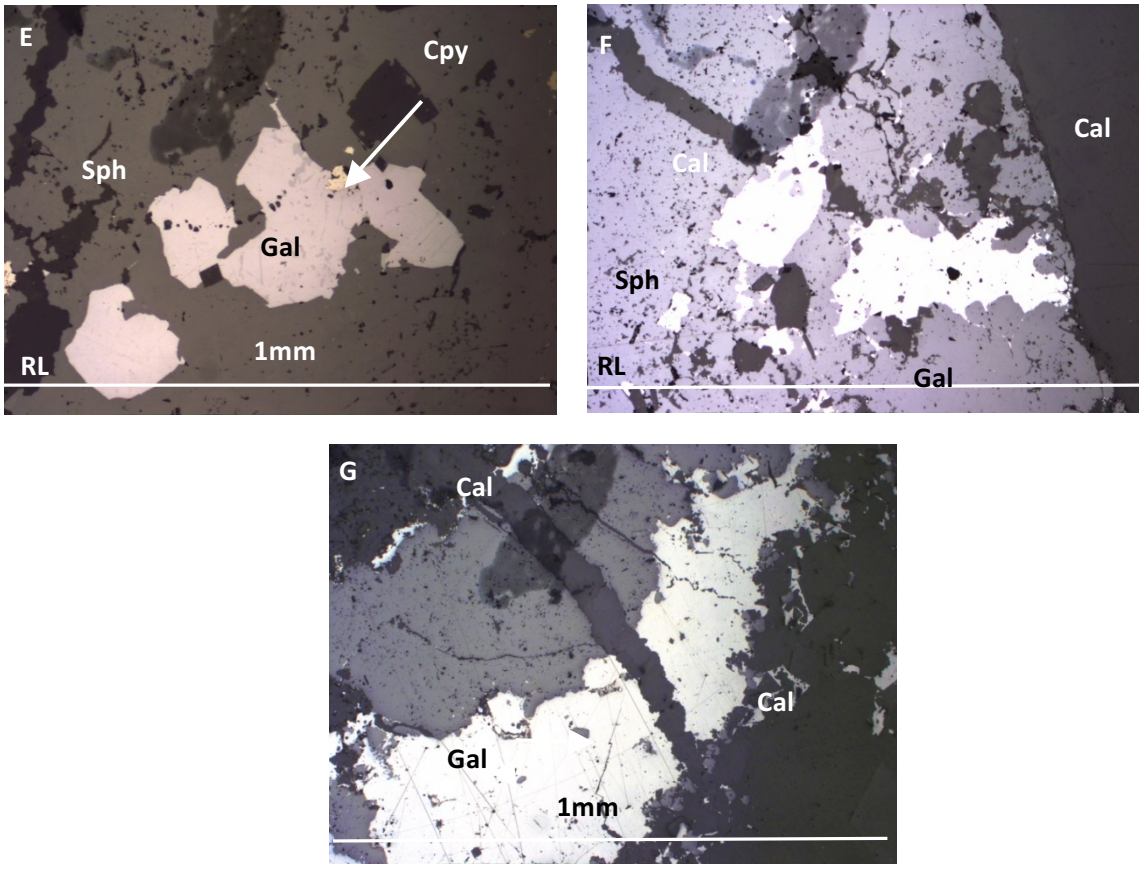

Figure 5.24 – Photomicrographs of sulphides from the A1 Transect

Figure A – N02045-2 – Subhedral galena with co-precipitated dolomite rhombs

Figure B – N01022-1 – Thin galena veinlet retaining relict ooid textures

Figure C – N01972-1 – Galena and co-precipitated planar dolomite being overprinted by late-stage pyrite

Figure D – N01628-2 – Twinned galena-tennantite crystal

Figure E – N01628-1 – Minor chalcopyrite overprinting galena in a sphalerite cement

Figure F – N01628-1 - Sphalerite cross-cut by calcite veinlets, in turn overprinted by late-stage galena

5.3.3. Chalcopyrite in drillhole N02230:

Copper-quartz veining in drillhole N02230 is paragenetically separate from sphalerite and galena hangingwall mineralisation (Fig 5.23 and 5.25) and occurs in a 10.5 metre thick dolomitised calcarenite. Chalcopyrite co-precipitated with quartz, marcasite and trace barite. Later-stage saddle dolomite and blocky calcite veining cross-cuts and transports minor Cpy-Qtz:

1) Initial calcite cementation followed by planar dolomite replacement of host rock.
2) Chalcopyrite-quartz-marcasite(-barite) mineralisation. Quartz textures show a progression towards the vein core, and are separated by discrete mosaic quartz bands:

- Outer vein/vein-wallrock contact - Mosaic quartz-(barite) with prominent co-precipitated chalcopyrite-marcasite (Fig 5.26.D)
- Vein interior - Blocky crystalline quartz and minor chalcopyrite. Chalcopyrite contains intergrown quartz and trace barite, suggesting co-precipitation. Blocky, euhedral quartz exhibits well-developed oscillatory zoning, suggesting several stages of crystallization (Fig 5.26.B)
- Vein core - Plumose, coarsely-crystalline quartz and minor mosaic quartz-barite. Accessory chalcopyrite is observed. Mosaic quartz replaces earlier acicular barites, suggesting quartz was a continued mineralisation phase post-barite (Fig 5.26.C).

3) Saddle dolomite and blocky, scanelohedral calcite. Dolomite-calcite are barren and possibly transported earlier-stage chalcopyrite-quartz-barite. Quartz-barite crystals exhibit limited corrosion by calcite.

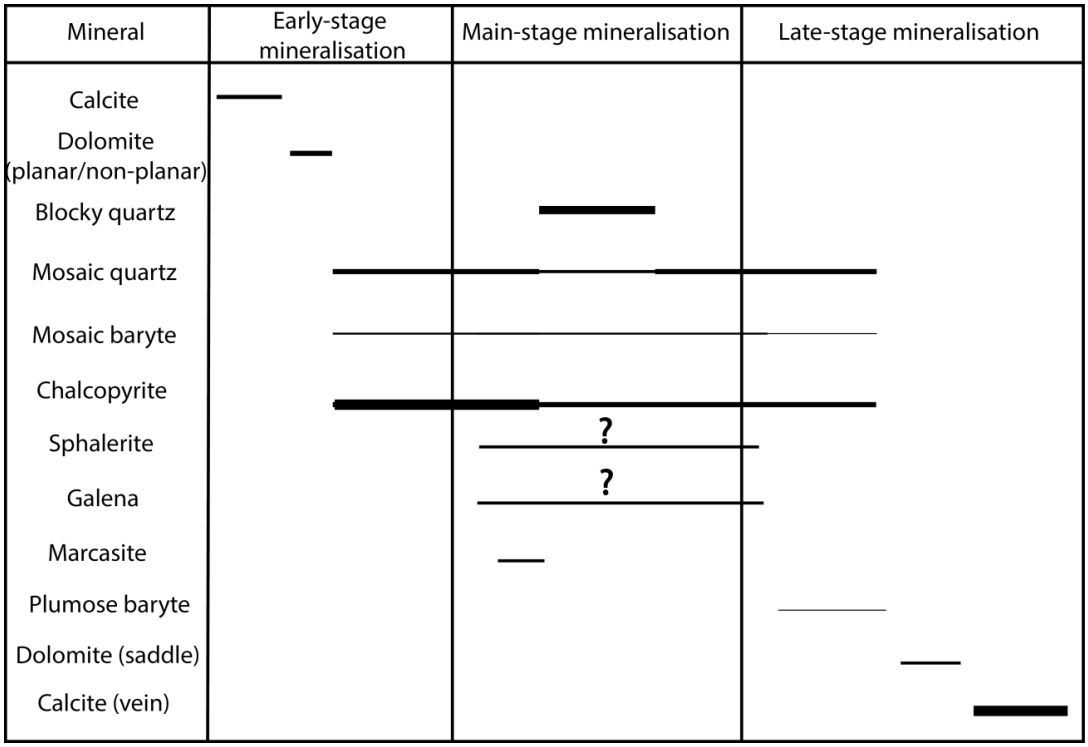

Figure 5.25 – Paragenesis of Cpy-quartz(-barite) veining in drillhole N02230.

Later-stage calcite-dolomite veining cross-cuts minor sph-gal-cpy veinlets in the wall-rock and brecciates and transports minor Cpy-Qtz(-bar) (Fig 5.26 J). As there are no cross-cutting relations between sphalerite and galena veinlets in the dolomite wall-rock with Cpy-Qtz(-barite) mineralisation, it is not known if veinlets co-precipitated with the chalcopyrite, or are related to hangingwall sphalerite and galena east of N02230.

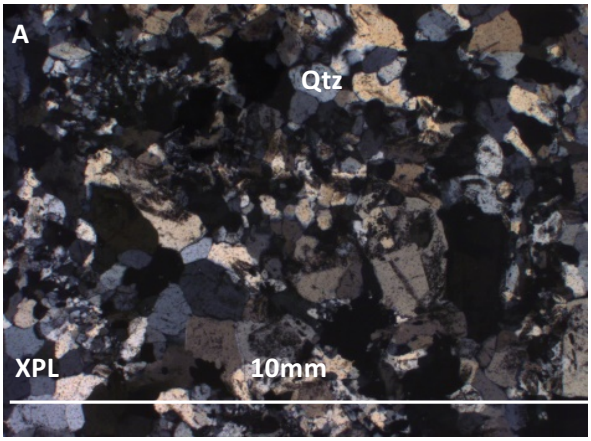
A
Qtz
XPL
10mm

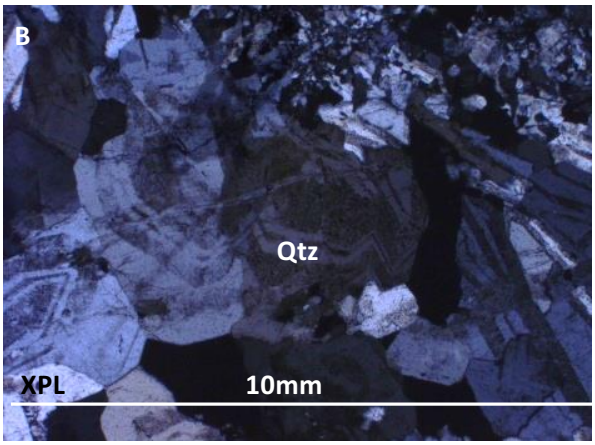
B
Qtz
XPL
10mm

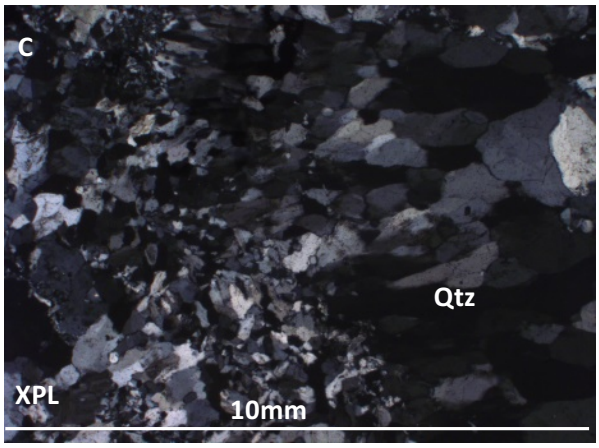
C
Qtz
XPL
10mm

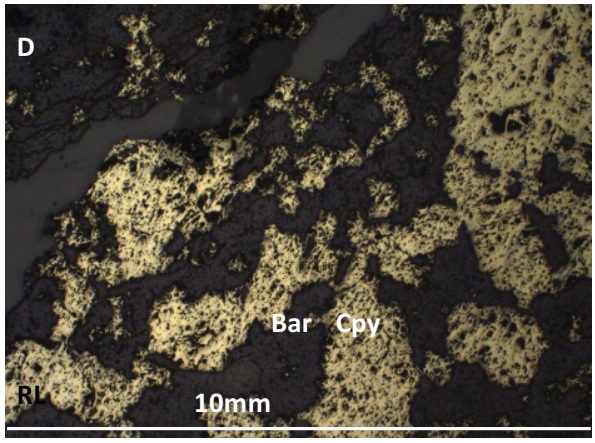
D
Bar
Cpy
RL
10mm

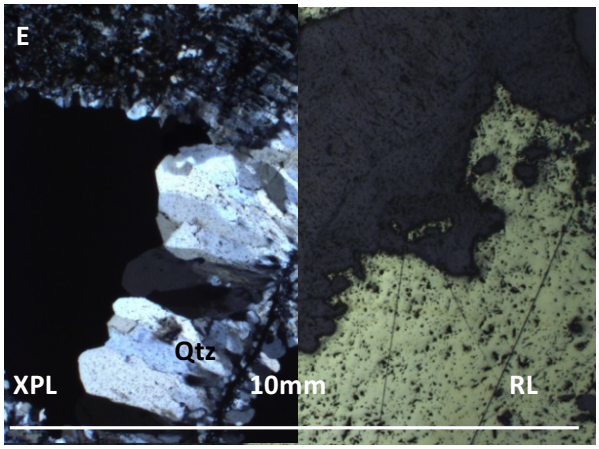
E
Qtz
XPL
10mm
RL

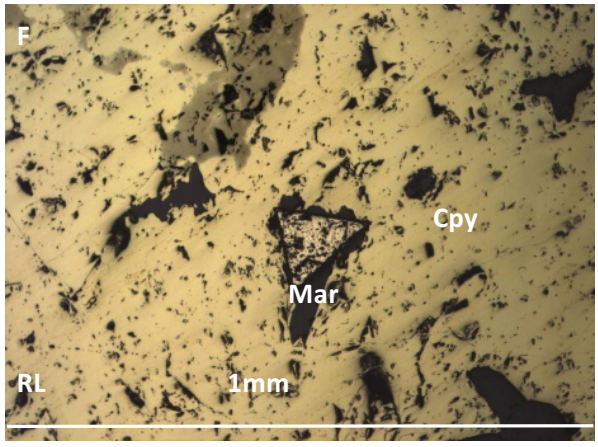
F
Cpy
Mar
RL
1mm

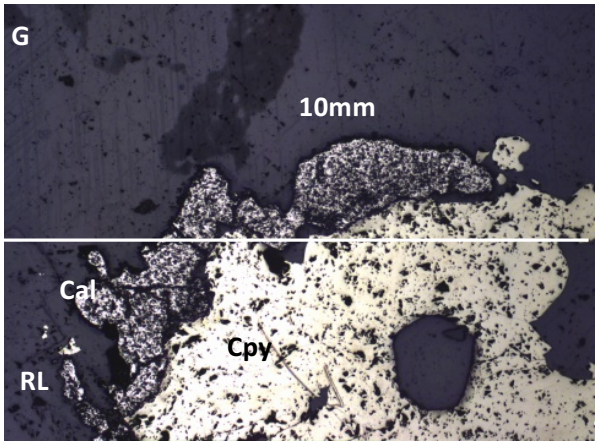
G
10mm
Cal
Cpy
RL

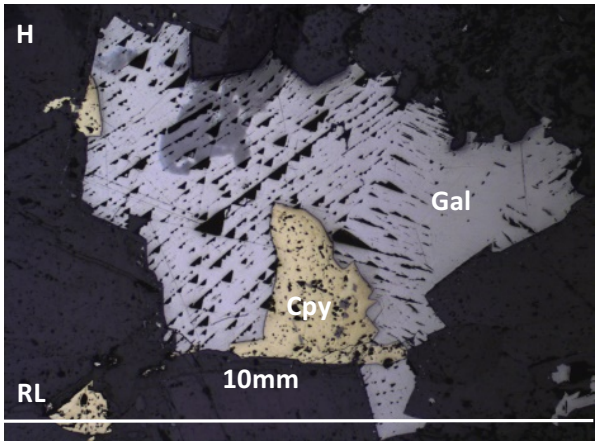
H
Gal
Cpy
10mm
RL

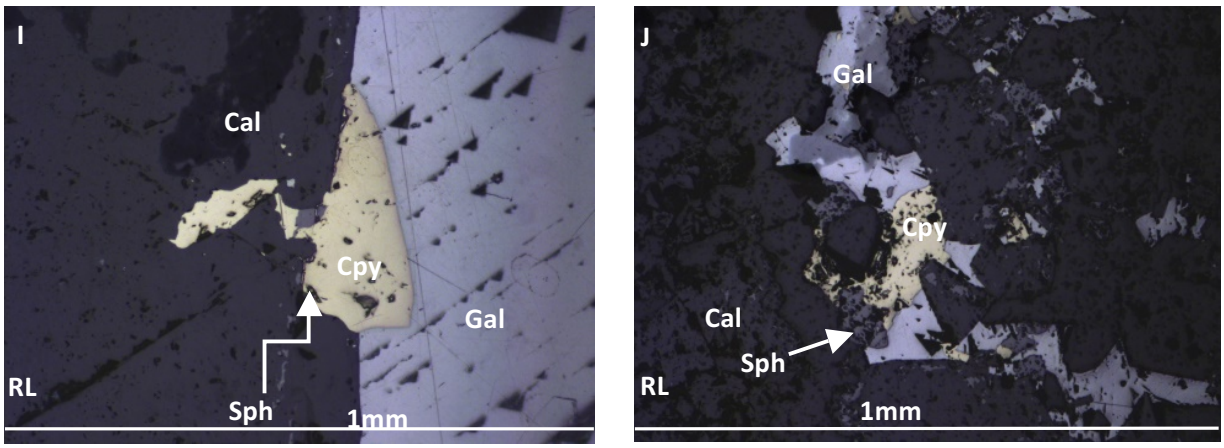

Figure 5.26 – Photomicrographs of sulphides from drillhole N02230

Figure A – N02230-5 Mosaic quartz in outer vein

Figure B – N02230-5 - Blocky, oscillatory-zoned quartz in inner vein

Figure C – N02230-5 – Mosaic and lattice-bladed quartz

Figure D – N02230-5 – Coarsely-crystalline co-precipitated with mosaic quartz

Figure E – N02230-4 – Chalcopyrite co-precipitated with plumose and mosaic quartz

Figure F – N02230-5 – Euhedral marcasite developed in pore space between chalcopyrite and co-precipitated mosaic quartz

5.3.4. A2 Transect – Footwall

The proposed sulphide paragenesis along the A2 Transect trending southeast of the 5 Lens is similar to that of hangingwall and main mine mineralisation (Fig 5.21, 5.23, 5.27), consisting of early calcite cementation, later planar/non-planar dolomitisation, pyrite mineralisation succeeded by galena-sphalerite-sulfosalt precipitation. Rare chalcopyrite replaces earlier-stage sulphides, and is cross-cut by late-stage calcite veins and fibrous veinlets:

1) Early calcite cementation followed by planar dolomite replacement.

2) Framboidal pyrite develops in silty/argillaceous matrix first, followed by later-stage, euhedral pyrite.

3) Fine-coarsely crystalline sphalerite and galena succeed pyrite, and may co-precipitate with calcite-dolomite (fig 5.28.B) or calcite-celestite veins. Disseminated, medium-crystalline galenas often exhibit relict ooid/bioclast textures. Sphalerites may exhibit well-

developed zoning, particularly in sample N01073-1, N01017-2, and co-precipiate with calcite-dolomite (N01579-1).

4) Sulphides are overprinted and cross-cut by finely-crystalline chalcopyrite and veinlets. Late-stage chalcopyrite may replace the rims of sphalerite and galena, occur along the pore space of galena-sphalerite and co-precipitated rhombic dolomites (Fig 5.28 B), or occur as a thin veinlet-style replacement. Later-stage pyrite-marcasite is observed in samples N01073-3 (Fig 5.28 E) and N01017-2 (Fig 5.28 D)

5) Stages one to four are cross-cut by finely-crystalline, fibrous calcite veins (e.g. fig 5.28 F)

Galenas are observed to co-precipitate with anhedral sphalerites and very finely-crystalline dolomite rhombs. Sulfosalts (tennantite-boulangerite) comprise very finely-crystalline laths in galena in samples N01017-1, N01269-2, and N01073-1. Sulphides in drillhole N00996 (approximately 200 metres southeast of the Randalstown Fault) comprise coarsely-crystalline sphalerite in a calcite-dolomite vein breccia with minor galena and trace chalcopyrite (Fig 5.28 A)

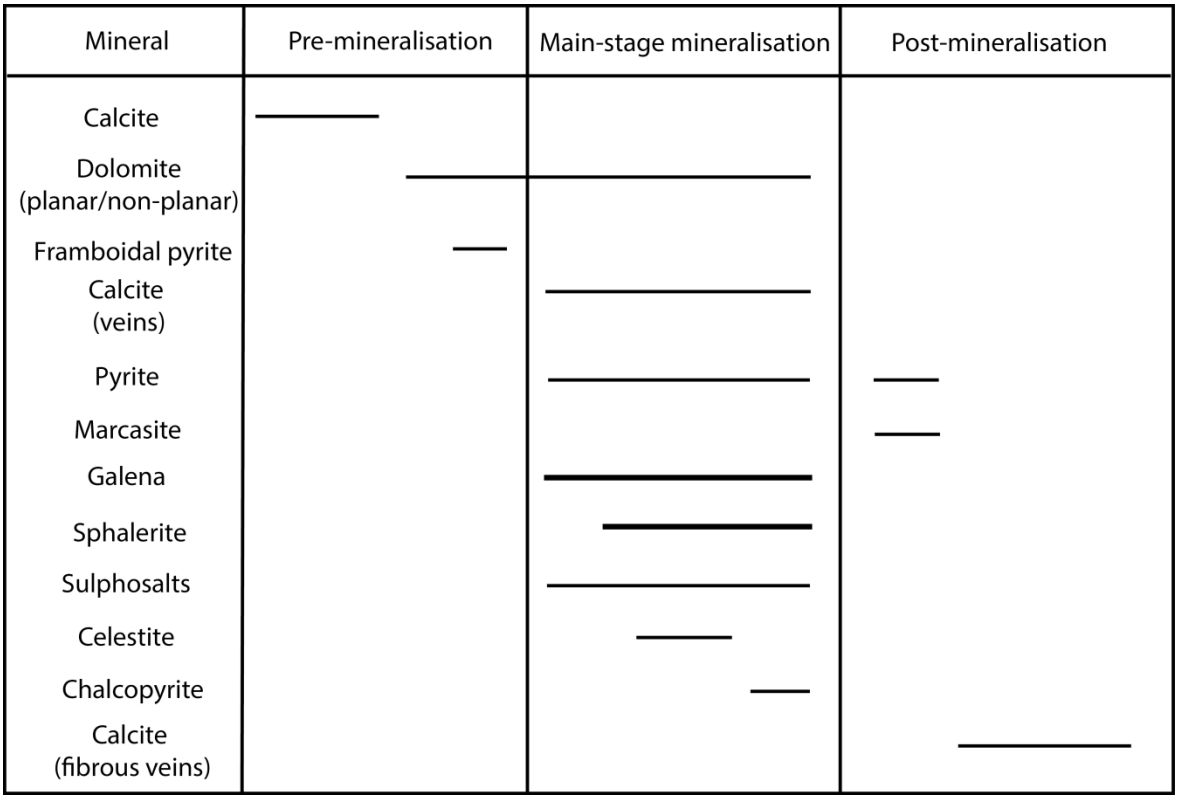

Figure 5.27 – Paragenesis of A2 Transect sulphides

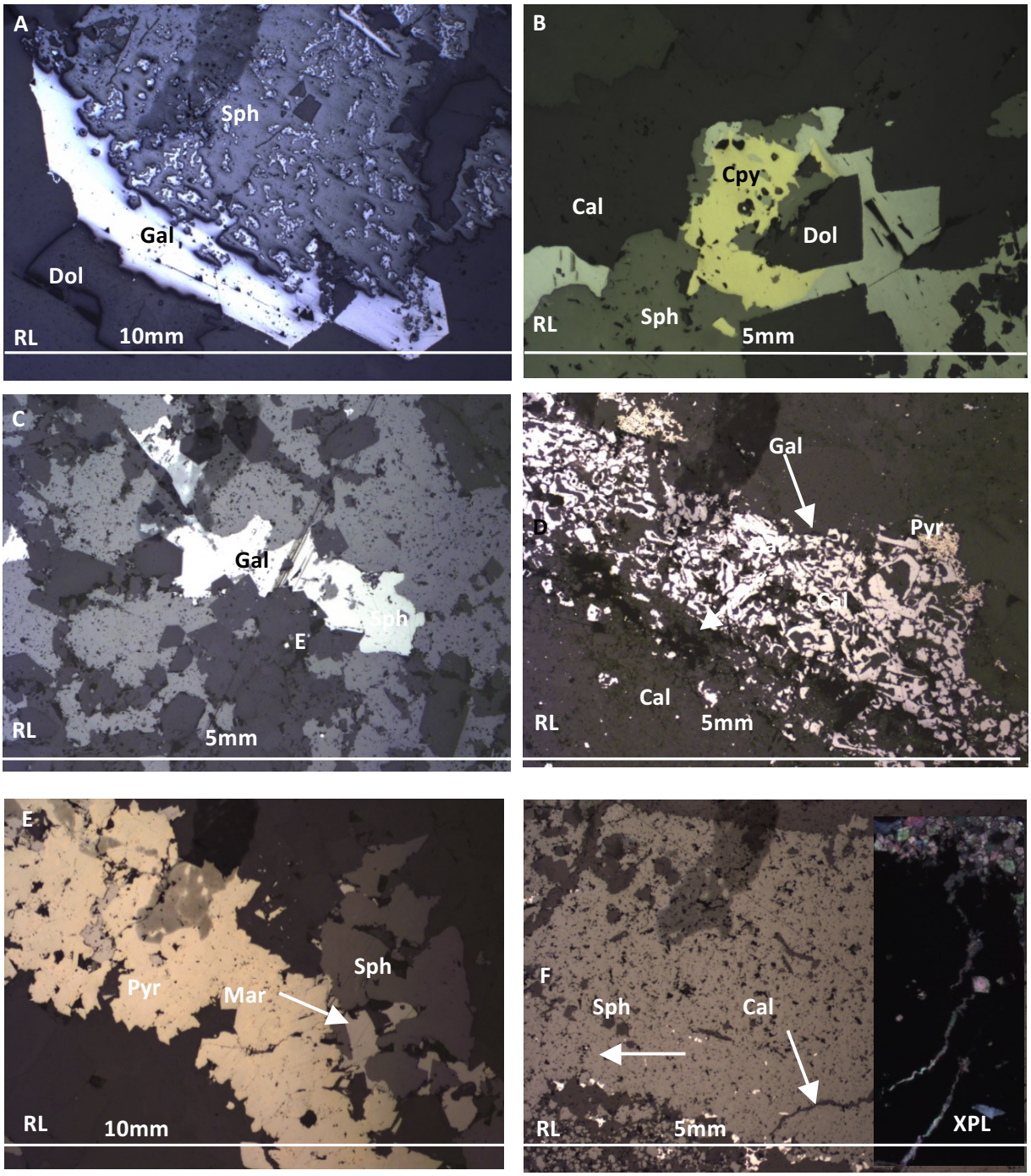

Figure 5.28 – Photomicrographs of sulphides from the A2 Transect

Figure A - N01579-2 – Galena heavily replaced and resorbed by sphalerite, exhibiting pseudodendritic textures

Figure B – N00996-3 - Chalcopyrite overprinting galena-sphalerite

Figure C – N01269-2- Thin galena veinlet cross-cutting colloform sphalerite

Figure D –N01073-3- - Unusual galena bioclast replacement (with minor cavity infill?) exhibiting

Chapter 6

Isotopic and fluid inclusion studies of the Navan transects

Stable isotope geochemistry and fluid inclusion studies have helped to unravel the process of fluid mixing at Navan. Sulphur isotope studies of Navan ore have constrained two sulphide species – those with $\delta^{34}S$ values ranging from -23 to -5‰ threshold are interpreted to be bacteriogenic, those falling within a $\delta^{34}S$ 0 to 15 ‰ range are considered hydrothermal and sulphides with intermediate values were produced by varying degrees of fluid-mixing (Anderson et al, 1998). Altinok (2005) identified exceedingly light pyrite in the Upper Dark Limestone sequence overlying the Navan-bearing Pale Beds sequence. $\delta^{34}S$ values of -28 to -40‰ are interpreted to be diagenetic (Altinok, 2005). Blakeman et al (2002) identified that galenas within three metres of minor normal faults in the Main Orebody have high $\delta^{34}S$ (hydrothermal), becoming rapidly low $\delta^{34}S$ and negative (bacteriogenic input) greater than three metres away.

6.1. S isotope studies:

Seventy-nine sulphur isotope values were obtained from galena, sphalerite and chalcopyrite form the A1 Transect, sphalerite and galena from the A2 Transect, and sphalerite, galena and pyrite along the B and C Transects. Sulphur isotope ratios for sulphides along the B and C Transects are bimodal, agreeing with the hydrothermal-bacteriogenic end-members observed by Anderson et al (1998), Fallick et al (2002), and Blakeman et al (2002) (Fig 6.2-6.5). Sulphides along the A1 Transect are hydrothermal (Fig 6.6, 6.8), while A2 Transect sulphides have a mixed hydrothermal-bacteriogenic (Fig 6.7-6.8) signal. The transition is sharp crossing over from the northwest of the Randalstown Fault to the southeast. Sulphide sulphur ratios vary by texture – Veins, veinlets and disseminated mineralisation are hydrothermal with a small bacteriogenic input, while replacive, banded and chaotic sulphides both $\delta^{34}S$ hydrothermal bacteriogenic sulphur signals (Table 6.1-6.4)

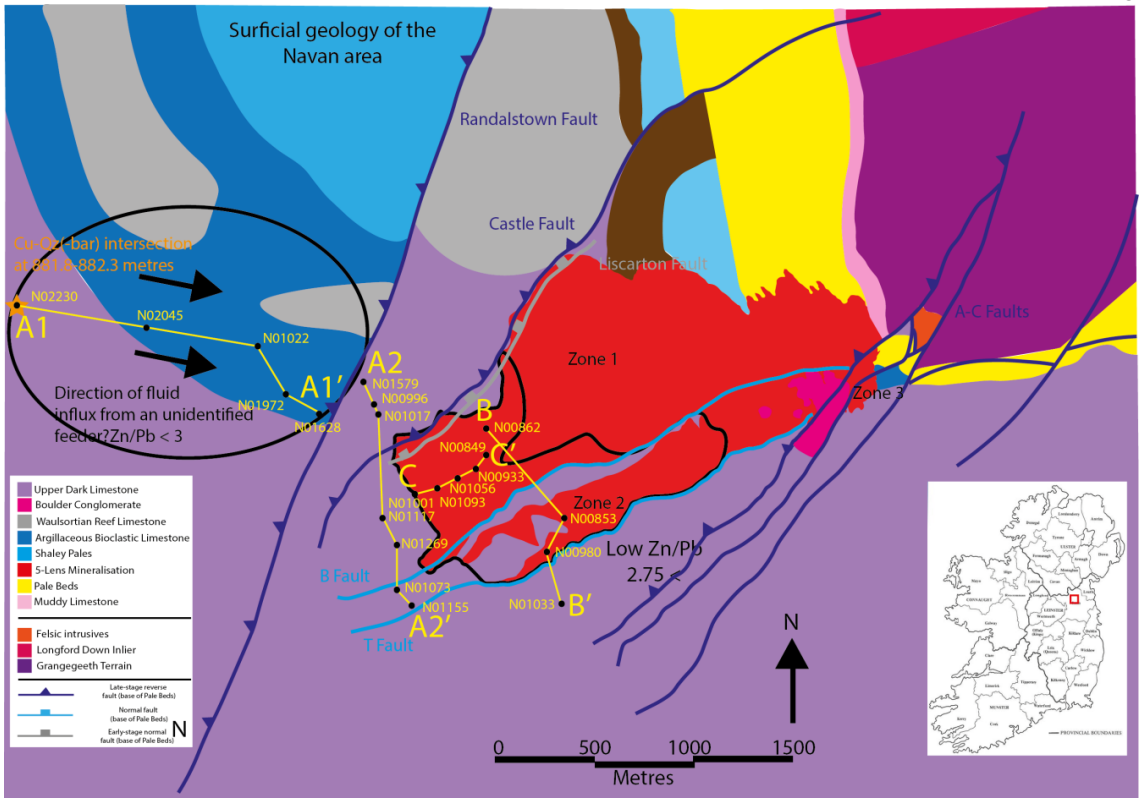

Figure 6.1 – Geological map of Navan area with Main Mine 5 Lens outline (red), low Zn/Pb populations (circled black) and A-C Transects (yellow). For a more detailed Zn/Pb map of the Main Mine, refer to Figure 1.4

6.1.1. B-B' Transect:

Sulphur isotope ratios along the B-B' Transect are bimodal in each drillhole and typical of the hydrothermal-bacteriogenic range which typifies Main Mine sulphides (Fig 6.2-6.3). Of the thirteen hydrothermal sulphides sampled along B-B', eight were obtained from galena and eight from sphalerite. Sulphides from drillholes N00862, N00853 and N01033 – dominantly banded sulphides, replacive sulphide and thin veins – have a strong $\delta^{34}S$ bimodality at respective ranges of -15.1 to 5.2‰, -17.3 to 6.4‰, and -13.7 to 8.1‰. N00980 samples, comprising fabric replacement textures, nodules and veins, have a lower $\delta^{34}S$ spread of 0.9-7‰ and does not register for bacteriogenic sulphur.

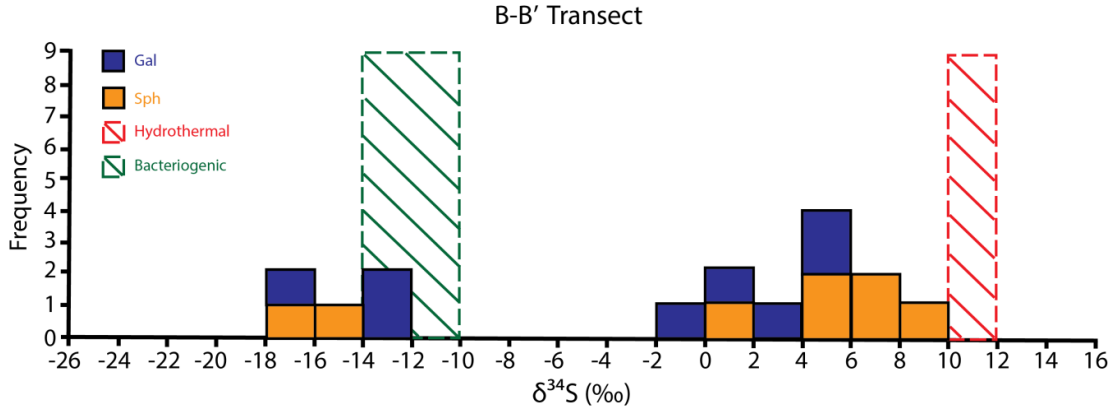

Figure 6.2 - $\delta^{34}S$ isotope histogram of sulphides taken from the B-B' Transect

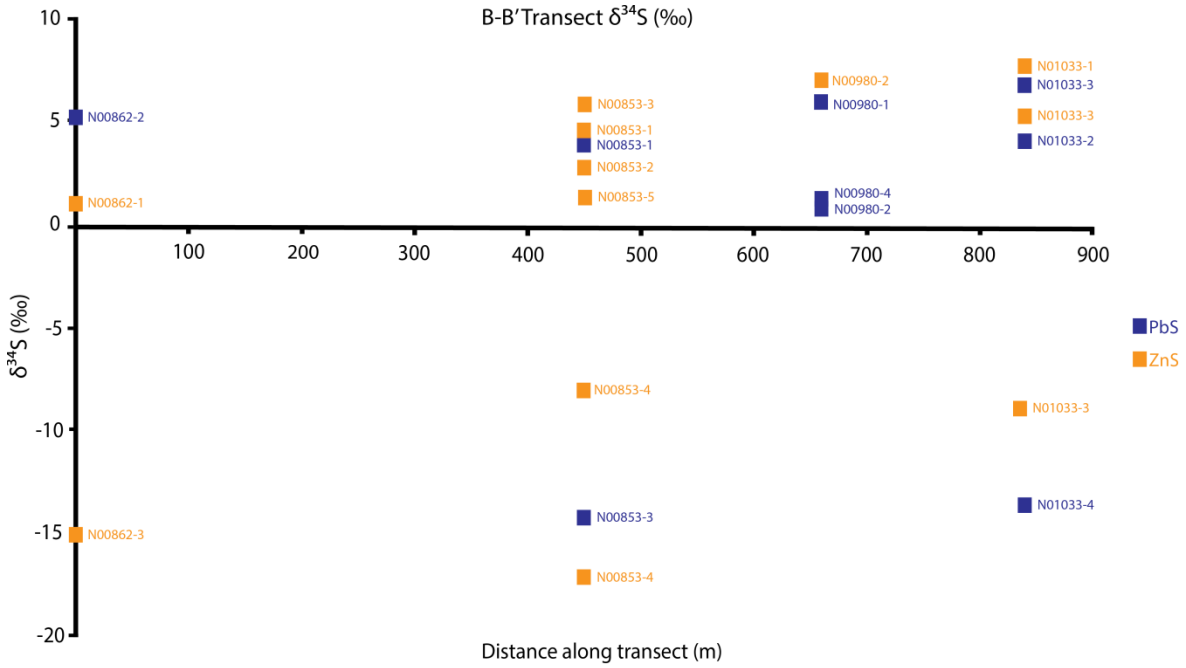

Figure 6.3 - $\delta^{34}S$ scatterplot of sulphides taken from the B-B' Transect

Sample	Description	PbS ($\delta^{34}S$‰)	ZnS ($\delta^{34}S$‰)
N00862-1	Banded sph-cal(-gal)	_	1
N00862-2	Gal-bearing dolomite	5.2	_
N00862-3	Sph-cal-dolomite vein	_	-15.1
N00853-1	Sph replacement	3.4	4.4
N00853-2		_	2.8
N00853-3	Sph-gal banding	-13.9	6.4
N00853-4	Sph-gal banding	-17.3	-7.6
N00853-5	Sph(-Gal)-cal vein	_	1.4
N00980-1	Gal(-sph) replacement	5.9	_
N00980-2	Gal-sph-cal nodule	0.9	7
N00980-4	Gal vein following stylolite	1.1	_
N01033-1	Sph-cal vein	_	8.1
N01033-2	Gal-sph vein	4.4	-7.3
N01033-3	Sph-gal vein	7.6	5.8
N01033-4	Galena vein (weak brecciation)	-13.7	_

Table 6.1 – Sulphur values for B-B' Transect samples

6.1.2. C-C' Transect:

C-C' Transect sulphides coincide with the low Zn/Pb area identified by Davidheiser-Kroll (2014) in the southwest Main Mine. A clear bimodal hydrothermal-bacteriogenic signal is observed *between* boreholes, where sulphides from drillholes N01001-N01056 are dominantly hydrothermal with a small number of very negative $\delta^{34}S$ samples, while those from N00933 and N00849 are overwhelmingly bacteriogenic (Fig 6.4-6.5) Samples from drillholes N01001, N01093 and N01056 comprise vein, veinlet, disseminated and replacive galena-sphalerite, with respective

$\delta^{34}S$ ranges of ‰ -6 – 6.6‰, -18 – 1.2‰, and -16.3 to 10.5‰. Sulphides from drillholes N00933 and N00849, comprising banded, layered and vein sphalerite-galena-(pyrite) have significantly lower $\delta^{34}S$ values that reflect bacteriogenic sulphur input, with respective $\delta^{34}S$ ranges of -18.1 to 2.3‰, and -32.7 to -3.9, respectively.

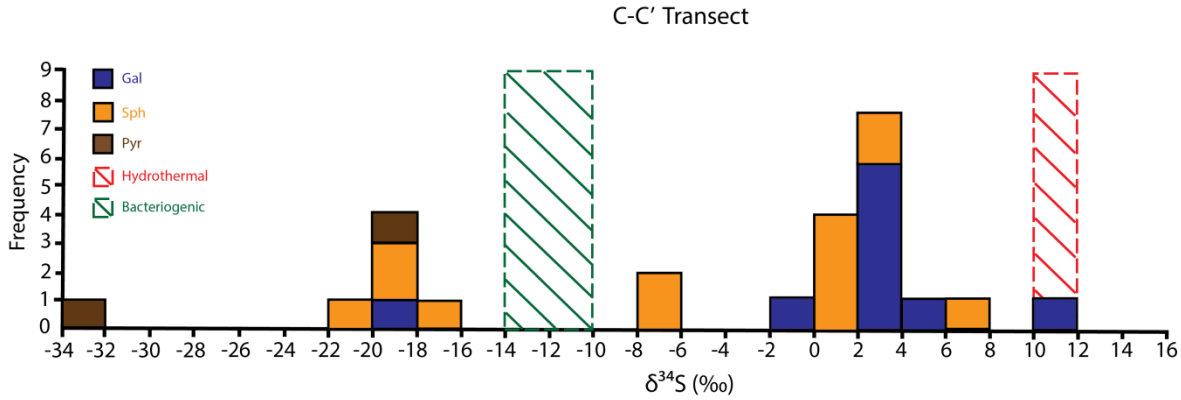

Figure 6.4 - $\delta^{34}S$ isotope histogram of sulphides taken from the C-C' Transect

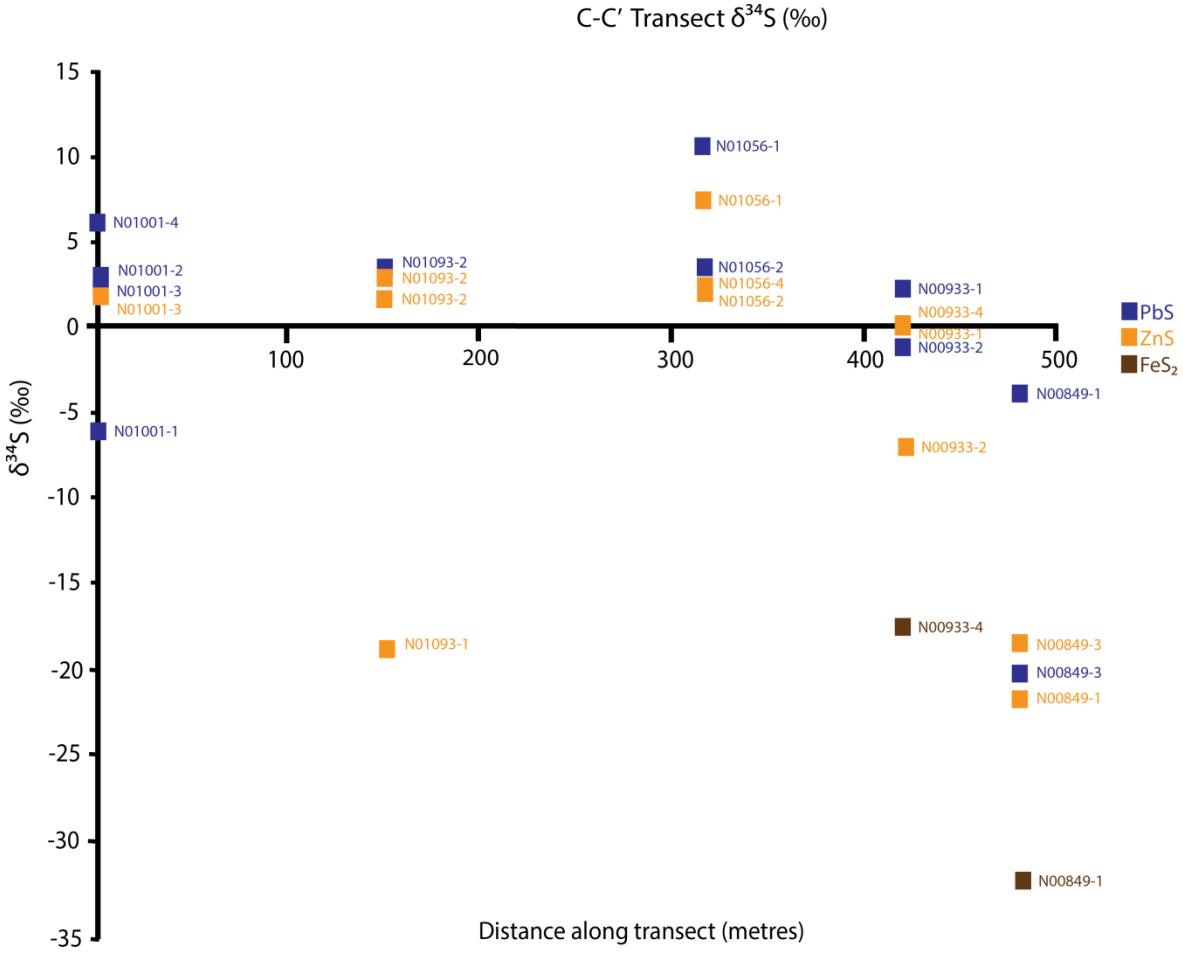

Figure 6.5 - $\delta^{34}S$ isotope scatterplot of sulphides taken along the C-C' Transect.

Sample	Description	Gal ($\delta^{34}S$‰)	Sph ($\delta^{34}S$‰)	FeS_2 ($\delta^{34}S$‰)
N01001-1	Sph(-gal)-cal replacement	_	-6	_
N01001-2	Dolomite cross-cut by gal-cal vein	3.2	_	_
N01001-3	5 Lens Dolomite containing sphalerite and rare galena	2.3	2.3	_
N01001-4	Gal-cal veining	6.6	_	_
N01093-1	Sph-gal banding	2.7	-18	_
N01093-2	Gal vein with disseminated sph	2.7	1.2	_
N01056-1	Gal-cal vein	10.5	6.4	_
N01056-2	Sph-gal replacement	3.2	-16.3	_
N01056-4	5 Lens Dolomite	_	2.5	_
N00933-1	Sph-gal-cal banding	2.3	0	_
N00933-2	Gal-sph-cal vein in micrite	-1.2	-6	_
N00933-4	Sph-py banding in oncholitic micrite	_	0.2	-18.4
N00849-1	Layered galena-sphalerite	-3.9	-22	-32.7
N00849-3	Galena-sphalerite vein	-19.4	-18.1	_

Table 6.2 – Sulphur values for C-C' Transect sulphides

6.1.3. A1-A2 transects:

A1 Transect sulphides northwest of the Randalstown Fault are hydrothermal (Fig 6.6, 6.8), while A2 Transect sulphides southwest of the Randalstown Fault have a bimodal hydrothermal and bacteriogenic signal (Fig 6.7, 6.8), demonstrating a dearth of bacteriogenic. Of the sulphides analysed along the A1-A1' Transect, 12 are hydrothermal and one euhedral galena hosted in fault gouge in drillhole N02230 has a value of -6.5‰. The $\delta^{34}S$ division of A2 Transect sulphides is equally hydrothermal and bacteriogenic.

6.1.4. A1 Transect:

A weak positive correlation between $\delta^{34}S$ and distance from the Randalstown Fault plane is observed, where a slight but steady increase in $\delta^{34}S$ is observed approaching the Randalstown Fault (Fig 6.6, 6.8). Vein, veinlet and disseminated galena-sphalerite characterise mineralisation in the Randalstown Fault hangingwall. Disseminated galenas from drillholes N02230 and N02045 have respective $\delta^{34}S$ values of -6.5 and 6.7‰, while replacive sphalerite in sample N01022-1 has a $\delta^{34}S$ value of -1.5‰. Drillholes N01972 and N01628 – characterised by sph-gal-cal sulphide veins (Fig 5.13 C-F) and blocky sulphides (Fig 5.19), respectively – have average $\delta^{34}S$ values of 11.2 and 5.4‰. Chalcopyrite from N02230 return $\delta^{34}S$ values between 0.8-3.3‰. Hydrothermal $\delta^{34}S$ values

obtained from hangingwall range galena-sphalerite ranges from -1.5 to 12.5‰ and register an average value of 6.2‰.

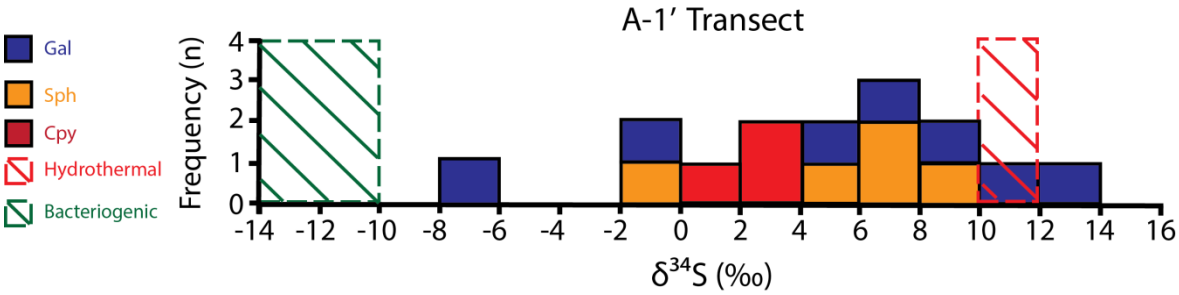

Figure 6.6 – $\delta^{34}S$ isotope histogram of sulphides from the A1 Transect (Randalstown Fault hangingwall)

Sample	Description	Gal ($\delta^{34}S$‰)	Sph ($\delta^{34}S$‰)	$CuFeS_2$ ($\delta^{34}S$‰)
N02230-1	Euhedral galena in shaley fault gouge	-6.5	_	_
N02230-4	Cpy-Qtz(-barite) vein	_	_	3.3
N02230-5	Cpy-Qtz(-barite) vein	_	_	2.9
N02230-7	Calcite vein in stratal dolomite. Contains allochtonous cpy	_	_	0.8
N02045-3	Gal-cal vein following stylolite	6.7	_	_
N01022-1	Sph replacement	_	-1.5	_
N01022-2	Galena veinlets	4.1	_	_
N01972-1	Gal-cal vein	11.2	_	_
N01972-2	Gal-sph-cal vein	12.5	5.4	_
N01628-1	Blocky sph-gal	-0.3	6.3	_
N01628-2	Sph(-gal) vein	_	9.2	_
N01628-3	Sph-gal veinlets in 5 Lens Dolomite	6.9	6.7	_

Table 6.3 - $\delta^{34}S$ values for sulphides from the A1 Transect

6.1.5. A2 Transect:

Sulphur isotopes from the A2 Transect are bimodal (Fig 6.7-6.8). Crossing over the Randalstown Fault plane and trending southeast along the footwall, sulphur isotope values in sulphides steadily decrease between drillholes N01579 and N01073. samples N01579-1 and N01579-2 – sphalerite-dolomite and galena-sphalerite-dolomite veins – are clearly bacteriogenic and have respective $\delta^{34}S$ values of -6.5, and -5.5 and -4.7‰. Trending southeast, samples N00996-2 and N00996-3 – a galena vein and sphalerite-calcite-dolomite vein breccia, respectively - have $\delta^{34}S$ values of -8.1‰, and 10.3 and 9.9‰. Galena vein sulphides from N01117 are hydrothermal and have an average $\delta^{34}S$ value of 3‰. Sulphides in drillholes southeast of N01117 have a steadily more negative $\delta^{34}S$ value. Diffuse sphalerite and galena replacement textures in drillholes N01117, N01269 and N01073 register for both hydrothermal and bacteriogenic sulphur, while galena-sphalerite-calcite veins and blocky sphalerite and galena in drillhole N01073 are bacteriogenic.

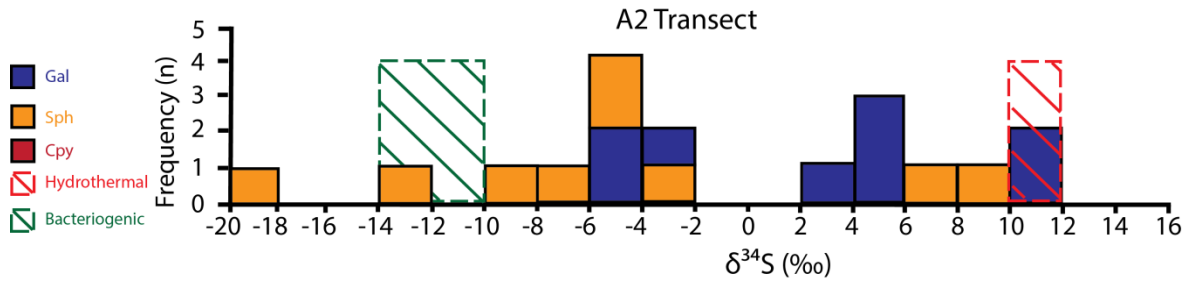

Figure 6.7 – $\delta^{34}S$ isotope histogram of sulphides from the A2 Transect (Randalstown Fault footwall)

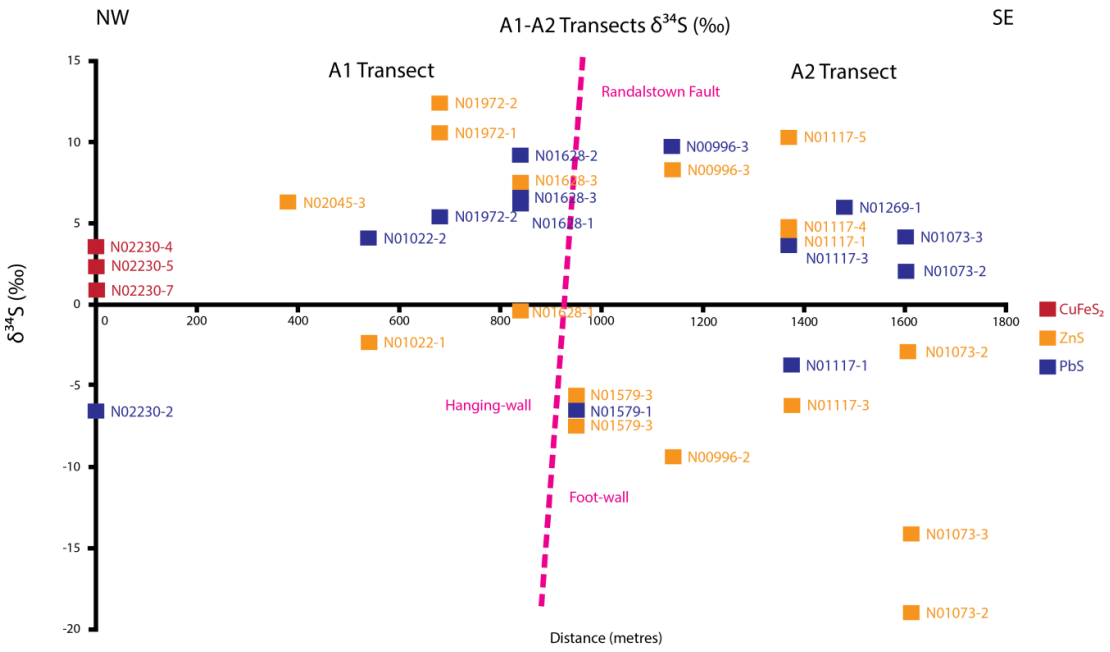

Figure 6.8 – $\delta^{34}S$ isotope scatterplot for the A1 and A2 Transect sulphides

Sample	Description	Gal ($\delta^{34}S‰$)	Sph ($\delta^{34}S‰$)
N01579-1	Sph-pink cal vein	_	-6.5
N01579-2	Gal-bearing dolomite	-5.5	-4.7
N00996-2	Sph replacement	_	-8.1
N00996-3	Gal vein	10.3	9.9
N01117-1	Sph-gal replacement	-2.1	5.3
N01117-3	Gal-cal vein	4.9	-5.8
N01117-4	Galena vein	5.1	_
N01117-5	Gal-cal vein	10.3	_
N01269-1	Sph replacement	_	6.4
N01073-1	Sph replacement	_	-2
N01073-2	sph-cal-gal nodule	2.5	-18.2
N01073-3	Sph-gal breccia	5.6	-13.7

Table 6.4 - $\delta^{34}S$ values for sulphides from the A2 Transect

This section identifies distinct $\delta^{34}S$ distributions along the A-C Transects:

- Sulphides from the B and C Transects return a bimodal $\delta^{34}S$ signal. No geographical distribution is observed along the B Transect, though drillholes N00849 and N00933 along the C Transect are overwhelmingly bacteriogenic.
- Gal-sph from the A1 Transect is hydrothermal, excluding one galena in drillhole N02230. Chalcopyrite in the same drillhole is hydrothermal. Sulphides from the A2 Transect have a bimodal hydrothermal-bacteriogenic signal.

Fluid inclusion thermometry

6.2. Fluid inclusion analysis

Obtaining accurate fluid inclusion temperature and salinity values from Navan ore is notoriously difficult due to the rarity and small size of suitable inclusions. Nonetheless, detailed studies by Probert (1983) Peace (1999), Everett & Wilkinson (2001), Peace & al (2003), Wilkinson (2010), and Treloar (2014) have been essential in constraining two fluids that produced the Navan ore – a low temperature, high salinity bacteriogenic sulphur enriched brine (70-100 °C, 20-25 wt%. NaCl), and a moderate temperature, moderate salinity metalliferous fluid (100-140^{o}C, 5-10% wt.% NaCl) that scavenged, transported, and deposited sulphides from the underlying Lower Palaeozoic basement (e.g. Everett & Wilkinson, 2001, Wilkinson, 2010). Treloar (2014) identified liquid-rich, high temperature inclusions from barite in the Southwest Extension, ranging from 173-184 ^{o}C, which are at least 30-40^{o}C hotter than the Main Mine hydrothermal fluid (100-140^{o}C) constrained by Wilkinson (2010).

Fluid inclusion analysis was carried out on quartz-hosted inclusions in Cpy-Qtz(-barite) samples in drillhole N02230, late-stage, cross-cutting calcite-dolomite veining that hosts minor Cpy-Qtz(-barite) in N02230, and sphalerite-galena-calcite in the Randalstown Fault hangingwall, footwall and main mine. Fluid inclusions can be divided into three types:

1) Ultra-fine, non-visible fluid inclusion “clouds” (Fig 6.9), giving gangue minerals a turbid appearance. Ultra-fine inclusions are common in drillhole N02230 late-stage calcite and saddle dolomites, and the host stratal dolomite.
2) Monophase (Fig 6.9), where a cavity is only occupied by aqueous liquid. Monophase inclusions are dominant in the quartz that co-precipitated with chalcopyrite in drillhole N02230.
3) Two-phase inclusions (Fig 6.10) where liquid and vapour are present in a single cavity. Two-phase inclusions are common in gangue calcite associated with sphalerite and galena mineralisation.

Ultra-fine and monophase inclusions are dominant in quartz, although two two-phase inclusions were identified and analysed for homogenisation temperature and salinity. The homogenisation temperature refers to the temperature at which the vapour phase of a fluid inclusion is completely resorbed into the aqueous fluid, forming one phase. While a homogenisation

temperature could not be obtained from most quartz-hosted fluid inclusions, freezing of an inclusion until solid (the "T_{FREEZE}") can help to determine the composition of dissolved solutes, while final melting of ice upon heating (the "$T_{M\text{-}ICE}$") can be used to estimate salinity. However, final melting is often determined by observing the behaviour of a nucleated bubble. Vapour bubbles in fluid inclusions move in cavities by Brownian Motion (Wilkinson, 2016: Pers comm), and this motion becomes increasingly exaggerated with additional ice melting. Upon final ice melt, a vapour bubble will often quickly migrate into the point of melting, before returning to a state of low motion, providing a final melting temperature which can then be used to determine salinity (e.g. Shepherd et al, 1985). For this reason, $T_{M\text{-}ICE}$ of monophase inclusions is difficult to accurately determine and is indirectly constrained from T_{FREEZE} and is best performed on a two-phase inclusion where the behaviour of a re-nucleated vapour bubble can be observed as the water ice is heated and melts.

Only primary fluid inclusions were selected for analyses. It is assumed from petrographic studies of the samples that calcites either co-precipitated with the sulphides, or precipitated immediately after. Primary fluid inclusions that were trapped as the calcite crystal face developed, therefore provide the closest mineralising fluid temperature and salinity. Determining whether a fluid inclusion in calcite is primary depends on the orientation and morphology of said inclusion. Those orientated parallel to cleavage were interpreted to form as the calcite crystal face developed and, therefore, provide an accurate representation of the mineralisation temperature, while those aligned oblique to cleavage were assumed to form after the primary fluid inclusion event (I.e. "secondary" fluid inclusions) and do not provide the correct mineralisation temperature and fluid salinity. Inclusions that lie on a cleavage plane, show fracturing or contain unusually large vapour bubbles relative to inclusion size were interpreted to have either been modified or leaked, thereby changing the inclusion bulk density, providing a false reading. Sphalerites from sample N01628-1 were inspected for two-phase fluid inclusions, though mineralisation was cryptocrystalline or showed very fine oscillatory zoning textures (Fig L1), suggesting rapid crystallisation. This is prohibitive for inclusion development (Wilkinson, 2016: Pers comm).

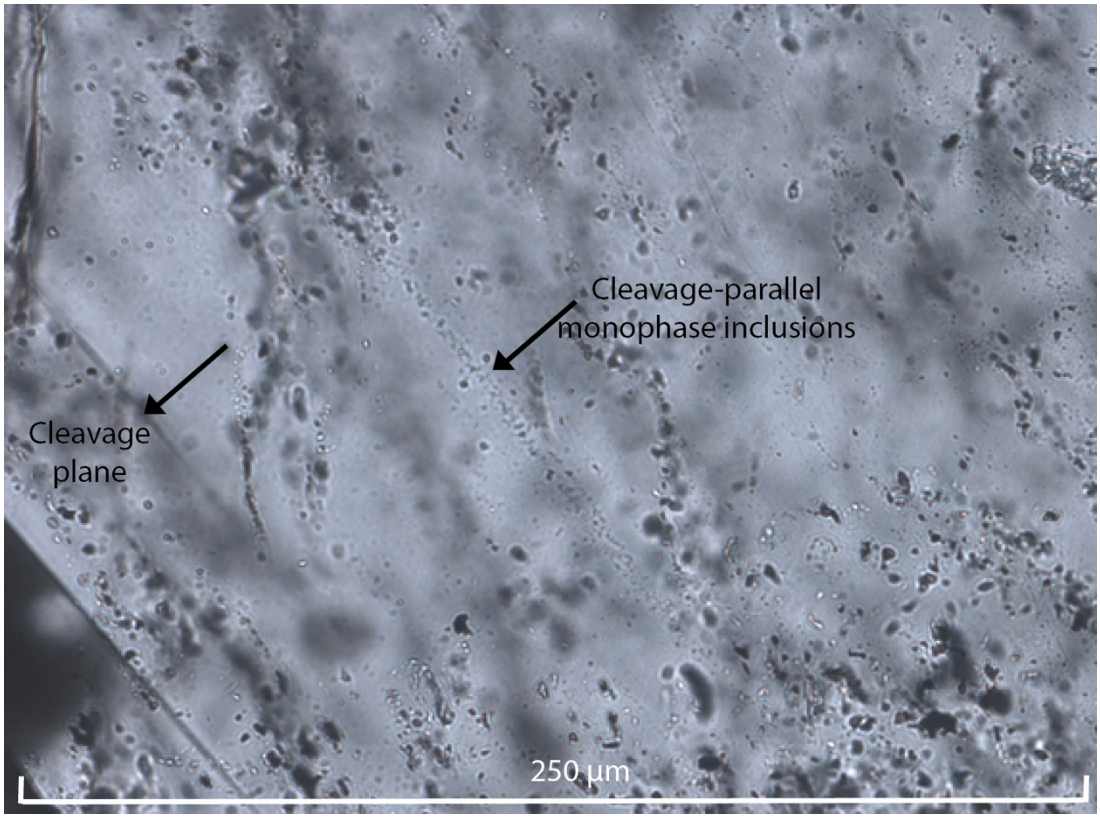

Figure 6.9 – Example of cleavage-parallel ultra-fine and monophase fluid inclusions in sample N02045-3 (calcite). Photos obtained in transmitted light

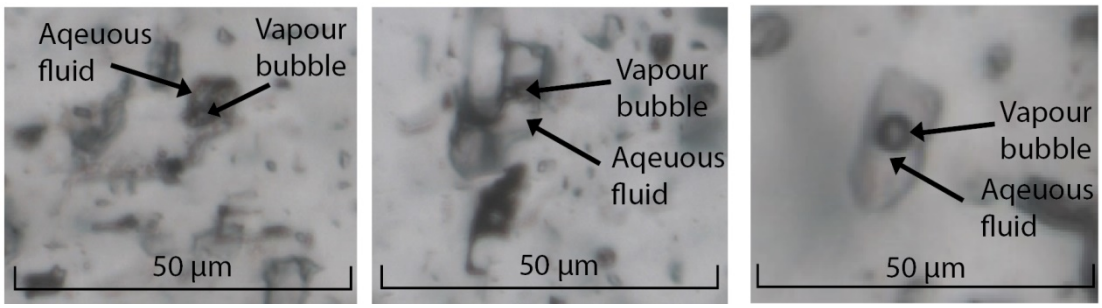

Figure 6.10 – Examples of two-phase, "boxy" fluid inclusions in sample N01056-1 (calcite). Photos obtained in transmitted light

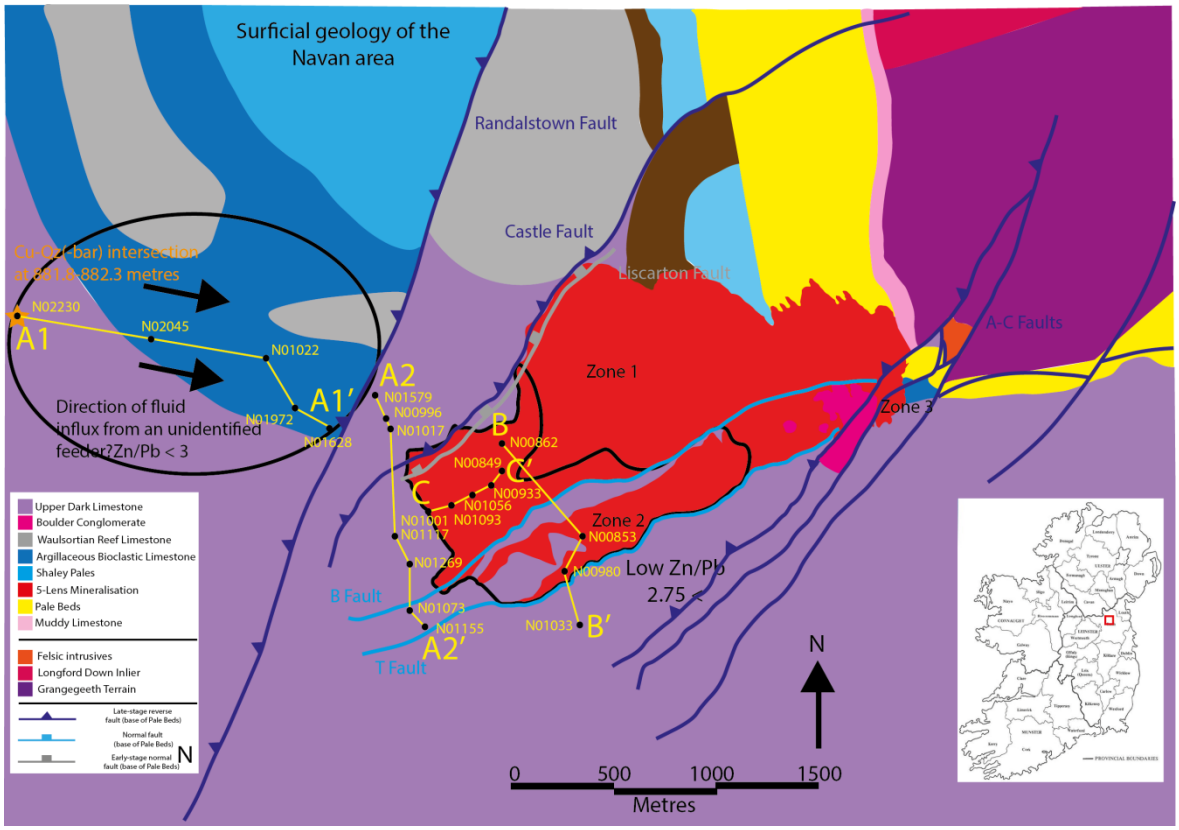

Figure 6.11 – Geological map of Navan area with Main Mine 5 Lens outline (red), low Zn/Pb populations (circled black) and A-C Transects (yellow). For a more detailed Zn/Pb map of the Main Mine, refer to Figure 1.4

6.2.1. C-C' Transect:

Homogenisation temperature and salinity values were obtained from fluid inclusion wafers prepared from samples N01001-4 (hydrothermal sph-cal vein), N01093-2 (minor hydrothermal gal-cal veins), N01056-1 (hydrothermal sph-gal-cal vein), N00933-1 (banded sph-gal-cal), and N00849-3 (bacteriogenic sph-gal-cal vein). Temperatures obtained from samples in drillholes N01001-N00933 are within range of the hydrothermal fluid end-member at the Main Mine (Wilkinson, 2010) though occasionally exceed 160°C (Fig 6.12- 6.14, Table 6.5). Samples N01001-4, N01093-2, N01056-1, and N00933-1 constrain a homogenisation temperature range of 95.5-164 and 7.3-22.7 wt.% NaCl (Fig 6.12- 6.14, Table 6.5). Analysis of N00849-3 fluid inclusions constrain a higher homogenisation temperature range of 150-204.5°C. This temperature range is both higher than Wilkinson's (2010) T_h range for the hydrothermal fluid, and is similar to values obtained by Treloar (2014) in barites from SWEX-South.

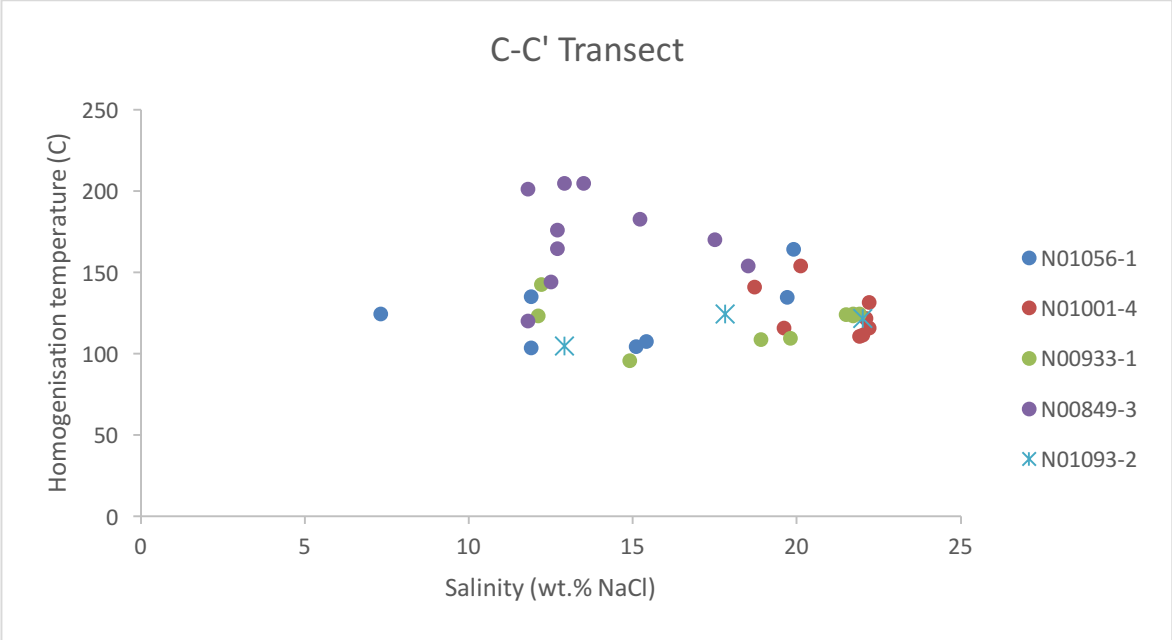

Figure 6.12 – Homogenisation temperature – salinity plot for C-C' Transect calcites. A weak negative correlation between T_h and salinity is observed, though sample N00849-3 yields anomalously high T_h

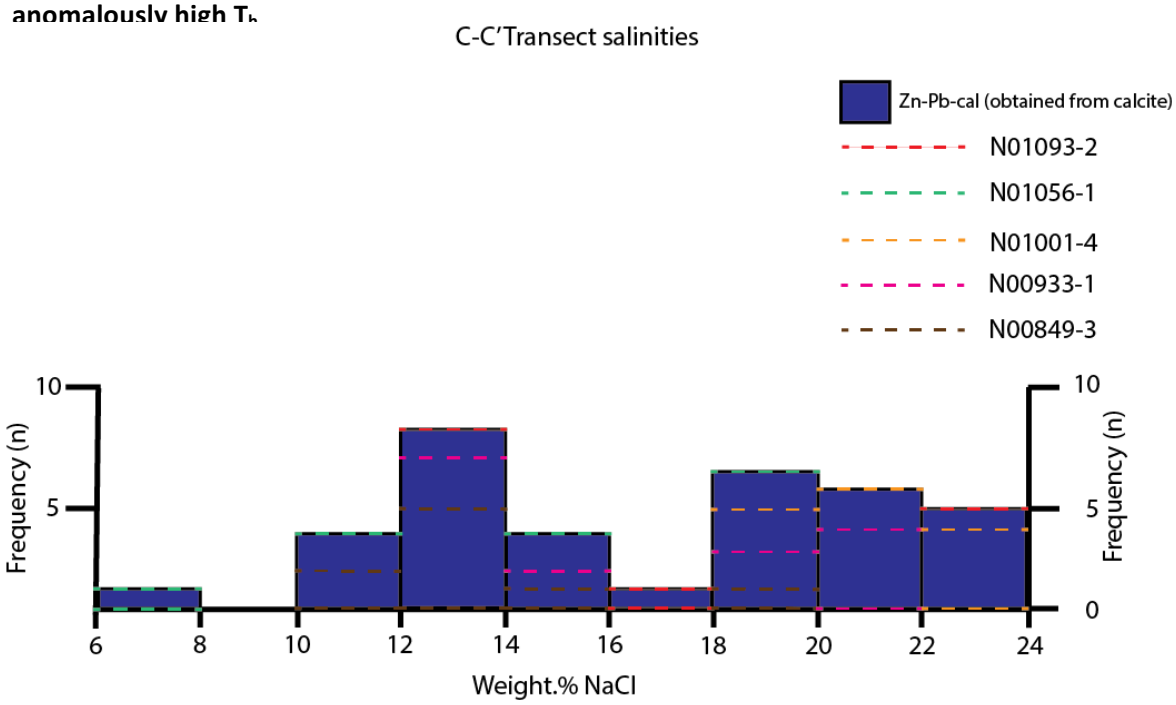

Figure 6.13 – Histogram for C-C' Transect calcite fluid inclusion salinity values

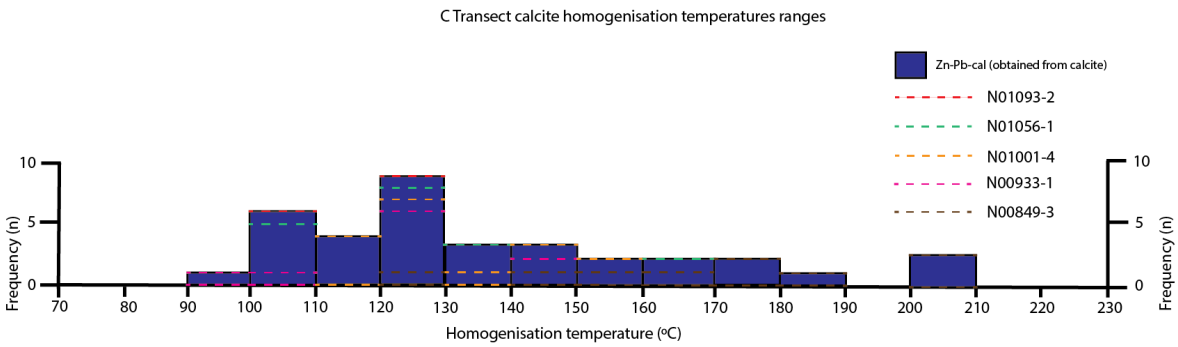

Figure 6.14 – Histogram for C-C' Transect calcite fluid inclusion homogenisation temperatures

Sample	Host mineral	Homogenisation temperature (°C)	Margin of error (°C)	Salinity (wt.% NaCl)	Average T_h	Average salinity
N01001-1	Calcite	110.5-154	±1	18.7-22.7	125.1	21.2
N01093-2	Calcite	104.5-124.5	±1	12.9-22	135.7	17.6
N01056-1	Calcite	103.5-164	±1	7.3-19.9	124.8	17.6
N00849-3	Calcite	120-204.5	±2	11.8-18.5	172.1	13.9
N00933-1	Calcite	95.5-142.5	±1	12.2-21.9	119.4	18.3

Table 6.5 - C-C' Transect calcite homogenisation temperatures and salinities

6.2.2. A1 Transect:

Hangingwall sulphide-calcite and quartz fluid inclusion analysis constrains three groups (Table 6.7) – Sph-gal-Cal mineralisation formed at a homogenisation temperature and salinity range of of 79-145.5 and 7.2-22.7wt.% NaCl, respectively, while late-stage calcite-dolomite veining in drillhole N02230 formed from a fluid at a respective homogenisation temperature and salinity range of 101-165°C and 14-22.7 wt.% NaCl. Only two two-phase fluid inclusions were observed in quartz, yielding a homogenisation temperature and salinity range of 191-223°C and 19.7-22 wt.% NaCl (Fig 6.15-6.17, Table 6.7), though monophase salinity measurements determine a wider salinity range of 10.1-22.7 wt.% NaCl.

Homogenisation temperature and salinities were obtained from samples from drillholes N02230, N02045, N01972 and N01628. Two-phase inclusions in sph-gal-cal veining in samples N02045-3, N01972-3 and N01628-1 yield a T_h range that is lower than the C-C' Transect sulphides, with respective T_h and salinity ranges of 82-145°C and 7.2-16.5 wt.% NaCl. A slight average T_h decrease is observed travelling west of the Randalstown Fault, though no clear salinity trend is observed (Fig 6.15-6.17, Table 6.7). Homogenisation temperature and salinity values of hangingwall Zn-Pb sulphides broadly coincide with that of the Main Mine hydrothermal fluid range (Wilkinson, 2010 – Fig 7.3).

Two-phase fluid inclusions from late-stage calcite in drillhole N02230 (samples N02230-6 and N02230-7) yield a wide homogenisation temperature and salinity range of 101-165°C and 14-22.5 wt.% NaCl, respectively. Fluid inclusions from saddle dolomite in sample N02230-7 (occurs between the calcite vein and wall-rock contact) constrain have a relatively narrow respective

temperature and salinity range of 106.5-126.5°C and 22.2-22.6 wt.% NaCl. Homogenisation temperature and salinity of late-stage calcite returns ranges between 79.5-136.5°C and 14-22.5 wt.% NaCl respectively. No relationship between T_h and salinity is observed.

Only two quartz-hosted fluid inclusions yielded homogenisation temperatures and salinities, at 191°C and 19.7 wt.% NaCl, and 223°C and 22.7 wt.% NaCl. A salinity range of 10.2-22.7 wt.% NaCl for quartz-hosted monophase inclusions was determined from T_{FREEZE}.

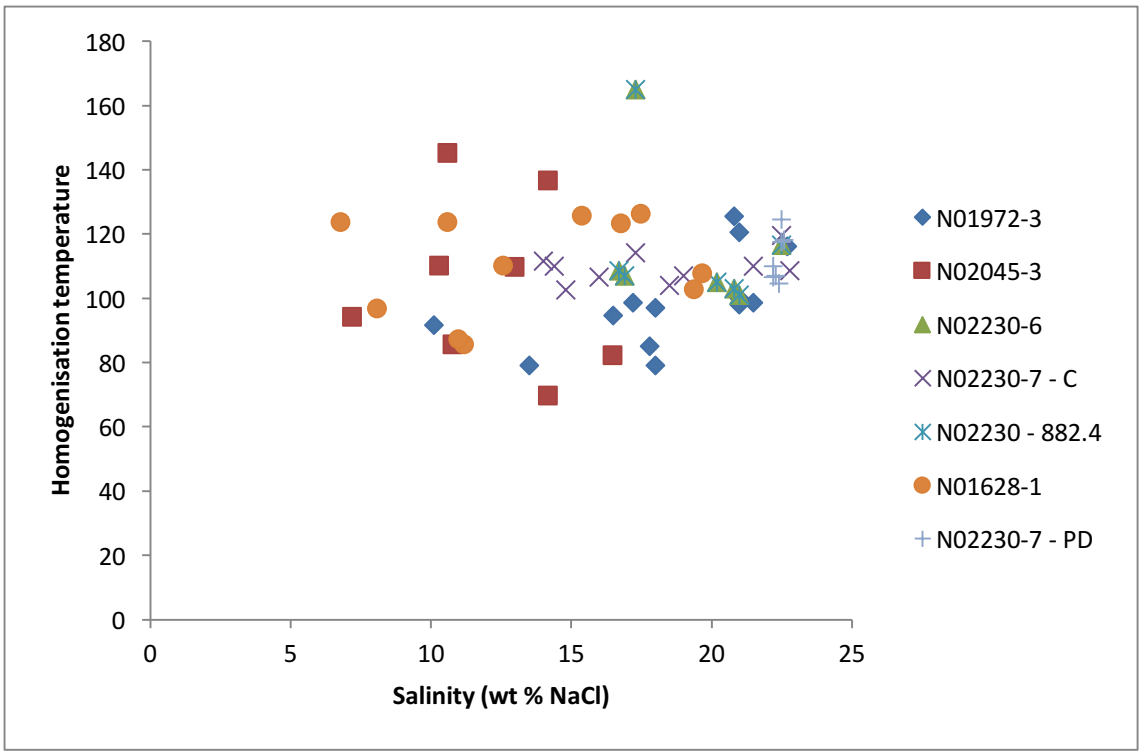

Figure 6.15 - Homogenisation temperature – salinity scatterplot for A1-A1' Transect calcites, dolomites and quartz.

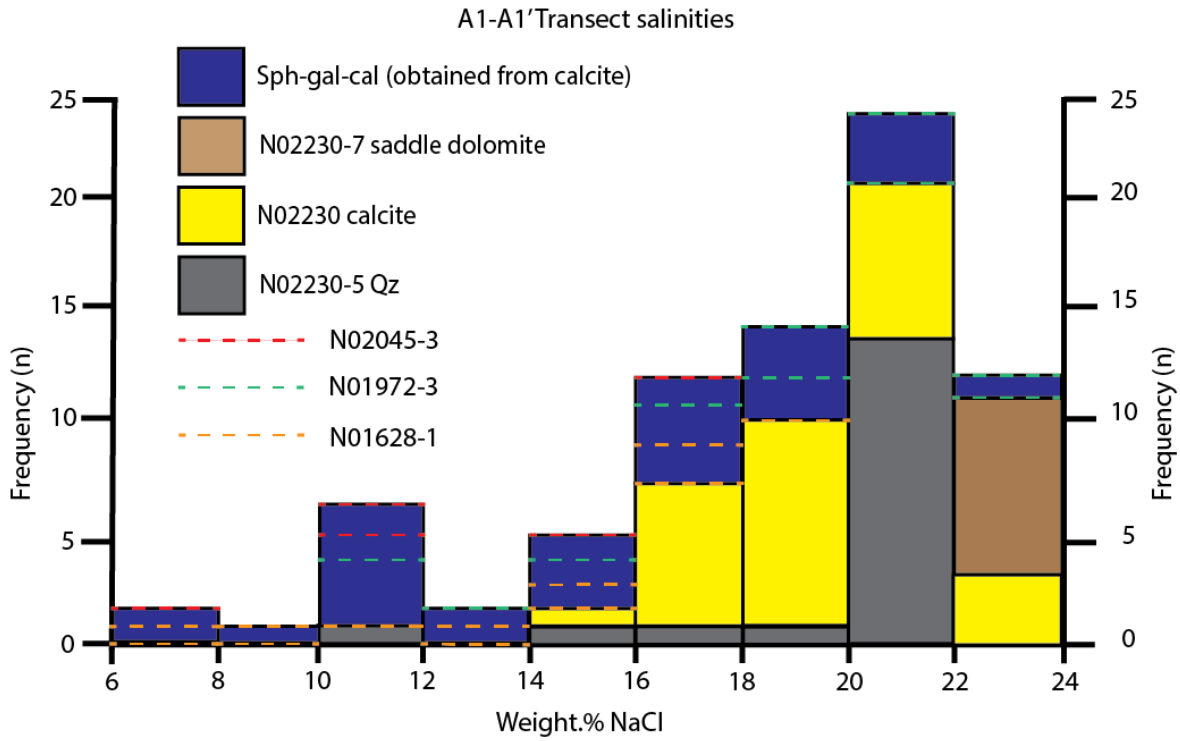

Figure 6.16 – Histogram for A1-A1' Transect calcite, dolomite and quartz salinities

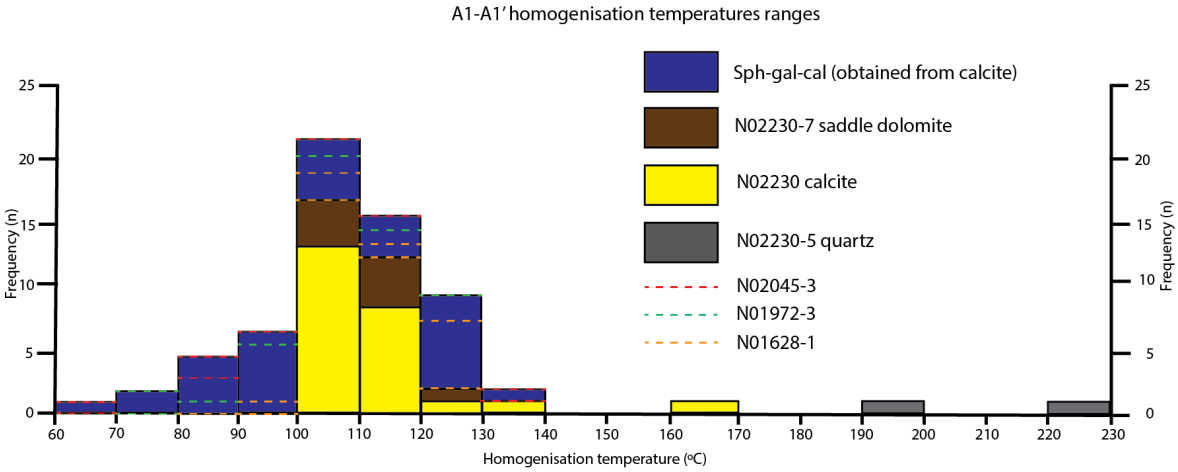

Figure 6.17 – Histogram for A1-A1' Transect calcite, dolomite and quartz homogenisation temperatures

Sample	Host mineral	Homogenisation temperature (°C)	Margin of error (°C)	Salinity (wt.% NaCl)	Average T_h	Average salinity
N02230-5	Quartz	191-223	±2	10.2-22.7 (determined from monophase inclusions)	207	20.9
N02230-6	Calcite	101-165	±1.5	16.9-22.5	112.1	18.7
N02230-7	Calcite	102.5-136	±2	14-22.5	110.9	18.5
N02230-7	Saddle dolomite	104.5-124.5	±1	22.2-22.6	112.6	22.4
N02045-3	Calcite	82-145	±1	7.2-16.5	103.9	15.2
N01972-3	Calcite	79-125.5	±1	10.1-22.7	98.7	18.4
N01628-1	Calcite	85.5-126	±1	8.1-19.7	110	13.6

Table 6.6 - A1-A1' Transect calcite homogenisation temperatures and salinities

6.2.3. A2 Transect:

Three sulphide-calcite samples in drillholes N01570, N00996 and N01117 were prepared for fluid inclusion analysis. N00996-1 – a hydrothermal sphalerite-calcite-dolomite stockwork – has a respective homogenisation temperature and salinity range 113-144°C and 7.1-10.3 wt.% NaCl. Inclusions from sample N01579-3 – a bacteriogenic galena-sphalerite-dolomite vein – yield a low T_h and high salinity range of 77.5-114°C and 19.1-20.4 wt.% NaCl, respectively. N01117-5 – a hydrothermal galena-calcite vein – constrains a very high homogenisation temperature and wide salinity range of 162-223°C and 7.4-20.2%, respectively. This temperature range is higher than the mineralising temperature for the main mine hydrothermal fluid (100-140°C – Wilkinson, 2010) and is more typical of Southwest Extension-South (Treloar, 2014) and other higher temperature Irish-types (e.g. Silvermines, Lisheen, Tynagh – e.g. Samson and Russell, 1987, Wilkinson, 2010 – Table 5.8).

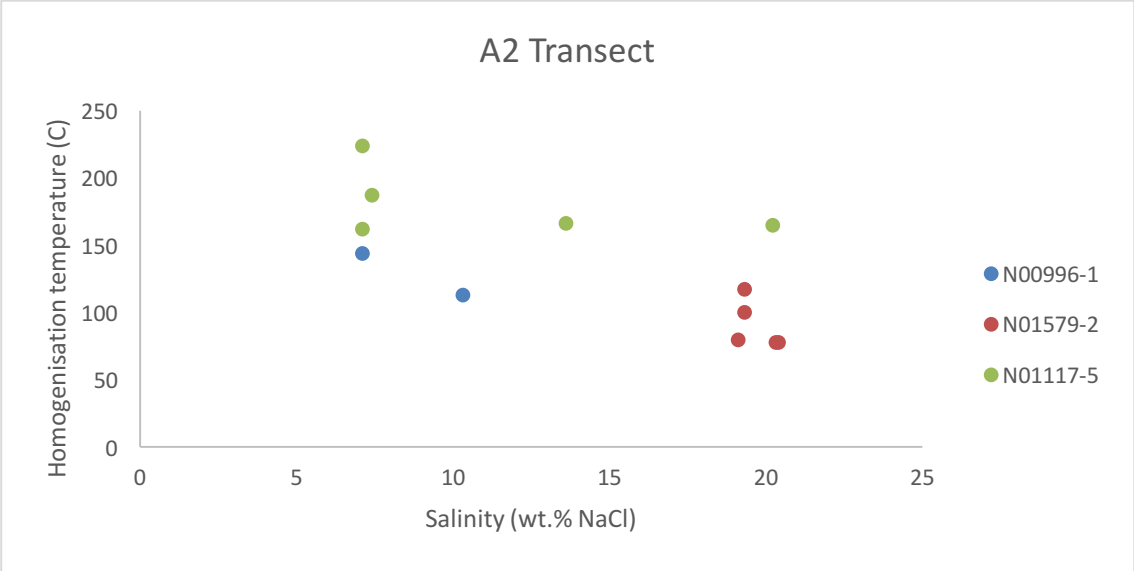

Figure 6.18 – Homogenisation vs salinity scatterplot for calcite fluid inclusions co-precipitated with A2-A2' Transect sulphides.

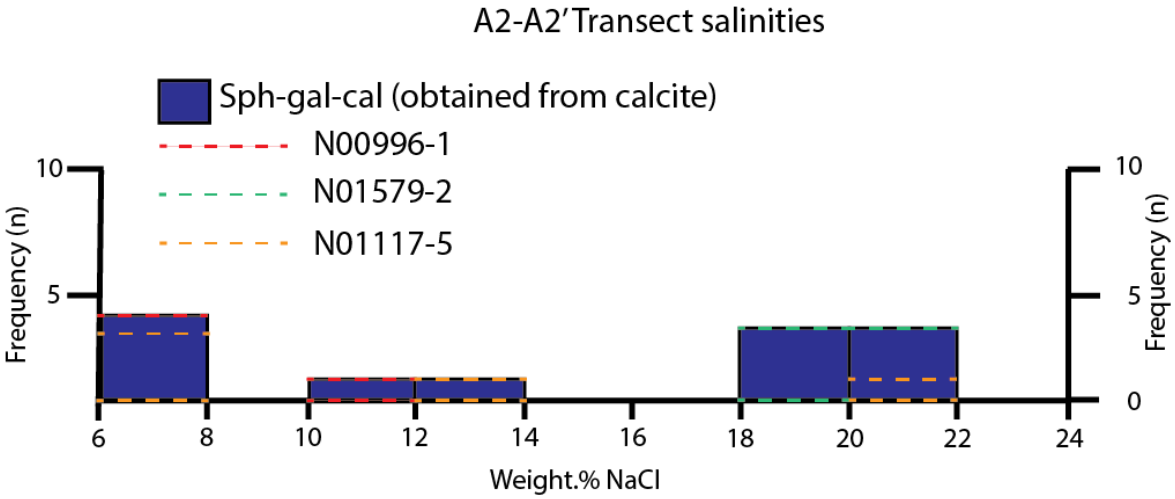

Figure 6.19 – Histogram for A2-A2' Transect calcite salinities

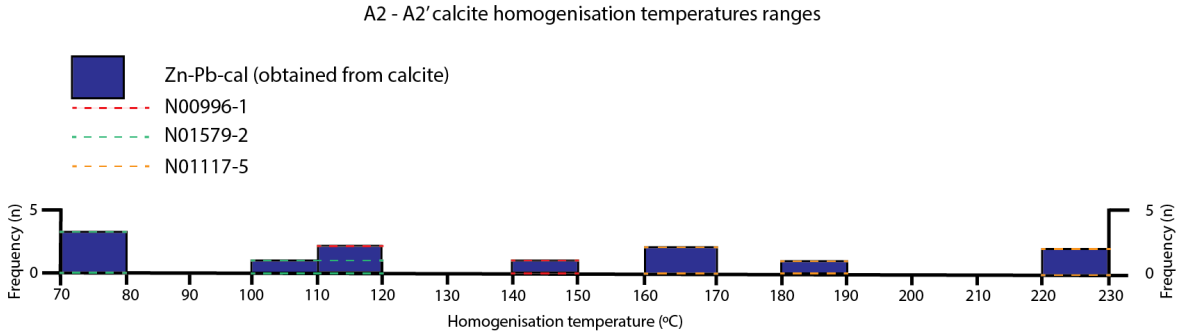

Figure 6.20 – Histogram for A2-A2' Transect calcite homogenisation temperatures

Sample	Host mineral	Homogenisation temperature (°C)	Salinity (wt.% NaCl)	Average T_h	Average salinity
N00996-1	Calcite	113-144	7.1-10.3	128.5	8.7
N01579-2	Dolomite	77.5-117	19.1-20.4	90.3	19.7
N01117-5	Calcite	162-223.5	7.1-20.1	180.6	11.8

Table 6.7 - A2-A2' Transect calcite homogenisation temperatures and salinities

Overall, fluid inclusion analysis of samples from the A1, A2 and C Transects reveals four separate fluid types:

- A high temperature, high salinity hydrothermal (determined by S isotope analysis in section 6.1) fluid along the C Transect, coinciding with the low Zn/Pb area in the southwest Main Mine identified by Davidheiser-Kroll (2014). This fluid species is also observed in samples from along the A2 Transect, and

- A low temperature, high salinity fluid which is likely the bacteriogenically sulphur-enriched brine. This is observed in sample N01579-2 from the A2 Transect, which yields a respective T_h and salinity range of 77.5-117^{o}C, and 19.1-20.4 wt.% NaCl. Unusually, fluid inclusions from sample N00849-3 along the C Transect – a bacteriogenic banded sphalerite-galena-pyrite – returned high homogenisation temperatures of 120-204.5^{o}C. This temperature range is much higher than what we would normally expect of a sulphide produced from the bacteriogenically sulphur-enriched brine (70-100^{o}C – Wilkinson, 2010).

- A high temperature, high salinity hydrothermal fluid responsible for Cpy-Qtz mineralisation in drillhole N02230 that appears to be separate from the hydrothermal fluid identified from sph-gal-cal mineralisation along the A1, A2, and C Transects. This fluid, based on limited observation of two-phase inclusions in quartz - was of significantly higher temperature than the hydrothermal fluid in the Main Mine, Randalstown Fault foot-wall and hanging-wall, constraining a range of 191-223^{o}C. $T_{M\text{-}ICE}$ values extrapolated from T_{FREEZE} of quartz-hosted monophase inclusions yielded a salinity range of 10.2-22.7 wt.% NaCl.

- A late-stage, lower temperature and high-salinity hydrothermal fluid responsible for calcite-saddle dolomite veining that-cross cuts cpy-qtz mineralisation in drillhole N02230. These veins formed from a high temperature, high salinity fluid with respective T_h and salinity ranges of 101-165^{o}C and 14-22.5 wt.% NaCl.

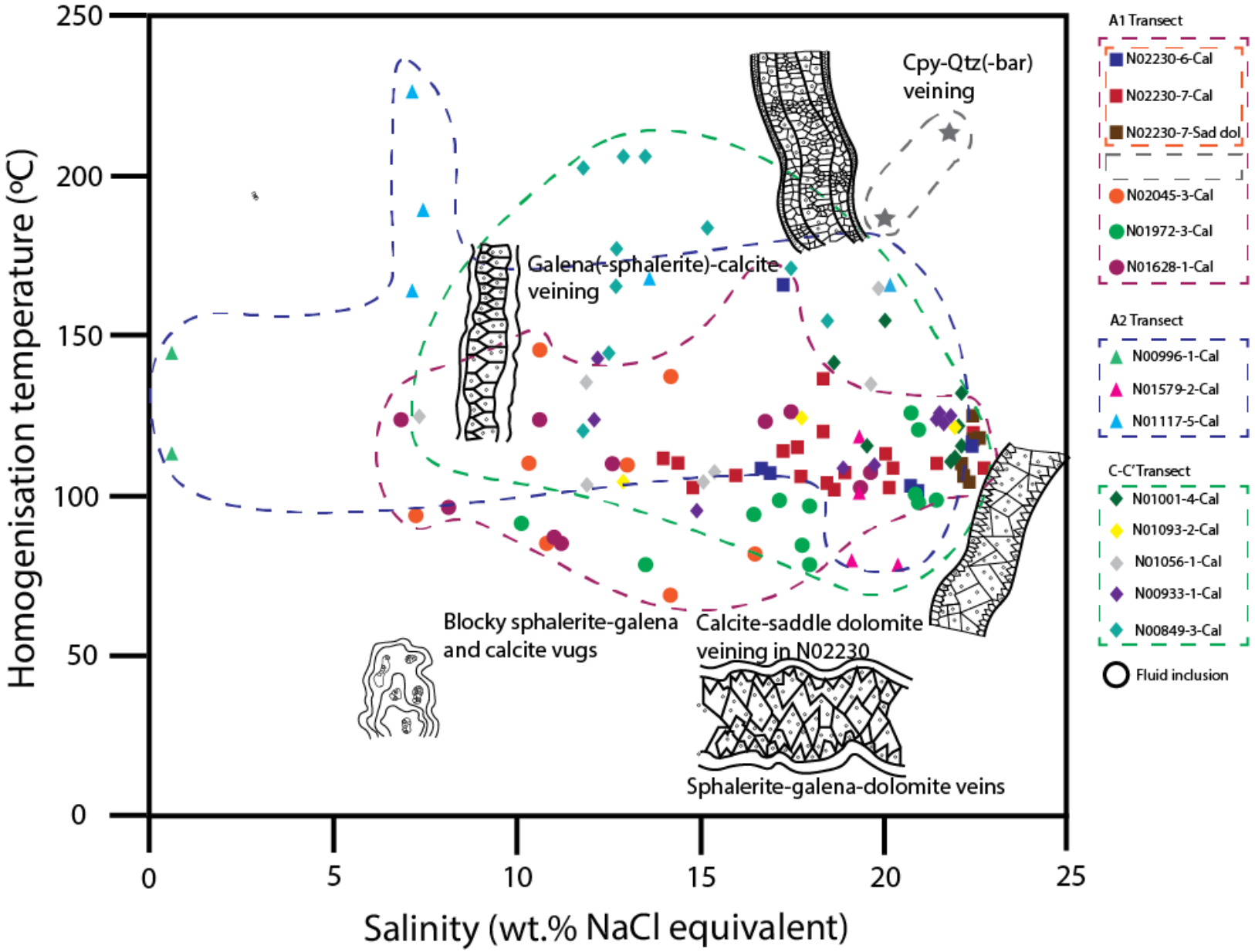

Figure 6.21 – Aggregated fluid inclusion data from the A1, A2 and C Transects

Carbon and oxygen isotopes

6.3. Carbon and oxygen isotope analysis:

Studies which use carbon and oxygen isotope in combination can help to fingerprint the properties of an original ore-forming fluid in a hydrothermal system (Zheng & Hoefs, 1997) and can help to constrain:

1) Carbonate mineralisation temperature
2) Fluid isotopic character, which can be used to trace an origin of the original parental fluid
3) The character of dissolved carbon in the mineralising fluid

Co-variation of the isotopes $\delta^{18}O$ and $\delta^{13}C$ has been used to assess 1) Fluid-mixing, 2) Fluid-rock interaction, and 3) Secondary alteration (I.e. successive generations of hydrothermal fluid) (Zheng & Hoefs, 1997). Gangue carbonate $\delta^{18}O$ values are generally controlled by the degree of interaction between the hydrothermal fluid and the host-rock, where $\delta^{18}O$ increases with progressing host-rock interaction (e.g. Zheng & Hoefs, 1997, Hoefs, 2015, USGS, 2010) – I.e. the "Water/Rock" mass ratio. Assuming that we know the initial $\delta^{18}O$ and $\delta^{13}C$ composition of unaltered host rock, high $\delta^{18}O$ and $\delta^{13}C$ in precipitated carbonates can, therefore be used to infer fluid palaeoflow in a hydrothermal system if we assume that this behaviour results from the hydrothermal fluid isotopically exchanging with an increasingly large rock volume.

This section describes $\delta^{13}C$ -$\delta^{18}O$ analysis results obtained from the "5 Lens Dolomite", "stratal dolomites" and calcite veining in drillhole N02230. In this section, the term " 5 Lens Dolomite" refers to the hydrothermal dolomite that replaces a 6-10 metre thick calcarenite horizon in the 5 Lens Micrite, while "stratal dolomite" describes all other hydrothermal dolomite horizons that do not include the 5 Lens Dolomite. In this case, stratal dolomite samples were obtained from an unbedded micro-conglomerate sequence from drillhole N02230 in what is believed to be 3-Lens equivalent. Eighteen C-O analyses were carried out on 5 Lens Dolomite samples from the A-C Transects, two stratal dolomites in drillhole N02230 in the A1 Transect, and three late-stage calcites hosting minor allochtonous cpy-Qtz(-barite) in N02230 (Fig 5.20, Table 6.8). C-O analysis distribution along each transect varies and does not display a clear geographical trend (Fig 6.23), where the term "W/R interaction line" refers to the "Water-rock ratio". As a fluid migrates and isotopically equilibrates with an effective increasing rock mass, this produces an increasingly low

W/R ratio, with a corresponding increase in $\delta^{13}C$ - $\delta^{18}O$ observed in precipitated carbonates. W/R curve modelling calculations are summarised by Everett (1999, In: Wilkinson (2003) and Ashton et al, 2015), where carbon speciation occurs in an H_2CO_3-dominated fluid, a temperature of 200^{o}C, XCO_2 = 0.04, and initial equilibration of the H_2CO_3 fluid with a basement-hosted calcite at respective $\delta^{18}O$ and $\delta^{13}C$ values of 14.7 ‰ and -4.7 ‰.

1) The B-B' Transect 5 Lens Dolomites are 2-3‰ $\delta^{18}O$ lower than the Main Mine 5 Lens Dolomite array (Fig 6.23). Dolomites exhibit a weak evolution along the W/R (water-rock) interaction line, though only a weak geographical correlation is observed.
2) The C-C' 5 Lens Dolomites broadly coincide with the 5 Lens Dolomite field $\delta^{13}C$. One dolomite exhibits a low $\delta^{18}O$ value of 19.6‰, while another registers at an even lower value of 16.3‰.
3) A1 Transect 5 Lens Dolomites have $\delta^{13}C$ - $\delta^{18}O$ compositions coinciding with those of Main Mine stratal dolomites (I.e. slightly decreased $\delta^{13}C$- $\delta^{18}O$ relative to 5 Lens), while late-stage calcite veins that host brecciated chalcopyrite mineralisation are notably low $\delta^{13}C$ - $\delta^{18}O$ (Fig 6.23).
4) A2 Transect dolomites exhibit general evolution along the W/R interaction line (Ashton et al, 2015), though do not demonstrate a geological correlation. One dolomite has a notably high $\delta^{13}C$ value of 4.3‰.

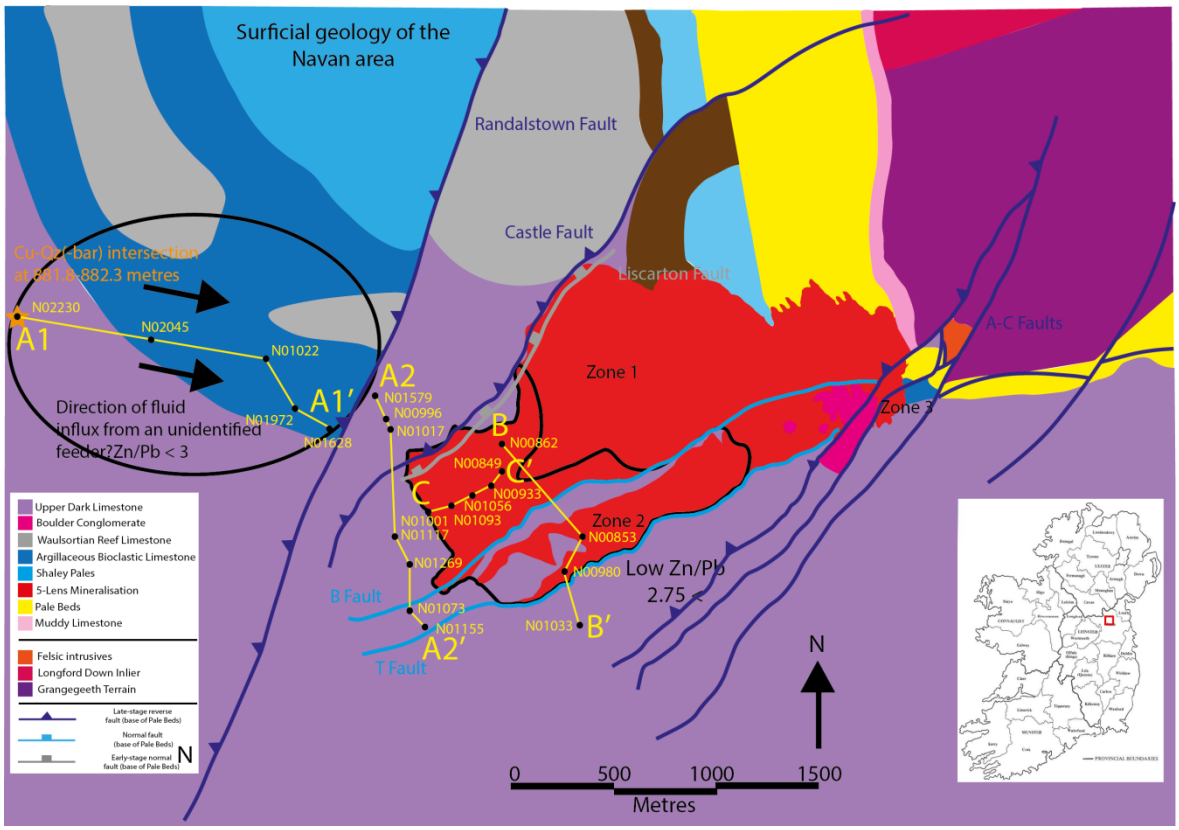

Fig 6.22 – Geological map of Navan area with Main Mine 5 Lens outline (red), low Zn/Pb populations (circled black) and A-C Transects (yellow). For a more detailed Zn/Pb map of the Main Mine, refer to Figure 1.4

6.3.1. B-B' Transect

B-B' 5 Lens Dolomites show generally lower $\delta^{18}O$ values than the Main Mine 5 Lens Dolomite, though contain similar $\delta^{13}C$. There is no obvious correlation with $\delta^{13}C$ - $\delta^{18}O$ and distance trending across the 5 Lens.

6.3.2. C-C' Transect:

C-C' 5 Lens Dolomites sampled from drillholes N01001, N01056 and N00933 coincide with the Main Mine 5 Lens Dolomite field, while the 5 Lens Dolomite from drillhole N01093 has a similar $\delta^{13}C$ value to the 5 Lens Dolomite array, though a lower $\delta^{18}O$ value of 19.6‰. There is no correlation between distance and $\delta^{13}C$ - $\delta^{18}O$ in C-C' Dolomites.

6.3.3. A1 Transect:

Only two 5 Lens Dolomite were identified and sampled in the A1 Transect in drillholes N02045 and N01628. Samples N02045-3 and N01628-3 return $\delta^{13}C$ - $\delta^{18}O$ values of 0.9 and 21.2‰, and 2.8 and 25.1‰, respectively. N02045-3 lies inside the stratal dolomite field. N01628-3 yields

respective $\delta^{13}C$ - $\delta^{18}O$ values 2.8 and 25.1‰, lying outside the 5 Lens Dolomite array. N02230-6 and N02230-7 – stratal dolomite samples that host Cpy-quartz(-barite) in drillhole N02230 - nearly coincide with the Main Mine stratal dolomite array, yielding $\delta^{13}C$ - $\delta^{18}O$ values of 0.7 and 19.9, and 0.6 and 20.8‰ in samples N02230-6 and N02230-7, respectively.

Late-stage, blocky crystalline calcite in drillhole N02230 is cross-cut by one generation of medium-crystalline, barren calcite veining (Fig 5.20). Chalcopyrite-bearing calcite (1st generation) veining in samples N02230-5 and N02230-6 have very low $\delta^{13}C$ - $\delta^{18}O$ at values of -2.2 and 12.7, and -2.1 and 13.8‰ respectively. A second, minor cross-cutting calcite vein (also barren) in sample N02230-6 yields slightly higher $\delta^{13}C$ - $\delta^{18}O$ values of 0.15 and 16‰, respectively.

6.3.4. A2 Transect:

5 Lens Dolomites from the A2 Transect show a random $\delta^{13}C$ - $\delta^{18}O$ distribution along the W/R interaction line. A2 Transect dolomites have notably lower $\delta^{18}O$ (0.3-0.9 ‰) than the Main Mine 5 Lens Dolomite array, though $\delta^{13}C$. The 5 Lens Dolomite from drillhole N01579 has lower $\delta^{13}C$ - $\delta^{18}O$ than the Main Mine 5 Lens Dolomite array at -0.04 and 21.6‰, respectively at similar $\delta^{13}C$ contents, while the N01155 5 Lens Dolomite has a notably higher $\delta^{13}C$ value than other A2 Transect Dolomites at 4.4‰. 5 Lens Dolomites in the A2 Transect have an average $\delta^{13}C$ - $\delta^{18}O$ value of 2.4 and 20.8‰, respectively.

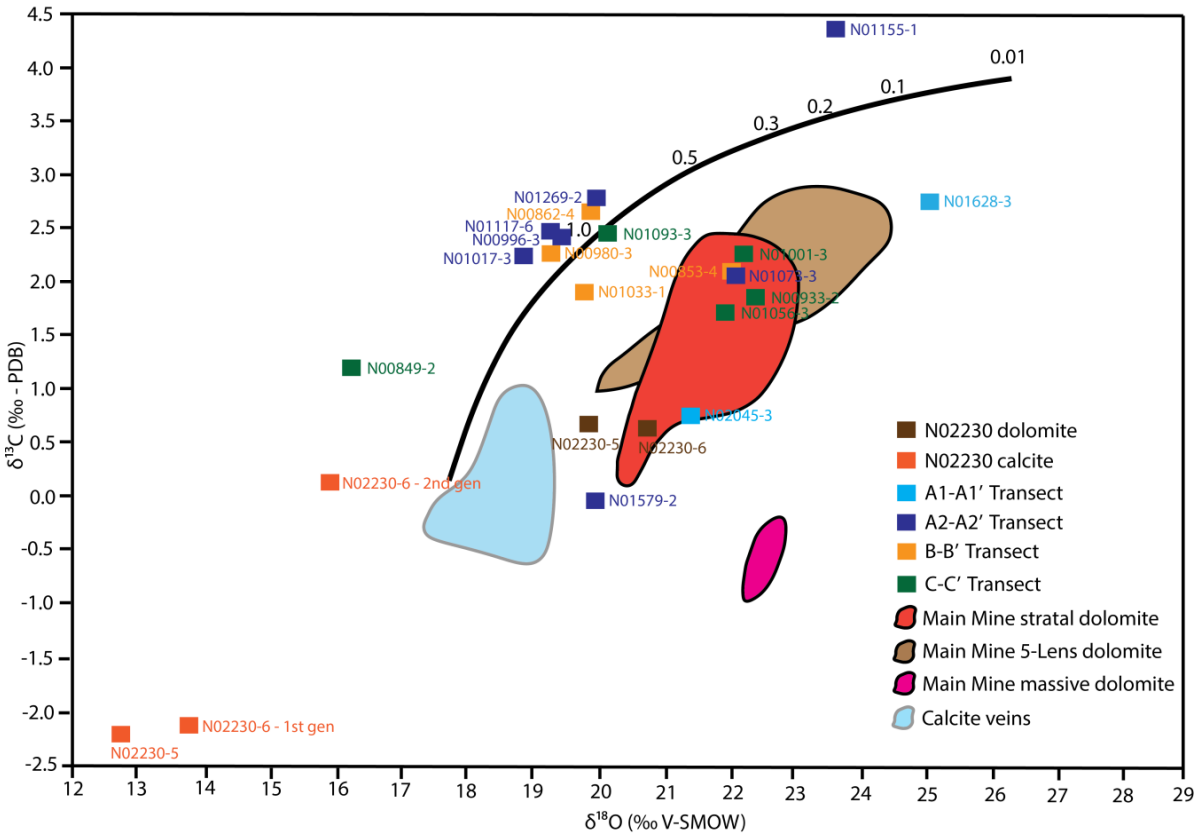

Figure 6.23 – Carbon versus oxygen isotope composition of 5 Lens Dolomites from the A-C Transects. Diagram modified from Ashton et al (2015) and Mane Mine dolomite field data compiled from Braithwaite and Rizzi (1997), Eyre (1998), Hitzman et al (1998), and Wilkinson (2003).

Sample	Mineral	$^{13}C_{V\text{-}PDB}$ (‰)	$^{18}O_{V\text{-}SMOW}$ (‰)	$^{18}O_{V\text{-}PDB}$ (‰)
A1 Transect				
N02230-5	Vein calcite	-2.2	12.7	-17.6
N02230-6	Stratal dolomite	0.7	19.9	-10.7
N02230-6 2nd generation	Vein calcite	0.15	16	-14.5
N02230-6 1st generation	Vein calcite	-2.1	13.8	-16.6
N02230-7	Saddle dolomite	0.6	20.8	-9.8
N02045-3	5 Lens Dolomite	0.9	21.2	-9.4
N01628-3	5 Lens Dolomite	2.8	25.1	-5.6
A2 Transect				
N01579-2	5 Lens Dolomite	-0.04	21.6	-9.1
N00996-3	5 Lens Dolomite	2.7	19.9	-10.6
N01017-3	5 Lens Dolomite	2.4	18.8	-11.8
N01117-6	5 Lens Dolomite	2.6	19.2	-11.3
N01269-2	5 Lens Dolomite	2.8	20.5	-10.1
N01073	5 Lens Dolomite	2.3	21.7	-8.9
N01155-1	5 Lens Dolomite	4.4	23.8	-6.8
B Transect				

N00853-2	5 Lens Dolomite	2.3	22	-8.7
N00862-4	5 Lens Dolomite	2.6	19.9	-10.7
N01033-1	5 Lens Dolomite	2.0	19.6	-10.9
N00980-3	5 Lens Dolomite	2.4	18.8	-11.8
C Transect				
N01001-3	5 Lens Dolomite	2.4	22.1	-8.6
N01093-3	5 Lens Dolomite	2.5	19.6	-10.9
N01056-3	5 Lens Dolomite	1.7	21.6	-9
N00933-3	5 Lens Dolomite	2.1	22.2	-8.4
N00849-2	5 Lens Dolomite	1.3	16.0	-14.4

Table 6.8 – ^{13}C and ^{18}O values from A-C Transect carbonates

This section identifies two key points:

- 5 Lens Dolomite samples from the A-C Transects have similar $\delta^{13}C$ values to samples analysed by Braithwaite & Rizzi (1997), though often have lower $\delta^{18}O$. There is no obvious relationship between the $\delta^{13}C$ and $\delta^{18}O$ isotope values of 5 Lens Dolomites and distance along any given transect. As noted by Rizzi (1992) and Braithwaite and Rizzi (1997), the 5 Lens Dolomite has a three-stage paragenesis. Sample powders were prepared for analysis by dental drilling), which risks homogenising potentially separate $\delta^{13}C$ and $\delta^{18}O$ values for different paragenetic stages. This withstanding, stratal dolomites from drillhole N02230 coincide with the $\delta^{13}C$ and $\delta^{18}O$ field for Main Orebody stratal dolomites.

- Late stage calcite in drillhole N02230 have significantly lower $\delta^{13}C$ and $\delta^{18}O$ values than recorded for the 5 Lens Dolomites and stratal dolomite that hosts cpy-qtz veining. Fluid inclusion thermometry has demonstrated that the calcite formed from a high temperature (101-165^{o}C) high salinity (14-22.6 wt.% NaCl) fluid.

Chapter 7

SYNTHESIS

Chapter 7 examines the results provided in Chapter 5 and 6, and discusses both the provenance of low Zn/Pb mineralisation west of the Randalstown Fault, and cpy-Qtz(-barite) mineralisation in drillhole N02230. This chapter examines feeder-zone potential based on petrographic, isotopic and fluid inclusion evidence. This report finds that heavy $\delta^{34}S$ from sulphides in the hanging-wall of the Randalstown Fault are consistent with a hydrothermal fluid origin, and likely derived from the same fluid event as the Main Orebody. This finding is consistent with A) a near-identical sulphide paragenesis in the A-C Transects, and B) fluid inclusion homogenisation temperature and salinity values that are coincident with that of Main Mine sulphides. Cpy-qtz in drillhole N02230 formed separately from both the Main Orebody and sph-gal in the Randalstown Fault hangingwall, evidenced by A) a separate paragenesis, and B) fluid inclusion homogenisation temperature values that are higher than the Main Mine

7. Discussion:

Previous studies by Anderson et al (1998), Fallick et al (2001), Blakeman et al (2002), Everett et al (2003), Wilkinson et al (2005B), Davidheiser-Kroll (2014), and Marks (2015) best summarise the conditions that formed the giant Navan Deposit:

1) An underlying volcanic and volcaniclastic basement enriched in Zn-Pb. The Lower Palaeozoic basement that underlies the Navan area comprises intrusives and volcaniclastics and low-grade (greenschist-facies) metasediments produced during Ordovician Benioff-style subduction, producing a volcanic rock suite enriched in base metals. These metals were scavenged by the hydrothermal fluid and re-deposited near the Lower Carboniferous seafloor during fluid-mixing.

2) An extensive normal fault system, capable of tapping mantle heat and providing conduits for upwelling hydrothermal fluids. Sufficient mantle heat is required to drive a vigorous hydrothermal system capable of scavenging, transporting and depositing metals from the Lower Palaeozoic basement (Davidheiser-Kroll, 2014). The Iapetus Suture, interpreted to underlie the Navan area is interpreted as important in determining the morphology of the

overlying normal fault network (considered synthetic), facilitating hydrothermal circulation.

3) A carbonate shelf limestone sequence interbedded by silty horizons, calcisiltite marker horizons and hydrothermal dolomites. These sequences focused fluid flow and provided lithological traps for sulphide mineralisation

4) Sufficient bacteriogenic reduction of seawater sulphate to sulphur in hypersaline brines, capable of mixing with upwelling hydrothermal fluids to precipitate Zn-Pb-Fe sulphides.

5) Removal of facies overlying the Pale Beds during Chadian extension, providing increased permeability and fracturing necessary for hydrothermal fluids to vertically migrate through the Pale Beds and mix with bacteriogenic sulphur on or near to the seafloor (Fig 3.1, Fig 7.1).

These conditions provided the geochemical, structural and lithological controls to concentrate high-grade Zn-Pb sulphide ore over a geographically small area, while geochemical haloes previously investigated by Walker (2005), Walker (2010) and Marks (2015) demonstrate that low-grade mineralisation relating to the Navan mineralising event was geographically widespread and controlled by the permeability of the Pale Beds and overlying Upper Dark Limestone during lateral and vertical fluid migration, respectively. The Erosion Surface determined the degree of Pale Beds un-roofing – an important control on the pore pressure regime and the resultant hydrothermal fluid flow direction (e.g. Davidheiser-Kroll, 2014) (Fig 3.1 Fig 7.1).

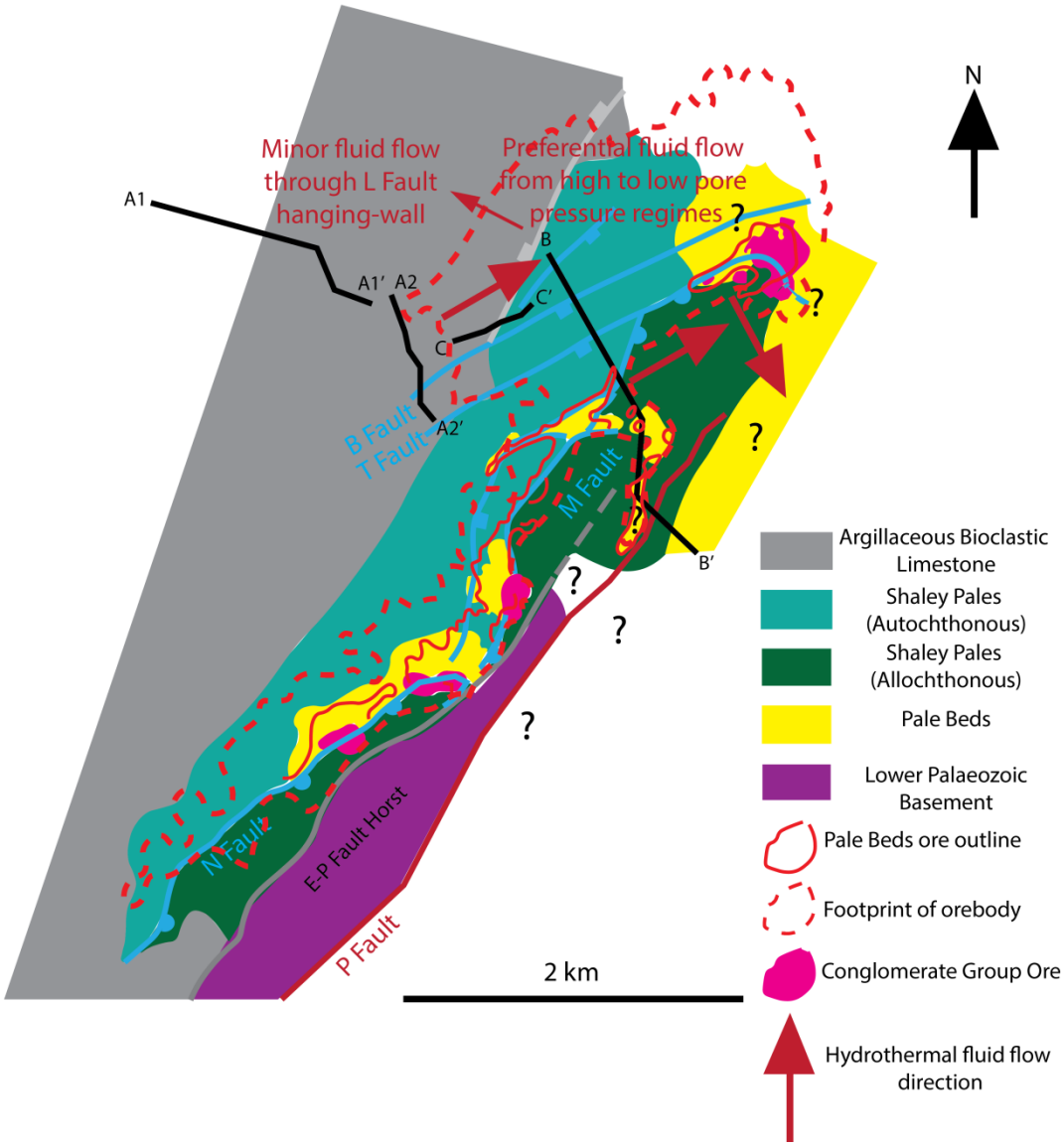

Figure 7.1 – Geology at the base of the Boulder Conglomerate at end-Chadian with Main Mine outline in dashed red (modified from Ashton et al, 2015). The Erosion Surface increasingly down-cuts to the southeast, un-roofing the Pale Beds sequence and exposing the Lower Palaeozoic basement at its deepest. Northwest of the L Fault, the Erosion Surface is poorly developed, meaning that the Argillaceous Bioclastic Limestone and Waulsortian Limestone overlie the Pale Beds sequence. Presumed hydrothermal fluid flow directions are based on the observations of Davidheiser-Kroll (2014), Marks (2015), and this study.

Geology and Zn/Pb ratios of the western Navan area and Main Mine

7.1. Geology and Zn/Pb ratios of the western Navan area and Main Mine:

The stratigraphy of the A1 Transect is similar to those of the A2, B and C Transects, recording a progression from clean micrite through to increasingly sandy and argillaceous facies up-stratigraphy. However, marker horizons are generally poorly developed in the A1 Transect, while the 5 Lens Dolomite is only observed in drillholes N02045 and N01628. Additionally, only one stratal dolomite occurrence is noted in the A1 Transect, in drillhole N02230. A "typical" Main Mine stratigraphic sequence of calcarenites, oolites and micro-conglomerates is observed between drillholes N01628 to N02045, until N02230 where the geology comprises repetitive calcarenites, interbedded micrites and unbedded micro-conglomerates. This may suggest progression away from deepening basinal environment, which may help to explain why bacteriogenic sulphur is not observed in hangingwall sulphides if we assume that bacteriogenic brines pooled in the topographic lows of the extending basin during faulting (discussed in section 6.2).

7.1.1. Zn/Pb ratios along the A-C Transects:

Zn/Pb ratios show a weak spatial association with normal faults, where low 5 Lens Zn/Pb is observed close to interpreted feeder zones (I.e. L, B and T Faults) in the A2 and B Transects (Fig 5.11, Fig 5.6). The A1 and C Transects register for low Zn/Pb in their respective 5 Lens stratigraphies, though ratios in the 1-4 Lenses are often higher (Fig 5.6, 5.10). In the A1 Transect, the average 5 Lens Zn/Pb ratio is 0.88, though the 1-4 Lenses have a much higher ratio of 3.14. One possibility for this difference is that migrating fluids initially precipitated galena in the absence of bacteriogenic sulphur, producing a Pb-depleted fluid that also underwent vertical migration. There was a clear vertical component as fluids migrated west of the Main Orebody, observed in vein textures that cross-cut bedding (Fig 5.13). The 5 Lens Dolomite, stratal dolomite and marker horizons (excluding the Upper Sandstone Marker and Upper Dark Marker) are very poorly developed or absent west of the Randalstown Fault. In the Main Orebody, stratiform mineralisation is observed at the base of certain marker horizons and dolomites (particularly the Nodular Marker at the top of the 2-Lens), and the 5 Lens Dolomite in the 5 Lens Micrite. This

suggests that the markers and dolomites acted as aquitards that focused mineralising fluids (Ashton et al, 2015). It has been repeatedly noted at Navan and other Irish-types that hydrothermal dolomites and calcisiltite horizons act as effective aquitards, focussing mineralising fluids (e.g. Anderson et al, 1998, Wilkinson, 2003, Ashton et al, 2015). A cleaner and un-dolomitised stratigraphic sequence west of the Randalstown Fault may have allowed wide-scale vertical fluid flow, producing very low-grade mineralisation observed in the A1 Transect, where Pb and minor Zn was initially deposited in the in the 5 Lens Micrite and base of the Pale Beds sequence (I.e. low Zn/Pb), while Pb-depleted fluids migrated vertically through the overlying lenses and deposited higher Zn/Pb mineralisation in the 1 to 4 Lenses. Observation of galena with minor sphalerite in hangingwall 5 Lens samples, followed by later minor sphalerite is consistent with this interpretation. A dearth of bacteriogenic sulphur in the hanging-wall of the Randalstown Fault was likely an important geochemical control, preventing potential mineralisation from being concentrated, therefore allowing low-grade mineralisation to occur

Petrography and mineral paragenesis of the A-C Transects

7.2. Thin section microscopy:

The paragenesis of hangingwall, footwall and Main Mine sulphides are very similar (Fig 5.21, 5.23, and 5.27), comprising - 1) Early-stage calcite cementation, dolomitisation and framboidal and euhedral pyrite mineralisation, 2) Sphalerite and galena (galena and minor sphalerite in drillholes N01022, N02045 and N02230 along the A1 Transect) mineralisation, 3) Later-stage chalcopyrite and fibrous calcite veining. This common paragenesis may be interpreted as Zn-Pb mineralisation west of the Randalstown Fault deriving from the same mineralising fluid as the Main Orebody (fig 5.21, 5.23, 5.27). This observation is supported by fluid inclusion analysis of hangingwall sphalerite-galena-calcites that constrain a homogenisation temperature range similar to that of the Main Mine hydrothermal fluid, though is often of higher salinity (discussed in section 6.2 –Fig 6.12, 6.21, 7.3) and B) a $\delta^{34}S$ range that constrains hangingwall galena-sphalerite to a hydrothermal source (discussed in section 6.1, 7.3).

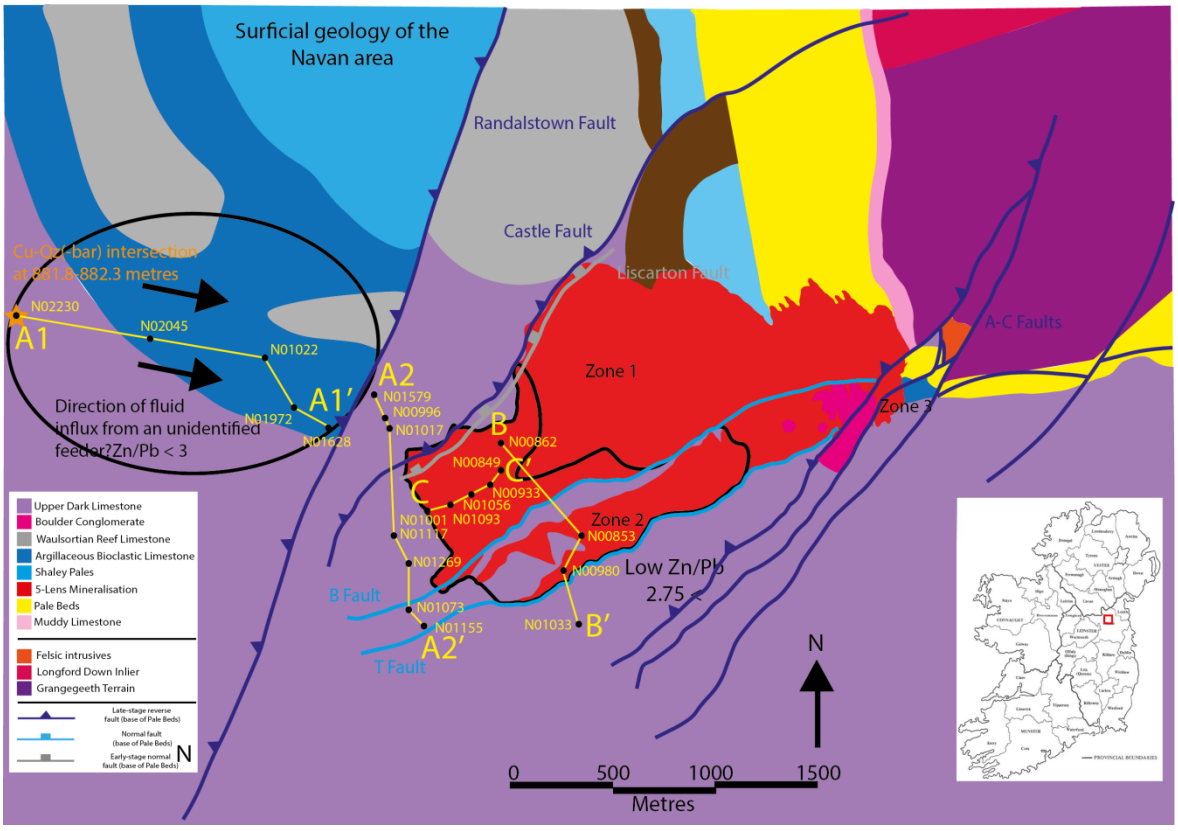

Figure 7.2 – Geological map of Navan area with Main Mine 5 Lens outline (red), low Zn/Pb populations (circled black) and A-C Transects (yellow). For a more detailed Zn/Pb map of the Main Mine, refer to Figure 1.4

Hitzman and Beaty (1996) identify that paragenetically early iron sulphides in vent-proximal settings in other Irish-types are cross-cut by later-stage Zn-Pb-Fe sulphides, chalcopyrite, bornite and tennantite containing Fe-sulphide inclusions. In the A1 Transect, sulfosalt mineralisation is only observed in galenas in drillholes N01628 and N01972 (Fig 5.24), occurring either in solid state with galena or as intergrowths, while trace chalcopyrite is also only observed as an overprinting stage for galena-sphalerite in N01628 and N01972 – Randalstown Fault-proximal holes at 40 and 220 metres west, respectively. Late-stage Fe-sulphide is only observed in sample N01972-2 (Fig 5.24), where pyrite-marcasite develops between the pore space in galenas and co-precipitated dolomite rhombs (Fig 5.24). If we assume that mineralisation in the Randalstown Fault hangingwall was produced by a westward-migrating hydrothermal fluid, absence of sulfosalts, chalcopyrite and significant pyrite moving west into drillhole N01022 suggest that all three may have been exhausted in the migrating hydrothermal fluid beyond drillhole N01972 – the last drillhole that has a Pale Beds stratigraphic sequence similar to that of the Main Mine. This common paragenesis between hangingwall, footwall and Main Mine suggests that sulphides in the hangingwall were coeval with the Main Mine. Excluding sulphides in drillhole N01972 and N01628 (Fig 5.24), cross-cutting relations with later-stage sulphides that characterise the Main Mine ore development are not observed, nor do we see exotic copper sulphide assemblages that point to a feeder (e.g. Boast et al, 1981, Hitzman and Beaty, 1996, Banks et al, 2002, Wilkinson et al, 2005A)

Cpy-Qtz(-barite) mineralisation in drillhole N02230 is paragenetically separate from Navan mineralisation and appears to be a distinct higher temperature and high salinity, based on fluid inclusion findings (Section 6.2). Progression of quartz textures from mosaic, becoming blocky, oscillatory zoned and plumose towards the vein core suggests multiple stages of gangue mineralisation while chalcopyrite-marcasite co-precipitated (Fig 5.26). Chalcopyrite is a trace mineral in Navan ore. Therefore, we need to look for other copper occurrences in Ireland that might shed light on chalcopyrite mineralisation in western Navan. Three potential analogues for chalcopyrite mineralisation exist in other Irish-type deposits and southern Ireland.

The first analogue is the “Pink Dolomite” – a late-stage vein assemblage that cross-cuts and replaces earlier carbonates and sulphides. Pink dolomite has been observed in Lisheen, Silvermines and Galmoy, and is a late-stage feature that cross-cuts mineralisation and precipitated with minor chalcopyrite and pyrite (Boast et al, 1981, Andrew, 1986, Redmond, 1997, Eyre, 1998, Hitzman et al, 2002, Wilkinson, 2003, Wilkinson, 2005A). Pink dolomite is interpreted to derive from a regionally migrating brine during Variscan compression and may be similar to

what is observed in western Navan, though a critical differences lies in the paragenetic vein order. Cpy-Qtz(-barite) is paragenetically first and cross-cut by later-stage blocky calcite-saddle dolomite veining with minor allochtonous cpy-Qtz brecciated and transported. Minor pink dolomite is observed in drillhole N02230, though is barren and no cross-cutting relations with Cpy-Qtz(-barite) are observed.

The second analogue is stratabound and vein copper sulphide deposits in southern Ireland. These are sub-economic polymetallic vein and disseminated deposits observed in the Old Red Sandstone sequence, particularly in the Munster Basin where it forms a terriguonous fill of up to five kilometres thickness (Meere, 1995) Based on very low $\delta^{34}S$ sulphur isotope values, Wen et al (1998) suggested that copper-sulphide deposits in County Cork were sourced from the Old Red Sandstone facies enriched in bacterially and diagenetically reduced sulphides (-15.8 to -4.2‰), and that sulphides were remobilised by Variscan fluids with little isotopic modification. This scenario is unlikely in western Navan for two reasons – 1) The Old Red Sandstone sequence does not underlie Navan, and 2) sulphur isotope values obtained from the chalcopyrite (discussed in section 6.1) suggest that the mineralising fluid was likely hydrothermal. Alternatively, Kinnaird et al (2001) constrain a Lower Palaeozoic basement source for polymetallic veins in the Old Red Sandstone in southern Ireland based on Pb isotopic evidence from co-precipitated galenas. This may provide a chalcopyrite source, assuming that an unidentified basement high lies west of drillhole N02230. However, calcite veining in drillhole N02230 is volumetrically minor, clearly cross-cuts *in-situ* cpy-qtz veining (Fig 5.20), and it is geologically unlikely that significant Cpy–Qtz(-barite) observed could be transported in pore space.

The third is feeder zone mineralisation. Chalcopyrite is a trace mineral at Navan, though minor chalcopyrite-tennantite-arsenopyrite-bornite-(barite) assemblages have been observed in proximity to normal faults in Lisheen, Silvermines, Galmoy and Tynagh interpreted as deposit "feeder zones", and are observed to cross-cut and preserve early iron-sulphide textures (e.g. Hitzman and Beaty, 1996, Boast et al, 1981; Banks et al, 2002, Wilkinson et al, 2005A). Additionally, chalcopyrite-quartz mineralisation – similar to that observed in drillhole N02230 – is noted by Samson and Russell (1987) at Gortnadyne in Silvermines. Mineralisation at Gortnadyne comprises cpy-gal-sph-bar hosted in brecciated quartz-chalcedony. Banks et al (2002) carried out fluid inclusion analysis of quartz from Gortnadyne, constraining a homogenisation temperature range of 164-195^{o}C, and salinity value of 15 wt.% NaCl. No major Randalstown Faults or fractures are observed in drillhole N02230, though this does not discount feeder-zone potential further west. As discussed in sections 5.6.1 and 6.5, only two T_h and salinity readings (191^{o}C – 19.7 wt.%

NaCl, and 223^{o}C and 22 wt.% NaCl) were obtained from quartz. Monophase inclusions yield a wider salinity range of 10.2-22.7 wt.% NaCl. Assuming that these values are accurate and representative of the original mineralising fluid, they suggest both a higher mineralisation temperature and salinity than the Main Mine hydrothermal fluid (Wilkinson, 2010). Importantly cpy-Qtz(-barite) in drillhole N02230 has closer mineralogical similarities to Gortnadyne than Navan. This may have important implications for further exploration in western Navan, and could point to mineralisation that is temporally related to Navan (I.e. Irish-type), though hotter and potentially related to an unidentified normal fault set further west.

Sulphur isotopes

7.3. Sulphur isotope analysis:

Sulphur isotope studies of Navan ore and mineralisation have helped to constrain the genetic model for the deposit and highlight the role of bacteriogenic sulphur in concentrating high-grade Zn-Pb sulphide ore (e.g. Boast et al, 1981, Anderson, 1990, Anderson et al, 1998, Fallick et al, 2001, Wilkinson, 2005A, Treloar, 2014, Marks, 2015). Anderson et al (1998) identified two distinct sulphur sources – Sulphides falling within a $\delta^{34}S$ -23 to -5‰ threshold are considered bacteriogenic, those coinciding with a $\delta^{34}S$ 0 to 15 ‰ range are considered hydrothermal and sulphides with intermediate values were produced by varying degrees of fluid-mixing. Fallick et al (2001) identified from Zn and Pb concentrates that approximately 90% of Navan ore sulphur is bacteriogenic, demonstrating the importance of bacteriogenically-reduced sulphur in producing high-grade ore. Blakeman et al (2002) identified that galenas proximal to minor normal faults exhibit high $\delta^{34}S$, becoming rapidly low $\delta^{34}S$ and negative within three metres distance. This behaviour was interpreted to reflect the dominance of locally reduced bacteriogenic sulphur. Marks (2015) studied the "epigenetic halo" of the Navan Deposit – low-grade mineralisation that extends laterally from the Main Mine previously examined by Walker (2010). Marks identified that sulphide sulphur isotope values in the "E1" and "E2" (broad, low-grade mineralisation areas interpreted to form from fluid migration away from the Main Orebody) are hydrothermal.

Sulphide sulphur isotope distributions obtained from the B and C Transects are consistent with Anderson et al (1998), Fallick et al (2001), Blakeman et al (2002), and Altinok (2005), identifying a bimodal hydrothermal-bacteriogenic signal (Fig 6.2-6.5). The steep drop in $\delta^{34}S$ observed between drillholes N01001 and N00849 (Fig 6.5) in the C-C' Transect reflects an increasing bacteriogenic input, likely controlled by topographic lows in the extending basin where sulphur-enriched brines pooled (Ashton et al, 2015), while the mixed hydrothermal-bacteriogenic signal observed along B-B' and lack of geographical correlation between $\delta^{34}S$ and distance along the transect may reflect the input of the F1-F27 minor Fault array.

A1 Transect sulphides are hydrothermal, while bacteriogenic and hydrothermal sulphur are present in A2 Transect sulphides (Fig 6.6-6.8). This observation is consistent with the "epigenetic

halo" identified by Marks (2015). There are three possible reasons to explain the prevalence of hydrothermal sulphur and low Zn/Pb ratios west of the Randalstown Fault:

1) A lack of interconnected secondary porosity produced by early normal faulting during basinal extension. From observation of core along the A1 Transect, there is not an extensive normal fault system in western Navan area compared to the B and C Transects along the Main Orebody. This prevented extensive hydrothermal circulation or seawater down-welling (Fig 8.1, 8.2).
2) The Erosion Surface is absent in the western Navan area. The Erosion Surface unroofed the Pale Beds sequence and down-cuts to the Lower Palaeozoic basement at its deepest in the east Main Mine area. This provided a major control on or distribution, and likely provided hydrothermal fluids with open access to the seafloor to mix with the brine and precipitate ore (Ashton et al, 2015). Assuming that bacteriogenic sulphide-enriched brines pooled in western Navan, a thick overlying Shaley Pales, Argillaceous Bioclastic Limestone and Waulsortian Reef sequence and low interconnected porosity and permeability would have been prohibitive to fluid down-welling, upwelling and mixing. However, as discussed in section 6.3, 5 Lens Dolomites in drillholes N02045 and N01628, and stratal dolomite in N02230 suggests that some seawater was capable of down-welling to at least the base of the Pale Beds sequence.
3) Bacteriogenic sulphide-enriched brines, responsible for providing sufficient sulphur to the Navan system were not present in the present-day Randalstown Fault hangingwall. As discussed in section 7.1, the geology of western Navan is less silty, argillaceous, and dolomitic than the "typical" Main Mine sequence, and grades into repetitive calcarenite sequences. This suggests a transition into a separate depositional regime, and one where brine pools did not sufficiently accumulate (I.e. not on a palaeo-topographic low).

Marks (2015) identified two textures suggested to form in the presence of a low bacteriogenic sulphur budget – "Texture A", comprising coarse-grained galena, and "Texture C" consisting of vein/veinlet galena-sphalerite-calcite. These textures were produced from galena precipitating first and exhausting the sulphur budget, while relatively soluble Zn remained in solution in hydrothermal fluid. Indeed, in the A1 Transect galena is observed to be either paragenetically earlier than sphalerite, co-precipitate with minor sphalerite, or exhibit weak rim replacement by sphalerite. Sulphur isotope and mineralisation style is closely interlinked – Vein and disseminated mineralisation is hydrothermally derived, while fine-grained replacement and nodule styles are a result of bacteriogenic sulphur – common mineralisation styles in the A2 Transect (Randalstown Fault footwall) are bacteriogenic (Fig 6.7-6.8). While low Zn/Pb and hydrothermal sulphur are

identified as tell-tale signs for a nearby feeder (e.g. Taylor and Andrew, 1978, Andrew and Ashton, 1982, Taylor, 1984, Blakeman et al, 2002), high-grade ore will not develop without bacteriogenic sulphur to fix upwelling, metalliferous fluids. Chalcopyrite from drillhole N02230 yields a $\delta^{34}S$ range of 0.8-3.3‰, suggesting that mineralisation derived from a hydrothermal fluid.

Overall, sulphur isotope and petrographic analysis gives credence to galena-sphalerite in the Randalstown Fault hangingwall precipitating from a hydrothermal fluid that migrated laterally northwest of the Main Orebody, while chalcopyrite-quartz-barite developed from a separate hydrothermal fluid. A low Zn/Pb ratio does not necessarily suggest that a feeder zone is nearby, but rather points to the sulphur regime during mineralisation. The distribution of the bacteriogenic sulphide-enriched brine is suggested to be controlled by developing half graben structures during early extensional faulting (Ashton et al, 2015). If we assume that the hangingwall of the Randalstown Fault was basin-distal, we would, therefore, expect brine pooling to be limited. Chalcopyrite in drillhole N02230 was sourced from a high temperature hydrothermal fluid (discussed in section 6.2), and, as previously discussed is interpreted to be paragenetically separate from Navan.

Fluid inclusions

7.4. Fluid inclusions:

Detailed fluid inclusion studies of Navan sulphides and carbonates have helped to constrain the genetic model of the deposit and, in conjunction with sulphur isotope analysis, identify a bimodal fluid-mixing model (e.g. Probert, 1983, Braithwaite & Rizzi, 1997, Peace, 1999: Hitzman & al, 2002, Peace & al, 2003, Wilkinson, 2010, Treloar, 2014). Fluid inclusion analysis has helped identify two fluids responsible for ore formation – a low temperature, high salinity bacteriogenic sulphur enriched brine (70-100 °C, 20-25 wt%. NaCl), and a moderate temperature, moderate salinity metalliferous fluid (100-140^{o}C, 5-10% wt%. NaCl) (Wilkinson, 2010) that scavenged, transported, and deposited sulphides from the underlying Lower Palaeozoic basement (e.g. Russell, 1978, Everett & Wilkinson, 2001).

Calcites in galena-sphalerite-calcite samples along the A1 Transect yield homogenisation temperatures typical of the low end of the Navan hydrothermal fluid identified by Wilkinson (2010), though are often more saline (fig 6.18-6.20, Fig 7.3, Table 6.8), at respective average values of 98.7^{o}C and 18 wt.% NaCl. This observation is coupled with a slight temperature decrease travelling west of the Randalstown Fault, though salinity range travelling west from the Randalstown Fault slightly increases. This may point to mixing with down-welling, evaporated seawater as fluids migrated west, though mixing would likely have been limited due to the thick overlying sequence of Argillaceous Bioclastic Limestone and Waulsortian Limestones (Fig 8.1-8.2). Higher temperature, lower salinity inclusion values obtained from the low Zn/Pb area southwest of the 5 Lens cut-off lie outside the temperature field of the hydrothermal fluid at the Main Mine. Indeed, homogenisation temperatures constrained from samples N01117-5 and N00849-3 are significantly higher and lie closer to the SWEX-S mixing field identified by Treloar (2014) (Fig 7.3). This is supportive of Davidheiser-Kroll's (2014) findings, suggesting that fluids likely migrated northeast before mixing with brines in the Main Mine site. Fluids may have upwelled from the southwest between the early L and E Faults, as well as the F1-F27 minor fault network that extends southwest past the 5 Lens cut-off.

The low Zn/Pb ratio examined both in the southwest 5 Lens, and in the Randalstown Fault hangingwall may be controlled by a low bacteriogenic sulphur budget and reflects the geographical distribution of the brine. High homogenisation temperatures from calcites in

drillholes N01117 and N00849-3 may reflect feeder input from the B and T Faults, and the F1-F27 minor fault array, respectively. This observation would be consistent with Davidheiser-Kroll's (2014) hypothesis that the faults focus localised (low-grade) mineralisation in southwest Navan. Homogenisation temperatures of hangingwall sulphides fall within the lower end of the temperature range of the Main Orebody hydrothermal fluid (Wilkinson, 2010). Fluid inclusion and sulphur isotope values can be used to constrain why these two low Zn/Pb areas of mineralisation formed via different processes

- The low Zn/Pb area immediately southwest of the 5 Lens cut-off represents the initial migration site for upwelling, unmodified hydrothermal fluids. A steady increase in bacteriogenic sulphur prevalence is observed along the C-C' Transect, suggesting that the low temperature, high salinity brine was geographically restricted and was likely an important determinant on the grade and Zn/Pb ratio of mineralisation and ore.

- The low Zn/Pb mineralisation in the Randalstown Fault hangingwall formed from lateral movement away from the Main Mine site. The migrating hydrothermal fluid mixed was weakly modified by down-welling evaporated seawater and/or pore water. This hypothesis is satisfied by fluid inclusion evidence confirming that mineralisation formed from a moderate temperature, moderate-high salinity fluid.

Late-stage calcite-dolomite in drillhole N02230 yield respective average homogenisation temperature and salinity of 112.1^{o}C and 18.7 wt % NaCl, and 112.4^{o}C and 22.4 wt.% NaCl. These values are similar to those obtained from hangingwall sulphide-calcite veins and fall within the Main mine hydrothermal fluid field, though respective salinities exceed that of the Main Mine hydrothermal fluid (Wilkinson, 2010). Analyses of two quartz-hosted inclusions from Cpy-Qtz(-barite) veining return respective homogenisation temperatures and salinity values of 193^{o}C and 19 wt.% NaCl, and 223^{o}C and 22.5 wt.% NaCl. Monophase inclusions constrain a wider salinity range of 10.2-22.7 wt.% NaCl (Fig 6.12-6.17, Fig 7.3, Table 6.5-6.6) Should these values be accurate they are higher than Navan ore (Wilkinson, 2010), and much closer to Gortnadyne at Silvermines (e.g. Banks et al, 2002). This observation is the most significant piece of evidence for an unidentified potential feeder in western Navan, and may be an expression of a separate hotter and deeper system.

Due to the small size of most inclusions, high refractive index of the calcite (and dolomite) where most inclusions were hosted, and heavily reduced resolution with 100X magnification, analysis of each inclusion was conducted at least twice to ascertain T_{FREEZE}, T_E, and $T_{M\text{-}ICE}$. Whilst T_{FREEZE} can often be more readily measured for most inclusions larger than 2µm and can be observed by a "flash" change in inclusion colour, T_E is represented by the emergence of a "granular" texture as the inclusion separates into saline liquid and water ice. At a high magnification where resolution deteriorates, this texture is often very difficult to pinpoint at the exact moment the inclusion reaches the eutectic melting point, and may require multiple cycles of freezing and subsequent re-heating to correctly identify. Most inclusions observed reached T_{FREEZE} at a range of -50 to -70°C, and achieved T_E at an approximate temperature range of -50 to -60°C. These are temperatures well below what is achieved in a binary H_2O-NaCl system, and suggest that inclusions hosted both within the calcites from the A1, A2 and C Transect, and quartz from drillhole N02230 along the A1 Transect, contain a significant $CaCl_2$ component and belong two a H_2O-NaCl-$CaCl_2$ system – a common three-component system in Mississippi Valley-Type and Irish-type systems (e.g. Wilkinson, 2001, Lowenstein et al, 2002, Hanor and Macintosh, 2007).

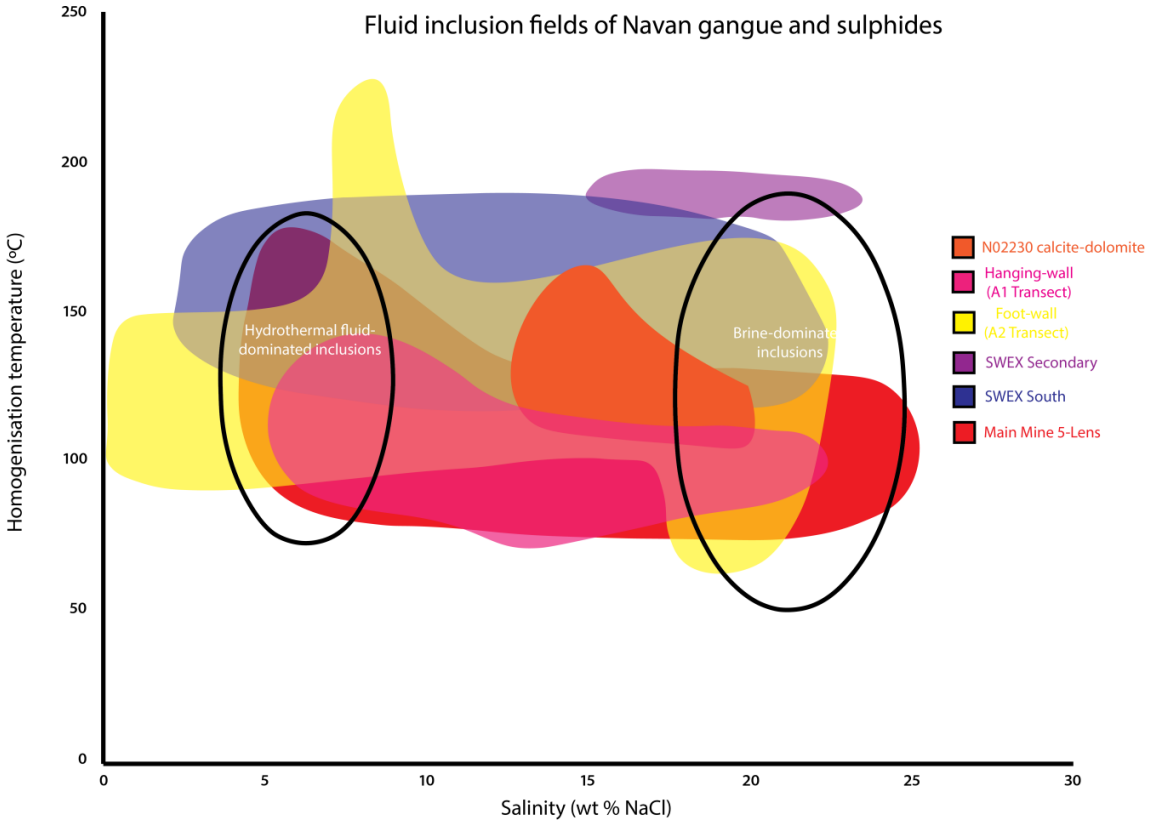

Figure 7.3 – Fluid inclusion homogenisation temperature and salinity fields for Navan gangue and sulphides. Hangingwall sulphide T_h and salinity closely coincide with the Main Mine 5 Lens field, while N02230 calcite-dolomite are typically high-salinity. Plot modified from Davidheiser-Kroll (2014) and original data compiled from Everett (1999), Everett & Wilkinson (2001) and Treloar (2014)

Carbon and oxygen isotopes

7.5. Carbon and oxygen isotopes:

A defining shared characteristic of the Irish-type deposits is that hydrothermal dolomitisation of the host rock precedes ore formation, where the dolomitising fluid is sourced from heated Carboniferous seawater (e.g. Rizzi, 1992, Braithwaite and Rizzi, 1997, Peace, 1999, Wilkinson, 2003), while dolomite and calcite co-precipitate with Zn-Pb sulphides, and are overprinted by late-stage carbonates (e.g. Hitzman et al, 1998, Ashton et al, 2015). At Navan, dolomitisation preferentially develops in calcarenites and calcisiltites, often affecting siltier horizons (e.g. Anderson et al, 1998). In Waulsortian-hosted deposits, dolomitisation is restricted to micrite horizons in the Waulsortian Limestone Formation – the main host rock for Zn-Pb ore. Analysis of hydrothermal carbonates in the Irish-type deposits have helped to constrain the relationship between pre-stage host rock dolomitisation and subsequent ore formation. Hitzman (1995) and Hitzman et al (1998) concluded that progressively higher $\delta^{18}O$ values in precipitated carbonate phases from south to north Midlands were indicative of a regional fluid flow model (I.e. purely MVT), originating from the Munster Basin. This interpretation would be consistent with a regional-scale, MVT fluid-flow model for the Irish Zn-Pb deposits, though Wilkinson (2003) identifies that seemingly strong $\delta^{18}O$ trends from south to north are derived from samples from Mallow, and do not show a systematic increase along the Rathdowney Trend, nor a correlating fluid inclusion temperature decrease that might be expected if the ore fluids were migrating over hundreds of kilometres. Wilkinson (2003) attributes systematic $\delta^{18}O$ increases to variations in the $\delta^{18}O$ resulting from mixing with host rock pore water. Hitzman & Beaty (1996) analysed hydrothermal carbonates from close to interpreted feeder zones from Tynagh, Silvermines, Lisheen, and Garrycam/Keel. These samples yielded a $\delta^{13}C$ range of -6 to -3‰, which was interpreted to reflect precipitation of hydrothermal carbonates from a high temperature, low $\delta^{13}C$ hydrothermal fluid (Fig 7.4). These initial values reflect a high fluid/rock ratio – I.e. the original, host rock-unbuffered $\delta^{18}O$ - $\delta^{13}C$ composition of the hydrothermal fluid. Steadily increasing $\delta^{18}O$ - $\delta^{13}C$ in hydrothermal carbonates reflects precipitation from the hydrothermal fluid as it undergoes steady temperature decrease and increasing isotopic exchange with the Waulsortian limestone sequence. This reflects a decreasing fluid/rock ratio as the migrating ore fluid isotopically equilibrates with an increasingly large rock volume.

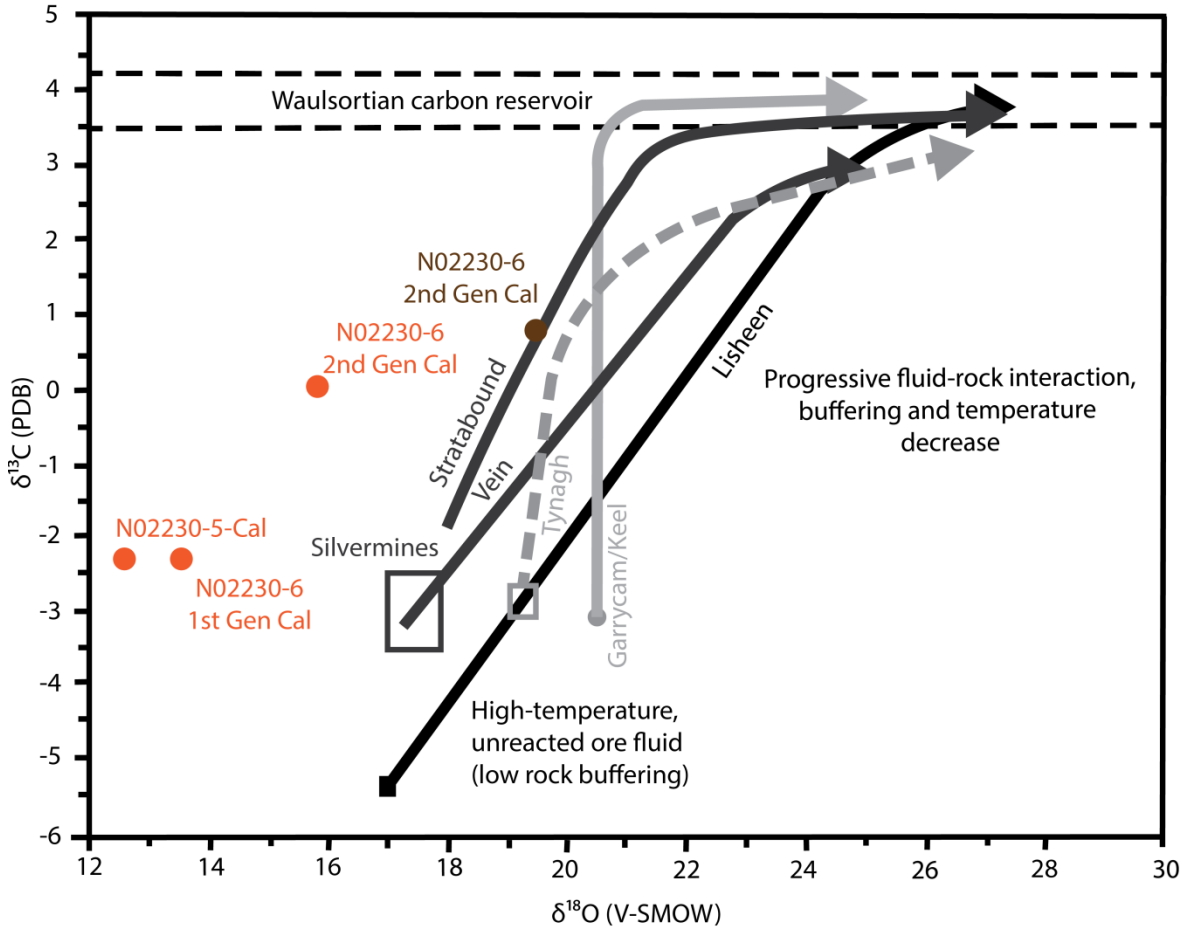

Figure 7.4 – $\delta^{18}O$ - $\delta^{13}C$ trajectory lines for hydrothermal carbonates from Silvermines, Tynagh, Lisheen and Garrycam-Keel with N02230 carbonate points. Very low $\delta^{18}O$ - $\delta^{13}C$ values are obtained from "feeder zone"-proximal carbonates derived from a high temperature, low $\delta^{18}O$ - $\delta^{13}C$ fluid (high fluid-rock ratio). Trajectories reflect cooling temperature and increasing fluid-rock interaction as the hydrothermal fluids equilibrate with Waulsortian limestones. Plot modified from Hitzman and Beaty (1996) and data originally collated from Boast et al (1981), Dixon (1990) and Slowey et al (1995). N02230 calcites have even lower $\delta^{18}O$ than feeder zone hydrothermal carbonates in other Irish-type deposits, though are similar $\delta^{13}C$.

C-O isotope analysis of the hydrothermal dolomites that comprise the "dolomite plume" described by Rizzi (1992) have helped to shed light on the paragenetic relationship of stratal dolomites, the 5 Lens Dolomite and Main Mine mineralisation. Braithwaite and Rizzi (1997) constrained respective 5 Lens Dolomites $\delta^{18}O_{V\text{-}SMOW}$ and $\delta^{13}C_{V\text{-}PDB}$ of - 6.6 to - 10.4‰, and 1.3 to 2.9‰ from gross sampling, while fluid inclusion analysis yielded a respective T_h range of 82.6-159.3^{o}C. This was interpreted to be consistent with a heated Carboniferous seawater source, and one that became hotter through time (I.e. corresponding increasing T_h and decreasing $\delta^{18}O$ values). Ashton et al (2015) interprets the C-O compositions of 5 Lens and stratal dolomites to result from an evolving system, where a moderate temperature, low $\delta^{13}C$- $\delta^{18}O$ hydrothermal fluid of constant temperature and composition equilibrated with the Pale Beds sequence and *in-situ* pore waters. An initial negative shift in $\delta^{18}O$ and increasingly negative trend in $\delta^{13}C$ was produced by isotope exchange with a hydrothermal fluid of constant C-O and temperature as a function of variable water/rock ratio. Higher $\delta^{18}O$ values obtained from the 5 Lens and stratal dolomites are suggested to derive from interaction with initially high $\delta^{18}O$ fluids or CO_2, greater cooling (I.e. lower temperature fluids than those that produced paragenetically later, low $\delta^{18}O$ carbonates), or interaction with pore waters.

This study finds that 5 Lens Dolomites obtained from the A-C Transects show that $\delta^{18}O$ - $\delta^{13}C$ is seemingly independent of geographical distribution along transect. One C-O isotope value for the stratal dolomite in drillhole N02230 coincides with the Main Mine stratal dolomite field produced from datas by Braithwaite and Rizzi (1997), while another has similar $\delta^{13}C$, though $\delta^{18}O$ is 0.5‰ lower. The $\delta^{18}O$ - $\delta^{13}C$ composition of 5 Lens Dolomites is random, and does not exhibit a geographical distribution along the transects. The 5 Lens Dolomites show two distinct $\delta^{18}O$ - $\delta^{13}C$ populations – those that coincide with the 5 Lens Dolomite field constrained by the datas from Braithwaite and Rizzi (1997), and those that have similar $\delta^{13}C$ though typically have $\delta^{18}O$ values 0.5-1‰ lower than the 5 Lens Dolomite field. This is an observation that is true of the majority of 5 Lens Dolomite sample from the A-C transects, though one A2 Transect 5 Lens Dolomite sample has a significantly higher $\delta^{13}C$ value than the 5 Lens Dolomite field at 4.3‰, while sample N00849-2 has a significantly lower $\delta^{18}O$ value at 16.0‰. Dolomitisation is rare along the A1 Transect – The 5 Lens Dolomite is only observed in drillholes N02045 and N01628, while stratal dolomitisation is only observed in drillhole N02230, which may be suggestive of unidentified faulting further west. Two considerations need to be made when approaching these results and discussion:

1) The distance between drillholes along the A1 Transect is, on average, 160 metres. This provides a low resolution picture of dolomitisation west of the Randalstown Fault. Therefore, stratal dolomites may be more regionally widespread than is observed along the A1 Transect.
2) C-O analysis was obtained from dolomite powders produced by drilling (I.e. gross sampling). Under thin section microscopy, only one dolomitisation stage is observed (I.e. planar/non-planar carbonate replacement), though Rizzi (1992) identified that dolomites from three stages of dolomitisation using cathodoluminescence. This homogenisation of dolomite phases through gross sampling potentially affects the overall $\delta^{18}O$ - $\delta^{13}C$ of samples. Wilkinson et al (2003) noted from fluid inclusion thermometry that dolomitisation appears to become hotter through time – a characteristic that may be reflected in lower $\delta^{18}O$ with progress dolomite stages through time.

Given that 5 Lens Dolomite samples show two distinct $\delta^{18}O$ - $\delta^{13}C$ value clusters, we might expect that this occurs due to the spatial distribution of dolomites close to major normal faults – I.e. dolomites that have low $\delta^{18}O$ may reflect precipitation from a higher temperature parental fluid, while those with higher $\delta^{18}O$ reflect greater degrees of fluid cooling. If we assume that the highest temperature dolomitising fluids were likely concentrated close to interpreted normal fault zones and lower temperature, higher $\delta^{18}O$ fluids extended laterally from fault zones, we would expect hope that this behaviour is observed along the A2 and B Transects. This may be observed in low $\delta^{18}O$ in samples N00862-4 (L Fault-proximal) and N00980-3 (E Fault-proximal), while higher $\delta^{18}O$ in sample N01033-1 may indicate dolomitisation resulted from a cooler fluid (I.e. one that has migrated away from the early-forming normal faults), though sample N00853-4 is unusual in that it has notably higher $\delta^{18}O$. Additionally, if we assumed that Randalstown Fault hanging-wall 5 Lens Dolomites are temporally related to the dolomite plume, we would expect to find that the dolomitising fluid originated from the early forming normal faults along the Main Orebody and migrated west. This would result in the 5 Lens Dolomite from drillhole N01628 (R Fault-proximal) to have lower $\delta^{18}O$, while the 5 Lens Dolomite from drillhole N02230 would have much higher $\delta^{18}O$, the inverse of which is observed. Additionally, the stratal dolomite from the 3-Lens Equivalent of drillhole N02230 coincides with the stratal dolomite field and has similar to $\delta^{18}O$ to the N02230 5 Lens Dolomite sample. These lower $\delta^{18}O$ values than that observed in N01628 may suggest that an unidentified fault is positioned in western Navan, and may have delivered hotter dolomitising fluids responsible for stratal and 5 Lens Dolomites in drillhole N02230.

Late-stage calcite that cross-cuts, brecciates and transports minor cpy-Qtz(-barite) veining have very low $\delta^{13}C_{V\text{-}PCB}$ and $\delta^{18}O_{V\text{-}SMOW}$ values (Fig 6.22). Hitzman and Beaty (1996) identified that hydrothermal carbonates deposited close to feeder zones at Silvermines, Lisheen, Tynagh and Garrycam-Keel contain very low initial $\delta^{18}O$ - $\delta^{13}C$. This behaviour is interpreted to represent crystallisation from a high-temperature, Waulsortian limestone-unbuffered hydrothermal fluid (I.e. a high fluid/rock ratio). Steadily increasing $\delta^{18}O$ - $\delta^{13}C$ towards Waulsortian Limestone-normative $\delta^{13}C$ (+4) reflects decreasing temperature coupled with increasing fluid-rock interaction. The profile of the model curve reflects fluid-rock interaction, where steep profiles indicate a low fluid/rock ratio (I.e. a small amount of hydrothermal fluid isotopically equilibrating with Waulsortian Limestone), while shallow gradients are suggestive of a much higher fluid-rock ratio (I.e. a high fluid volume equilibrating with the host rock).

Fluid inclusion analysis for late-stage calcite and saddle dolomite constrain a homogenisation temperature range of 101-165^{o}C (Fig 6.21, 7.6). This is below that of feeder zone carbonates in the higher temperature, Waulsortian Limestone-hosted Irish-types (e.g. Samson and Russell, 1987, Hitzman and Beaty, 1996), Wilkinson et al, 2005A, Wilkinson, 2010). Assuming a range of 101-165^{o}C, the hydrothermal fluid can be modelled to $\delta^{18}O$ range of -4.4 to 4.4‰, respectively (Fig 7.6) - values consistent with a surface fluid source (Sheppard, 1986). Late-stage calcites in drillhole First and second generation late-stage calcites in drillhole N02230 have very low $\delta^{13}C$ (Fig 6.23, Table 6.8) at -2.2 to -2.1‰, and 0.15‰, respectively. Very low $\delta^{13}C$ in meteoric water can be produced by interaction with low $\delta^{13}C$ organic matter (Wright et al, 2004), though the stratigraphy of drillhole N02230 is notably shale, silt and argillite poor. One potential source for organic matter may be the overlying Shaley Pales, Argillaceous Bioclastic Limestone and Upper Dark Limestone facies – limestones interbedded by thickly bedded shale horizons (e.g. Philcox, 1984, Altinok, 2005). If we assume that the salinities constrained in fluid inclusions from hangingwall hydrothermal fluid resulted from the fluid gaining the salinity of *in-situ*, saline pore waters during transit (discussed in section 6.2), this explanation may also be applied to down-welling meteoric waters. Cross-cutting relations suggests that calcite-dolomite post-dates chalcopyrite mineralisation. Therefore, $\delta^{13}C$ - $\delta^{18}O$ values that constrain a meteoric fluid source suggest that calcite veining occurred post-re-emergence and may have resulted from a fluid modified by down-welling surface fluids.

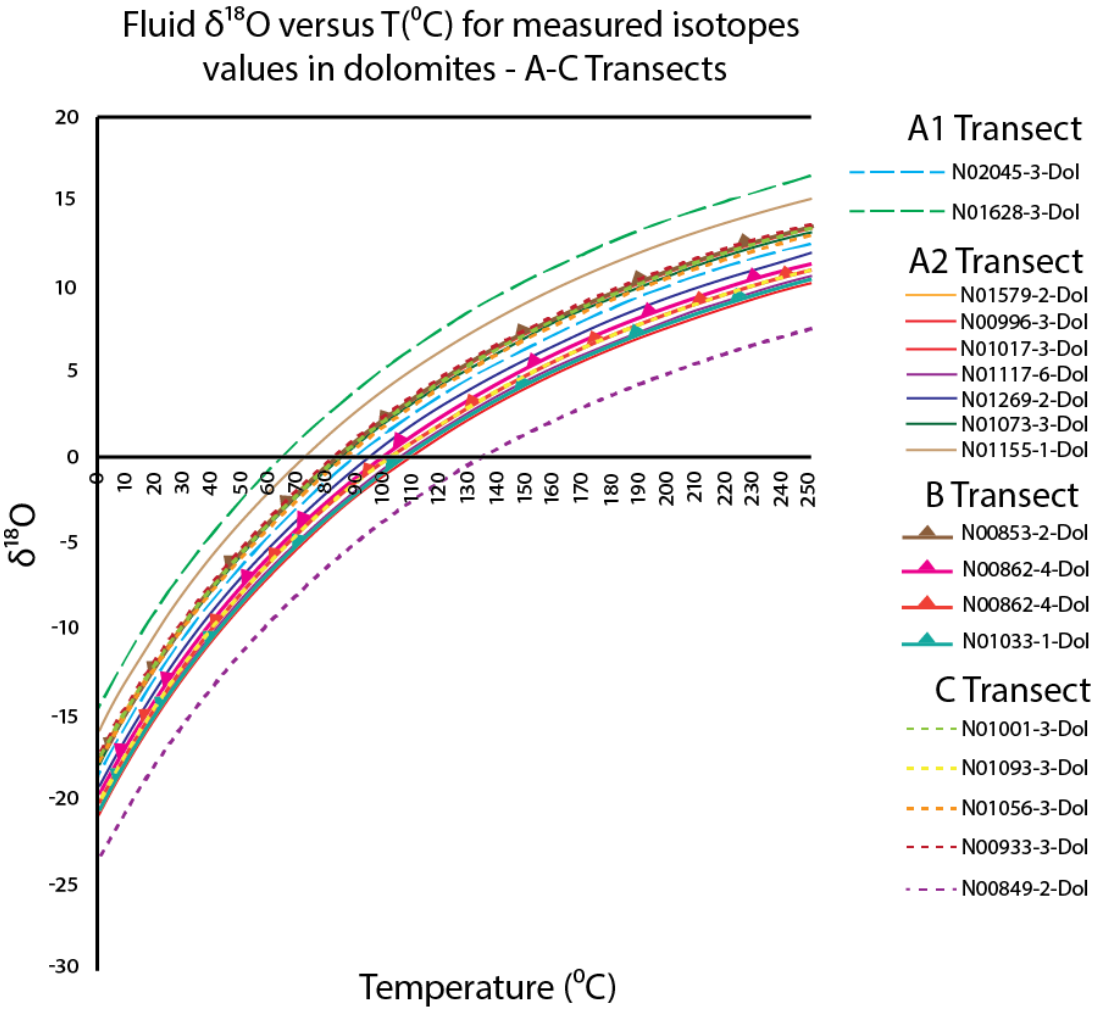

Figure 7.5 - $\delta^{18}O$ over temperature plot showing calculated $\delta^{18}O$ isotope composition of A-C Transect dolomitising fluid at 0-250°C.

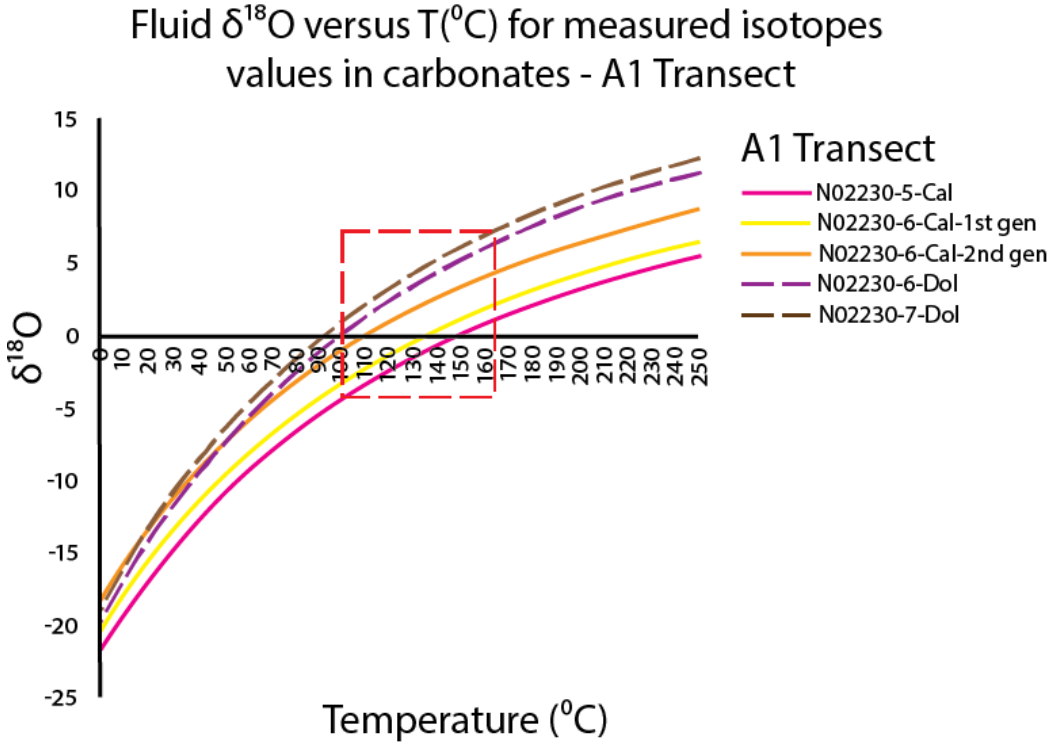

Figure 7.6 - $\delta^{18}O$ over temperature plot showing possible O isotope composition of A1 Transect calcites and dolomites at 0-250°C. The dashed red line represents the homogenisation temperature range constrained by fluid inclusion analysis of calcites and

Chapter 8

Concluding remarks and implications for exploration

Chapter 8 summarises this study's findings and outlines its potential exploration implications

8. **Concluding remarks:**

Sphalerite and galena in the hangingwall of the Randalstown Fault is paragenetically linked to the Main Mine. The Zn/Pb ratio was controlled by the availability of bacteriogenic sulphur and does not indicate a nearby, unidentified feeder zone. Marks (2015) interpreted galena prevalence in the northwest transect as resulting from a low bacteriogenic sulphur budget - consistent with the observations of this study. Lead, being less soluble in a hydrothermal fluid precipitates first with minor sphalerite, followed by minor replacive sphalerite, suggesting that available bacteriogenic sulphur was depleted before sufficient sphalerite could crystallise. The dominance of hydrothermal sulphur in the hangingwall corroborates this, and can explain why low Zn/Pb is identified immediately southwest of the 5 Lens cutoff near the B and T Faults, though does not point to a feeder in the Randalstown Fault hangingwall. Bacteriogenically sulphur-enriched hypersaline brines accumulated in the topographic lows of the extensional basin and mixed with metalliferous hydrothermal fluids upwelling from a normal fault relay ramp system (Ashton et al, 2015). There are three significant reasons why feeder zone potential, or the possibility to produce high-grade ore, is low in western Navan:

- An insufficient secondary porosity network for efficient hydrothermal fluid upwelling and brine downwelling. Extensional faulting and fracturing associated with mineralisation are primarily concentrated between the early-forming L and E Faults, interpreted to form a fault terrace (Ashton et al, 2015).

- The Erosion Surface is poorly developed in the western Navan area. Slope collapse in the Lower Carboniferous is considered essential to allowing open access by hydrothermal fluids to the sea floor. The Erosion Surface in the Main Mine down-cuts into the Pale Beds, while the Boulder Conglomerate is interpreted to have originally controlled the development of sulphur-enriched brine pools and focussed low pore pressure zones in

the underlying Pale Beds (Davidheiser-Kroll, 2014). Absence of the Erosion Surface in western Navan likely determined availability (or lack thereof) of bacteriogenic sulphur, as well limited lateral hydrothermal fluid flow. Alternatively,

- The western Navan geology is cleaner and less argillaceous than the Main Mine geological sequence. Calcisiltite marker horizons that define the upper and lower limits of each ore lens are mostly absent from the sequence, while the 5 Lens Dolomite are only observed in drillholes N02045 and N01628. Additionally, stratal dolomite is only observed in drillhole N02230. These are important aquitards that dominantly focused mineralising fluids to migrate laterally in the Main Orebody (e.g. Anderson, 1998, Ashton et al, 2015). Absence of impermeable lithologies, therefore, may have allowed free vertical migration of hydrothermal fluids, producing broad, low-grade mineralisation. Low Zn/Pb in the 4/5 Lenses were likely produced from the migrating hydrothermal deposit depositing galena in the lower Pale Beds. This was followed by vertical migration of the now Pb-depleted ore fluid depositing minor sphalerite in the 0-3 Lenses.

Textural evidence of sulphides from the Randalstown Fault hangingwall, footwall and Main Mine sulphides point to a similar paragenesis (Fig 5.21, 5.23, 5.27), suggesting that Randalstown Fault hangingwall mineralisation was likely produced from the same fluid as Navan ore. Results corroborate with Marks' (2015) "epigenetic halo", identifying that mineralisation is related to the Main Mine mineralisation event, though bacteriogenic sulphur was absent, preventing high-grade ore from developing. Either a lack of access to bacteriogenic sulphur (I.e. that brines were present on the seafloor but could not downwell effectively), or the absence of bacteriogenic sulphur from the system entirely contributed to the low ore-grade and low Zn/Pb ratio observed. 5 Lens Dolomite and stratal dolomite occurrences west of the Randalstown Fault, with broadly similar does not disprove the presence of an underlying feeder zone in western Navan, but without bacteriogenic sulphur to mix with upwelling hydrothermal fluids high-grade ore will not develop.

Cpy-Qtz(-barite) mineralisation in drillhole N02230 is of more interest. It is paragenetically separate from Navan ore, developing from a separate hydrothermal fluid and comprises a mineral assemblage not observed in the Main Mine. Mineralisation is unusual in that sulphide almost exclusively comprises chalcopyrite with minor marcasite. Limited analysis of two-phase inclusions in quartz yields a respective homogenisation temperature and salinity range of 193-223^{o}C, and 19-22.5 wt.% NaCl, while monophase inclusions constrain a wider salinity range of 10.2-22.5 wt.% NaCl. Assuming that these values are accurate and representative of the mineralising fluid, they point to a higher temperature regime similar to the one constrained by Treloar (2014) in SWEX-S

and other Waulsortian-hosted Irish-types (e.g. Taylor, 1984, Banks and Russell, 2002, Wilkinson, 2003). These results point to a potentially higher temperature mineralising system (Fig 7.3).

8.1. Implications for exploration:

This report builds on the findings of Davidheiser-Kroll (2014) and Marks (2015) and concludes that the low Zn/Pb areas of mineralisation identified southwest of the Main Mine and in the hangingwall of the Randalstown Fault were ultimately controlled by the same factor – the absence of bacteriogenic sulphur. Low Zn/Pb mineralisation in the Randalstown Fault hangingwall is of low economic interest and is not predictive of a feeder zone. However, cpy-Qtz(-barite) veining is of significantly more interest, and may point to a deeper, hotter mineralisation system west of drillhole N02230.

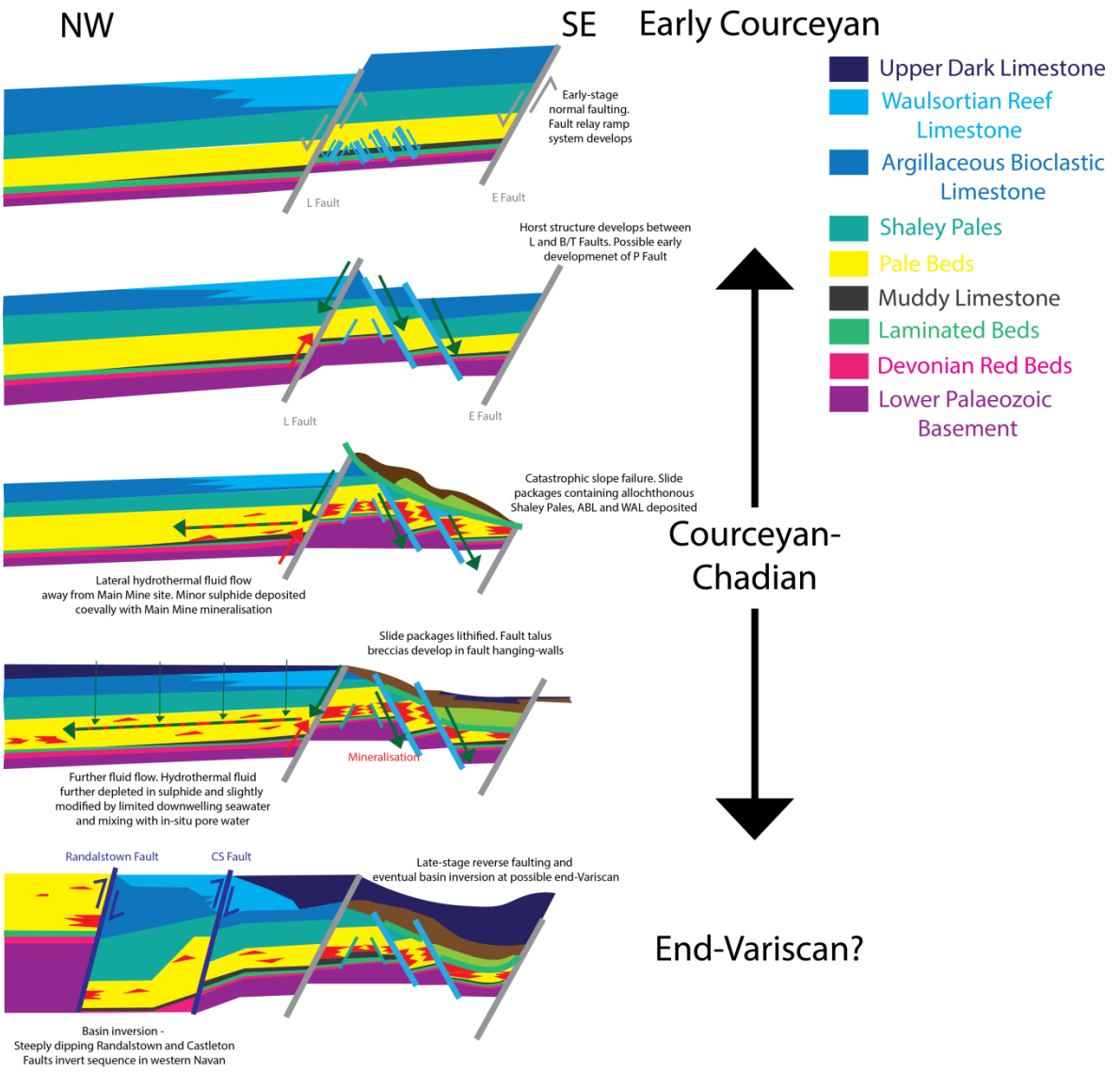

Figure 8.1 – Genetic model for lateral hydrothermal fluid flow (modified from Ashton et al, 2015) responsible for mineralisation in the Randalstown Fault hangingwall. Hydrothermal fluids upwelled from extending normal faults in the Lower Palaeozoic basement and dominantly mixed with bacteriogenic brines in the fault relay systems between the L and E Faults. Limited lateral migration of hydrothermal fluids is produced by low secondary porosity and high pore pressure produced by overlying Argillaceous Bioclastic Limestone and Waulsortian Limestone sequences

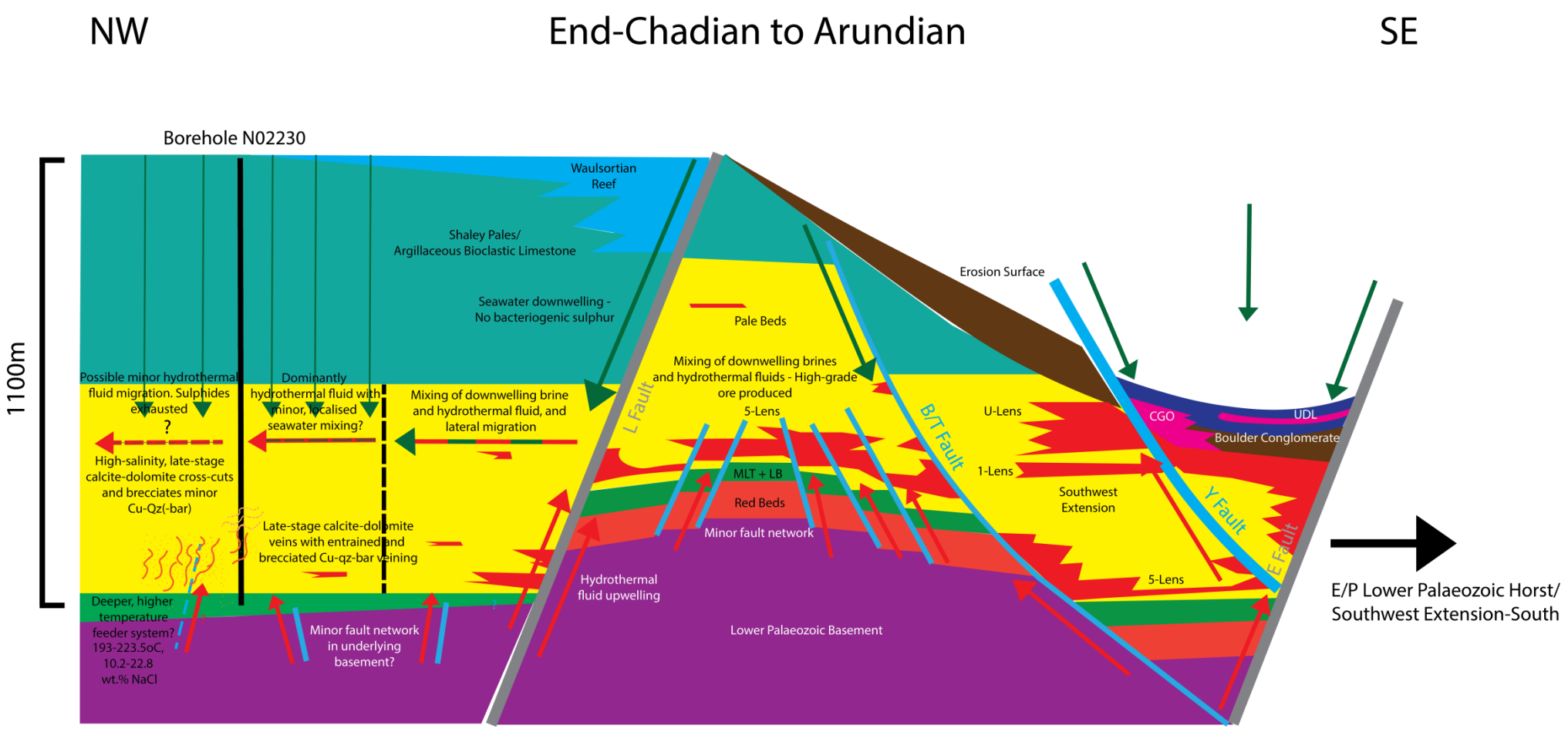

Figure 8.2 – Cartoon diagram for proposed for low Zn/Pb and cpy-Qtz(-barite) veining in western Navan. This model draws heavily on the existing model provided by Ashton et al (2015), and Marks (2015) epigenetic halo model. Hydrothermal fluids migrated along the Liscarton (L) Fault, mixed with bacteriogenic sulphur-deficient brines, and laterally migrated. Migrating fluids mixed with limited, down-welling evaporated seawater and/or in-situ saline pore water. Cpy-Qtz(-barite) formed separately from Navan and hangingwall Zn-Pb, and may be an expression of a deeper, hotter system

9. References:

ALTINOK, E. 2005. Zn-Pb-Fe Mineralization Process, Evolution of Sea Water Oxidation State in a Restricted Basin, and Diagenesis of Deep Water Calcareous Sediments: Geochemical and Geological Study of the Navan Deposit, Dublin Basin, Ireland. Ph. D, Colorado School of Mines, In: Davidheiser-Kroll, B.J. 2014. Understanding the fluid pathways that control the Navan ore body, *Ph.D thesis, University of Glasgow*, 232 p.

ANDERSON, G. M. 1975. Precipitation of Mississippi Valley-type ores. *Economic Geology*, 70, 937-942.

ANDERSON, G.M. & MACQUEEN, R.W. 1982, Ore deposit models-6. Mississippi Valley-type lead-zinc deposits: *Geoscience Canada*, 9, 107-117.

ANDERSON, I. K., ANDREW, C. J., ASHTON, J. H., BOYCE, A. J., CAULFIELD, J. B. D., FALLICK, A. E. & RUSSELL, M. J. 1989. Preliminary sulphur isotope data of diagenetic and vein sulphides in the Lower Paleozoic strata of Ireland and southern Scotland: implications for Zn + Pb +Ba mineralization. *Journal of the Geological Society, London*, 146, 715-720.

ANDERSON, I. K. 1990. Ore depositional processes in the formation of the Navan zinc/lead deposit, Co. Meath, Ireland. *Ph. D, The University of Strathclyde*.

ANDERSON, I.K, ASHTON., J.H, BOYCE, A.J., FALLICK, A.E., & RUSSELL, M.J., 1998. Ore Depositional processes in the Navan Zn-Pb deposit, *Ireland. Economic Geology*, 93, 535-563.

ANDREW, C. J. & ASHTON, J. H. 1982. Mineral textures; metal zoning and ore environment of the Navan orebody, Co. Meath, Ireland.

ANDREW, C.J. AND ASHTON, J.H. 1985. The regional setting, geology and metal

distribution patterns of the Navan orebody, Ireland. *Trans. Instn Min. Metall.* (Sect B: Appl. Earth Sci.), 94, 66-93.

ANDREW, C.J. 1986, A diagrammatic representation of the Courceyan stratigraphy of the Irish Midlands. In: Andrew, C.J., Crowe, R.W.A., Finlay, S., Pennell, W.M. and Pyne, J.F., Eds., *Geology and Genesis of Mineral Deposits in Ireland. IAEG, Dublin*, p. 239.

ASHTON, J.H. 2016. Re: *Written communication*

ASHTON, J. H., HOLDSTOCK, M. P., GERAGHTY, J. F., O'KEEFE, W. G., MARTINEZ, N., PEACE, W. & PHILCOX, M. E. 2003.. The Navan Orebody - Discovery and Geology of the South West Extension. In: Kelly, J.G., Andrew, C.J et al. *Europe's Major Base Metal Deposits. IAEG, Dublin*, 405-430.

ASHTON, J. H., BLAKEMAN, R. J., GERAGHTY, J. F., BEACH, A., COLLER, D., PHILCOX, M. E., BOYCE, A. J. & WILKINSON, J. J.. The Giant Navan Carbonate-Hosted Zn-Pb Deposit – *A Review, Irish Association for Economic Geology – Current Perspectives on Zinc Deposits*, 85-122.

BANKS, D.A. & RUSSELL, M.J. 1992. Fluid mixing during ore deposition at the Tynagh base-metal deposit, Ireland: *European Journal of Mineralogy*, 4, 921-931

BANKS, D.A., BOYCE, A.J, & SAMSON, I.M. 2002. Constraints on the origins of fluids forming Irish Zn-Pb-Ba deposits: Evidence from the composition of fluid inclusions. *Economic Geology*, 97, 441-480.

BEAMISH, D & SMYTH, D.K. 1986. Geophysical images of the deep crust: the Iapetus suture, *Journal of the Geological Society*, London, 143, 489-497.

BLAKEMAN, R.J. 2002. The Compositions and routes of the fluids generating the Navan giant base-metal orebody. *Unpublished PhD thesis, University of Glasgow,* 207 p.

BLAKEMAN, R. J., ASHTON, J. H., BOYCE, A. J., FALLICK, A. E. & RUSSELL, M. J.. 2002. Timing of Interplay between Hydrothermal and Surface Fluids in the Navan Zn+Pb Orebody, Ireland: Evidence from Metal Distribution Trends, Mineral Textures, and $\delta^{34}S$ Analyses, *Economic Geology*, 97, 73-91

BLAKEMAN, R.J. 2015. Re: Spoken communication.

BLANEY, D. & REDMOND, P. 2010. The Limerick Basin - an important emerging sub-district of the Irish Orefield, In Archibald, S.M. (Ed.) Proc. of Zinc 2010 Meeting, Cork, Irish *Association for Economic Geology,* 103-108.

BLYTH, H. 2016. Trace element zonation in sulphides at the Navan Zn-Pb deposit, Ireland: Controls on distribution and implications for exploration and recovery, *MSCi, University of Southampton.*

BOAST, A. M., COLEMAN, M. L. & HALLS, C. 1981a, Textural and stable isotopic evidence for the genesis of the Tynagh base metal deposit, Ireland, *Economic Geology*, 76, 27-55.

BODNAR, R.J. 2003. Introduction to aqueous fluid systems, In SAMSON, I, ANDERSON, A & MARSHALL, D, eds. Fluid Inclusions: Analysis and Interpretation. Mineral. Assoc. Canada, Short Course 32, 81-99.

BODNAR, R.J & VITYK, M.O (1994). Interpretation of microthermometric data for H_2O-NaCl fluid inclusions, *in* Fluid Inclusions in Minerals, Methods and Applications, DE VIVO, B & FREZZOTTI, M.L, eds, Virginia Tech, Blacksburg, VA, 117-130.

BOYCE, A.J, 1990. Sedimentation, exhalation, and sulphur isotope geochemistry of the Silvermines Zn + Pb + Ba deposits, County Tipperary, Ireland, *Unpublished Ph.D. thesis, University of Strathclyde*, 355 p.

BOYCE, A.J. 2015. Re: Spoken communication.

BOYCE, A.J., ANDERTON, R., & RUSSELL, M.J. 1983A. Rapid subsidence and early Carboniferous mineralisation in Ireland. Trans, *Instn Min. Metall. (Sect. B, Appl. Earth Sci.),* 92, 55-66.

BOYCE, A. J., COLEMAN., M. L. & RUSSELL., M. J. 1983b. Formation of fossil hydrothermal chimneys and mounds from Silvermines, Ireland. *Nature,* 306**,** 545-550.

BOYCE, A.J., FALLICK, A.E., FLETCHER, T.J., RUSSELL, M.J., AND ASHTON, J.H, 1994, Detailed sulphur isotope studies of Lower Palaeozoic-hosted pyrite below the giant Navan Zn + Pb mine, Ireland: Evidence of mass transport of crustal S to a sediment-hosted deposit: *Mineralogical Magazine*, 58A, 109–110.

BOYCE, A.J., LITTLE, C.T.S., & RUSSELL, M.J. 2003. A new fossil vent biota in the Ballynoe barite deposit, Silvermines, Ireland: Evidence for intracratonic sea-floor hydrothermal activity about 352 Ma. *Economic Geology and the Bulletin of the Society of Economic Geologists*, 98(3), pp. 649-656.

CARNE, R.C, & CATHRO, R.J. 1982, Sedimentary exhalative (sedex) zinc-lead-silver deposits, northern Canadian Cordillera: *CIM Bulletin*, 1974,, 75, 66–78.

COOMER, P.G. & ROBINSON, B.W. 1976. Sulphur and sulphate-oxygen isotopes and the origin of the Silvermines deposits, Ireland: Mineralium Deposita, v11, 155-169, In: HITZMAN, M.W. & BEATY, D.W. 1996. The Irish Zn-Pb(-Ba) orefield, in Sangster, D.F, ed, Carbonate-hosted lead-zinc deposits: Society of Economic Geologists*, Special Publication 4*, 112-143.

DAVIDHEISER-KROLL, B.J., BOYCE, A.J., ASHTON, J.H., BLAKEMAN, R & GERAGHTY, J. 2013. How did it get there? Searching for “the feeder” at the Navan Zn + Pb deposit, Ireland. Abstract. In ERIK JONNSON ET AL, (Eds). Mineral Deposit Research for a Hi- Tech World. *Proceedings of the 12th Biennial SGA Meeting, Uppsala, 1*, 616-619.

DAVIDHEISER-KROLL, B.J. 2014. Understanding the fluid pathways that control the Navan ore body, *Ph.D thesis, University of Glasgow,* 232 p.

DAVIDHEISER-KROLL. 2015. Re. Personal communication.

DIXON, P.R., LEHURAY, A.P & RYE, D.M. 1990. Basement geology and tectonic evolution of Ireland as deduced from Pb isotopes. *Journal of the Geological Society,* London, 147, 121-132.

ELLIOT, H. A., GERNON, T. M., ROBERTS, S. & REDMOND, P. B.. 2013. Diatreme volcanism facilitating PbZn mineralization in the Irish Orefield? *Volcanic and Magmatic Studies Group of the Geological Society*.

EMSBO, P. 2009. Geologic Criteria for the Assessment of Sedimentary Exhalative (Sedex) Zn-Pb-Ag Deposits, U.S Geological Survey, *Open-File Report 2009-1209*.

EVERETT, C. E., WILKINSON, J. J. & RYE, D. M. 1999. Fracture-controlled fluid flow in the Lower Palaeozoic basement rocks of Ireland: implications for the genesis of Irish-type Zn-Pb deposits. *Geological Society, London, Special Publications,* 155**,** 247-276.

EVERETT, C. E., RYE, D. M. & ELLAM, R. M. 2003. Source or Sink? An Assessment of the Role of the Old Red Sandstone in the Genesis of the Irish Zn-Pb Deposits. Economic Geology, 98, 31-50.

EYRE, S.L. 1998. Geochemistry of dolomitization and Zn-Pb mineralization in the Rathdowney Trend, Ireland. *PhD Thesis, University of London,* 414 p, In: WILKINSON, J.J. 2003. On diagenesis, dolomitisation and mineralisation in the Irish Zn–Pb orefield. *Mineralium Deposita*, 38, 968-983

FALLICK, A.E., ASHTON, J.H., BOYCE, A.J., ELLAM, R.M. AND RUSSELL, M.J., 2001, Bacteria were responsible for the magnitude of the world-class hydrothermal base metal sulfide orebody at Navan, Ireland. *Economic Geology*, 96, 885-890.

FORD, C.V. 1996. The integration of petrologic and isotopic data from the Boulder Conglomerate to determine the age of the Navan orebody, Ireland. *Unpublished PhD thesis, University of Glasgow*, 176 p.

GEOLOGICAL SURVEY OF IRELAND

GERAGHTY, M & MCCONNELL, B. 1999, Bedrock geology 1:100,000 scale map series, sheet 13, Meath. Geological Survey of Ireland, In: Ashton, J.H, Blakeman, R.J et al .2015. The Giant Navan Carbonate-Hosted Zn-Pb Deposit – *A Review, Irish Association for Economic Geology – Current Perspectives on Zinc Deposits*, 85-122.

GOODFELLOW, W.D. 1987. Anoxic stratified oceans a source of sulphur is sediment-hosted stratiform Zn-Pb deposits (Selwyn Basin, Yukon, Canada), *Chemical Geology*, 65, 359–382.

GOODFELLOW, W.D & LYDON, J.W. 2007. Sedimentary exhalative (SEDEX) deposits

GOODFELLOW, W.D., LYDON, J.W., & TURNER, R.J.W. 1993. Geology and genesis of stratiform sediment-hosted (SEDEX) zinc-lead-silver sulphide deposits: *Geological Association of Canada Special Paper* 40, 201–251.

GRAHAM, R.A. 1970. The Mogul base-metal deposits, Co. Tipperary, Ireland: Unpublished Ph.D thesis, University of Western Ontario, 235 p, In: Taylor, S. 1984. Structural and paleotopographical controls of lead-zinc mineralization in the Silvermines ore bodies, Republic of Ireland: *Economic Geology*, 79, 529–548

HANOR, J. S. and MCINTOSH, J. C. 2007. Diverse origins and timing of formation of basinal brines in the Gulf of Mexico sedimentary basin. *Geofluids* 7, 227-237

HEYL, A.V. 1983. Geologic characteristics of three Mississippi Valley-Type districts, In: United States Geological Survey. 2010. A Deposit Model for Mississippi Valley-Type Lead-Zinc

Ores, Chapter A of Mineral Deposit Models for Mineral Resource Assessment, *Scientific Investigations Report 2010-5070-A.*

HITZMAN, M.W. 1995. Mineralization in the Irish Zn-Pb-(Ba-Ag) orefield, In: WILKINSON, J.J. 2003. On diagenesis, dolomitisation and mineralisation in the Irish Zn–Pb orefield. *Mineralium Deposita*, 38, 968-983.

HITZMAN, M. W. 1999. Extensional faults that localize Irish syndiagenetic Zn-Pb deposits and their reactivation during Variscan compression. *Geological Society of London, Special Publications*, 155, 233-245.

HITZMAN, M. W. & LARGE, D. 1986. A review and classification of the Irish carbonate-hosted base metal deposits, in Andrew, C. J., Crowe, R. W. A., Finlay, S., Pennell, W. M., and Pyne, J. F., eds., *Geology and Genesis of Mineral Deposits in Ireland: Dublin, Irish Association for Economic Geology,* 217-238.

HITZMAN, M.W. & BEATY, D.W. 1996. The Irish Zn-Pb(-Ba) orefield, in Sangster, D.F, ed, Carbonate-hosted lead-zinc deposits: *Society of Economic Geologists, Special Publication 4*, 112-143.

HITZMAN, M.W, REDMOND, P.B. & BEATY, D.W. 2002. The carbonate-hosted Lisheen Zn-Pb-Ag deposit, County Tipperary, Ireland. *Economic Geology*, 97, 1627-1655.

HOEFS, J. 2015. Stable Isotope Geochemistry, *Seventh Edition, Springer*.

HOLLIS, S.P., ROBERTS, S., EARLS, G., HERRINGTON, R., COOPER, M.R., PIERCEY, S.J., ARCHIBALD, S.M & MOLONEY, M. 2014. Petrochemistry and hydrothermal alteration within the Tyrone Igneous Complex, Northern Ireland: implications for VMS mineralization in the British and Irish Caledonides, *Mineralium Deposita*, 49, 575-593.

JOHNSTON, J. D. 1999. Regional fluid flow and the genesis of Irish Carboniferous base metal deposits. *Mineralium Deposita,* 34**,** 571-598.

KELLEY, K.D., SEAL, R.R.II., SCHMIDT, J.M., HOOVER, D.B & KLEIN, D.P. 1986. Sedimentary Exhalative Zn-Pb-Ag Deposits, *U.S Geological Survey*.

KENNAN, P.S. 1978. The Origin of the Sulphide Deposits in the Leinster Granite, *Journal of Earth Sciences*, 1, 41-47.

KINNAIRD, J.A., IXER, R.A., BARREIRO, B & NEX P A.M. 2002. Contrasting sources for lead in Cpy-polymetallic and Zn–Pb mineralisation in Ireland: constraints from lead isotopes, *Mineralium Deposita*, 37, 495-511.

KNIGHT, H. 2012. Seeking The deep fluid feeder zone of the Navan Zn-Pb deposit, Republic of Ireland. *Unpublished MSci thesis, Imperial College*, 44 p, In: Ashton, J.H, Blakeman, R.J et al. 2015. The Giant Navan Carbonate-Hosted Zn-Pb Deposit – *A Review, Irish Association for Economic Geology – Current Perspectives on Zinc Deposits, 85-122.*

LARGE, D. & WALCHER, E 1999. The Rammelsberg massive sulphide Cpy-Zn-Pb-Ba-Deposit, Germany: an example of sediment-hosted, massive sulphide mineralisation. *Mineralium Deposita*, 34, 522-538.

LEACH, D.L., VIETS, J.B., Ayuso, N.F & Klein, D.P. 1986. Mississippi Valley-Type Pb-Zn Deposits, U.S Geological Survey.

LEACH, D.L, & SANGSTER, D.F. 1993, Mississippi Valley-type lead-zinc deposits*: Geological Association of Canada Special Paper 40*, 289–314.

LEACH D.L., BRADLEY D., LEWCHUK, M.T., SYMONS, D.T., DE MARSILY, G & BRANNON, J. 2003. Mississippi Valley-type lead-zinc deposits through geological time: inplications from recent age-dating research. *Mineral Deposits*, 36, 711–740

LEACH, D., SANGSTER, D., KELLEY, K., LARGE, R. R., GARVEN, G., ALLEN, C., GUTZMER, J. &

WALTERS, S. 2005. Sediment-hosted lead-zinc deposits: A global perspective. *Economic Geology,* 100**,** 561-607.

LEACH, D.L., TAYLOR, R.D., FEY, D.L., DIEHL, S.F. & SALTUS, R.W. 2010. A deposit model for Mississippi Valley-Type lead-zinc ores, chap. A of Mineral deposit models for resource assessment: *U.S. Geological Survey Scientific Investigations Report 2010–5070–A*, 52 p.

LEE, M.J. & WILKINSON, J.J. 2002. Cementation, hydrothermal alteration, and Zn-Pb mineralization of carbonate breccias in the Irish Midlands: textural evidence from the Cooleen Zone, near Silvermines, County Tipperary. *Economic Geology*, 97, p. 653-662.

LOWENSTEIN, T. K, HARDIE, L. A., TIMOFEFF, M. N, & DEMICCO, R. V., 2003. Secular variation in seawater chemistry and the origin of calcium chloride basinal brines. *Geology,* 31, 857- 860.

LYONS, T.W, GELLATLY, A.M., MCGOLDRICK, P.J & KAH, L.C. 2006. Proterozoic sedimentary exhalative (SEDEX) deposits and links to evolving global ocean chemistry, *Geological Society of America, Memoir 198,* 169-184

MARKS, F.R. 2015. Re: Personal communication.

MARKS, F.R. 2015. Remote Detection of Irish-type Orebodies: An Investigation of the Navan Halo. *Unpublished Ph.D Thesis, University College Dublin*, 266. p

MCCONNELL, B., PHILCOX, M. & GERAGHTY, M. 2001. Geology of Meath, A geological description to accompany the bedrock geology 1:100,000 scale map series, sheet 13, Meath. Geological Survey of Ireland, 78 p, In: ASHTON, J. H., BLAKEMAN, R. J., GERAGHTY, J. F., BEACH, A., COLLER, D., PHILCOX, M. E., BOYCE, A. J. & WILKINSON, J. J.. The Giant Navan Carbonate-Hosted Zn-Pb Deposit – *A Review, Irish Association for Economic Geology – Current Perspectives on Zinc Deposits*, 85-122.

MEERE, P.A. 1995, Sub-greenschist facies metamorphism from the Variscides of SW Ireland: an early syn-extensional peak thermal event. *Journal of the Geological Society of London*, 152, 511-521, In: Wen, N, Boyce, A.J et al. 1996. The genesis of Cpy-bearing quartz veins by metamorphic remobilisation from stratiform red bed deposits, SW County Cork, Ireland, *Mineralogy and Petrology*, 57, 73-89.

MEERE, P.A & BANKS, D.A. 1997. Upper crustal fluid migration: an example from the Variscides of SW Ireland, *Journal of the Geological Society,* London, 154, 975-985.

MENZIE, W.D. & MOSIER, D.L. 1986. Grade and tonnage model of sedimentary exhalative Zn-Pb, in Cox, D.P, and Singer, D.A, eds, Mineral deposit models: *U.S. Geological Survey Bulletin 1693,* 212-215.

MILLS, H., HALLIDAY, A.N., ASHTON, J.H., ANDERSON, I.K. & RUSSELL, M.J. 1987. Origin of a giant orebody at Navan, Ireland. *Nature*, 327, 223-226.

MULHALL, C.M., BAKER, S, BOYCE. A.J & SEVASTOPULO, G.D. 2001. Regional dolomite at Newcastle West, Co. Limerick, Ireland and its implications for the models of fluid flow related to base-metal mineralization in Ireland, *GSA 2001*.

MURPHY, F.C., ANDERSON, T.B., DALY, J.S., GALLAGHER, V., GRAHAM, J.R., HARPER, D.A.T., JOHNSTON, J.D., KENNAN, J.S., KENNEDY, M.J., LONG, C.B., MORRIS, J.H ., O'KEEFFE, W.G., PARKES, M., RYAN, P.D., SLOAN, R.J., STILLMAN, C.J., TIETZSCH-TYLER, D., TODD, S.P & WRAFTER, J.P. 1991. An appraisal of Caledonian suspect terranes in Ireland. *Irish Journal of Earth Sciences*, 11-41.

PARADIS, S, HANNIGAN, P & DEWING, K. 2007. Mississippi Valley-Type Lead-Zinc Deposits (MVT), 1-15.

PEACE, W.M. 1999. Carbonate-hosted Zn-Pb mineralisation within the Upper Pale Beds at Navan, Ireland: *Unpublished Ph.D. thesis, University of Melbourne*, 284 p, ASHTON, J. H., BLAKEMAN, R. J., GERAGHTY, J. F., BEACH, A., COLLER, D., PHILCOX, M. E., BOYCE, A. J. & WILKINSON, J. J.. The Giant Navan Carbonate-Hosted Zn-Pb Deposit – *A Review, Irish Association for Economic Geology – Current Perspectives on Zinc Deposits*, 85-122.

PEACE, W.M. & WALLACE, M. 2000. Timing of mineralization at the Navan Zn-Pb deposit: A post-Arundian age for Irish mineralization. *Geology*, 28, 711-714.

PEACE, W. M., WALLACE, M. W., HOLDSTOCK, M. P. & ASHTON, J. H. 2003. Ore textures within the U lens of the Navan Zn-Pb deposit, Ireland. *Mineralium Deposita,* 38**,** 568-584.

PHILCOX, M.E. 1984. Lower Carboniferous lithostratigraphy of the Irish Midlands: Dublin, *Irish Association for Economic Geology, Special Publication*, 89

PHILCOX, M. E. 1989. The mid-Dinantian unconformity at Navan, Ireland. The role of tectonics in Devonian and Carboniferous sedimentation in the British Isles. *Yorkshire Geological Society,* Bradford, 67-81.

PHILLIPS, W.E & SEVASTOPULO, G.D. 1986. The structural and stratigraphic setting of Irish mineral deposits, In: ANDREW, C.J., CROWE, R.W.A., FINLAY, S., PENNELL, W.M., AND PYNE, , Geology and genesis of mineral deposits in Ireland: Dublin, *Irish Association for Economic Geology*, Economic Geology, 1–30.

PIRAJNO, F. 2009. Hydrothermal processes and mineral systems. *Springer Science + Business Media, Perth*, 781–809

PROBERT, K. 1983. Fluid inclusion data from carbonate hosted Irish base metal deposits [abstract]: *Mineral Deposits Studies Group Annual Meeting*, Programme with Abstracts, University of Manchester, In: ASHTON, J. H., BLAKEMAN, R. J., GERAGHTY, J. F., BEACH, A., COLLER, D., PHILCOX, M. E., BOYCE, A. J. & WILKINSON, J. J.. The Giant Navan Carbonate-Hosted Zn-Pb Deposit – *A Review, Irish Association for Economic Geology – Current Perspectives on Zinc Deposits*, 85-122.

RANDELL, R.N, AND ANDERSON, G.M. 1996. Geology of the Polaris Zn-Pb deposit and surrounding area, Canadian Arctic Archipelago, in Sangster, D.F, Carbonate-hosted lead-zinc deposits: *Society of Economic Geologists Special Publication, 4*, 307–319

RAO, C.K., JONES, A.G & MOORKAMP, M. 2007. The geometry of the Iapetus suture zone in central Ireland deduced from a magnetotelluric study*. Physics of the Earth and Planetary Interiors*, 161, 134-141.

REDMOND, P.B., 1991, The production of a complete NW strike section across the Navan orebody with a study of the stratigraphy, mineralization and diagenetic history across the section, accompanied by a study of mineralization in underground

exposure. *Unpublished BSc thesis, Trinity College Dublin*, 111 p, In: ASHTON, J. H., BLAKEMAN, R. J., GERAGHTY, J. F., BEACH, A., COLLER, D., PHILCOX, M. E., BOYCE, A. J. & WILKINSON, J. J.. The Giant Navan Carbonate-Hosted Zn-Pb Deposit – *A Review, Irish Association for Economic Geology – Current Perspectives on Zinc Deposits*, 85-122.

REDMOND, P.B, 1997, Structurally controlled mineralization and hydrothermal dolomitization at the Lisheen Zn-Pb-Ag deposit, Co. Tipperary, Ireland. Unpublished M.Sc. thesis, Dublin, Ireland, Trinity College, 126 p. In: HITZMAN, M.W., REDMOND, P.B. & BEATY, D.W. 2002. The carbonate-hosted Lisheen Zn-Pb-Ag deposit, County Tipperary, Ireland. *Economic Geology,* 97, 1627-1655.

REED, C.P. & WALLACE, M.W. 2001. Diagenetic evidence for an epigenetic origin of the Courtbrown Zn-Pb deposit, Ireland, *Mineralium Deposita,* 36, 428-441.

RIEDEL, D. 1980. Ore structures and genesis of the lead-zinc-deposit Tynagh, Ireland, *Interrnational Journal of Earth Sciences, 69, 361-383*

RIZZI, G. 1992. The sedimentology and petrography of Lower Carboniferous limestones and dolomites, host rocks to the Navan zinc-lead deposit, Ireland. *Unpublished Ph.D thesis, University of Glasgow*, 369 p.

RIZZI, G & BRAITHWAITE, C. J. R. 1997. Sedimentary cycles and selective dolomitisation in limestones hosting the giant Navan zinc-lead ore deposit, Ireland. *Exploration and Mining Geology,* 6, 63-77.

ROBINSON, B. W. & KUSAKABE, M. 1975. Quantitative preparation of sulfur dioxide, for sulfur-34/sulfur-32 analyses, from sulfides by combustion with cuprous oxide. *Analytical Chemistry,* 47**,** 1179-1181.

ROEDDER, E. 1971. Metastability in Fluid Inclusions, *Mining Geol. Japan, Spec, Issue, 3,* 327-334

ROEDDER E & BELKIN, H.E. 1988. Significance of monophase fluid inclusions in minerals, *Mineralogy*, 306, 283-287

ROMANO, M. 1980, The stratigraphy of the Ordovician rocks between Slane and Collon, Eastern Ireland. *Earth Sci. R. Dubl. Soc,* 3, 53-79.

RUSSELL, M.J. 1978. Downward-excavating hydrothermal cells and Irish type ore deposits: Importance of an underlying thick Caledonian prism. *Trans. Instn Min. Metall. (Sect B: Appl. Earth Sci.),* 87, 168-171.

RUSSELL, M.J. 1986. Extension and convection: a genetic model for the Irish Carboniferous base metal and barite deposits. In: ANDREW, C.J., CROWE, R.W.A., FINLAY, S., PENNELL, W.M., AND PYNE, , Geology and genesis of mineral deposits in Ireland: Dublin, *Irish Association for Economic Geology*, Economic Geology, 1–30.

RUSSELL, M., SOLOMON, M. & WALSHE, J. 1981. The genesis of sediment-hosted, exhalative zinc+lead deposits. *Mineralium Deposita,* 16**,** 113-127.

SANGSTER D. F. 1983. Mississippi Valley-type deposits: a geological melange. In: PIRAJNO, F. 2009. Hydrothermal processes and mineral systems. Springer Science + Business Media, Perth, 781–809

SAMSON, I.M & RUSSELL, M.J. 1987. Genesis of the Silvermines Zinc-Lead-Barite Deposit, Ireland: Fluid Inclusion and Stable Isotope Evidence, *Economic Geology,* 82, 371-394

SANGSTER, D.F. 1990. Mississippi Valley-Type and sedex lead-zinc deposits: A comparative examination: *Transactions of the Institution of Mining and Metallurgy, sec. B,* 99, 21–42

SANGSTER, D.F & HILLARY, E.M. 2000. SEDEX lead-zinc deposits—Proposed subtypes and their characteristics: *Exploration and Mining Geology*, 7, 341–357.

SHEPHERD, T.J., RANKIN, A.H. & ALDERTON, D.H. (1985). A practical guide to fluid inclusion studies. Blackie, *Glasgow*, 239 p.

SHEPPARD, S.M.F. 1987. Characterization and isotopic variations in natural waters, *Reviews in Mineralogy,* 165-184

SHEPPARD, W.A. 2007. Avoca Mine, a Volcanic Hosted Massive Sulphide Deposit in the Southwest of the European Caledonides, *LiaMin Report 171.07*.

STROGEN, P., JONES, G.L. & SOMERVILLE, I. 1990. Stratigraphy and sedimentology of Lower Carboniferous (Dinantian) drillholes from West Co. Meath, Ireland, *Geological Journal*, 25, 103-137.

TAYLOR, S. 1984. Structural and paleotopographical controls of lead-zinc mineralization in the Silvermines ore bodies, Republic of Ireland: *Economic Geology and the Bulletin of the Society of Economic Geologists,* 79, 529–548.

TAYLOR, S, & ANDREW, C.J, 1978, Silvermines orebodies, Co. Tipperary, Ireland: *Transactions of the Institution of Mining and Metallurgy*, 87B, 111–124.

THOMPSON, T.B., HITZMAN, M.W. & BEATY, D.W. 1992. Paragenesis and fluid inclusions of the Lisheen Zn-Pb deposit, Co. Tipperary, Ireland (abs.): *Geological Society of America, Abstracts with Programs*, 24, A354, In: HITZMAN, M.W, REDMOND, P.B. AND BEATY, D.W. 2002. The carbonate-hosted Lisheen Zn-Pb-Ag deposit, County Tipperary, Ireland. *Economic Geology*, 97, 1627-1655.

TRELOAR, M. 2014. The South West Extension - South (SWEXS) Mineralisation of the Giant Navan Zn-Pb Deposit, Genesis and Relation to the Main Orebody, unpublished MSci, *Imperial College London*.

UNITED STATES GEOLOGICAL SURVEY. 2010. A Deposit Model for Mississippi Valley-Type Lead-Zinc Ores, Chapter A of Mineral Deposit Models for Mineral Resource Assessment, *Scientific Investigations Report 2010-5070-A*.

VAUGHAN, A. 1991. The Lower Palaeozoic geology of the Iapetus Suture zone in eastern Ireland. Unpublished Ph.D thesis. Trinity College Dublin, 237 p, In: DAVIDHEISER-KROLL, B.J. 2014. Understanding the fluid pathways that control the Navan ore body, Unpublished Ph.D thesis, *University of Glasgow,* 232 p.

VAUGHAN, A. & JOHNSTON, J. D. 1992. Structural constraints on closure geometry across the Iapetus suture in eastern Ireland. *Journal of the Geological Society of London,* 149, 65-74.

WAGNER, T., BOYCE, A. J. & FALLICK, A. E. 2002. Laser combustion analysis of δ34S of sulfosalt minerals: determination of the fractionation systematics and some crystal-chemical considerations. *Geochimica et Cosmochimica Acta,* 66**,** 2855-2863.

WALKER, N. 2005. The Distribution Patterns of Pathfinder Elements in the Upper Dark Limestone Cover Sequence above the SWEX-B Mineralisation. *MSc Thesis. National University of Ireland, Galway.*

WALKER, M.J. 2010. Lithogeochemical Exploration Surrounding the Carbonate Hosted Zn-Pb Navan Orebody: A Historic Review, Analysis of Results and the Establishment of Future Exploration Programmes, *MSc thesis, University of Exeter*.

WALSHAW, R. D., MENUGE, J. F. & TYRRELL, S. 2006. Metal sources of the Navan carbonatehosted base metal deposit, Ireland: Nd and Sr isotope evidence for deep hydrothermal convection. *Mineralium Deposita*, 41, 803-819.

WARR, L. N. 2012. The Variscan Orogeny: the Welding of Pangaea. Geological History of Britain and Ireland. *John Wiley & Sons, Ltd.*

WEN, N., BOYCE, A.J., FALLICK, A.E., ASHWORTH, J.R & IXER, R.A. 1996. The genesis of Cpy-bearing quartz veins by metamorphic remobilisation from stratiform red bed deposits, SW County Cork, Ireland, *Mineralogy and Petrology*, 57, 73-89.

WILKINSON, J.J. 2003. On diagenesis, dolomitisation and mineralisation in the Irish Zn–Pb orefield. *Mineralium Deposita*, 38, 968-983.

WILKINSON, J.J. 2010. A Review of Fluid Inclusion Constraints on Mineralization in the Irish Orefield and Implications for the Genesis of Sediment-Hosted Zn-Pb deposits. *Economic Geology*, 105, 417-442.

WILKINSON, JJ. 2016. Metastable freezing: A new method for the estimation of salinity in aqueous fluid inclusions, Economic Geology. Abstract. ISSN: 0013-0109

WILKINSON, J.J. 2016. Re: Personal comunication

WILKINSON J.J, BOYCE A.J, EVERETT C.E & LEE M.J. 2003. Timing and depth of mineralization in the Irish Zn-Pb orefield. In: Proc IAEG Galway Conf 2000, Europe's Major Base Metal Deposits, *Irish Association for Economic Geology*, Dublin.

WILKINSON, J.J, EYRE, S.L. AND BOYCE, A.J. 2005A. Ore-forming processes in Irish-type carbonate-hosted Zn-Pb deposits: Evidence from mineralogy, chemistry and isotopic composition of sulfides at the Lisheen Mine: *Economic Geology*, 100, 63-86.

WILKINSON, J.J, EVERETT, C.E et al. 2005B. Intracratonic crustal seawater circulation and the genesis of sub-seafloor Zn-Pb mineralization in the Irish orefield. *Geology*, 33, 805-808.

WRIGHT, W.R., SOMERVILLE J.M., GREGG, J/M., SHELTON K.L & JOHNSON, A.W. 2004, Irish Lower Carboniferous replacement dolomite: isotopic modelling evidence for a diagenetic origin involving low-temperature modified seawater, Geological Society, London, Special Publications, 235, 75-97

WILKINSON, J.J, CROWTHER, H.L & COLES, B.J. 2011. Chemical mass transfer during hydrothermal alteration of carbonates: Controls of seafloor subsidence, sedimentation and Zn–Pb mineralization in the Irish Carboniferous, *Chemical Geology*, 289, 55-75.

YARDLEY, B.W., BARNICOAT, A.C., FREEMAN, S., BANKS, D., GLEESON, S., WILKINSON, J.J., BOYCE, A.J., BLAKEMAN, R., EVERETT, K. AND ASHTON, J. 2005. Multi-scale fluid-flow path analysis: Calibration and modelling using mineralisation systems, in Shaw, R.P. (ed.) Understanding the micro to macro behaviour of rock-fluid systems: *Geological Society of London Special Publications,* 249, 148-149.

ZHENG, Y.F & HOEFS, J. 1997. Carbon and oxygen covariations in hydrothermal calcites - Theoretical modeling on mixing processes and application to Pb-Zn deposits in the Harz Mountains, Germany, *Mineralium Deposita*, 28, 79-89.

10. Appendices

10.1. Sample locations and descriptions:

The following table provides drillhole sample collar, depth of collection and description in hand specimen.

Drillhole ID	From (metres)	To (metres)	Sample ID	Sample description
A1-A1' Transect				
N02230	1002.8	1002.9	N02230-1	Honeyblende Sph-calcite vein
N02230	1005.8	1005.9	N02230-2	Disseminated sph in MU
N02230	1011.5	1011.6	N02230-3	Sph-pyr-cal vein in tight fault plane
N02230	882	882.1	N02230-4	Cpy-qtz in calcite
N02230	882.1	882.1	N02230-5	Cpy-qtz vein
N02230	882.3	882.3	N02230-6	Blocky calcite vein in stratal dolomite
N02230	882.5	882.5	N02230-7	Blocky calcite vein in stratal dolomite
N02045	652.5	652.6	N02045-1	Banded sph-gal-cal
N02045	659.8	659.9	N02045-2	Very fine gal-cal sample
N02045	656.9	657	N02045-3	5 Lens Dolomite
N01022	490.4	490.5	N01022-1	Banded sph (4-Lens)
N01022	492.1	492.2	N01022-2	Speckled galena (4-Lens)
N01972	426.6	426.7	N01972-1	Gal-cal vein
N01972	454.4	454.5	N01972-2	Sph-pyr-cal vein
N01972	441.2	441.3	N01972-3	5 Lens Dolomite
N01972	454.5	454.7	N01972-4	Speckled gal-cal vein
N01628	408.6	408.7	N01628-1	Weak sph replacement
N01628	409.6	409.7	N01628-2	Sph-cal vein
N01628	409.8	409.9	N01628-3	5 Lens Dolomite
A2-A2' Transect				
N01579	373.7	373.8	N01579-1	Sph-pyr-cal banding
N01579	352.6	352.7	N01579-2	5 Lens Dolomite
N01579	379.7	379.8	N01579-3	Thick gal-cal vein
N00996	572.9	573	N00996-1	Sphalerite veined dolomite
N00996	580.7	580.8	N00996-2	5 Lens Dolomite
N00996	580.3	580.4	N00996-3	Coarse-grained sphalerite-calcite-dolomite vein breccia
N00996	577.4	577.5	N00996-4	Coarse-grained sphalerite-calcite-dolomite vein breccia
N01017	581.8	581.9	N01017-1	5 Lens Dolomite
N01017	580.1	580.2	N01017-2	5 Lens Dolomite
N01017	561.7	561.8	N01017-3	Sph-cal banding

N01117	635.1	635.2	N01117-1	Gal-sph-cal banding
N01117	635.2	635.3	N01117-2	Dol with sph shell replacement?
N01117	635.9	636	N01117-3	Banded sph-cal in dolomite
N01117	658.3	658.4	N01117-4	Gal accumulation around stylolite
N01117	658.7	658.8	N01117-5	Gal-cal veining
N01117	657.5	657.6	N01117-6	5 Lens Dolomite
N01269	656.1	656.2	N01269-1	Pyr-cal banding
N01269	655.9	656.1	N01269-2	5 Lens Dolomite
N01269	686	686.1	N01269-3	5 Lens Dolomite
N01073	720.7	720.8	N01073-1	Sph-gal-cal nodule
N01073	727.7	727.8	N01073-2	Sph breccia matrix fill
N01155	769.3	769.4	N01155-1	5 Lens Dolomite
N01155	772	772.1	N01155-2	Sph replacement
N01155	770.2	770.3	N01155-3	5 Lens Dolomite
N01155	769	769.1	N01155-4	5 Lens Dolomite
B-B' Transect				
N00862	478.1	478.2	N00862-1	Weakly banded Sph-gal-cal
N00862	481.2	481.3	N00862-2	Strongly banded sph, speckled gal
N00862	477.2	477.3	N00862-3	Dol
N00862	474.3	474.4	N00862-4	Sph stylolite fill
N00853	601	601.1	N00853-1	Sph-gal breccia replacement
N00853	598	598.1	N00853-2	5 Lens Dolomite
N00853	598.8	598.9	N00853-3	Sph-gal-cal banding
N00853	602.4	602.5	N00853-4	Sph-gal-cal banding
N00853	589.1	589.2	N00853-5	Sph replacement, gal-cal vein
N00853			N00853-6	Granular sph replacement at upper MU/5 Lens Dolomite contact
N00980	677.6	677.7	N00980-1	Sph-gal replacement
N00980	678	678.1	N00980-2	Gal-cal nodule
N00980	701.1	701.3	N00980-3	5 Lens Dolomite
N00980	710.7	710.8	N00980-4	Galena stylolite fill
N01033	634.3	634.4	N01033-1	Gal-cal vein
N01033	635.6	635.8	N01033-2	Galena vein
N01033	637	637.1	N01033-3	Sphalerite vein
N01033	640.6	640.8	N01033-4	Galena vein (weak brecciation)
N01033	643.4	643.5	N01033-5	Sph-gal replacement
N01033	646.2	646.3	N01033-6	Sph-gal replacement
N01033	634.2	633.3	N01033-7	5 Lens Dolomite
N01033	647.7	647.8	N01033-8	Gal-cal vein
C-C' Transect				
N01001	613.7	613.8	N01001-1	Sph-gal-cal replacement
N01001	623.1	623.2	N01001-2	5 Lens Dolomite

N01001	629.4	629.5	N01001-3	5 Lens Dolomite
N01001	622.1	622.2	N01001-4	Gal vein
N01093	593.7	593.8	N01093-1	Sph-cal vein
N01093	592.6	592.7	N01093-2	Sph-gal replacement
N01093	586.8	586.9	N01093-3	5 Lens Dolomite
N01093	584.1	584.2	N01093-4	5 Lens Dolomite - minor sph-gal
N01056	532.3	532.4	N01056-1	Sph-gal-cal vein
N01056	544.4	544.5	N01056-2	Sph-gal replacement
N01056	543	543.1	N01056-3	5 Lens Dolomite
N01056	560.4	560.5	N01056-4	Sph-gal-cal banding
N00933	507.4	507.5	N00933-1	Banded Sph-gal-cal in dolomite
N00933	508.6	508.7	N00933-2	Banded sph-cal, minor gal
N00933	506.8	506.9	N00933-3	5 Lens Dolomite
N00933	511.5	511.6	N00933-4	Sph-pyr banding and fracture fill
N00849	484.4	484.5	N00849-1	Banded sph-pyr-cal
N00849	479.2	479.3	N00849-2	5 Lens Dolomite
N00849	490.6	490.7	N00849-3	Sph vein
N00849	482.1	482.2	N00849-4	5 Lens Dolomite
N00849	484.4	484.5	N00849-5	Sph-gal-cal replacement

Table 10.1 – Sample collection depths and descriptions

10.2. Zn+Pb core assays

The following table provides core assay data for Zn, Pb, Fe, and Ag, total sulphide %, and Zn/Pb ratio. Bulk assay was performed on half-core, in-house by Boliden Tara Mines Limited

Drillhole	Assay from (metres)	Assay to (metres)	Zn (%)	Pb (%)	Fe (%)	Ag (ppm)	Zn+Pb (%)	Zn/Pb
A1 Transect								
N02230	757.7	760.5	0.09	1.09	1.81	2	1.18	0.0825688
N02230	760.5	762	0.01	0.01	0.8	1	0.02	1
N02230	762	763.5	0.52	1	1.5	109	1.52	0.52
N02230	763.5	766.5	0.09	0.05	1.26	2	0.14	1.8
N02230	880.1	881.8	0.05	0.02	1.64	1	0.07	2.5
N02230	881.8	882.8	0	0.01	1.93	1	0.01	0
N02230	882.8	883.8	0.09	0.6	2.25	3	0.69	0.15
N02230	883.8	885.3	0.84	1	2.39	14	1.84	0.84
N02230	885.3	889.1	0.13	0.22	2.35	2	0.35	0.5909091
N02230	889.1	892	0.24	0.09	0.99	1	0.33	2.6666667
N02230	892	895	0	0.09	0.87	1	0.09	0
N02230	895	898	0.1	0.05	0.99	2	0.15	2
N02230	898	901	0.02	0.05	0.94	1	0.07	0.4
N02230	901	904	0.11	0.03	0.52	1	0.14	3.6666667
N02230	904	907	0.13	0.07	0.65	1	0.2	1.8571429
N02230	907	910	0.08	0.37	0.52	5	0.45	0.2162162
N02230	960.8	963.8	0	0.16	1.73	1	0.16	0
N02230	963.8	966.8	0	0.26	1.46	3	0.26	0
N02230	999.7	1002.7	0	0	1.21	1	0	_
N02230	1002.7	1005.7	0	0.01	0.76	1	0.01	0
N02045	30.1	31.1	0	0	0.79	0	0	#DIV/0!
N02045	36.1	37.1	0.01	0	0.71	0	0.01	#DIV/0!
N02045	42.7	43.7	0	0	1.05	0	0	#DIV/0!
N02045	48.2	49.2	0.01	0	1.07	0	0.01	#DIV/0!
N02045	55.7	56.7	0	0	0.74	0	0	#DIV/0!
N02045	60.2	61.2	0.01	0.01	0.97	0	0.02	1
N02045	66.3	67.3	0	0	0.67	0	0	#DIV/0!
N02045	73.8	74.8	0.01	0	0.65	0	0.01	#DIV/0!
N02045	78.3	79.3	0.01	0	1.07	0	0.01	#DIV/0!
N02045	82.6	83.6	0	0	0.73	0	0	#DIV/0!
N02045	83.6	84.9	0.01	0	0.89	0	0.01	#DIV/0!
N02045	84.9	86.4	0.01	0	1.16	0	0.01	#DIV/0!
N02045	86.4	87.4	0.01	0	1.17	0	0.01	#DIV/0!
N02045	87.4	88.4	0.01	0	1.27	0	0.01	#DIV/0!
N02045	93.4	94.4	0.01	0	1.48	0	0.01	#DIV/0!
N02045	99.4	100.4	0.03	0	3.16	0	0.03	#DIV/0!
N02045	105.5	106.5	0	0	2.35	0	0	#DIV/0!
N02045	110	111	0	0.01	2.54	0	0.01	0
N02045	464.1	468.6	0.07	0	1.13	0	0.07	#DIV/0!
N02045	478.9	483.7	0.02	0	0.58	0	0.02	#DIV/0!
N02045	483.7	488.2	0.16	0.01	0.79	0.8	0.17	16
N02045	488.2	492.8	0.02	0	0.77	0	0.02	#DIV/0!

N02045	536.8	541	0.06	0.01	0.85	0.8	0.07	6
N02045	541	545.5	0.24	0.03	0.78	0.8	0.27	8
N02045	545.5	550	0.49	0.26	0.49	1.4	0.75	1.8846154
N02045	599.8	604.3	0	0.01	0.63	0	0.01	0
N02045	604.3	608.8	0	0.01	0.6	0	0.01	0
N02045	634.4	637.6	0.01	0.01	0.64	0	0.02	1
N02045	637.6	642	0	0.01	1.09	0	0.01	0
N02045	642	646.2	0.02	0.02	0.92	0.5	0.04	1
N02045	646.2	649.1	0	0.01	0.36	0	0.01	0
N02045	649.1	651	0	0.02	0.35	0	0.02	0
N02045	651	652.5	0	0.34	0.76	1.6	0.34	0
N02045	652.5	654	0	3.5	1.3	13.1	3.5	0
N02045	654	655.5	0	0	1.7	0	0	#DIV/0!
N02045	655.5	657	0	0.02	2.68	0	0.02	0
N02045	657	658.5	0	0	1.82	0	0	#DIV/0!
N02045	658.5	660	0	0.02	1.78	0	0.02	0
N02045	660	661.5	0	0.03	0.79	0	0.03	0
N02045	661.5	663.1	0	0.39	2.72	1.6	0.39	0
N02045	663.1	664.6	0	0.45	0.91	1.8	0.45	0
N02045	664.6	666.1	0	0	0.63	0	0	#DIV/0!
N02045	666.1	667.6	0	0	0.89	0	0	#DIV/0!
N02045	667.6	672.1	0	0	0.44	0	0	#DIV/0!
N02045	672.1	677.1	0	0	0.38	0	0	#DIV/0!
N02045	677.1	681.1	0	0.01	0.64	0	0.01	0
N02045	30.1	31.1	0	0	0.79	0	0	#DIV/0!
N01022	346	350.4	0.04	0	0.57	0.5	0.04	#DIV/0!
N01022	350.4	354.9	0.02	0	0.58	0.5	0.02	#DIV/0!
N01022	354.9	359.4	0.02	0.06	0.66	0.5	0.08	0.3333333
N01022	359.4	363.9	0.01	0.01	0.59	0.5	0.02	1
N01022	441.6	446	0.03	0.1	0.79	1.4	0.13	0.3
N01022	446	450.5	0.01	0	0.62	0.5	0.01	#DIV/0!
N01022	450.5	455	0.01	0.01	0.66	0.6	0.02	1
N01022	455	459.5	0	0.01	1.26	0.7	0.01	0
N01022	481.6	483.1	0.33	0.11	1.07	3.3	0.44	3
N01022	483.1	486.1	1.09	0.05	1.08	0	1.14	21.8
N01022	486.1	487.4	0.35	0.05	0.69	0	0.4	7
N01022	490.5	495	0.01	0.45	0.42	3.4	0.46	0.0222222
N01022	495	496.5	0.39	1.88	0.39	16	2.27	0.2074468
N01022	496.5	498	0.13	0.92	0.83	0	1.05	0.1413043
N01022	498	499.5	0.05	4.88	0.89	36	4.93	0.0102459
N01022	523.8	527.5	0.07	0.04	1.58	1.8	0.11	1.75
N01022	527.5	529.5	2.45	1.29	0.52	36	3.74	1.8992248
N01022	529.5	531	0.68	0.34	0.86	0	1.02	2
N01022	531	532.5	0.18	0.05	1.18	0	0.23	3.6
N01022	532.5	534	0.11	0.21	0.87	0	0.32	0.5238095
N01022	534	535.5	0.53	1.37	0.93	14	1.9	0.3868613
N01022	535.5	537	0.91	1.97	1.03	19	2.88	0.4619289
N01022	537	538.5	0.25	0.37	0.64	0	0.62	0.6756757
N01022	546	548.9	0	0	0.43	0.5	0	#DIV/0!
N01022	346	350.4	0.04	0	0.57	0.5	0.04	#DIV/0!
N01022	350.4	354.9	0.02	0	0.58	0.5	0.02	#DIV/0!
N01022	354.9	359.4	0.02	0.06	0.66	0.5	0.08	0.3333333
N01022	359.4	363.9	0.01	0.01	0.59	0.5	0.02	1

N01022	441.6	446	0.03	0.1	0.79	1.4	0.13	0.3
N01022	446	450.5	0.01	0	0.62	0.5	0.01	#DIV/0!
N01022	450.5	455	0.01	0.01	0.66	0.6	0.02	1
N01022	455	459.5	0	0.01	1.26	0.7	0.01	0
N01022	481.6	483.1	0.33	0.11	1.07	3.3	0.44	3
N01022	483.1	486.1	1.09	0.05	1.08	0	1.14	21.8
N01022	486.1	487.4	0.35	0.05	0.69	0	0.4	7
N01022	490.5	495	0.01	0.45	0.42	3.4	0.46	0.0222222
N01022	495	496.5	0.39	1.88	0.39	16	2.27	0.2074468
N01022	496.5	498	0.13	0.92	0.83	0	1.05	0.1413043
N01022	498	499.5	0.05	4.88	0.89	36	4.93	0.0102459
N01022	523.8	527.5	0.07	0.04	1.58	1.8	0.11	1.75
N01022	527.5	529.5	2.45	1.29	0.52	36	3.74	1.8992248
N01022	529.5	531	0.68	0.34	0.86	0	1.02	2
N01022	531	532.5	0.18	0.05	1.18	0	0.23	3.6
N01022	532.5	534	0.11	0.21	0.87	0	0.32	0.5238095
N01022	534	535.5	0.53	1.37	0.93	14	1.9	0.3868613
N01022	535.5	537	0.91	1.97	1.03	19	2.88	0.4619289
N01022	537	538.5	0.25	0.37	0.64	0	0.62	0.6756757
N01022	546	548.9	0	0	0.43	0.5	0	#DIV/0!
N01022	346	350.4	0.04	0	0.57	0.5	0.04	#DIV/0!
N01022	350.4	354.9	0.02	0	0.58	0.5	0.02	#DIV/0!
N01022	354.9	359.4	0.02	0.06	0.66	0.5	0.08	0.3333333
N01022	359.4	363.9	0.01	0.01	0.59	0.5	0.02	1
N01022	441.6	446	0.03	0.1	0.79	1.4	0.13	0.3
N01022	446	450.5	0.01	0	0.62	0.5	0.01	#DIV/0!
N01022	450.5	455	0.01	0.01	0.66	0.6	0.02	1
N01022	455	459.5	0	0.01	1.26	0.7	0.01	0
N01022	481.6	483.1	0.33	0.11	1.07	3.3	0.44	3
N01022	483.1	486.1	1.09	0.05	1.08	0	1.14	21.8
N01022	486.1	487.4	0.35	0.05	0.69	0	0.4	7
N01022	490.5	495	0.01	0.45	0.42	3.4	0.46	0.0222222
N01022	495	496.5	0.39	1.88	0.39	16	2.27	0.2074468
N01022	496.5	498	0.13	0.92	0.83	0	1.05	0.1413043
N01022	498	499.5	0.05	4.88	0.89	36	4.93	0.0102459
N01022	523.8	527.5	0.07	0.04	1.58	1.8	0.11	1.75
N01022	527.5	529.5	2.45	1.29	0.52	36	3.74	1.8992248
N01022	529.5	531	0.68	0.34	0.86	0	1.02	2
N01022	531	532.5	0.18	0.05	1.18	0	0.23	3.6
N01022	532.5	534	0.11	0.21	0.87	0	0.32	0.5238095
N01022	534	535.5	0.53	1.37	0.93	14	1.9	0.3868613
N01022	535.5	537	0.91	1.97	1.03	19	2.88	0.4619289
N01022	537	538.5	0.25	0.37	0.64	0	0.62	0.6756757
N01022	546	548.9	0	0	0.43	0.5	0	#DIV/0!
N01972	256.5	258	0.6	0.12	1.1	0	0.72	5
N01972	258	259.5	0.05	0.05	0.86	0	0.1	1
N01972	259.5	261	0.08	0.05	1.41	0	0.13	1.6
N01972	274.5	276	0.12	0.09	0.99	0	0.21	1.3333333
N01972	276	277.5	0.38	0.11	1.1	0	0.49	3.4545455
N01972	277.5	279	0.11	0.05	1.04	0	0.16	2.2
N01972	279	281.5	0.08	0.05	2.76	0	0.13	1.6
N01972	354	355.5	0.09	0.05	1.7	0	0.14	1.8
N01972	355.5	357	0.14	0.05	1.04	0	0.19	2.8

N01972	357	358.5	0.12	0.05	0.93	0	0.17	2.4
N01972	370.5	372	0.05	0.07	0.83	0	0.12	0.7142857
N01972	423	424.5	0.48	0.94	1.38	0	1.42	0.5106383
N01972	424.5	426	0.31	1.97	1.67	0	2.28	0.1573604
N01972	426	427.5	0.18	0.63	1.01	0	0.81	0.2857143
N01972	427.5	429	0.21	0.16	0.55	0	0.37	1.3125
N01972	429	430.5	0.05	0.05	0.66	0	0.1	1
N01972	430.5	432	0.05	0.1	0.56	0	0.15	0.5
N01972	442.5	444	0.05	0.92	0.69	0	0.97	0.0543478
N01972	444	445.5	0.05	1.14	0.79	0	1.19	0.0438596
N01972	445.5	447	0.05	0.86	1.2	0	0.91	0.0581395
N01972	447	448.5	0.06	0.19	0.6	0	0.25	0.3157895
N01972	448.5	450	0.05	0.07	1.02	0	0.12	0.7142857
N01972	450	451.5	0.06	1.96	0.68	0	2.02	0.0306122
N01972	451.5	453	0.06	0.54	1.01	0	0.6	0.1111111
N01972	453	454.5	0.06	0.51	0.9	0	0.57	0.1176471
N01972	454.5	456	0.25	2.26	0.5	0	2.51	0.1106195
N01972	456	457.5	0.06	1.13	0.54	0	1.19	0.0530973
N01972	457.5	459	0.08	0.16	0.5	0	0.24	0.5
N01972	459	460.5	0.06	0.14	0.48	0	0.2	0.4285714
N01628	403.5	405	D19723	0.64	2.17	1.91	0	2.81
N01628	405	406.5	D19724	3.23	3.09	1.75	0	6.32
N01628	406.5	407.6	D19725	1.39	1.24	1.73	0	2.63
N01628	407.6	409.5	D19726	15.38	11.11	0.87	0	26.49
N01628	409.5	411.1	D19727	5.86	4.18	0.73	0	10.04
N01628	411.1	412.6	D19728	3.95	0.48	0.33	0	4.43
N01628	412.6	414.1	D19729	4.89	1.9	0.45	0	6.79
N01628	414.1	415.6	D19730	4.72	0.04	0.3	0	4.76
N01628	415.6	417.1	D19731	0.27	0.03	0.89	0	0.3
A2-A2’ Transect								
N01579	346.6	348.1	0.69	0.13	0.76	0	0.82	5.3076923
N01579	352.6	354.1	0.78	0.65	1.98	0	1.43	1.2
N01579	357.1	358.7	0.52	0.16	0.4	0	0.68	3.25
N01579	358.7	360.2	0.25	0.11	0.75	0	0.36	2.2727273
N01579	366.2	367.7	1.3	0.31	1.93	0	1.61	4.1935484
N01579	369.2	371.4	1.83	0.39	1.69	0	2.22	4.6923077
N01579	372.9	374.4	1.17	0.3	0.8	0	1.47	3.9
N00996	575.8	577.3	0.05	0.05	1.37	0	0.1	1
N00996	577.3	578.8	0.27	0.28	1.57	0	0.55	0.9642857
N00996	578.8	580.3	5.28	3.84	1.32	72	9.12	1.375
N00996	580.3	582.3	10.3	1.48	0.92	82	11.78	6.9594595
N00996	582.3	583.5	1.1	0.13	0.57	0	1.23	8.4615385
N01628	409.5	411.1	D19727	5.86	4.18	0.73	0	10.04
N01017	484.5	486	0.59	0.05	1.11	0	0.64	11.8
N01017	486	487.5	2.18	0.16	2.1	0	2.34	13.625
N01017	490.5	492	0.26	0.05	0.94	0	0.31	5.2
N01017	492	493.5	1.26	0.05	1.01	0	1.31	25.2
N01017	556.1	557.6	0.48	0.11	0	0	0.59	4.3636364
N01017	557.6	559.1	0.29	0.59	1.49	0	0.88	0.4915254
N01017	559.1	560.6	0.56	2.05	1.48	32	2.61	0.2731707
N01017	560.6	562.1	0.65	0.63	1.16	0	1.28	1.031746
N01017	562.1	563.6	0.14	0.25	1.24	0	0.39	0.56
N01017	583.1	584.4	0.38	0.05	0.56	0	0.43	7.6

N01017	584.4	585.9	0.39	0.25	0.42	0	0.64	1.56
N01017	585.9	597.4	0.11	0.05	0.52	0	0.16	2.2
N01117	608.1	609.6	2.58	0.21	1.42	0	2.79	12.285714
N01117	618	620.5	1.41	0.63	1.64	0	2.04	2.2380952
N01117	630.9	632.5	0.27	0.18	1.11	0	0.45	1.5
N01117	632.5	634.1	6.53	0.57	1.91	0	7.1	11.45614
N01117	634.1	636.1	3.62	3.12	1.13	18	6.74	1.1602564
N01117	636.1	637.8	0.7	1	1.33	0	1.7	0.7
N01117	646.7	649.3	0.23	1.03	1.15	30	1.26	0.223301
N01117	657.6	660.6	0.15	6.41	0.82	14	6.56	0.0234009
N01269	486	489	0.71	0	2.41	0	0.71	#DIV/0!
N01269	489	492	0.99	0	2.21	0	0.99	#DIV/0!
N01269	492	495	0.63	0	1.46	0	0.63	#DIV/0!
N01269	495	498	0.64	0	1.43	0	0.64	#DIV/0!
N01269	498	501	0.55	0	1.45	0	0.55	#DIV/0!
N01269	541.7	543	0.51	0.13	1.13	0	0.64	3.9230769
N01269	543	544.5	0.07	0	1.17	0	0.07	#DIV/0!
N01269	544.5	546.4	0.68	0.01	0.96	0	0.69	68
N01269	553.5	555	2.49	1.35	6.16	16	3.84	1.8444444
N01269	555	558	1.29	0.45	2.82	0	1.74	2.8666667
N01269	558	561	1.08	0.01	2.42	0	1.09	108
N01269	561	564	2	0.94	2.88	0	2.94	2.1276596
N01269	564	565.5	1.91	1.59	3.32	16	3.5	1.2012579
N01269	609	610.5	0.92	0.17	0.58	0	1.09	5.4117647
N01269	610.5	612	0.44	0	0.24	0	0.44	#DIV/0!
N01269	612	613.5	1.6	0.21	0.59	0	1.81	7.6190476
N01269	656	656.7	2.25	0.27	0.36	0	2.52	8.3333333
N01269	660	661.5	1.05	1.2	0.05	14	2.25	0.875
N01269	661.5	663	0.34	0.65	0.27	0	0.99	0.5230769
N01073	539.8	541.3	0.86	0.04	0.92	0	0.9	21.5
N01073	541.3	542.8	5.76	0	0.82	0	5.76	#DIV/0!
N01073	542.8	544.3	1.06	0.01	1.56	0	1.07	106
N01073	544.3	545.8	2.67	0	1.19	0	2.67	#DIV/0!
N01073	545.8	547.3	0.43	0	1.69	0	0.43	#DIV/0!
N01073	586.5	588	0.6	0.02	1.9	0	0.62	30
N01073	588	589.5	1.54	0.16	2.35	0	1.7	9.625
N01073	589.5	591	0.77	0.08	1.9	0	0.85	9.625
N01073	591	592.5	2.87	0.18	2.64	0	3.05	15.944444
N01073	615.1	616.6	1.73	0.18	2.4	0	1.91	9.6111111
N01073	625	626.5	1.97	0.67	1.6	0	2.64	2.9402985
N01073	626.5	628	0.31	0.05	1.25	0	0.36	6.2
N01073	628	630.6	2.91	2.48	1.12	8	5.39	1.1733871
N01073	652.4	654.4	0.77	0.05	7	0	0.82	15.4
N01073	709.1	710.6	3.53	0.3	1.24	0	3.83	11.766667
N01073	710.6	712.1	1.17	0.46	1.2	0	1.63	2.5434783
N01073	712.1	713.6	0.3	0.88	1.2	0	1.18	0.3409091
N01073	713.6	715	0.05	0.18	1.02	0	0.23	0.2777778
N01073	715	716.5	0.72	0.16	1.29	0	0.88	4.5
N01073	716.5	718.2	1.5	0.7	0.87	0	2.2	2.1428571
N01073	718.2	721.2	0.49	0.79	1.11	0	1.28	0.6202532
N01073	721.2	723	5.88	8.82	1.39	57	14.7	0.6666667
N01073	723	725	1.74	2.37	0.77	18	4.11	0.7341772
N01073	753.7	755.2	0.57	0.18	1.12	0	0.75	3.1666667

N01155	525.6	528.6	1.36	0.08	1.7	0	1.44	17
N01155	528.6	531.7	6.44	1.01	1.38	3	7.45	6.3762376
N01155	531.7	533.2	4.17	0.07	1.06	0	4.24	59.571429
N01155	533.2	534.7	0.4	0.03	0.91	0	0.43	13.333333
N01155	566.4	568.3	2.23	0.12	2.2	0	2.35	18.583333
N01155	578.1	580	0.13	0.06	1.96	0	0.19	2.1666667
N01155	580	582	0.67	0.15	2.09	0	0.82	4.4666667
N01155	582	585	0.75	0.17	2.49	0	0.92	4.4117647
N01155	585	586.6	5.4	1.05	6.46	10	6.45	5.1428571
N01155	586.6	589.6	1.98	0.24	3.1	0	2.22	8.25
N01155	589.6	591.2	0.82	0.16	2.99	0	0.98	5.125
N01155	591.2	592.7	7.43	0.51	2.91	0	7.94	14.568627
N01155	592.7	595.7	1.83	0.36	1.66	0	2.19	5.0833333
N01155	595.7	598.8	0.43	0.1	1.22	0	0.53	4.3
N01155	626	627.5	2.11	0.26	0.82	0	2.37	8.1153846
N01155	627.5	629	0.25	0	0.55	0	0.25	#DIV/0!
N01155	642	643.2	4.14	0.07	1.5	0	4.21	59.142857
N01155	665.4	666.9	0.3	0.04	0.94	0	0.34	7.5
N01155	666.9	668.6	1.85	0.17	0.74	0	2.02	10.882353
N01155	769.1	772.1	0.03	0.41	0.99	0	0.44	0.0731707
N01155	772.1	773.6	0.04	0.04	0.59	0	0.08	1
B-B’ Transect								
N00862	405.5	406	0.59	0.1	3.76	0	0.69	5.9
N00862	406	407.5	1.1	0.29	4.03	0	1.39	3.7931034
N00862	407.5	409	2.04	0.32	6.34	0	2.36	6.375
N00862	409	410.5	0.66	0.12	4.08	0	0.78	5.5
N00862	473.5	475	0.12	0.47	1.6	0	0.59	0.2553191
N00862	475	476.5	0.19	0.26	1.46	0	0.45	0.7307692
N00862	476.5	478	0.06	0.11	1.42	0	0.17	0.5454545
N00862	478	479.5	6.21	2.36	0.77	0	8.57	2.6313559
N00862	479.5	481	2.79	2.33	0.59	0	5.12	1.1974249
N00862	481	482.5	0.1	0.08	0.33	0	0.18	1.25
N00862	482.5	484	1.63	0.81	0.72	0	2.44	2.0123457
N00862	484	485.5	0.22	0.13	0.35	0	0.35	1.6923077
N00862	502	503.5	1.12	0.18	0.92	0	1.3	6.2222222
N00853	441.2	443	2.19	0.07	2	0	2.26	31.285714
N00853	566.1	567.6	0.05	0.05	1.04	0	0.1	1
N00853	567.6	569.1	1.2	0.17	1.17	0	1.37	7.0588235
N00853	569.1	570.6	0.32	0.05	0.84	0	0.37	6.4
N00853	596.5	598	0.05	0.05	1.13	0	0.1	1
N00853	598	599.5	2.15	0.9	1.21	0	3.05	2.3888889
N00853	599.5	601	1.2	0.77	0.5	19	1.97	1.5584416
N00853	601	602.5	15.22	19.63	1.58	153	34.85	0.7753439
N00853	602.5	604	7.79	5.43	1.74	43	13.22	1.4346225
N00853	604	605.6	2.42	10.1	1.75	82	12.52	0.239604
N00853	605.6	607.1	0.76	1.14	1.25	15	1.9	0.6666667
N00853	607.1	608.6	4.44	1.03	2.39	22	5.47	4.3106796
N00853	608.6	610.1	0.08	0.11	1.08	0	0.19	0.7272727
N00853	610.1	611.7	0.13	0.1	0.95	0	0.23	1.3
N00853	611.7	613.2	1.25	1.21	1.3	0	2.46	1.0330579
N00853	613.2	614.7	0.35	0.31	1.48	0	0.66	1.1290323
N00853	614.7	616.2	0.81	0.57	0.52	0	1.38	1.4210526
N00853	616.2	617.8	0.05	0.14	1.01	0	0.19	0.3571429

N01033	491.9	493.4	3.07	1.26	1.67	2	4.33	2.4365079
N01033	493.4	494.9	2.7	1.49	1.49	0	4.19	1.8120805
N01033	494.9	496.4	2.3	1.26	1.26	0	3.56	1.8253968
N01033	496.4	497.9	1.78	1.88	1.88	0	3.66	0.9468085
N01033	497.9	499.4	12.39	3.98	3.98	0	16.37	3.1130653
N01033	499.4	500.9	12.07	5.39	5.39	0	17.46	2.2393321
N01033	500.9	502.3	9.99	1.01	3.62	0	11	9.8910891
N01033	502.3	503.8	1.97	0.47	1.35	0	2.44	4.1914894
N01033	503.8	505.3	0.49	0.18	0.64	0	0.67	2.7222222
N01033	505.3	506.8	2.2	0.31	0.77	0	2.51	7.0967742
N01033	506.8	508.2	2.72	0.35	1.07	0	3.07	7.7714286
N01033	508.2	509.7	1	0.26	0.67	0	1.26	3.8461538
N01033	509.7	511.2	2.2	0.63	0.87	0	2.83	3.4920635
N01033	511.2	512.7	0.54	0.29	0.49	0	0.83	1.862069
N01033	512.7	514.1	0.23	0.2	0.53	0	0.43	1.15
N01033	514.1	515.3	0.59	0.22	0.43	0	0.81	2.6818182
N01033	515.3	516.8	5.62	0.57	0.4	0	6.19	9.8596491
N01033	583.7	586.5	0.67	0.32	0.4	0	0.99	2.09375
N01033	586.5	588.2	2.91	0.47	1.32	0	3.38	6.1914894
N01033	588.2	589.7	3.4	0.5	1.33	0	3.9	6.8
N01033	589.7	592	1.74	0.77	1.71	0	2.51	2.2597403
N01033	592	593.5	0.49	0.66	1.34	0	1.15	0.7424242
N01033	593.5	595	0.26	1.9	1.79	0	2.16	0.1368421
N01033	595	596.5	0.08	0.93	1.32	0	1.01	0.0860215
N01033	596.5	598	0.05	3.55	1.91	16	3.6	0.0140845
N01033	633.5	653.5	0.05	2.65	0.22	17	2.7	0.0188679
N01033	635.3	636.8	0.72	7.57	0.52	40	8.29	0.0951123
N01033	636.8	638.1	0.17	6.16	0.46	42	6.33	0.0275974
N01033	638.1	639.7	0.24	5.14	0.79	32	5.38	0.0466926
N01033	639.7	641.2	0.71	6.27	1.11	41	6.98	0.1132376
N01033	641.2	642.7	0.6	6.04	0.92	39	6.64	0.0993377
N01033	642.7	644.2	1	7.26	0.92	43	8.26	0.137741
N01033	644.2	645.6	0.05	0.37	1.21	0	0.42	0.1351351
N01033	645.6	647.1	0.62	0.62	0.84	0	1.24	1
N01033	647.1	648.6	0.56	1.26	0.49	12	1.82	0.4444444
N01033	648.6	650.1	0.69	0.45	0.42	0	1.14	1.5333333
N01033	650.1	651.5	0.61	1.09	0.71	11	1.7	0.559633
N01033	651.5	653	0.05	3.09	0.69	24	3.14	0.0161812
N01033	653	654.5	0.91	0.38	0.43	0	1.29	2.3947368
N01033	654.5	656	0.05	0.17	0.78	0	0.22	0.2941176
N01033	656	657.4	0.73	0.44	0.38	0	1.17	1.6590909
N01033	657.4	658.9	0.05	0.16	0.27	0	0.21	0.3125
C-C’ Transect								
N01001	437	438.5	1.42	0.05	9.02	0	1.47	28.4
N01001	438.5	440	0.94	0.16	7.45	0	1.1	5.875
N01001	440	441.5	0.4	0.05	1.84	0	0.45	8
N01001	441.5	443	1.76	0.12	1.76	0	1.88	14.666667
N01001	456.5	458	0.16	0.05	1.37	0	0.21	3.2
N01001	458	459.5	0.52	0.05	1.69	0	0.57	10.4
N01001	519.5	521	0.14	0.05	1.68	0	0.19	2.8
N01001	561.5	563	1.58	0.19	1.37	0	1.77	8.3157895
N01001	611	612.5	0.57	3.01	1.01	0	3.58	0.1893688

N01001	612.5	614	0.73	4.54	1.21	0	5.27	0.160793
N01001	614	615.5	0.28	1.44	1.5	0	1.72	0.1944444
N01001	620	621.5	0.63	4.26	1.28	0	4.89	0.1478873
N01001	621.5	623	0.86	5.79	1.36	0	6.65	0.148532
N01001	623	624.5	0.51	0.58	0.79	0	1.09	0.8793103
N01001	624.5	626	0.66	0.5	0.97	0	1.16	1.32
N01001	629	630.5	1.77	4.33	0.98	0	6.1	0.408776
N01001	630.5	632	0.81	1.83	0.71	0	2.64	0.442623
N01001	632	633.5	0.05	0.05	0.63	0	0.1	1
N01001	633.5	635	0.41	0.15	0.6	0	0.56	2.7333333
N01093	418.2	421.2	1.84	0.04	2.5	0	1.88	46
N01093	421.2	422.7	1.08	0.06	2.76	0	1.14	18
N01093	422.7	424.2	2.41	0	2.6	0	2.41	#DIV/0!
N01093	424.2	425.7	4.51	0.02	4.67	0	4.53	225.5
N01093	439.3	442.3	0.82	0.08	4.36	0	0.9	10.25
N01093	442.3	443.8	0.67	0.28	3.84	0	0.95	2.3928571
N01093	560	561.5	0.5	0.14	1.4	0	0.64	3.5714286
N01093	561.5	563	1.39	0.38	1.48	0	1.77	3.6578947
N01093	563	564.5	0.31	0.04	1.3	0	0.35	7.75
N01093	564.5	566	0.97	0.05	1.37	0	1.02	19.4
N01093	566	569	0.73	0.19	1.62	0	0.92	3.8421053
N01093	569	570.5	1.52	0.21	1.61	0	1.73	7.2380952
N01093	570.5	572	1.09	0.27	1.87	0	1.36	4.037037
N01093	572	575.1	0.31	0.03	1.09	0	0.34	10.333333
N01093	575.1	578.1	0.9	0.81	1.41	0	1.71	1.1111111
N01093	578.1	579.6	0.55	1.59	1.5	12	2.14	0.3459119
N01093	579.6	581.1	0.46	0.37	1.79	0	0.83	1.2432432
N01093	581.1	584.1	0.8	0.98	1.46	0	1.78	0.8163265
N01093	584.1	587.1	1.35	0.59	1.45	0	1.94	2.2881356
N01093	587.1	588.6	1.06	1.6	1.49	9	2.66	0.6625
N01093	588.6	590.1	5.45	10.91	1.64	63	16.36	0.4995417
N01093	590.1	593.2	2.33	3.46	1.21	22	5.79	0.6734104
N01093	593.2	594.7	1	1.38	0.73	11	2.38	0.7246377
N01093	594.7	596.2	0.26	0.04	0.96	0	0.3	6.5
N01093	596.2	597.7	0.06	0	0.79	0	0.06	#DIV/0!
N01093	597.7	599.2	11.61	8.31	1.83	31	19.92	1.3971119
N01093	599.2	600.7	2.56	0.48	1.01	0	3.04	5.3333333
N01093	600.7	602.2	0.07	0.48	0.63	0	0.55	0.1458333
N01056	358.5	361.5	1.21	0.05	1.9	0	1.26	24.2
N01056	361.5	364.5	1.87	0.05	2.21	0	1.92	37.4
N01056	364.5	367.5	0.77	0.05	1.58	0	0.82	15.4
N01056	501	502.8	2.72	1.59	1.15	0	4.31	1.7106918
N01056	502.8	504.6	2.37	0.63	1.23	0	3	3.7619048
N01056	509.4	512.6	0.8	0.11	0.93	0	0.91	7.2727273
N01056	531.3	532.8	1.56	1.18	0.73	0	2.74	1.3220339
N01056	540	541.5	0.65	0.19	1.07	0	0.84	3.4210526
N01056	541.5	543	0.23	0.05	1.17	0	0.28	4.6
N01056	543	544.5	0.71	0.44	0.95	0	1.15	1.6136364
N01056	555.5	557	0.05	0.05	0.55	0	0.1	1
N01056	557	558.5	4	0.72	1.37	0	4.72	5.5555556
N01056	558.5	560	1.81	0.62	0.69	0	2.43	2.9193548
N01056	560	562.3	0.44	2.43	0.6	0	2.87	0.18107
N01056	562.3	564	0.23	0.42	0.44	0	0.65	0.547619

N00933	388	389.5	0.35	0.12	2.94	0	0.47	2.9166667
N00933	397	398	0.22	0.07	3.08	0	0.29	3.1428571
N00933	398.5	400	0.28	0.13	2.98	0	0.41	2.1538462
N00933	475	476.5	4.39	2.73	1.45	0	7.12	1.6080586
N00933	486	497.5	1.14	1.24	1.07	0	2.38	0.9193548
N00933	497.5	499	0.9	2.11	1.36	0	3.01	0.4265403
N00933	506.5	508	2.38	0.94	1	0	3.32	2.5319149
N00933	508	509.5	2.95	0.71	0.86	0	3.66	4.1549296
N00933	509.5	511	3.54	0.8	1.11	0	4.34	4.425
N00933	511	512.5	3.78	0.36	1.01	0	4.14	10.5
N00933	512.5	514	0.35	0.1	0.62	0	0.45	3.5
N00933	514	515.5	0.59	0.23	0.59	0	0.82	2.5652174
N00933	515.5	517	1.8	0.88	0.98	0	2.68	2.0454545
N00933	517	518.5	1.01	0.49	1.05	0	1.5	2.0612245
N00933	529	530.5	8.78	2.47	1.43	0	11.25	3.5546559
N00849	482.1	483.6	3.83	1.07	0.83	0	4.9	3.5794393
N00849	483.6	485.2	3.24	1.07	1.38	0	4.31	3.0280374
N00849	485.2	486.7	1.79	0.72	0.69	0	2.51	2.4861111
N00849	486.7	488.2	1.14	0.4	0.69	0	1.54	2.85
N00849	488.2	489.7	0.06	0.06	0.66	0	0.12	1
N00849	489.7	491.2	4.34	0.87	0.65	0	5.21	4.9885057
N00849	491.2	492.7	1.19	0.63	0.94	0	1.82	1.8888889
N00849	492.7	494.2	0.39	0.54	0.83	0	0.93	0.7222222
N00849	494.2	495.7	1.66	4.91	4	0	6.57	0.3380855

Table 10.2 – Zn, Pb and Fe core assay values

10.3. Thin section petrography

Introduction

This appendix provides a brief summary, photomicrographs and simple paragenesis for samples along the A1, A2 and C Transects. The petrography section in the results chapter (5.1) and later discussion (section 6.1) are based on the observations of this appendix. Abbreviations used in photomicrographs are provided below:

PPL – Plane-polarised light

XPL – Cross-polarised light

RL – Reflected light

Qtz – Quartz

Bar – Baryte

Cpy – Chalcopyrite

Mar – Marcasite

Pyr – Pyrite

Gal – Galena

Sph – Sphalerite

Tenn – Tennantite

Boul - Boulangerite

Cal – Calcite

Dol – Dolomite

Cel - Celestite

Arg - Argillite

10.3.1

A1-A1' Transect

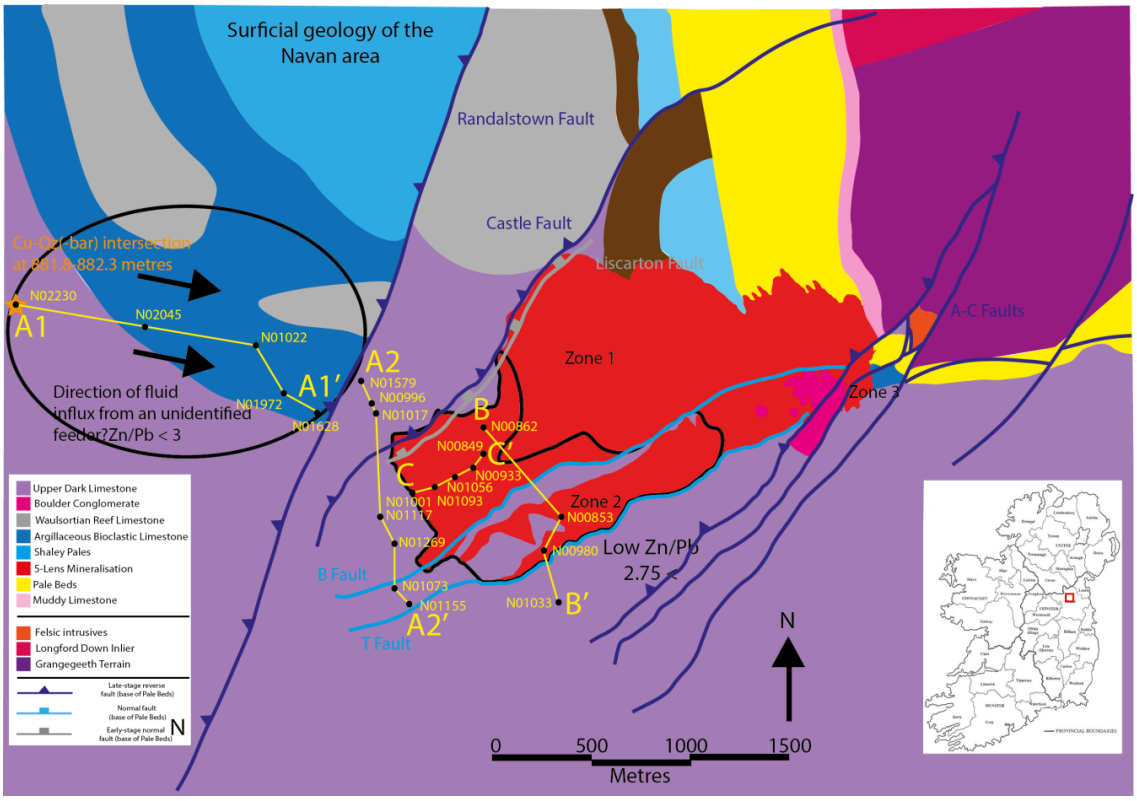

Fig 10.1. Geology of the Navan area with 5-Lens, low Zn/Pb areas and drillhole transects overlain on surficial geology

10.3.1.1 N02230-4 – 882 metres (3-Lens)

Lithology – Calcite veining with entrained cpy-qtz clasts

Transmitted light - Sample comprises coarsely-crystalline, scanelohedral calcite vein containing allochtonous cpy-qtz(-bar) vein clasts. Coarsely-crystalline calcite comprises approximately ninety percent of the sample, while the remaining ten percent consists of fine-medium crystalline cpy-qtz. Cpy-qtz and calcite crystal contacts are sharp, planar and show limited resorption.

Reflected light – Sulphides comprise chalcopyrite. Chalcopyrite is typically subhedral and coarsely-crystalline, though also occurs as thin veinlets following quartz-quartz intercrystalline boundaries, or as a fine, intercrystalline dissemination.

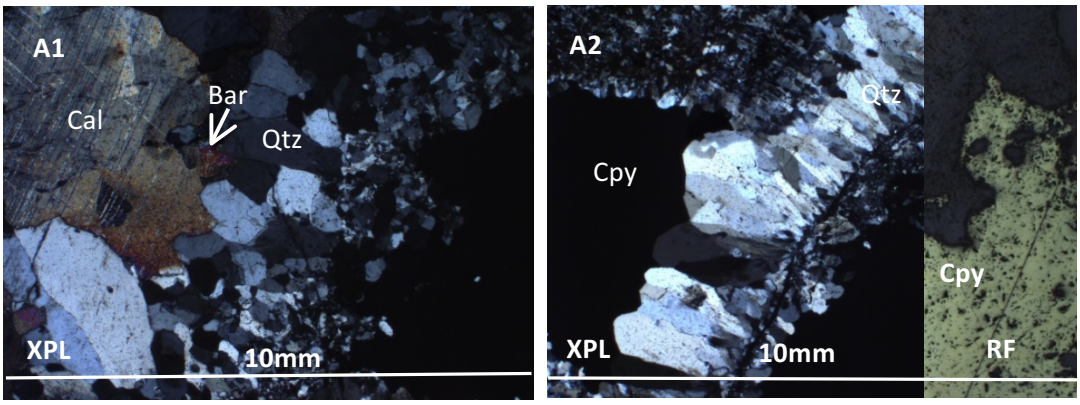

Fig A1 – Cross-polarised light exhibiting blocky and mosaic quartz(-bar) textures (Outer vein)

Fig A2 – Left: Cross-polarised light exhibiting plumose and quartz-baryte textures (Vein core). Right – Chalcopyrite in reflected light

Mineral	Pre-mineralisation	Main-stage mineralisation	Post-mineralisation
Calcite	—		
Dolomite (planar/non-planar)	—		
Jigsaw quartz		—	
Plumose quartz		—	
Baryte		—	
Chalcopyrite		—	
Dolomite (saddle)			—
Calcite (vein)			—

Fig A3 - Paragenesis of N02230-4

10.3.1.2. N02230-5 – 882.1 metres (3-Lens)

Lithology – Cpy-qtz(-baryte) vein

Transmitted light – Sample groundmass comprises alternating fine-coarsely crystalline quartz and trace baryte. Quartz crystal morphology ranges from subhedral, finely-crystalline mosaic, blocky-crystalline to plumose bands that show an undulose extinction. Barytes are a trace gangue phase, occurring as finely-crystalline individual crystals, or rarely co-precipitate with chalcopyrite. Crystal size and distribution generally increases towards the vein core. Outer, inner and vein core are separated by discreet mosaic quartz-(baryte) bands:

Outer vein – Outer vein assemblage comprises mosaic quartz-(baryte) with significant chalcopyrite. Mosaic texture is succeeded by blocky, coarsely-crystalline quartz with well-developed oscillatory zoning and significant chalcopyrite (Fig B1).

Inner vein – Blocky, oscillatory-zoned quartz with rare chalcopyrite (Fig B2).

Vein core – Finely-crystalline mosaic quartz(-baryte), and fine-coarsely-crystalline jigsaw quartz (Fig B3 and B4)

Reflected light – Chalcopyrite is the dominant sulphide mineral with minor co-precipitate quartz (Fig B6 and B7). Euhedral marcasite develops between pore space in chalcopyrite and co-precipitated quartz

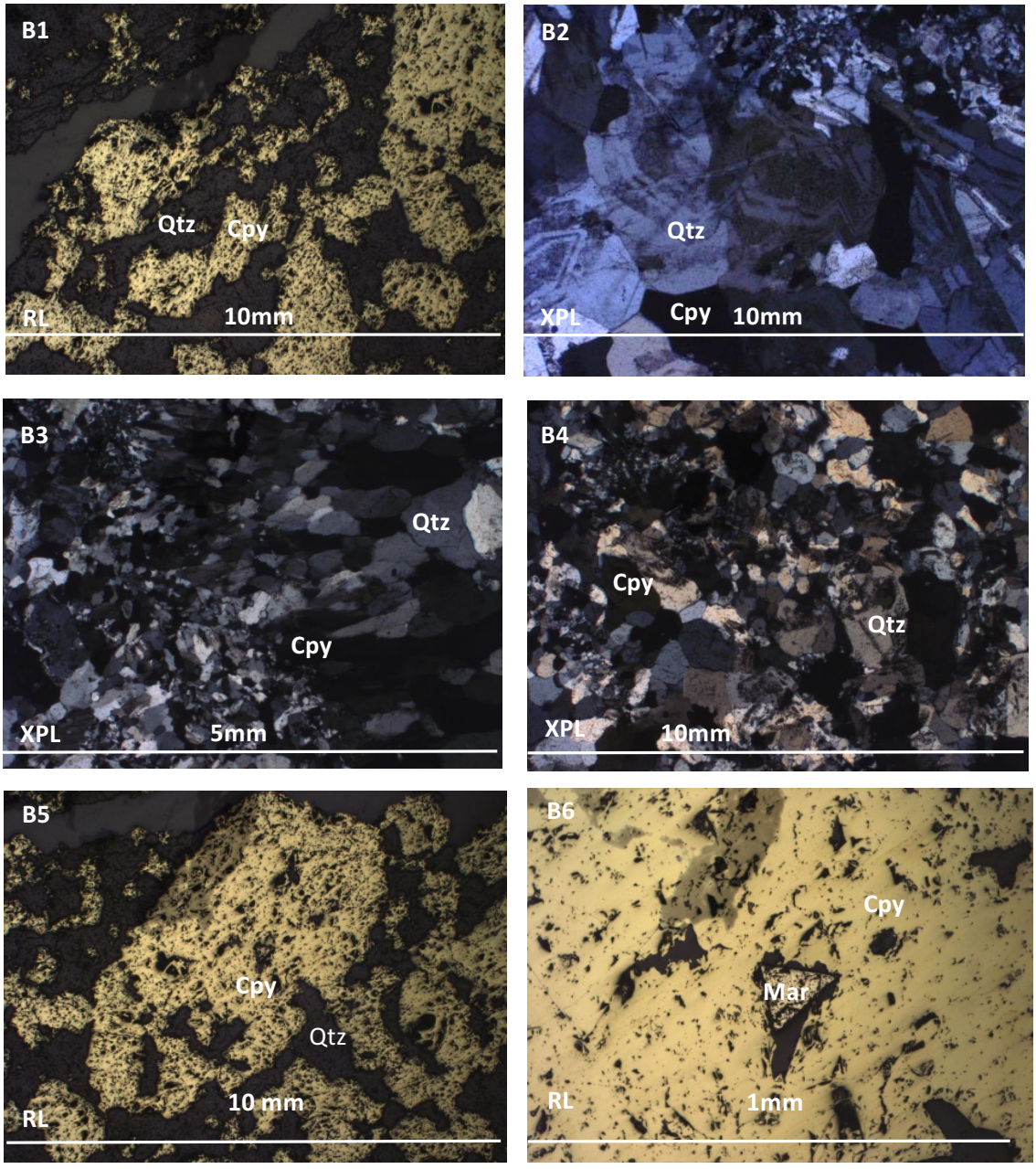

Fig B1 - Chalcopyrite mineralisation

Fig B2 - Blocky, oscillatory-zoned quartz. Mosaic quartz-(baryte) observed in top-centre.

Fig B3 – Blocky, oscillatory zoned quartz, and finely crystalline jigsaw quartz

Fig B4 – Moisac quartz-baryte (centre-left) and lattice-bladed, plumose baryte (centre-right)

Fig B5 – Chalcopyrite mineralisation

Fig B6 – Euhedral marcasite developing in intracrystalline chalcopyrite pore space

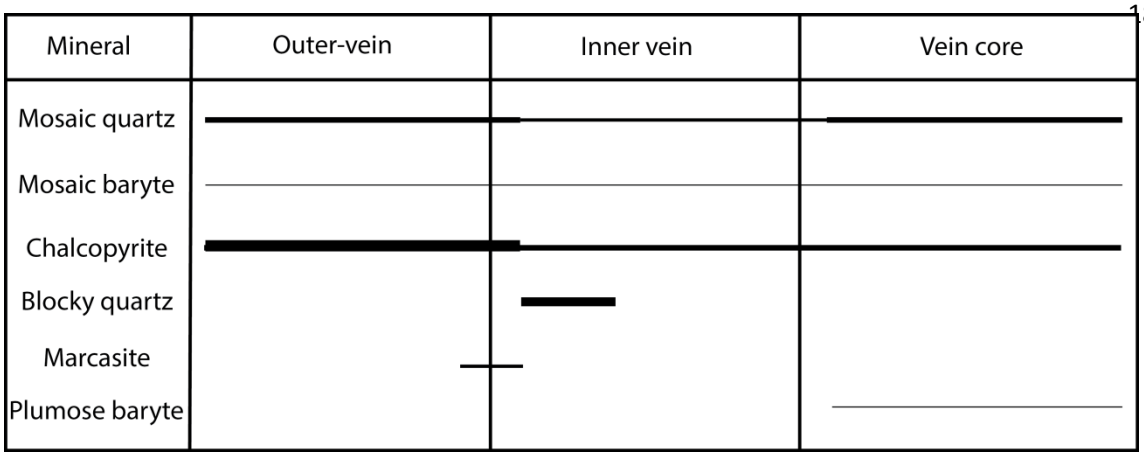

Fig B8 - Paragenesis of N02230-5

10.3.1.3. N02230-6 – 882.3m (3-Lens)

Lithology – Dolomitised calcarenite cross-cut by calcite-saddle dolomite veining

Transmitted light – Wall-rock is a pervasively dolomitised, fine-grained calcarenite. Wall-rock comprises equigranular, sub-rounded to well-rounded quartz in a silty, dolomitised matrix. Coarsely crystalline calcite-saddle dolomite cross-cuts stratal dolomite and exhibits a sharp, planar contact with enclosing wall-rock, though minor calcite veinlets splay off from the main vein. Dolomites developed along the vein-wallrock contact have a well-developed “saddle” texture and have a minor cleavage deformation. Calcites are scalenhoedral and show a weak cleavage deformation. Calcite-dolomite veining cross-cuts minor sph-gal veinlets.

Reflected light – Sulphide assemblage observed in descending abundance: 1) Chalcopyrite–marcasite–galena–sphalerite. Coarsely-crystalline (>3mm) chalcopyrite and minor co-precipitated quartz are hosted in the calcite vein, though also an overprinting phase for galena and sphalerite veinlets in the wall-rock. Marcasite either mantles (Fig C5) or overprints (Fig C6) minor chalcopyrite. Minor sph-gal veinlets observed in the wallrock (Fig C1-C4) are overprinted by chalcopyrite (Fig C1) and minor chalcopyrite and sphalerite (Fig C2).

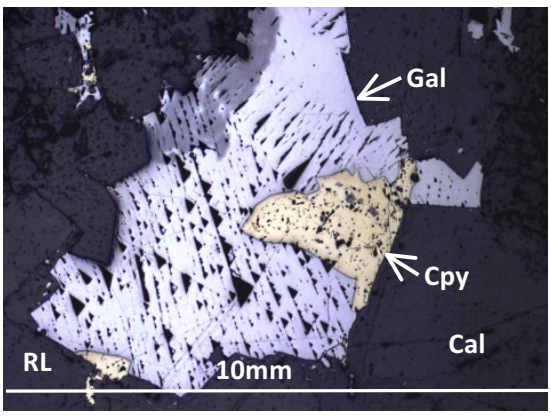

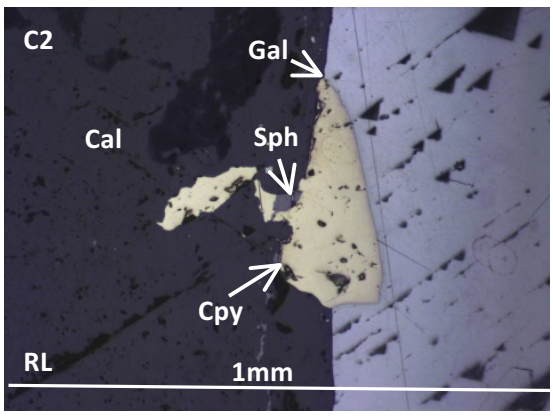

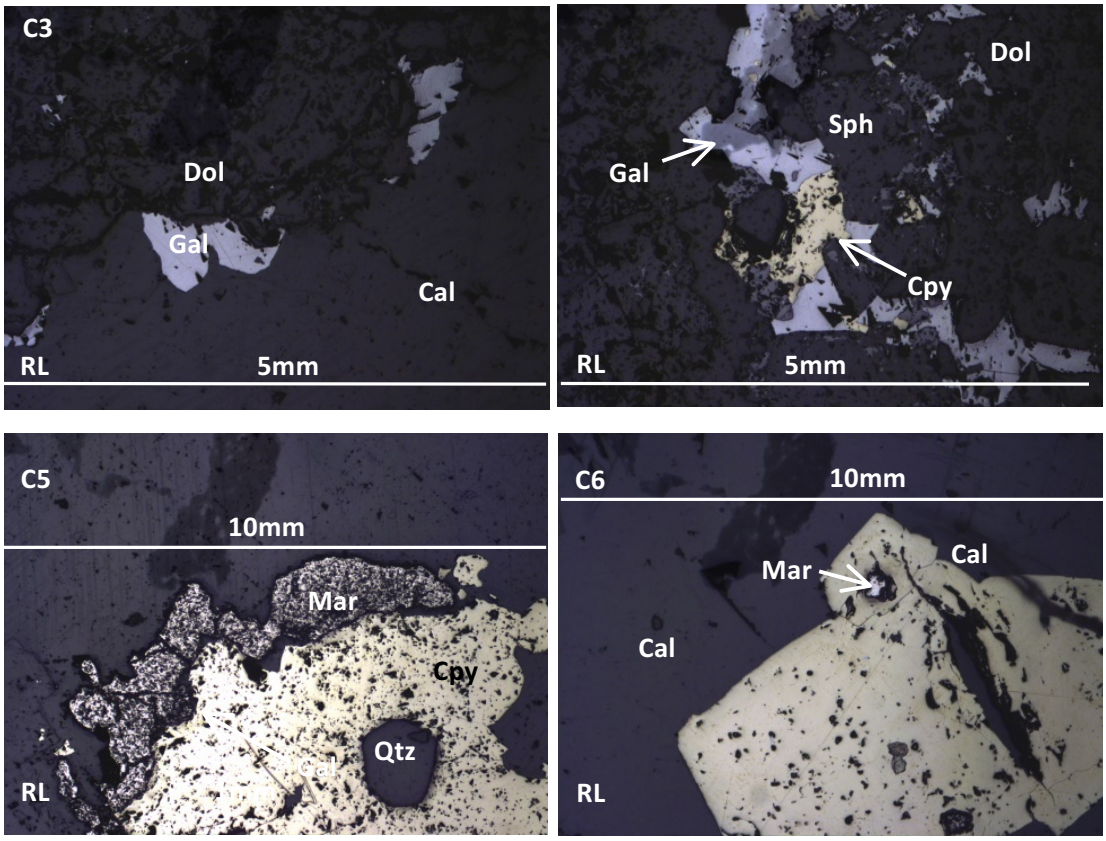

Fig C1 – Euhedral galena exhibiting chalcopyrite (along cleavage?).

Fig C2 – Chalcopyrite marginally replacing galena with minor sphalerite overprinting.

Fig C3 – Chalcopyrite replacing galena veinlet, in turn overprinted by sphalerite

Fig C4 – Chalcopyrite exhibiting rare marcasite overprinting

Fig C5 – Minor euhedral galena mineralisation along the wall-rock – calcite vein contact

Fig C6 – Marcasite mantling anhedral chalcopyrite crystal

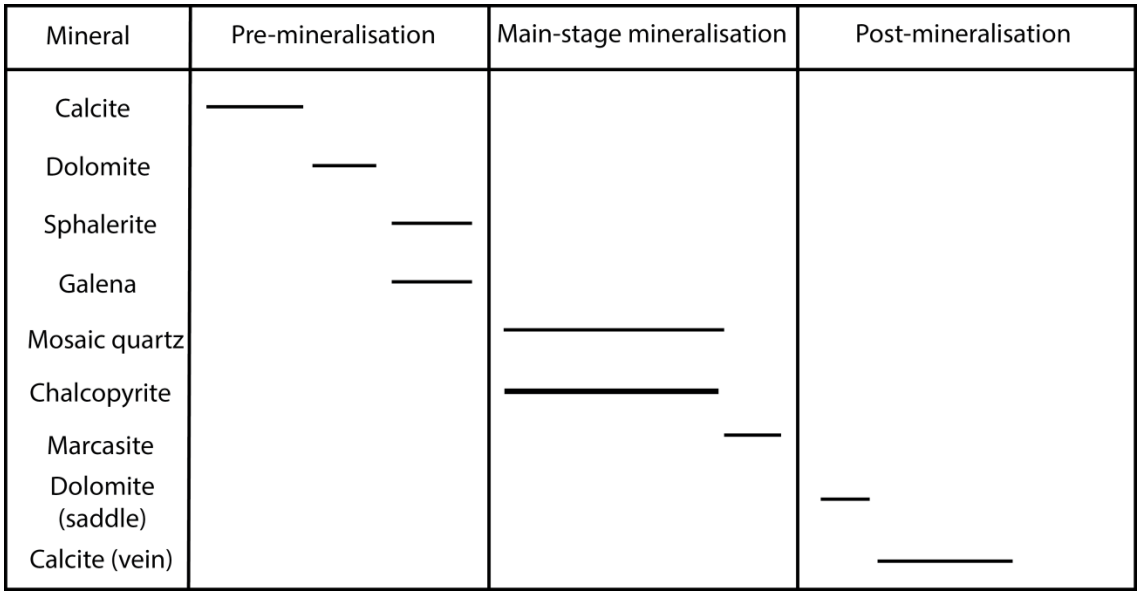

Fig C7 - Paragenesis chart of N02230-6

10.3.1.4. N02230-7 – 882.5 metres (3-Lens)

Lithology – Dolomitised calcarenite

Transmitted light – Sample matrix comprises dolomitised calcarenite cross-cut by blocky calcite-saddle dolomite veining containing minor allochtonous cpy-qtz. Host dolomite wall-rock is barren and veined by finely-crystalline calcite. Blocky calcite vein comprises coarsely crystalline scalenohedral calcites, while smaller, cross-cutting veins comprise finely-crystalline calcite and intercrystalline, non-pleochroic "silty" mineral. Blocky calcite-dolomite vein comprises two-stage mineralisation – 1) Very finely-crystalline saddle dolomite, and 2) coarsely-crystalline, scalenohedral calcite containing earlier-stage cpy-mar mineralisation.

Reflected light – Chalcopyrite is the primary sulphide, replacing galena developed between quartz crystals (Fig D1)

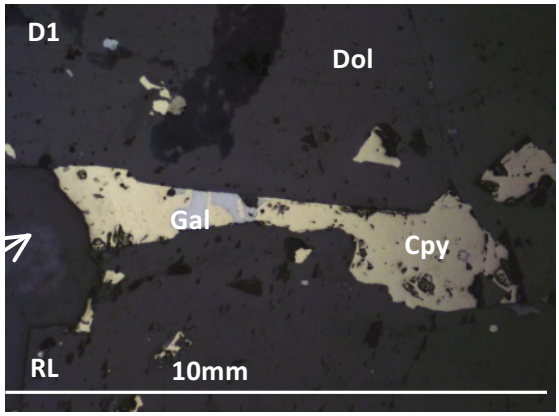

Fig D1 – Elongate galena crystal developed along intercrystalline quartz-quartz boundary heavily replaced by chalcopyrite

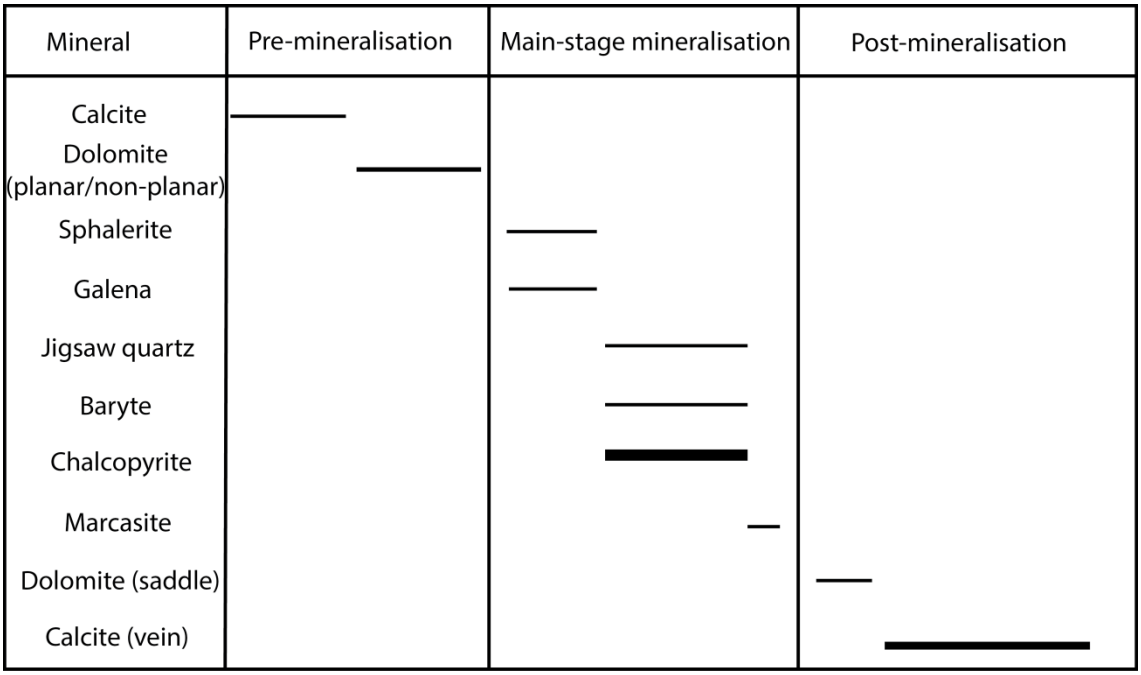

Fig D2 - Paragenesis chart of N02230-7

10.3.1.5. N02230-1 – 1002.8 metres (5-Lens)

Lithology – Shaley fault gouge

Transmitted light – Sample matrix comprises shaley fault gouge and brecciated, argillaceous micrite (weakly-dolomitised). Sample is veined by prominent, coarsely-crystalline calcite veins exhibiting weak cleavage deformation. Two stages of calcite veining are observed – 1) Stage one comprises finely crystalline calcite veining that cross-cuts galena, while stage 2 calcite veining cross-cuts both galena and stage 1 veining.

Reflected light – Sparse galena-pyrite mineralisation observed. Framboidal pyrite is paragenetically first, developing in shaley/silty gouge matrix. Galena develops later, occurring as a dissemination in matrix and occurs as coarsely-crystalline subhedral-euhedral crystals with trace co-precipitated sphalerite and dolomite rhombs (Fig E1-E2).

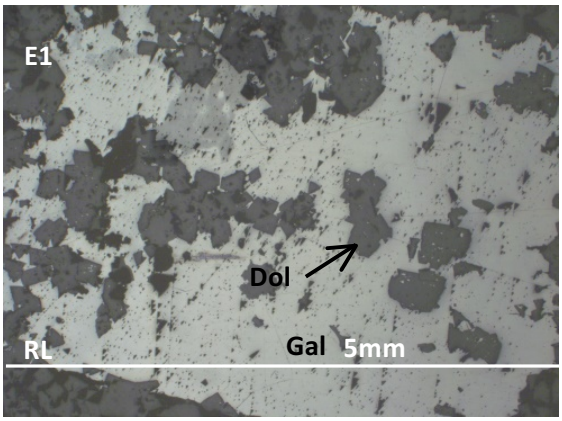

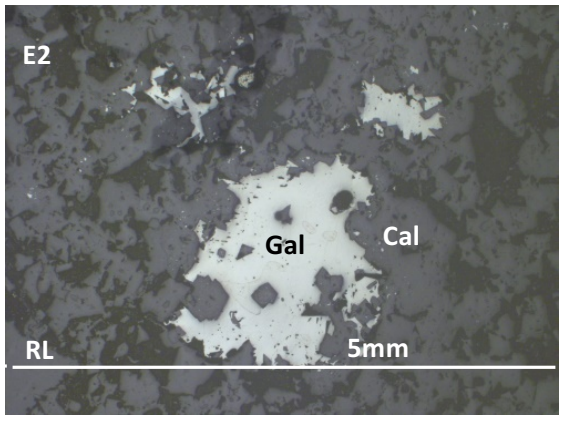

Fig E1 - Coarsely crystalline galena with co-precipitated subhedral dolomite rhombs

Fig E2 – Subhedral galena co-precipitated with anhedral dolomites

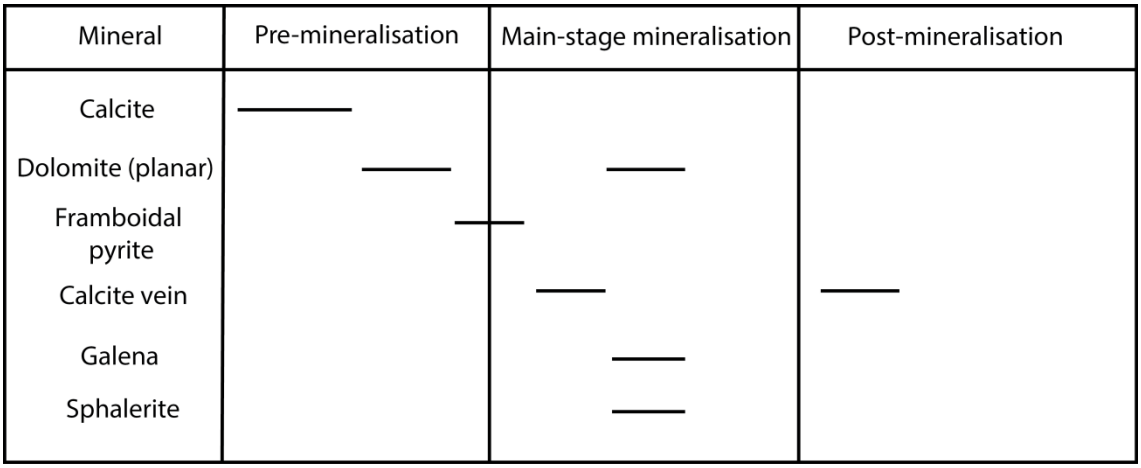

Fig E3 - Paragenesis of N02230-1

10.3.1.6. N02230-2 – 1005.8 metres (5-Lens)

Lithology –Fossiliferous micrite

Transmitted light - Sample matrix consists of abundant shelly bivalve debris, crinoid discs, and stick bryozoan in a calcite cement. Sample is cross-cut by two generations of

coarsely-crystalline calcite veining, one of which comprises “plastically” deformed calcite, exhibiting a “ropey” texture in plane polarised and cross-polarise light. “Ropey” calcite cross-cuts first generation calcite veining.

Reflected light – Sparse pyrite and galena is observed in matrix.

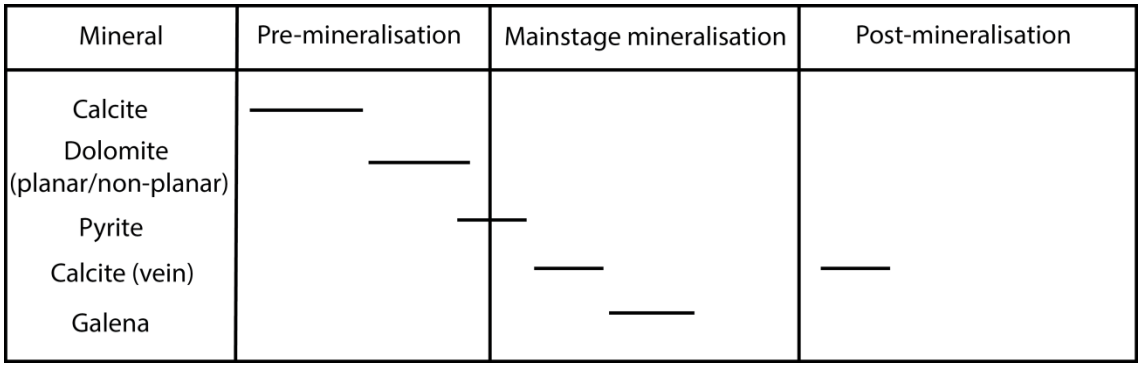

Fig F1 Paragenesis of N02230-2

10.3.1.7. N02045-2 – 659.8 metres (5-Lens)

Lithology – Fossiliferous, peloidal micrite

Transmitted light – Sample matrix consists of ooids, stick bryozoan and shelly bivalve debris in a finely-crystalline calcite cement. Sample is cross-cut by a single generation of fine-medium crystalline calcite veining. Matrix contains abundant disseminated opaques, which are also observed in coarsely-crystalline calcite veins.

Reflected light – Sulphides consist of a prominent galena-calcite vein following a thin styolite band. Galena mineralisation is clearly controlled by styolite banding, where mineralisation is observed on one side, and sparsely disseminated on the other. Galena mineralisation comprises two styles – Vein, or delicate replacement of ooids and fossil fragments. Sulfosalt mineralisation is near absent, and comprises rare laths around galena crystal rims. Rare, subhedral sphalerite co-precipitates with galena.

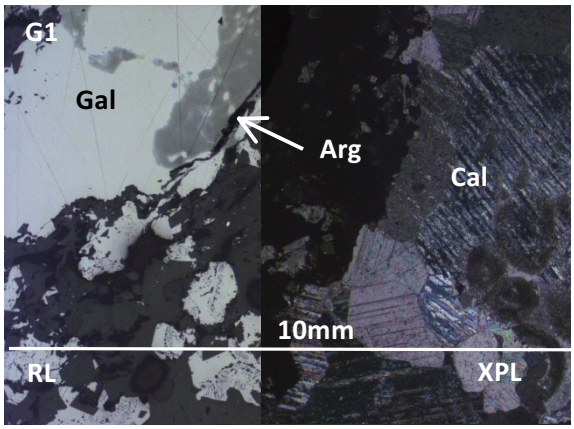

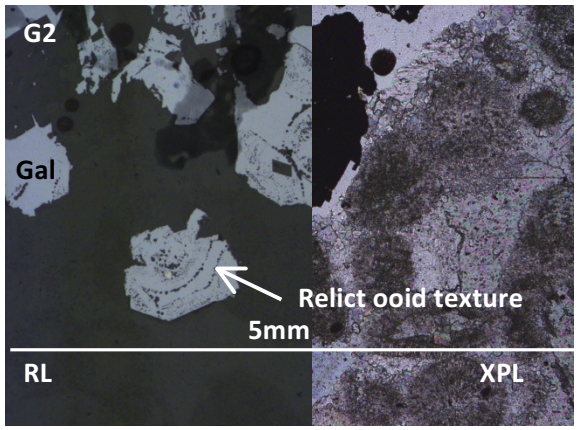

Fig G1 – Galena mineralisation developing along thin argillite band

Fig G2 – Relict ooid textures present in galena

Mineral	Pre-mineralisation	Main-stage mineralisation	Post-mineralisation
Calcite	—		
Sphalerite		—	
Galena		—	
Calcite (Vein)		—	
Sulphosalts		—	
Pyrite		—	

Fig G3 - Paragenesis of N02045-2

10.3.1.8. N02045-3 – 656.9 metres (5-Lens)

Lithology – 5-Lens Dolomite

Transmitted light – Sample comprises finely-crystalline planar/non-planar dolomite, sub-rounded to well-rounded quartz grains and abundant calcites with modal abundances of 60, 25, and 10% (Fig H1), respectively while the remainder consists of sparse opaques and argillite.

Reflected light – Sparse galena and pyrite are observed in matrix

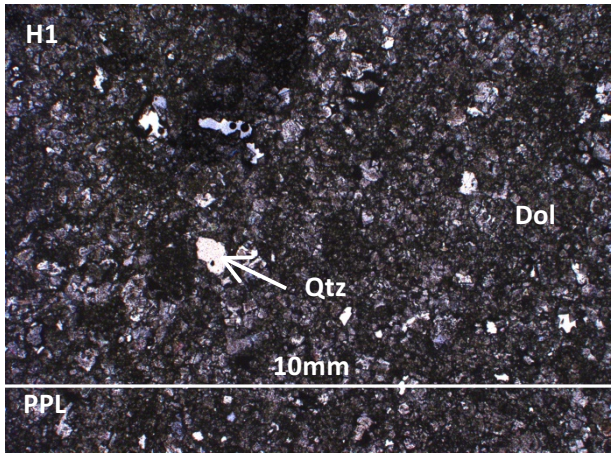

Fig H1 –Matrix texture of N02045-3

Mineral	Pre-ore	Main-stage ore	Post-ore
Calcite	—		
Dolomite (planar/non-planar)	—		
Galena		—	
Pyrite		—	

Fig H2 - Paragenesis of N02045-3

10.3.1.9. N01022-1 – 490.4 metres (4-Lens)

Lithology – Weakly mineralised, fossiliferous micrite (4-Lens)

Transmitted light – Sample matrix comprises abundant finely-crystalline calcite and microfossils. Microfossils consist of abundant forams and shelly bivalve debris (Fig I4). Microfossils exhibit weak dolomitisation along rims.

Reflected light – Sulphide assemblage comprises galena and framboidal pyrite (Fig I1). Framboidal pyrites are paragenetically earlier than galena are often observed, Galenas are typically coarsely-crystalline, euhedral and often retain relict ooid textures (Fig I2).

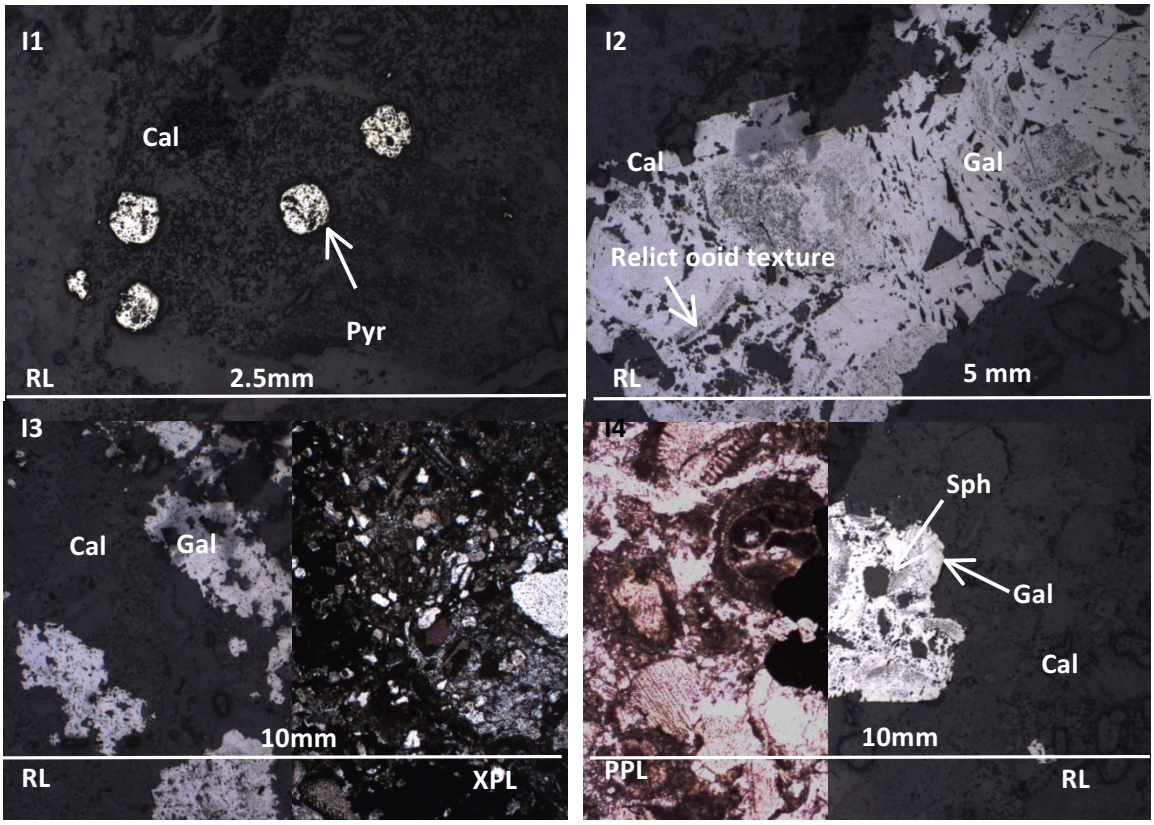

Fig I1 –Framboidal pyrite in silty matrix

Fig I2 – Coarsely-crystalline galena with relic fossil and ooid textures

Fig I3 – Galena mineralisation

Fig I4 – Partial galena replacement of bryozoan and peloidal debris

Mineral	Pre-mineralisation	Main-stage mineralisation	Post-mineralisation
Calcite	———		
Dolomite (planar/non-planar)	———		
Calcite (vein)		———	
Framboidal pyrite		—	
Galena		———	

Fig I5 – Paragenesis of N01022-1

10.3.1.10. N01972-2 – 454.4 metres (5-Lens)

Lithology – Veined dolomite

Transmitted light – Sample comprises dolomitised calcarenite, rare calcite and sub-rounded to well-rounded quartz grains. A three stage carbonate vein paragenesis is identified:

1) Coarsely crystalline dolomite rimmed by sphalerite and galena mineralisation (Fig J1).
2) Thin calcite veinlets cross-cutting sulphides (Fig J2).
3) Thin calcite veining cross-cutting both stages 1 and 2 (Fig J2).

Reflected light – Sulphide mineralisation comprises unbanded sphalerite and galena with minor, finely-crystalline pyrite (Fig J1 and J2). Galena and sphalerite likely co-precipitated and regularly occur as mutually interlocking coarse crystals, rimming coarsely crystalline calcite veining that cross-cuts the sample. Pyrite mineralisation dominantly occurs along the contact between co-precipitated calcite crystals and enclosing galena.

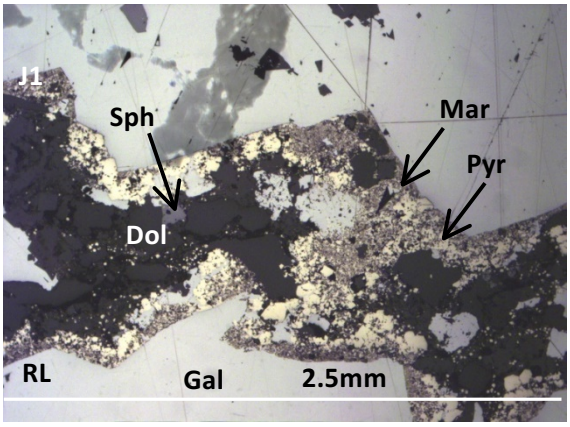

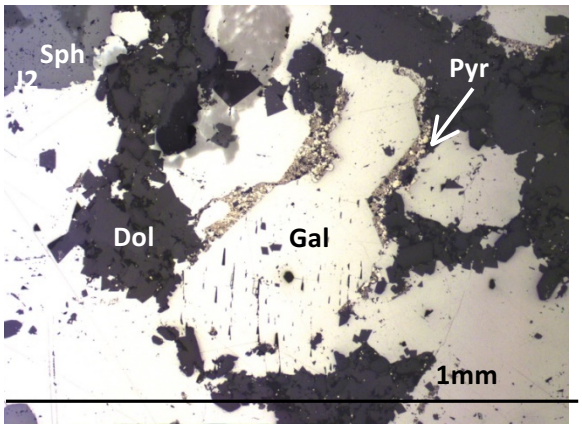

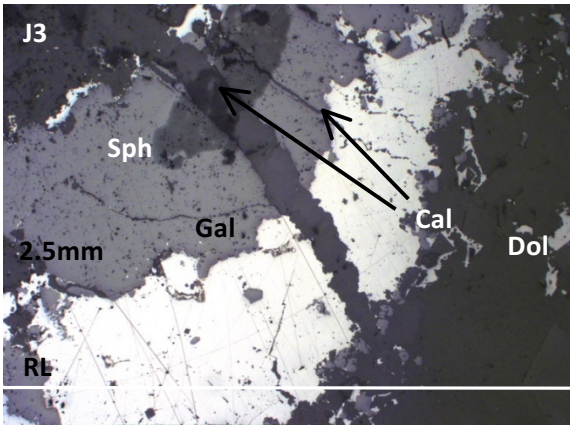

Fig J1 – Galena-calcite vein in matrix

Fig J2 – Sphalerite and galena banding cross-cut by late-stage calcite veinlets

Fig J3 – Fine-grained pyrite developing along pore space between two enclosing euhedral galenas and co-precipitated dolomite rhombs

Fig J4 – Pyrite developing in pore space between subhedral galenas

Mineral	Pre-mineralisation	Main-stage mineralisation	Post-mineralisation
Calcite	———		
Sphalerite		———	
Galena		———	
Sulphosalts		———	
Dolomite (planar)		———	
Pyrite/ marcasite		———	
Calcite (vein)			———

Fig J5 - Paragenesis of N01972-2

10.3.1.11. N01972-3 – 441.2 metres (5-Lens)

Lithology – Peloidal, fossiliferous micrite

Transmitted light – Sample matrix comprises peloidal and fossiliferous debris supported in a calcite cement, cross-cut by one, single-stage galena, sphalerite and calcite vein. Sample matrix consists of finely-crystalline calcite (30%), peloids (50%), and shelly bivalve debris, stick and branch bryozoan, solitary coral fragments and rare opaques. One stage of cross-cutting sulphide-calcite veining is observed, comprising a sulphide rim and coarsely-crystalline, barren calcite core (Fig K1-K3).

Reflected light – Sulphide assemblage comprises coarsely-crystalline galena and sub-ordinate galena in veining. Sphalerite and galena are a minor mineralisation phase in the matrix. Galena and sphalerite rim coarsely-crystalline veining, likely co-precipitating.

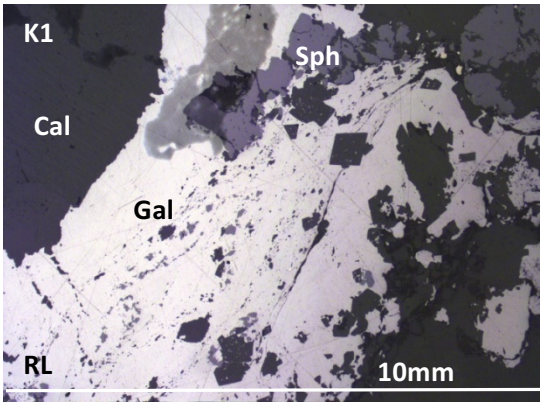

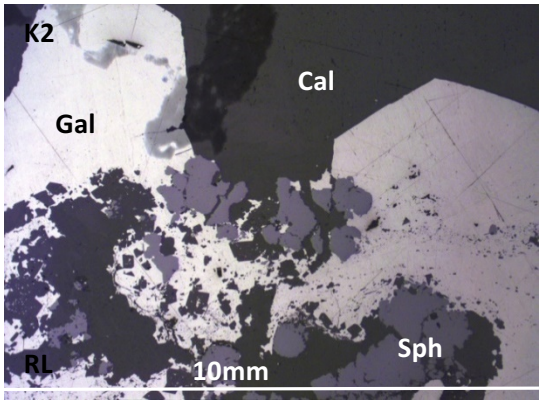

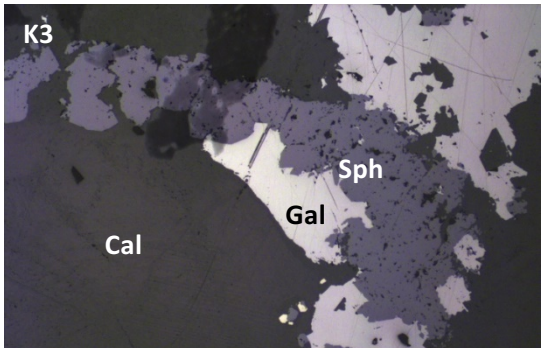

Fig K1 – Coarsely-crystalline galena cross-cut by finely-crystalline sphalerite

Fig K2 – Coarsely-crystalline galena marginally replaced by sphalerite

Fig K3 –Sphalerite replacing finely-crystalline galena

Mineral	Pre-mineralisation	Main-stage mineralisation	Post-mineralisation
Calcite	———		
Sphalerite		———	
Galena		———	
Calcite (vein)		———	—
Calcite (vugs)			—

Fig K4 - Paragenesis of N01972-3

10.3.1.12. N01628-1 – 408.6 metres (5-Lens)

Lithology – Blocky sulphide in mineralised micrite

Transmitted light – Sample consists of blocky sphalerite, galena and trace chalcopyrite, and large (> 10mm) unmineralised micrite clasts and intercrystalline calcites. In plane-polarised light, sphalerite exhibits weak-moderate planar banding, strongly developed kink banding, and individual sphalerite grains that form aggregate grains (Fig L1). Sphalerites are cross-cut by minor, finely-crystalline calcite veinlets. Calcite veinlets discontinuously follow and cross-cut well-developed kink banding (Fig L3 and L4). Calcite veinlets are overprinted by subhedral opaques. Sphalerite banding varies in colour from pale yellow-orange (typically outer rim) to a tangerine orange colour (core – Fig L1). Minor opaques are observed as an intergrowth between separate sphalerite crystals. Residual, unmineralised matrix comprises fossiliferous micrite, containing bryozoan and shelly bivalve debris in a finely crystalline calcite matrix.

Reflected light – Sulphide mineralisation dominantly comprises sphalerite and comparatively minor intergrown galena. Sulfosalts are abundant and form intergrowths with galena, or occur as lath-shaped inclusions in solid state (Fig L6-L8). Sphalerite and galena appear to have co-precipitated, both exhibiting mutually intergrown growth, or as a replacive phase for each other. Replacive galenas often exhibit thin, splaying veins comprising mutually intergrown galena and sulfosalts, and typically follow planar banding in sphalerites, suggesting persistent mineralisation. Chalcopyrite dominantly overprints sphalerite, though is rarely observed to replace galena (one instance of complete galena replacement observed). Galena is observed to overprint thin calcite veinlets cross-cutting sphalerite (Fig L3).

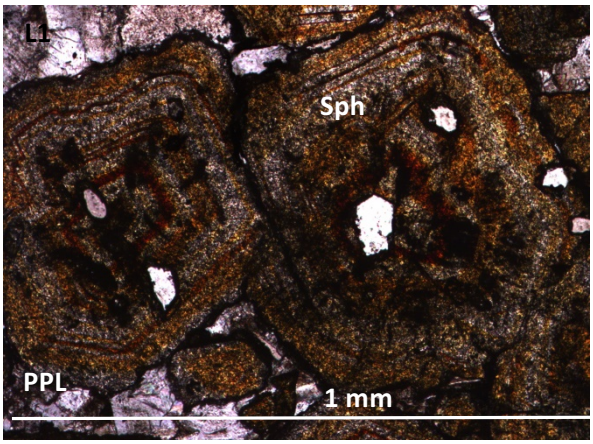
L1
Sph
PPL
1 mm

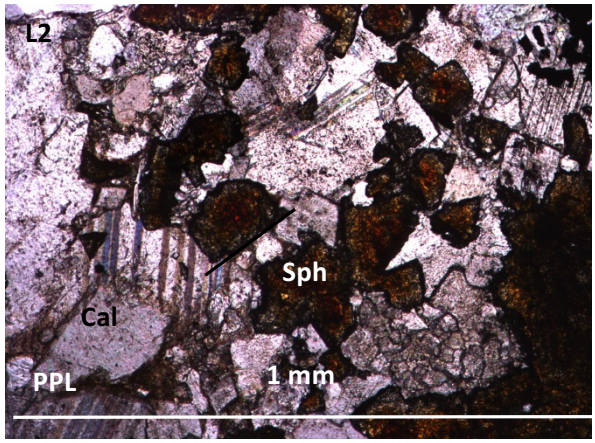
L2
Sph
Cal
PPL
1 mm

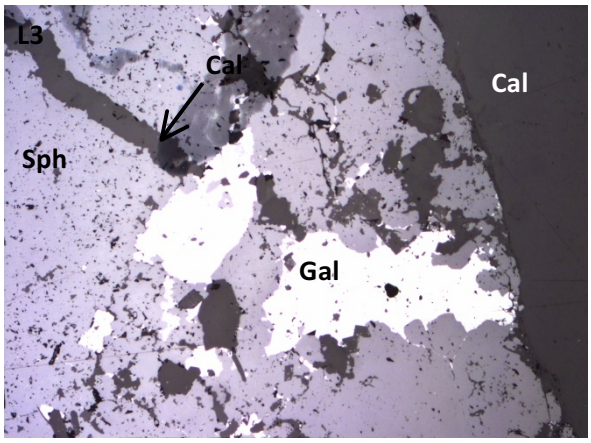
L3
Cal
Cal
Sph
Gal

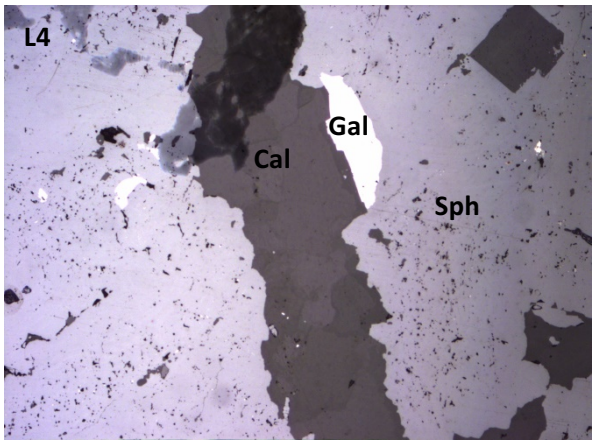
L4
Gal
Cal
Sph

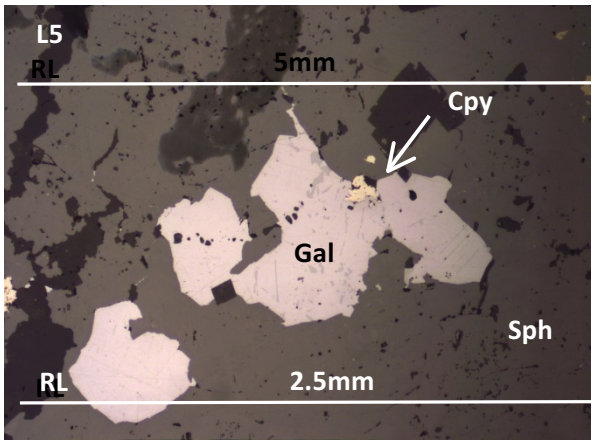
L5
RL
5mm
Cpy
Gal
Sph
RL
2.5mm

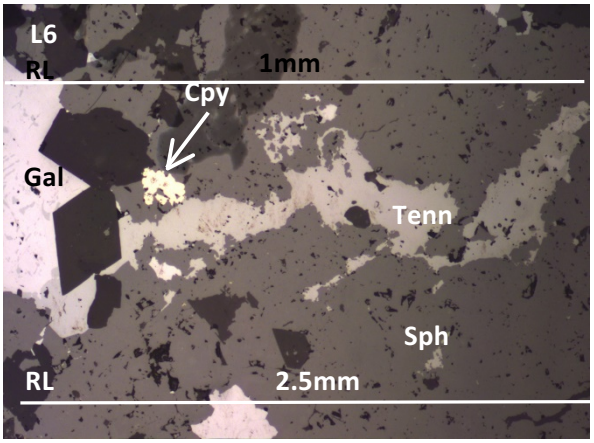
L6
RL
1mm
Cpy
Gal
Tenn
Sph
RL
2.5mm

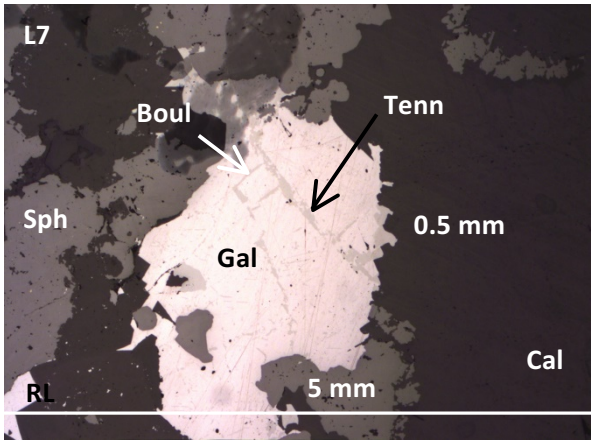
L7
Boul
Tenn
Sph
0.5 mm
Gal
Cal
RL
5 mm

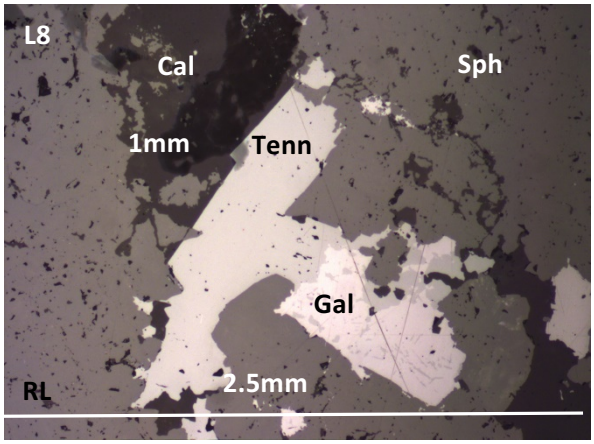
L8
Cal
Sph
1mm
Tenn
Gal
RL
2.5mm

Fig L1 – Mutually intergrown, euhedral oscillatory sphalerite crystals

Fig L2 – Intercrystalline, euhedral sphalerite crystals

Fig L3 – Sphalerite cross-cut by finely-crystalline calcite veining, in turn partially overprinted by galena

Fig L4 – Finely-crystalline, weakly oscillatory zoned sphalerite developing at intercrystalline calcite contacts

Fig L5 – Discontinuous galena development along sphalerite banding (not visible). Minor chalcopyrite replacement of galena is observed.

Fig L6 - Prominent galena development along sphalerite banding (not visible)

Fig L7 – Lath-shaped sulfosalts in solid state with galena

Fig L8 – Mutually intergrown galena-sulfosalts

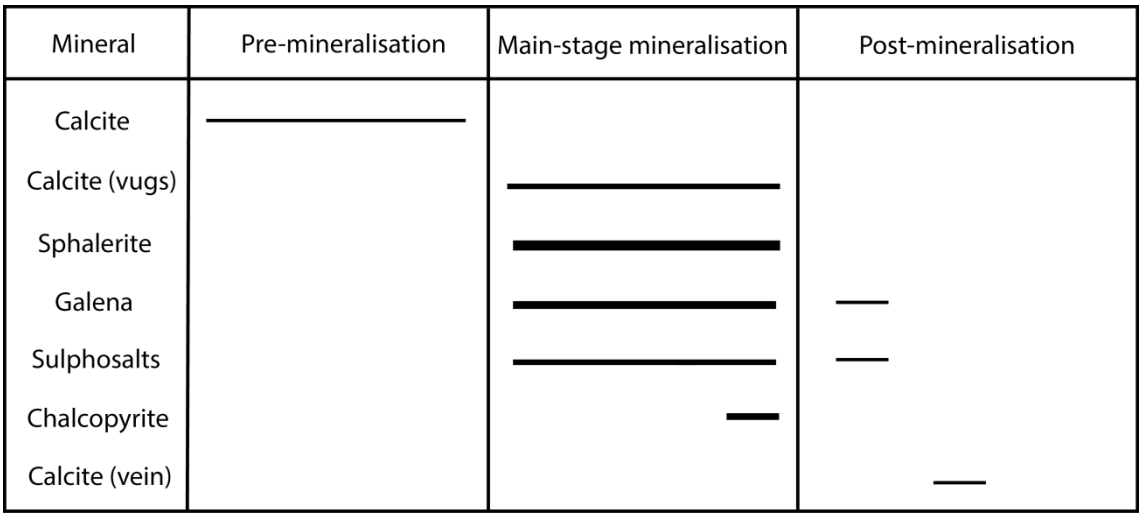

Fig L9 - Paragenesis of N01628-1

10.3.1.13. N01628-2 – 409.6 metres (5-Lens)

Lithology – 5-Lens Dolomite

Transmitted light –Sample consists of intensively dolomitised calcarenite – Modal abundances of 80% finely crystalline dolomite, 10% sub-rounded to well-rounded quartz, while the remainder comprises opaques.

Reflected light – Sulphide assemblage comprises finely-crystalline, sphalerite veining and sub-ordinate euhedral galena. Tennantites occur either in solid state with galena, or as an intergrowth (Fig M1 and M2). Sulphide-dolomite veining is cross-cut by one generation of calcite-galena veinlets (Fig M3 and M4).

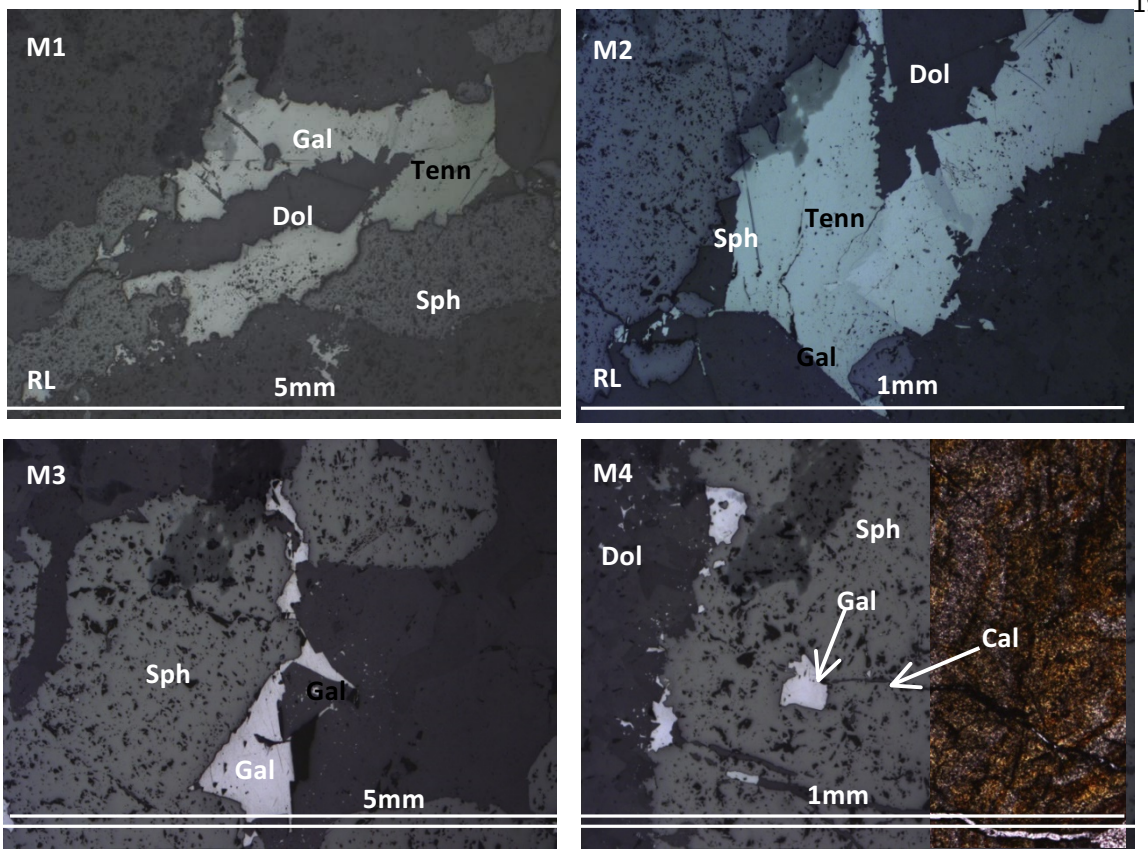

Fig M1 – Mutually intergrown sulfosalts (light green-grey) and subhedral galena with dolomite vein core

Fig M2 – Thin galena veinlet cross-cutting banded sphalerite

Fig M3 – Thin galena veinlet cross-cutting sphalerite

Fig M4 – Left: Cross-polarised light – Banded sphalerite and minor galena at termination of thin calcite veinlets. Right – Thin calcite veinlets cross-cutting sphalerite.

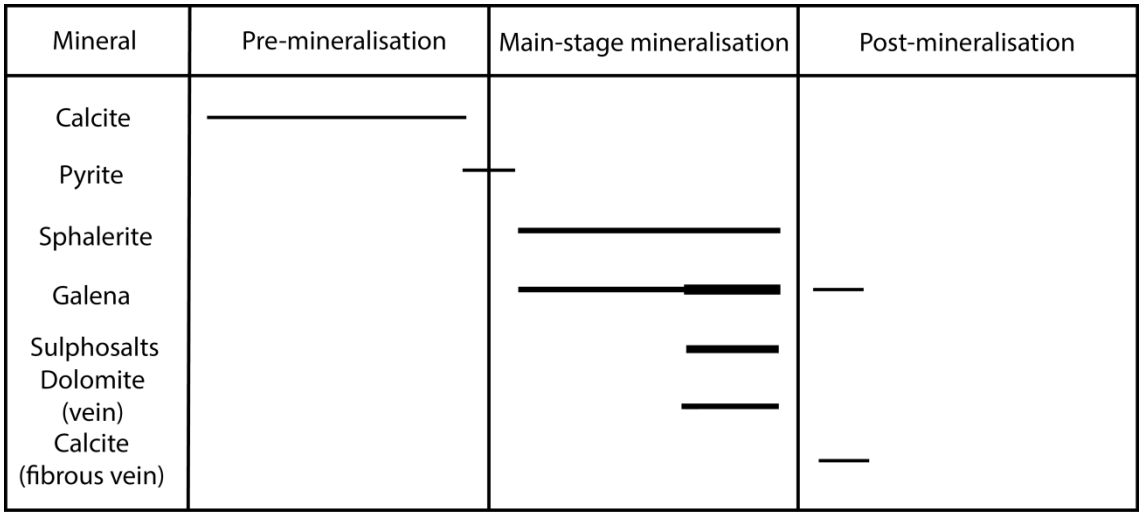

Fig M5 - Paragenesis of N01628-2

A2-A2' Transect

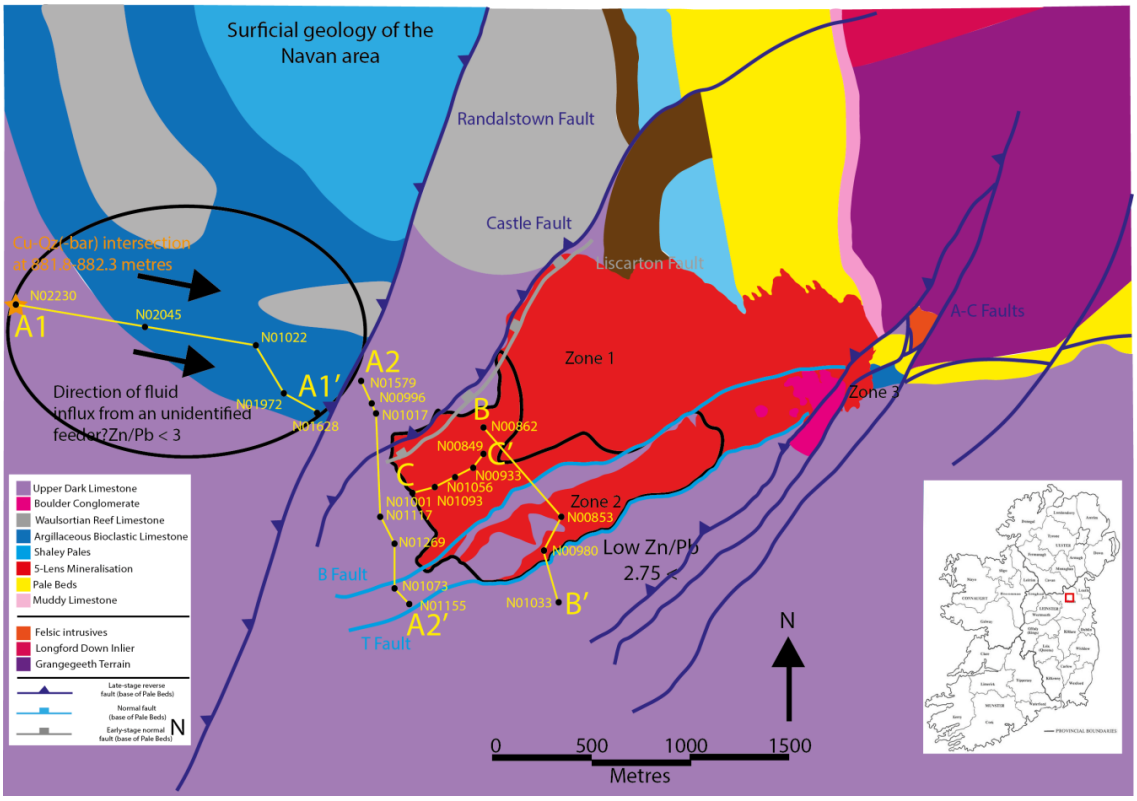

Fig 10.2. Geology of the Navan area with 5-Lens, low Zn/Pb areas and drillhole transects overlain on surficial geology

10.3.2

10.3.2.1. N01579-1 – 373.7 metres (5-Lens)

Lithology – Sphalerite and galena-dolomite veining in micrite

Transmitted light – Sample comprises finely-crystalline micrite intercalated by veined by opaques (sphalerite and galena) and dolomite.

Reflected light – Sulphide assemblage comprises sphalerite with sub-ordinate galena with dolomite vein core. Sphalerite and galena preferentially develops along intercrystalline calcite boundaries, particularly in finely-crystalline calcite. Galena is often subhedral and exhibits sphalerite overprinting, though sphalerite exhibits a psuedodendritic texture from heavily resorbed galena (Fig N1 and N2).

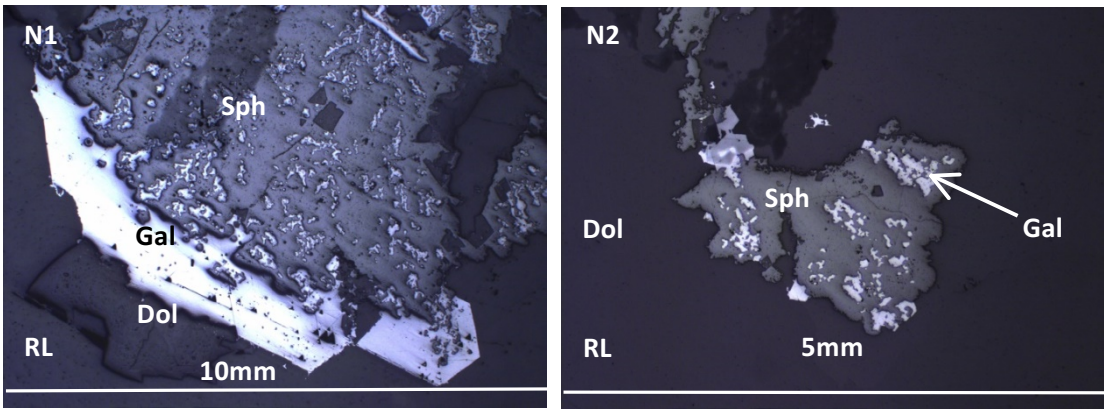

Fig N1 – Sphalerite replacing galena exhibiting heavily resorbed, pseudodendritic texture

Fig N2 – Pseudodendritic galena texture in replacive sphalerite

Mineral	Pre-mineralisation	Main-stage mineralisation	Post-mineralisation
Calcite	———		
Sphalerite		———	
Galena		———	
Sulphosalts		———	
Dolomite (vein)		———	

Fig N3 - Paragenesis of N01579-1

10.3.2.2. N00996-3 – 577.4 metres (5-Lens)

Lithology – Micrite

Transmitted light – Only minor matrix is still present, comprising finely crystalline calcite. Sample matrix and sulphide is cross-cut by fine-medium crystalline veins.

Reflected light – Sulphides comprises heavily banded sphalerite and sub-ordinate galenas. Banding varies from planar to showing a weakly-developed kink texture. Euhedral galenas are observed along outer margin of the sphalerite banding, while discontinuous galena banding is observed between sphalerite. Rare mutually intergrown galena and sphalerite are also observed, while rare intercrystalline galena is observed in matrix.

Framboidal pyrites are paragenetically first, followed by sphalerite and galena. Subhedral galenas often replace sphalerite margins (Fig O1) or occur as cross-cutting veins (Fig O2), though may also form discrete discontinuous banding in between sphalerites (Fig O3). Galena-calcite veining is observed to cross-cut both sphalerite and galena banding. Rare sulfosalts are observed in galena. Minor pyrite (Fig O5) and chalcopyrite overgrowth of galena (I.e. post sphalerite and galena co-precipitation) is observed.

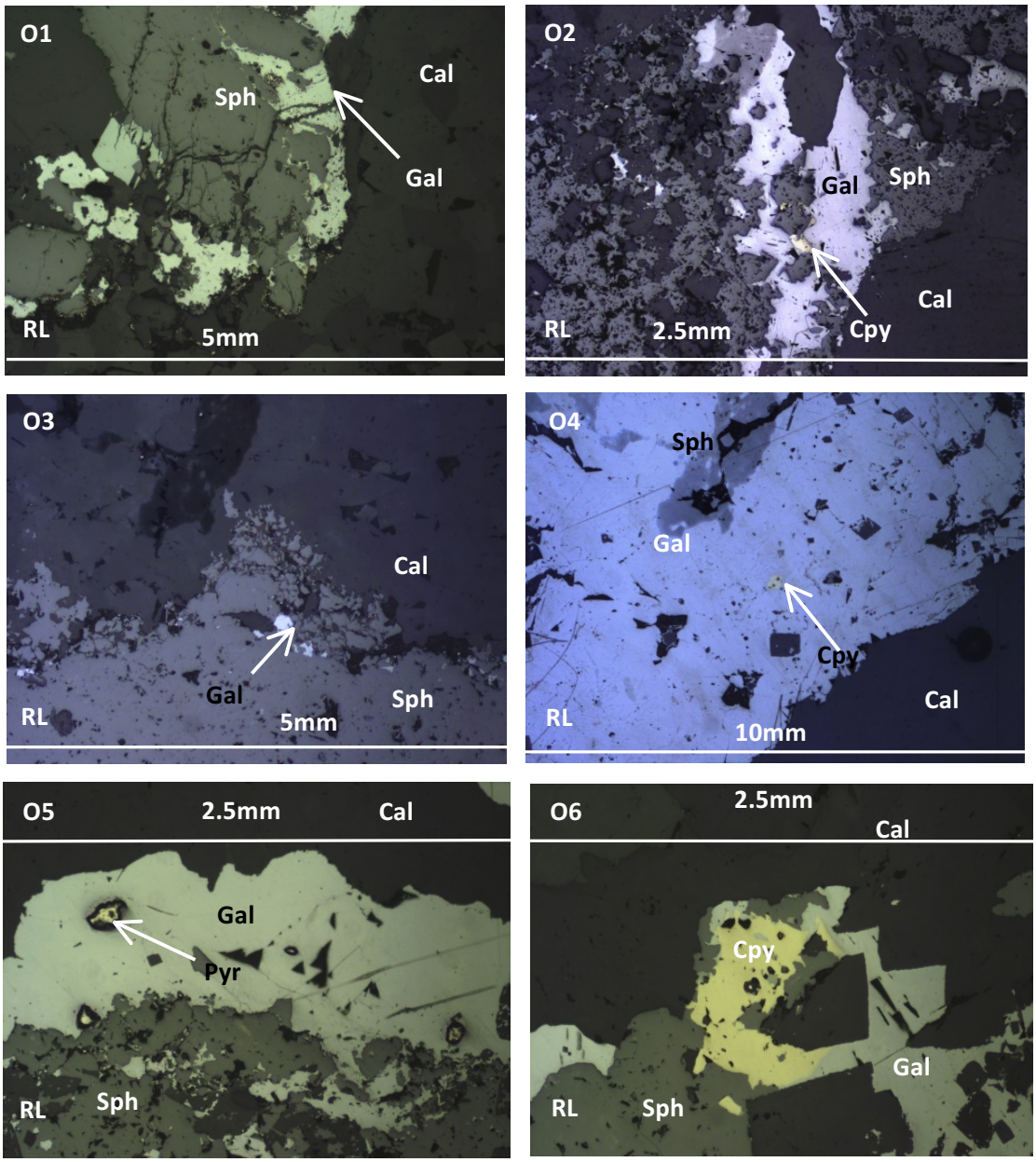

Fig O1 – Sphalerite variably replacing galena along thin calcite veinlets cross-cutting galena

Fig O2 – Finely-crystalline galena veinlet cross-cutting sphalerite banding

Fig O3 – Fig P1

Fig O4 – Coarsely-crystalline galena with minor chalcopyrite overprint

Fig O5 – Sphalerite mantled by galena, in turn exhibiting minor pyrite overprint

Fig O6 – Chalcopyrite overprinting euhedral sphalerite and galena

Mineral	Pre-mineralisation	Main-stage mineralisation	Post-mineralisation
Calcite			
Calcite (vein)			
Sphalerite			
Galena			
Sulphosalts			
Chalcopyrite			
Pyrite			
Calcite (fibrous vein)			

Fig O7 - Paragenesis of N00996-3

10.3.2.3. N00996-4 – 577.4 metres (5-Lens)

Lithology – 5-Lens Dolomite

Transmitted light – Sample matrix comprises finely-crystalline planar/non-planar dolomite, sub-rounded to well-rounded quartz grains, and finely-crystalline calcite with modal abundances of 50, 35, and 15%, respectively (Fig P1). Finely-crystalline calcite occurs as a single generation of thin calcite veinlets and nodules.

Reflected light – Sparse pyrite and galena are observed in matrix

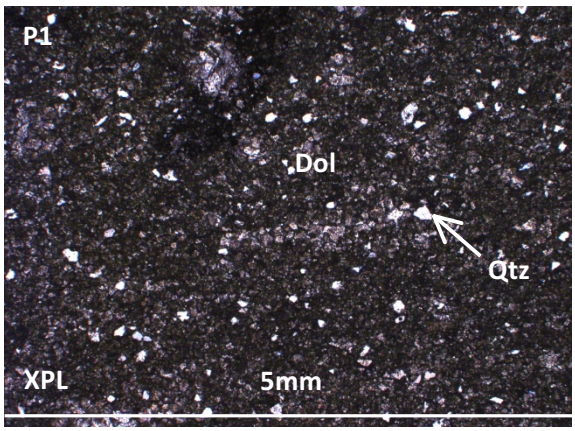

Fig P1 – PPL: Matrix texture of N00996-4

Mineral	Pre-mineralisation	Main-stage mineralisation	Post-mineralisation
Calcite			
Dolomite (planar/non-planar)			
Pyrite			
Galena			
Calcite (vein)			
Calcite (vugs)			

Fig P2 - Paragenesis of N00996-4

10.3.2.4. N01017-2 – 580.1 metres (5-Lens)

Lithology - Micrite

Transmitted light – Sample comprises finely-crystalline calcite, coarsely-crystalline celestite and fine-grained, euhedral quartz grains with a modal abundance of approximately 70, 25 and 5 percent, respectively. Sample matrix is cross-cut by three stages of calcite veining. The first comprises blocky crystalline calcite, in turn weakly cross-cut by radial celestites. Celestite is observed to mantle, though not overprint opaques. Calcite veining clearly cross-cuts sulphides at two stages – The first comprises blocky crystalline calcite, while the second consists of thin, finely-crystalline calcites which partially cross-cut sphalerite.

Reflected light – Sulphide assemblage comprises weakly banded sphalerite and accessory, non-overprinting galena. Banded sphalerite and galena is cross-cut by three generations of veining:

1) Coarsely-crystalline calcite veining fully cross-cutting and dislocating sulphide mineralisation.
2) Radial celestites that cross-cut coarsely-crystalline calcite veining and mantle banded sphalerites.
3) Thin, finely-crystalline calcites that partially cross-cut sphalerites.

Sphalerite and galena are disseminated in the groundmass. Sulfosalts in solid state with galena are rarely observed, though they may occur along galena crystal rims. Galena is also observed to be replaced by marcasite and minor chalcopyrite.

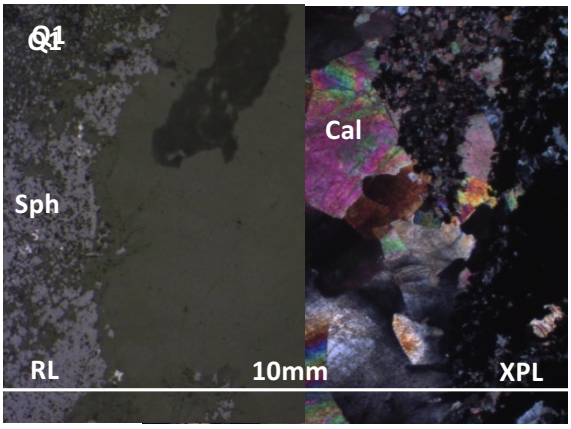

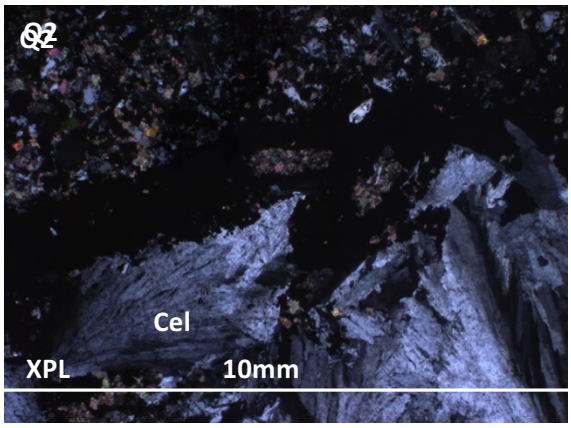

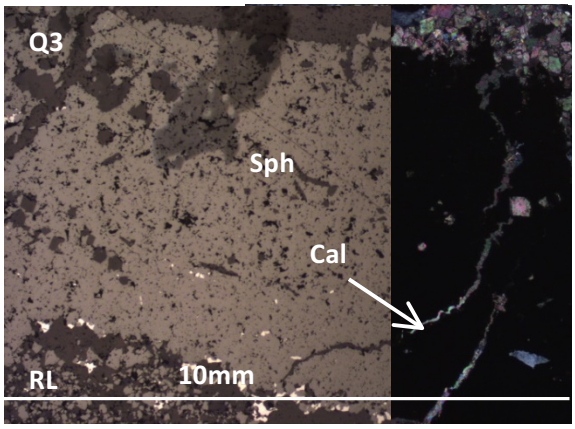

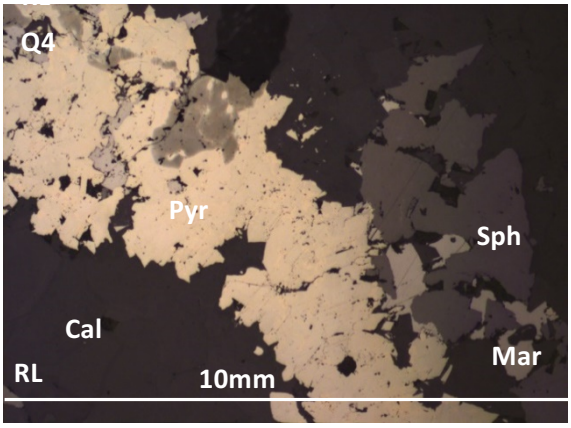

Fig XA –Coarsely-crystalline calcite cross-cutting weakly banded sphalerite

Fig XB –Celestite mantling and partially overprinting weakly banded sphalerite

Fig XC – Coarsely-crystalline sphalerite rimmed by minor galena and cross-cut by thin calcite veinlets

Fig XD –Coarsely-crystalline pyrite and marcasite mantling and partially replacing sphalerite and galena

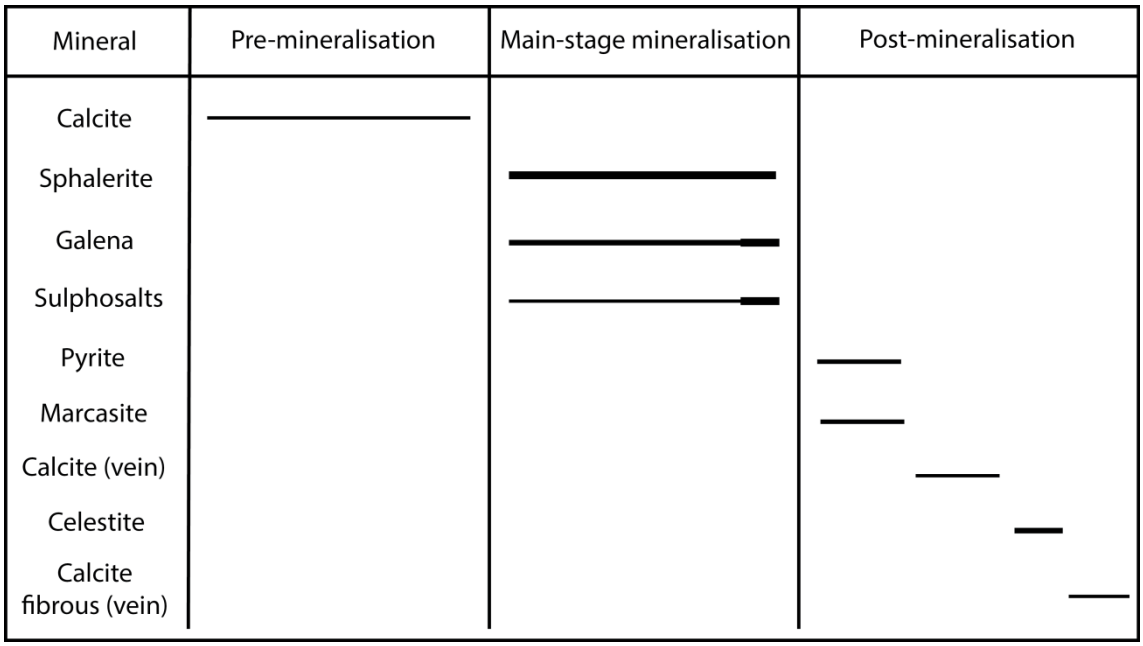

Fig Q5 - Paragenesis of N01017-2

10.3.2.5. N01117-3 – 635.9 metres (5-Lens)

Lithology – 5-Lens Dolomite

Transmitted light – Sample consists of abundant quartz, planar/non-planar dolomite and opaques with modal abundances of 50, 45, and 5%, respectively (Fig R1). Quartz grains are sub-rounded to well-rounded. Sample is cross-cut by one generation of thin calcite veinlets.

Reflected light – Sparse galena and sphalerite is observed in the matrix.

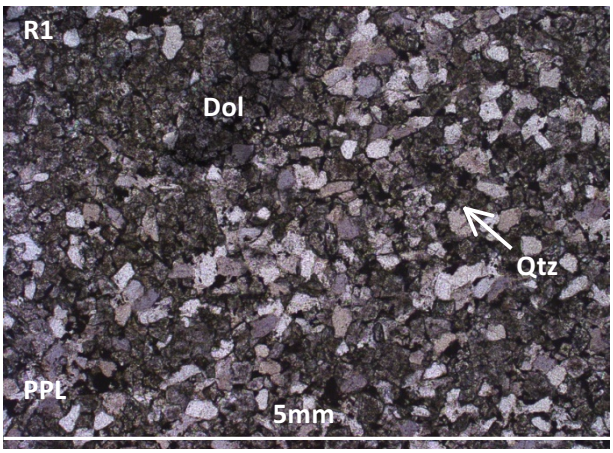

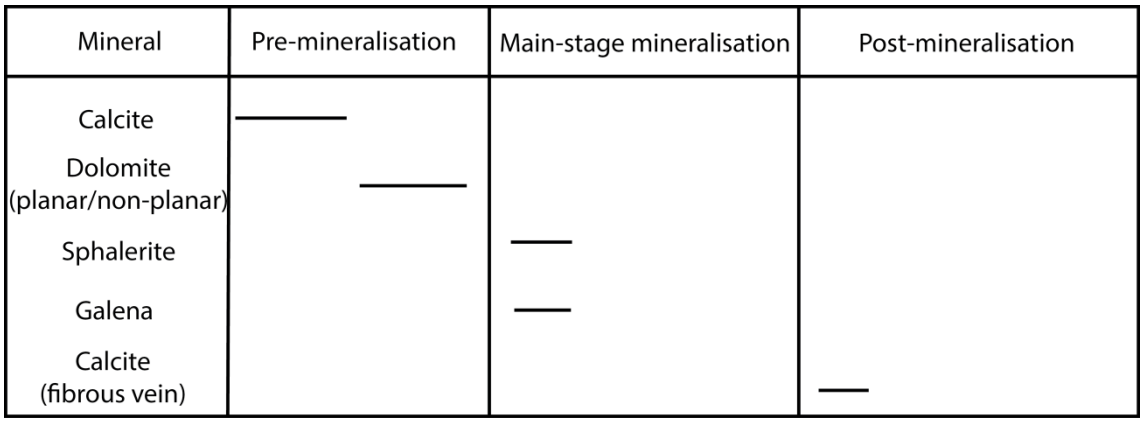

Fig R2 - Paragenesis of N01117-3

10.3.2.6. N01269-1 – 656.1 metres (5-Lens)

Lithology – 5-Lens Dolomite

Transmitted light – Sample comprises finely-crystalline dolomite, sub-rounded to well-rounded quartz grains and sparse calcite, with modal abundances of 50, 40 and 5%, respectively. The remainder comprises sparse opaques.

Reflected light – Sparse galena and sphalerite observed throughout matrix. Sphalerite is cross-cut by one generation of calcite veinlets.

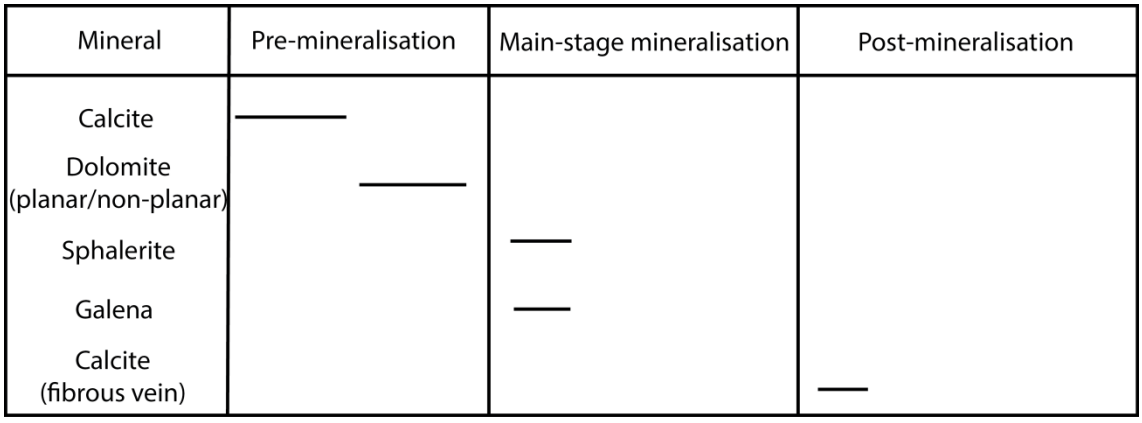

Fig S1 - Paragenesis of N01269-1

10.3.2.7. N01269-2 – 655.9 metres (5-Lens)

Lithology – Sphalerite-calcite veining

Transmitted light – Sample comprises coarsely-crystalline, interlocking calcite and celestite with abundant opaques (sphalerite). Sample matrix is variable, consisting of finely crystalline calcite, calcite nodules, coarsely-crystalline radial celestites and sphalerite. Paragenesis can be divided into five stages:

1) Initial finely-crystalline calcite cement

2) Sphalerite intergrown between finely-crystalline calcite cement (Fig T1)
3) Coarsely-crystalline, barren calcite veining.
4) Thin calcite veinlets cross-cutting sphalerite
5) Coarsely-crystalline radial celestites – Partially replace coarsely-crystalline calcite veining and mantles sphalerite mineralisation (Fig T2).

Reflected light – Sulphide assemblage comprises sphalerite with minor galena intergrowth and rare overprinting pyrite. Sphalerite comprises unbanded, subhedral crystals intergrown between calcite and co-precipitated with minor galena (contains abundant sulfosalts). Sphalerite post-dates calcite vein stages 1-3 and is cross-cut by stage 4 calcite veinlets, and late-stage pyrite overprinting. Celestite is observed to mantle, though not replace sphalerite and galena, and appears to preferentially develop in remaining pore space. Sulphides are cross-cut by stage 3 coarsely crystalline calcite, while galena veinlets cross-cut early sphalerite (Fig T3).

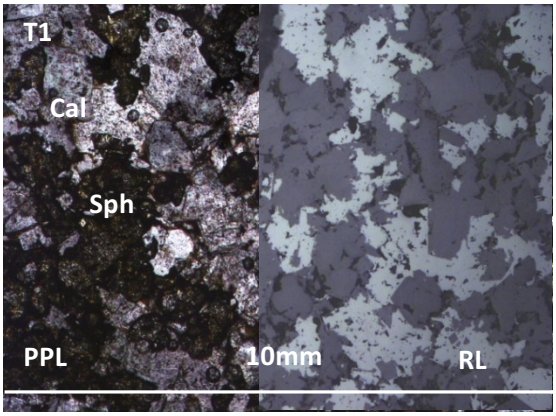

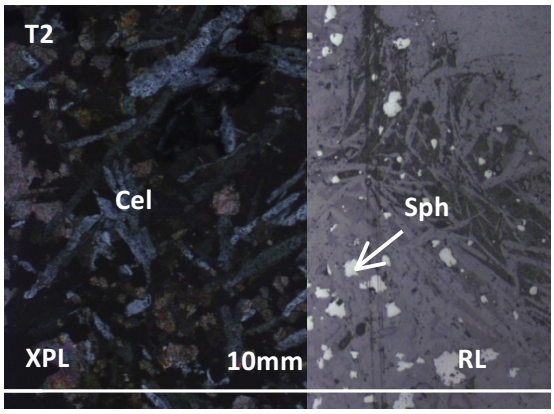

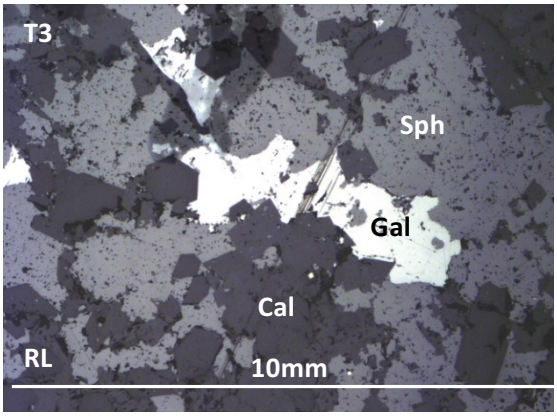

Fig T1 – Intercrystalline, anhedral sphalerite developing between calcites

Fig T2 – Left: XPL: Acicular, randomly orientated celestites. Right: RL: Finely-crystalline sphalerite intercalating celestite

Fig T3 – Minor galena cross-cutting sphalerite as thin veinlet

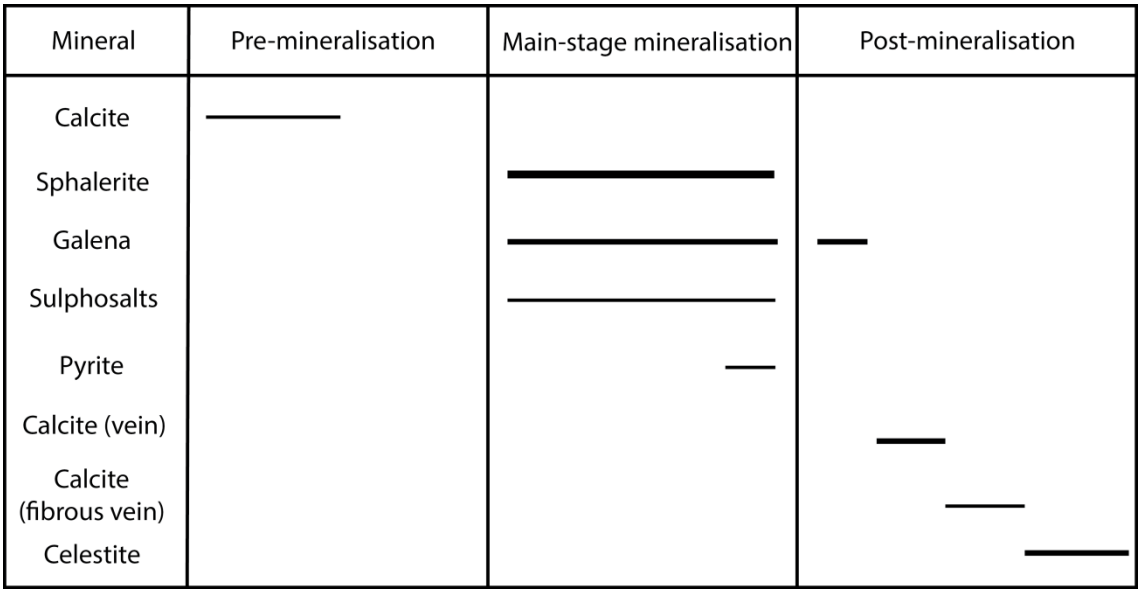

Fig T4 – Paragenesis of N01269-2

10.3.2.8. N01073-1 – 720.7 metres (5-Lens)

Lithology – Mineralised micrite

Transmitted light – Sample matrix comprises abundant fossil debris hosted in a calcite cement. Fossil debris comprises abundant stick bryozoan and shelly bivalve debris. Sample is cross-cut by a banded sulphide vein containing a blocky calcite-celestite core. Sphalerite is the dominant vein sulphide mineral, exhibiting well-developed planar banding and minor interstitial calcite. Calcite veining is observed at sphalerite and galena boundaries, and between sphalerite banding. Sphalerite exhibits well-defined planar-boytroidal banding and contains celestite laths (co-precipitated?) orientated perpendicular to the vein axis. Minor calcite cross-cut sphalerite banding.

Reflected light – Mineralisation consists of planar-boytroidal banded sphalerites, galena and replacive chalcopyrite, in turn overprinted by minor sphalerite. The outer- vein consists of discontinuous banded sphalerite, with a “halo” of disseminated sphalerite observed in the matrix (Fig U1). The next innermost vein phase comprises subhedral-euhedral galenas overprinted by minor subhedral sphalerite (Fig U2). Third stage veining consists of boytroidal sphalerite, accessory galena and minor, intercalating calcite (Fig U3). The centre of the vein comprises blocky, coarsely-crystalline calcite and intercalating celestite. Rare celestite laths trending perpendicular to the vein axis can be observed at all stages. Chalcopyrite is observed to overprint both galena and sphalerite, though is most abundant in second-stage veining and preferentially replaces galena. Sulfosalts in galena are almost entirely absent, though are rarely observed along the galena crystal rims. Minor gal-cal veinlets cross-cut stages one to three veining.

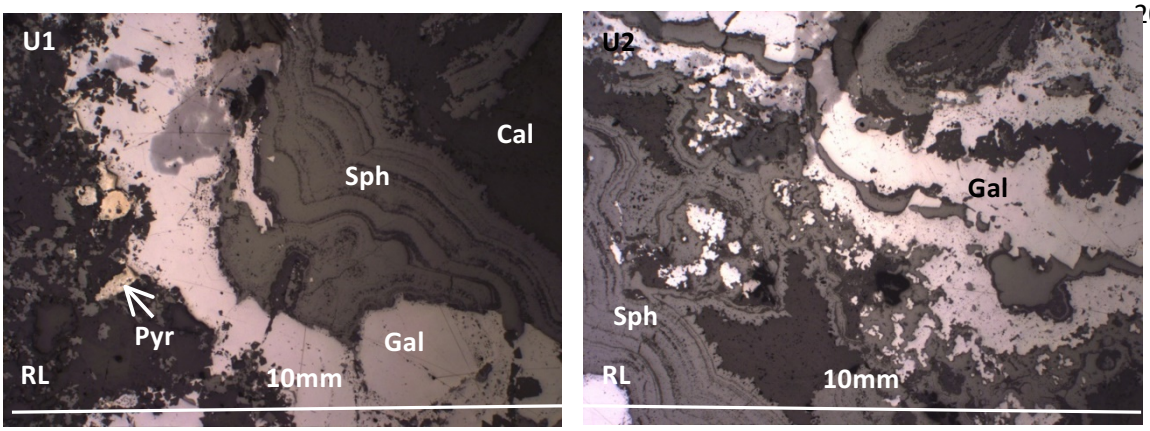

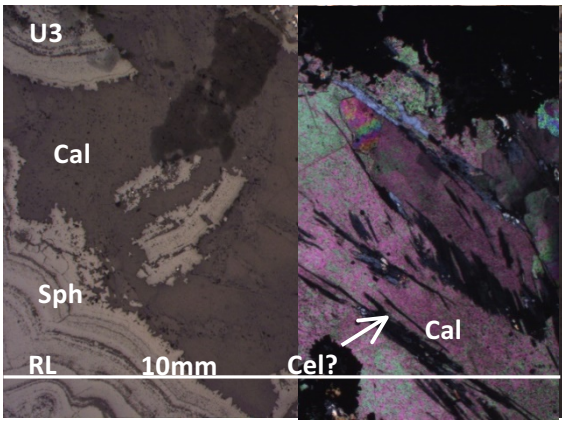

Fig U1 – Reflected light - Strongly-banded sphalerite mantled by blocky crystalline galena, exhibiting minor pyrite mantling and replacement (outer-inner vein)

Fig U2 – Reflected light - Strongly-banded sphalerite exhibiting mutual galena intergrowth (weakly boytroidal? – inner vein)

Fig U3 – Left: Reflected light – Strongly banded sphalerite texture in inner vein. Right – Cross-polarised light – Coarsely-crystalline calcite exhibiting intercalating medium-crystalline, acicular celestite (vein core)

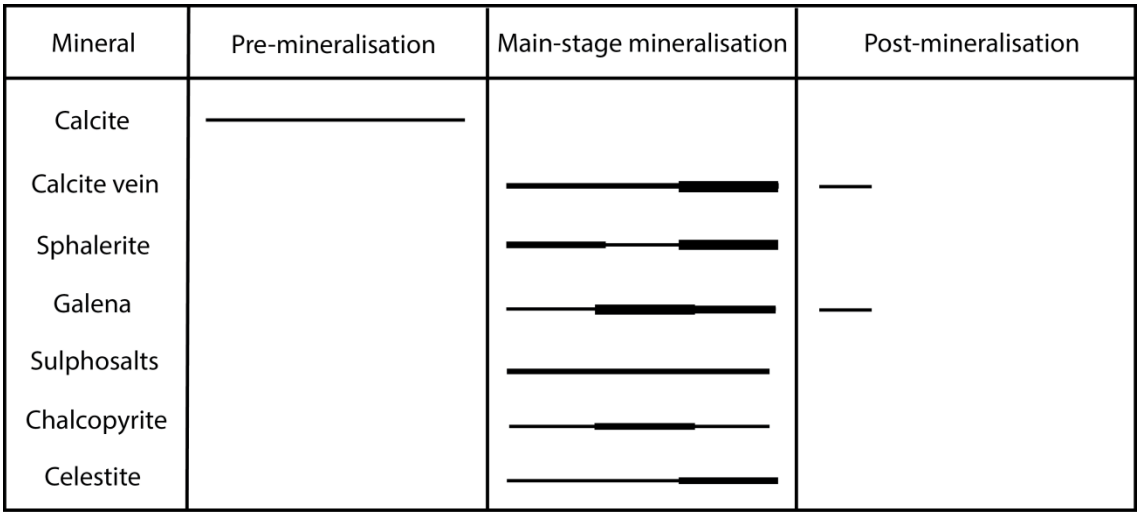

Fig U4 - Paragenesis of N01073-1

10.3.2.9. N01073-2 – 720.7 metres (5-Lens)

Lithology – Fossiliferous, peloidal micrite

Transmitted light – Sample comprises fossiliferous micrite exhibiting patchy dolomitisation, though shelly bioclasts show notably greater dolomitsation. Fossil content consists of abundant branch bryozoan and shelly bivalve debris. Sample matrix is cross-cut by one generation of thin, medium crystalline calcite veining

Reflected light – Sulphide assemblage comprises sphalerite and galena and abundant, later-stage replacive pyrite (Fig V1). Sphalerite is observed to occur as a weakly replacive phase for both bioclasts and galena. Galena may replace pre-existing bioclasts (shelly debris?), though also appears to be a cavity fill (Fig V2).

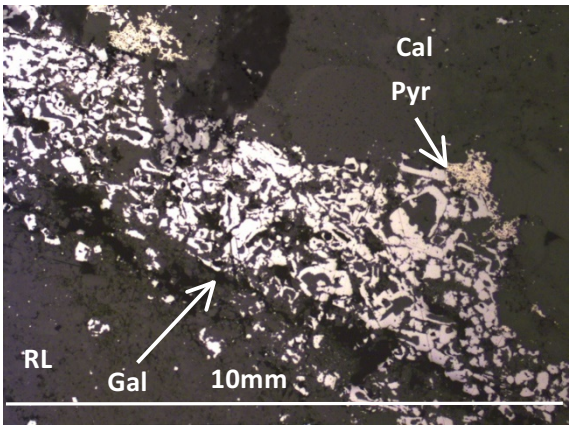

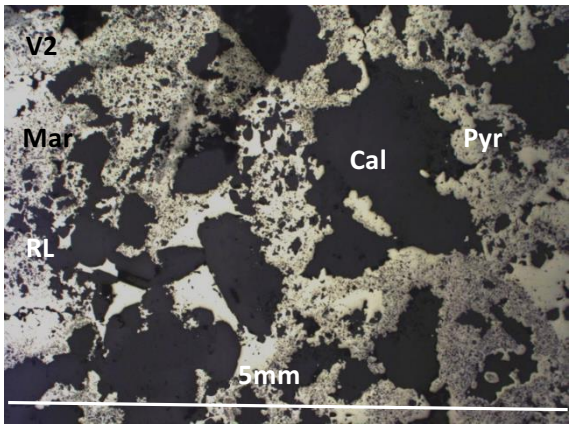

Fig V1 – Subhedral, tabular galenas variably developing around calcites (minor cavity fills)

Fig V2 – Anhedral pyrite developing between medium-crystalline calcite – galena contacts

Mineral	Pre-mineralisation	Main-stage mineralisation	Post-mineralisation
Calcite	—		
Calcite (vein)	—		
Galena		—	
Pyrite		—	
Marcasite		—	

Fig V3 - Paragenesis of N01073-2

10.3.2.10. N01073-2 - 727.7 metres (5-Lens)

Lithology – Dolomitised micrite

Transmitted light – Sample consists of fossiliferous and weakly peloidal micrite, exhibiting pervasive dolomitisation along a thin argillite band (Fig W1). Matrix consists of shelly bivalve, crinoid and stick bryozoan debris, peloids and calcite cement. At least two generations of finely-crystalline calcite veining are observed, one of which breaches argillite band.

Reflected light – Sulphide assemblage consists of pyrite (Fig W2) and rare subhedral galena. Pyrite preferentially develops in undolomitised matrix and mantles early-stage calcite veining.

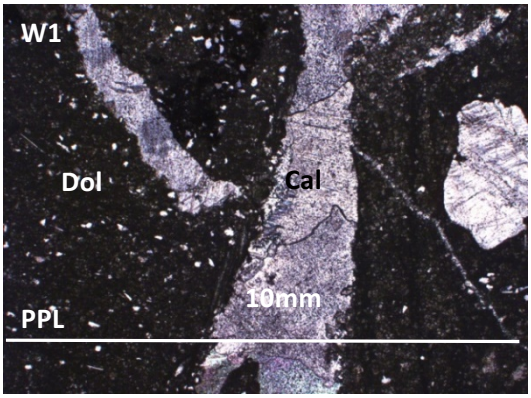

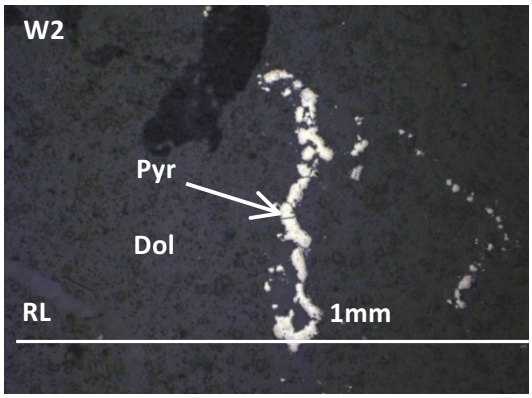

Fig W1 – Thick, coarsely-crystalline calcite vein breaching argillite band

Fig W2 – Anhedral pyrite

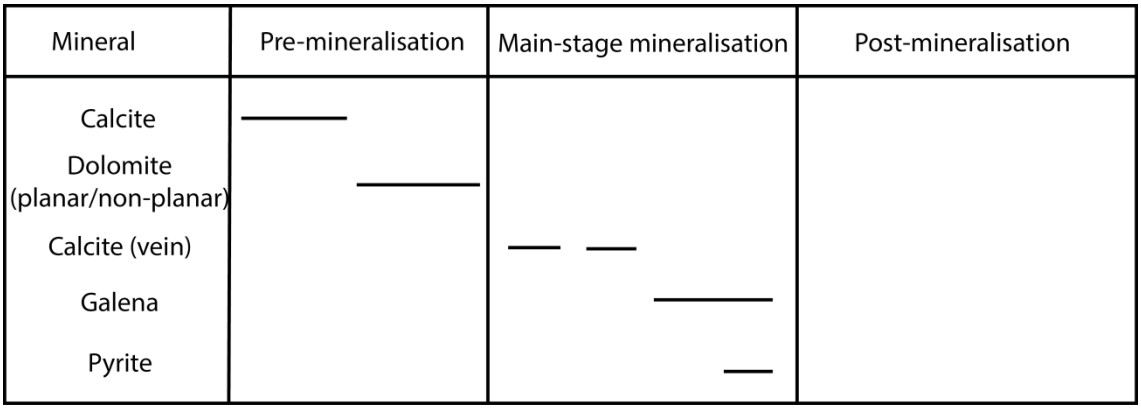

Fig W3 – Paragenesis of N01073-3

10.3.2.11. N01155-4 – 769 metres (5-Lens)

Lithology – 5-Lens Dolomite

Transmitted light – Sample comprises heavily dolomitised calcite cement and abundant sub-rounded to well-rounded quartz grains cross-cut by three generations of fine-coarsely crystalline calcite veins, veinlets and nodules. Calcite paragenesis can be divided into four stages:

1) Fine-coarsely crystalline calcite veining which post-dates dolomitisation
2) Coarsely crystalline calcite nodules rarely overprinting stage 1 veining
3) Finely crystalline calcite veinlets, cross-cutting stages 1 and 2

Reflected light – Sparse galena and sphalerite observed in thin styolite bands, as well as in matrix.

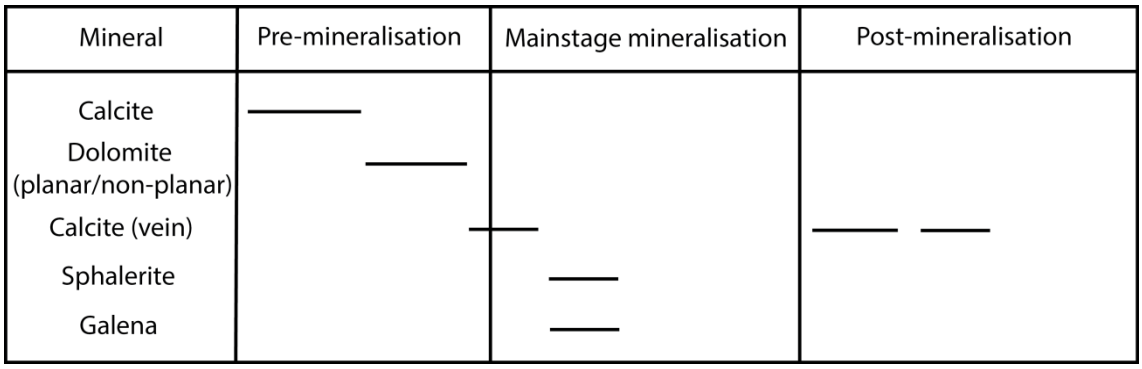

Fig X1 – Paragenesis of N01155-4

C-C' Transect

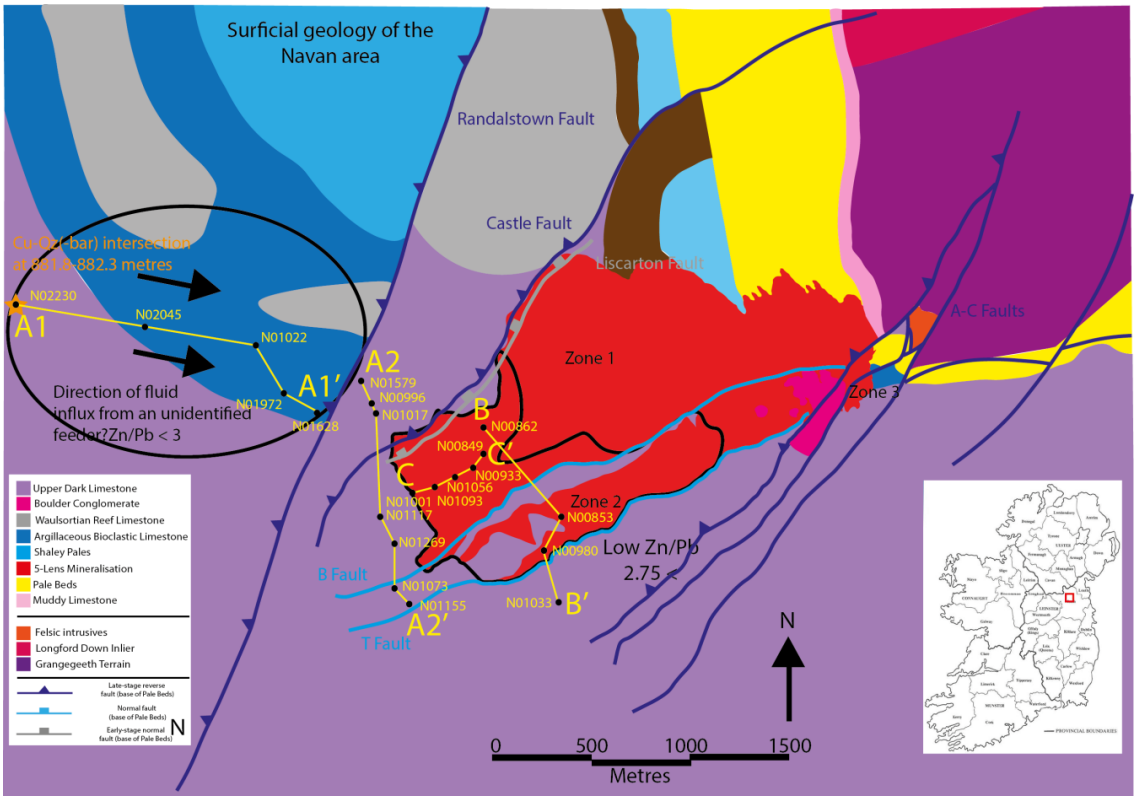

Fig 10.3. Geology of the Navan area with 5-Lens, low Zn/Pb areas and drillhole transects overlain on surficial geology

10.3.3.

10.3.3.1. N01001-1 – 613.7 metres (5-Lens)

Lithology – 5-Lens Micrite

Transmitted light – Sample matrix comprises rare ooids and sub-angular quartz grains hosted in finely-crystalline, variably dolomitised calcite matrix. At least two vein stages are identified:

1) Medium-crystalline, barren calcite.
2) Coarsely-crystalline, radiaxial fibrous celestite that variably cross-cut and overprint first-stage calcite veining. Celestites are often observed to mantle, though not replace opaques.

Reflected light – Sulphide assemblage comprises minor disseminated euhedral pyrites and later medium-crystalline, subhedral galenas with minor co-precipitated sphalerite. Sphalerite may also occur as a minor rim replacement phase, while galenas retain relict ooid textures (Fig Y2). Chalcopyrite is observed as a rare replacement phase. Rare sulfosalts are observed in solid state with galena.

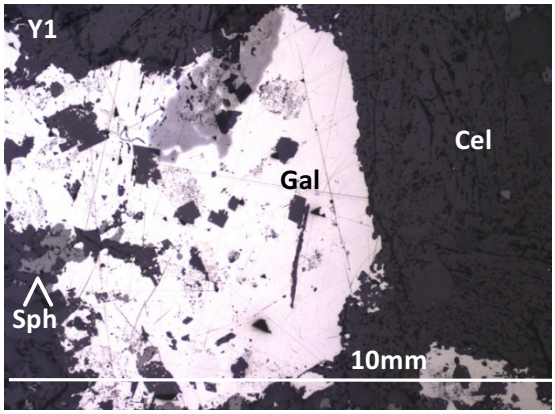

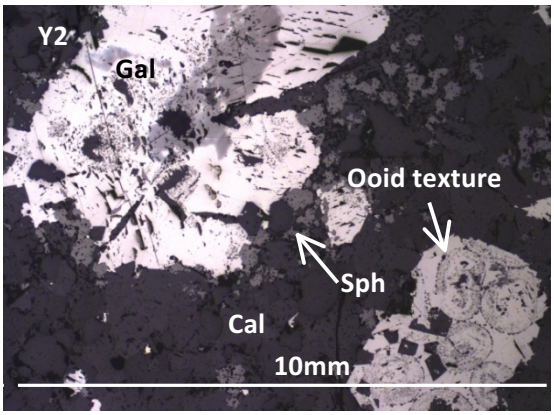

Fig Y1 – Coarsely-crystalline galena mantled by radiaxial celestite

Fig Y2 – Coarsely crystalline galenas retaining relict ooid textures

Mineral	Pre-mineralisation	Main-stage mineralisation	Post-mineralisation
Calcite	—		
Calcite (vein)	—		
Pyrite		—	
Galena		—	
Sphalerite		—	
Sulphosalts		—	
Celestite			—

Fig Y3 – Paragenesis of N01001-1

10.3.3.2. N01001-2 – 623.1 metres (5-Lens)

Lithology – Quartz grain-rich, fossiliferous micrite

Transmitted light – Sample comprises very finely-coarsely crystalline calcite, shelly bivalve and branch bryozoan debris, and abundant sub-angular quartz grains with modal abundances of approximately 40, 30, 20 and 10% respectively. Sample is cross-cut by three generations of calcite veinlets, the last of which is overprinted by coarsely-crystalline calcite nodules. Medium crystalline, semi-radiaxial celestites are cross-cut by calcite veining.

Reflected light – Sulphide assemblage comprises matrix-disseminated galena and rare co-precipitated sphalerite. Galena is co-precipitated with minor planar dolomite. Pyrite is commonly observed to mantle disseminated sulphides. Sulfosalt mineralisation in galenas is rare.

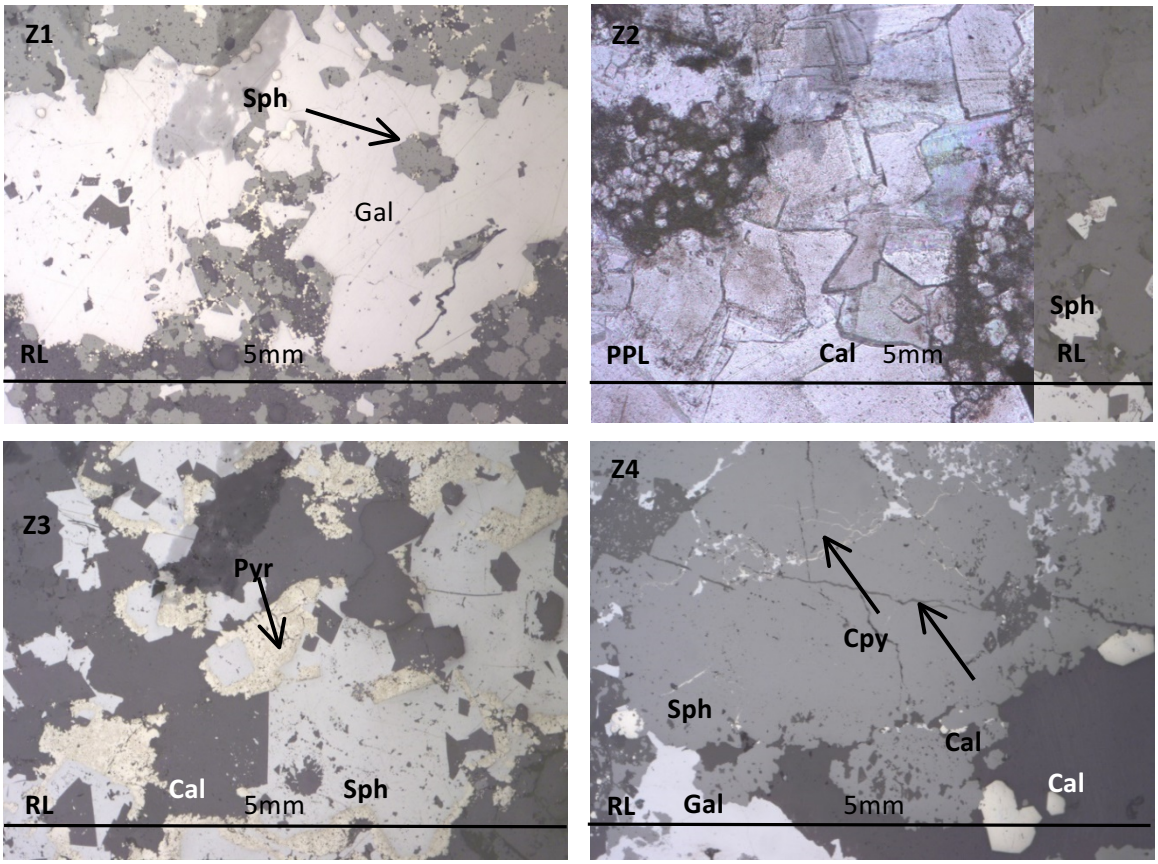

Fig Z1 – Coarsely-crystalline galena and co-precipitated minor sphalerite. Very finely-crystalline disseminated pyrite observed at gal-sph-cal crystal contacts.

Fig Z2 – Finely-crystalline galena at scalenohedral calcite vein – wall-rock contact

Fig Z3 – Pyrite variably overprinting euhedral galena

Fig Z4 – Coarsely-crystalline sphalerite cross-cut by fine chalcopyrite, in turn cross-cut by thin calcite veinlets

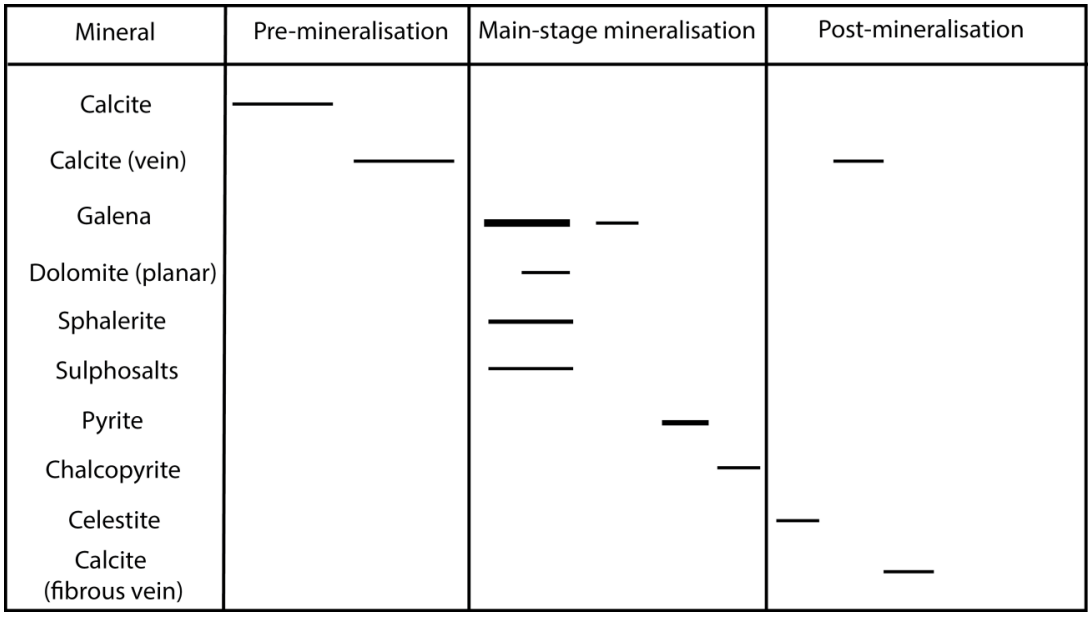

Fig Z5 – Paragenesis of N01001-2

10.3.3.3. N01001-4 – 622.1 metres (5-Lens)

Lithology – 5-Lens Dolomite

Transmitted light – Sample matrix comprises very finely-crystalline planar/non-planar dolomite. Four generations of veining that post-date dolomitisation are observed:

1) Early-stage coarsely-crystalline calcite veining rimmed by opaques (Fig AA1).
2) Single-stage opaques exhibiting rare cross-cutting relations with stage one veining (Fig AA3)
3) Medium-crystalline, barren calcite that cross-cuts vein stages 1 and 2 (Fig AA4).
4) Radiaxial fibrous calcite nodules that overprint stage 3 veining.

Reflected light – Sulphide assemblage comprises early-stage, matrix-disseminated pyrite, followed by later vein sphalerite and galena. Stage one vein sulphides comprise mutually intergrown sphalerite and galena exhibiting a pyrite overprint, while the coarsely-crystalline calcite vein core is barren. Stage 2 veining consists of galena, minor co-precipitated sphalerite and minor overprinting pyrite restricted to the vein rim. Minor sphalerite mantling galena is also observed.

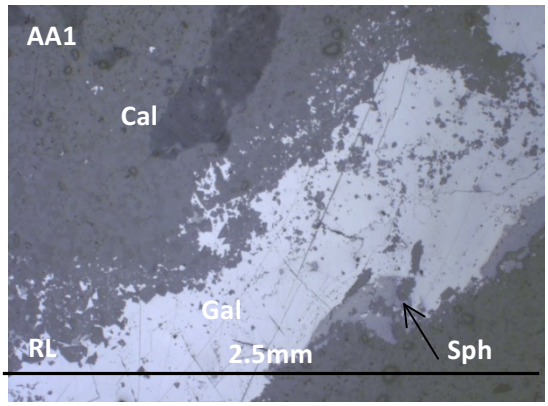

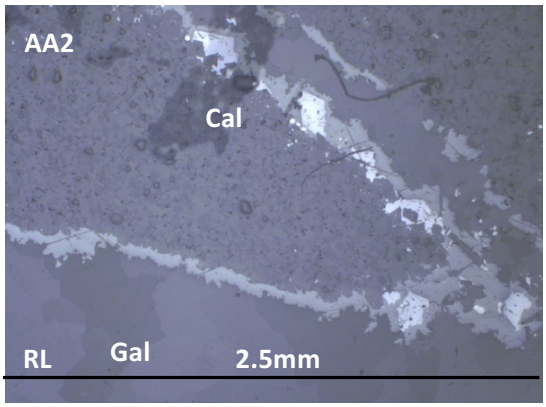

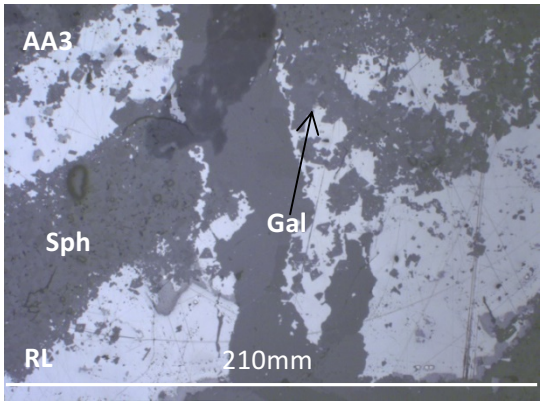

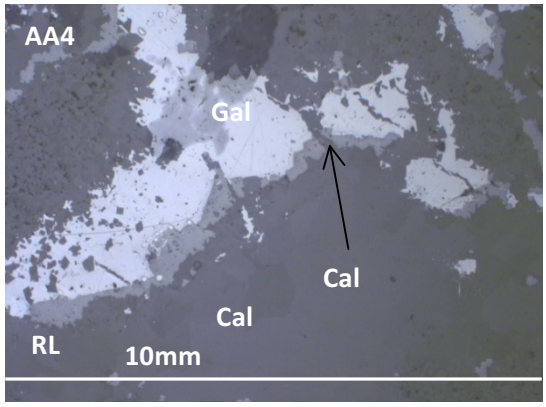

Fig AA1 – Coarsely-crystalline galena

Fig AA2 – Sphalerite and galena developing along vein – wall-rock contact

Fig AA3 – Coarsely-crystalline calcite vein cross-cutting galena

Fig AA4 – Sphalerite and galena variably cross-cut by calcite veining

Mineral	Pre-mineralisation	Main-stage mineralisation	Post-mineralisation
Calcite	———		
Dolomite (planar/ non-planar)	———		
Galena		———	
Sphalerite		———	
Calcite (RFC)		———	

Fig AA5 – Paragenesis of N01001-4

10.3.3.4. N01056-1 – 523.3 metres (5-Lens)

Lithology – 5-Lens Dolomite

Transmitted light – Sample comprises silt-rich, very finely-crystalline planar/non-planar dolomite. Radiaxial fibrous calcites are also observed.

Reflected light – Sulphide assemblage comprises banded sphalerite and galena-calcite veining and minor matrix-disseminated sphalerite and galena (Fig AB1 and AB2). Sulphide vein assemblage from wall contact inward comprises sph-gal – gal – sph-gal – calcite (Fig AB1 and AB2). Sphalerite exhibits weak interlayering with galenas, which in turn exhibit minor sphalerite co-precipitation. Inner vein sphalerite exhibits weak boytroidal banded sphalerites. Sulfosalts form very-finely crystalline as solid state laths in galena. Sulphides are cross-cut by minor calcite veinlets (Fig AB2) and minor galena (Fig AB3).

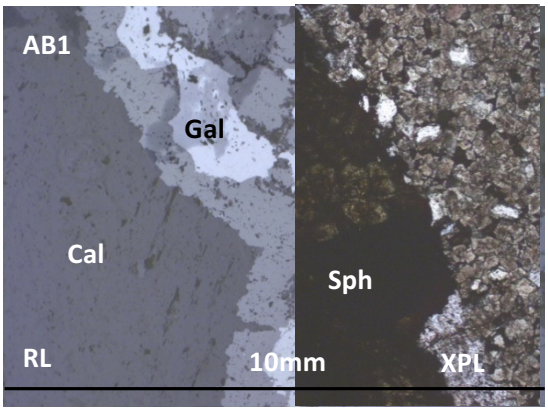

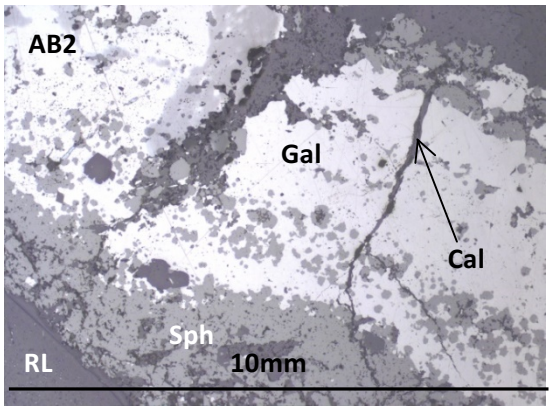

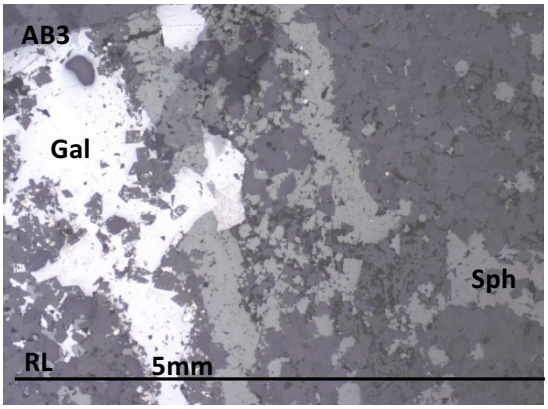

Fig AB1 – Sph-gal-sph vein

Fig AB2 – Banded sph-gal-sph cross-cut by late-stage calcite veining

Fig AB3 –Coarsely-crystalline galena with barely visible sulfosalts

Fig AB4 – Medium-crystalline galena cross-cutting sphalerite

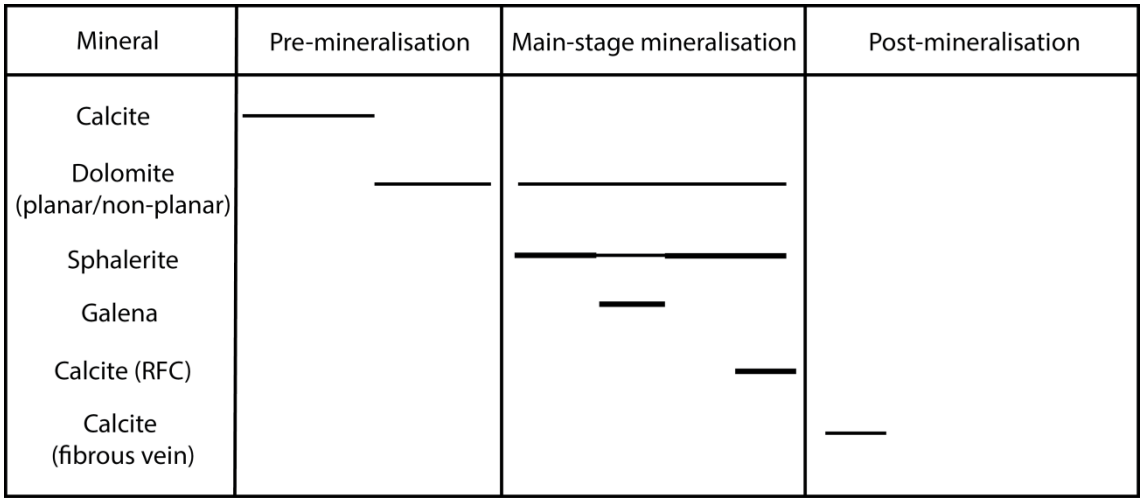

Fig AB5 – Paragenesis of N01056-1

10.3.3.5. N01093-1 – 593.7 metres (5-Lens)

Lithology – 5-Lens Dolomite

Transmitted light – Sample comprises very-finely crystalline dolomite. Matrix is non-pleochroic, non-birefringent and contains sparse calcite veinlets and nodules (single generation)

Reflected light – Sparse galena and pyrite observed

Mineral	Pre-mineralisation	Mainstage mineralisation	Post-mineralisation
Calcite	—		
Dolomite (planar/non-planar)	—		
Calcite (vein)	—		
Calcite (nodular)	—		
Sphalerite		—	
Galena		—	

Fig AC1 – Paragenesis of N01093-1

10.3.3.6. N01093-2 – 592.6 metres (5-Lens)

Lithology – Micrite

Transmitted light – Sample matrix comprises very finely-crystalline calcite, and shelly bivalve and finger and branch bryozoan. Sample is cross-cut by two generations of veining:

1) Medium-crystalline sulphide-calcite veining
2) Second generation calcite veining, often observed to mantle though not cross-cut stage 1 veining.

Reflected light – Sulphides comprise two textures – Vein sulphides consisting of sphalerite, galena and calcite (Fig AD1-AD2), and matrix disseminated sphalerite and galena associated with . Vein sulphides are multi-stage, comprising a “blebby” sphalerite and galena rim, outer coarsely-crystalline galena vein wall, finely-crystalline sphalerite interior and barren, coarsely-crystalline calcite core. Pyrite overprints sphalerite and galena vein mineralisation, particularly between sulphides and co-precipitated calcite crystals. Sphalerite and galena comprise the main matrix disseminated sulphides. Sulfosalt inclusions are observed in solid state with galenas.

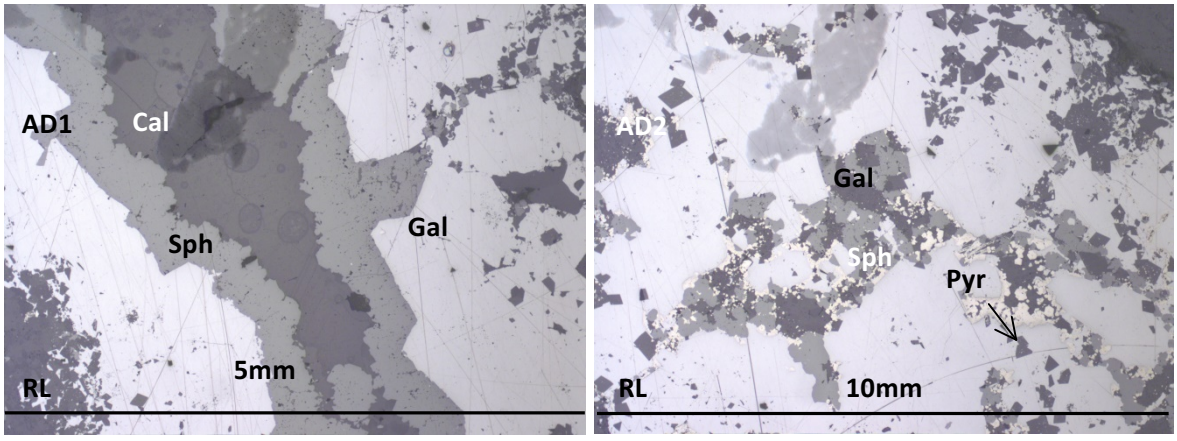

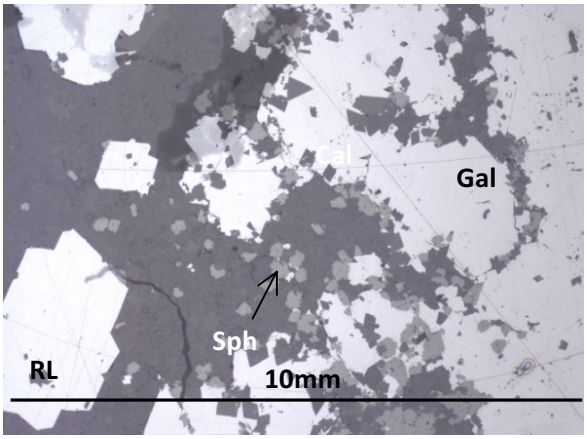

Fig AD1 – Subhedral galena co-precipitated with minor sphalerite and rhombic dolomites. Minor euhedral sphalerites observed to rim galena

Fig AD2 – Galena co-precipitated with dolomite rhombs. Tennantite laths are barely visible.

Fig AD3 – Galena rims being replaced by very finely-crystalline, euhedral sphalerites

10.3.3.7. N01093-4 – 584.1 metres (5-Lens)

Lithology – 5-Lens Dolomite

T**ransmitted light** – Sample comprises intensely dolomitised calcarenite – modal abundances of approximately 60% dolomite, 35% subhedral-euhedral quartz grains and 5% calcite (Fig AE1). Sparse, undolomitised calcite crystals may be observed.

Reflected light – Sparse galena and sphalerite observed as an intergranular phase in the matrix.

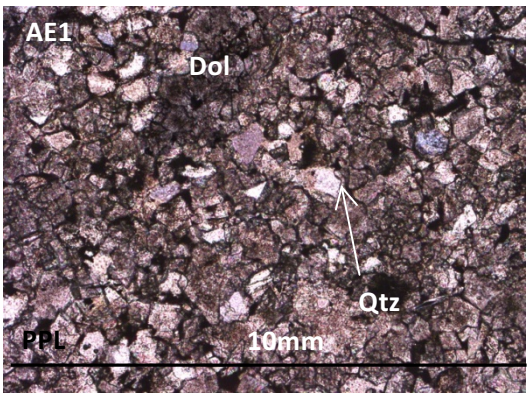

Fig AE1 – PPL: Matrix texture of N01093-4

Mineral	Pre-mineralisation	Mainstage mineralisation	Post-mineralisation
Calcite	———		
Dolomite (planar/non-planar)	———		
Sphalerite		———	
Galena		———	

Fig AE2 – Paragenesis of N01093-4

10.3.3.8. N00933-1 -507.4 metres (5-Lens)

Lithology – 5-Lens Micrite

Transmitted light – Sample comprises finely-crystalline calcite, fine-grained sub-angular quartz, and opaques, with respective modal abundances of approximately 60, 10 and 30%. The sample is cross-cut by coarsely-crystalline radiaxial fibrous calcite veining rimmed by medium-crystalline opaques. Minor, disseminated opaques are observed in the vein interior.

Reflected light –Vein sulphides associated with radiaxial fibrous calcite veining, and minor matrix-disseminated sphalerite and galena. Vein sulphides comprise medium-crystalline, mutually intergrown sphalerite, galena and dolomite rhombs, with a dolomite core (Fig AF1-AF3), while matrix-disseminated sphalerite and galena comprise very finely-crystalline subhedral-euhedral crystals (Fig AF4).

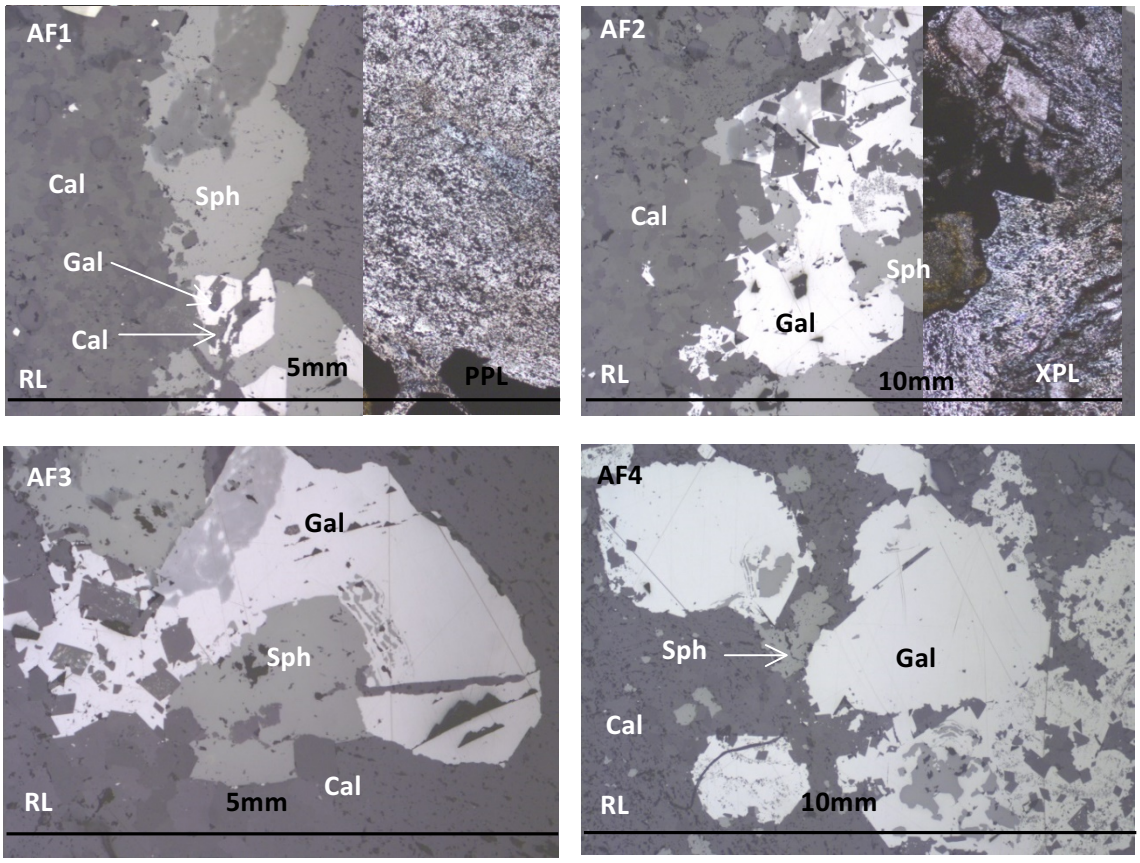

Fig AF1 – Mutually intergrown sphalerite and galena vein cross-cut by later-stage fibrous calcite

Fig AF2 – Subhedral galena variably replaced by sphalerite and intergrown with rhombic dolomites

Fig AF3 – Mutually intergrown sphalerite and galena with minor solid state sphalerite co-precipitation observed in galena crystal

Fig AF4 – Coarsely-crystalline galena and minor, co-precipitated sphalerite

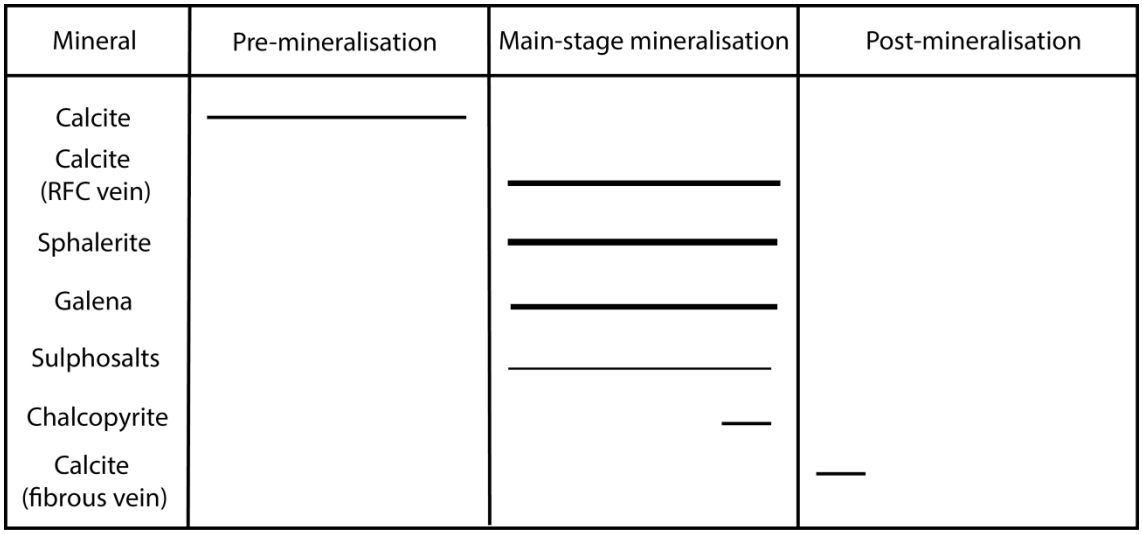

Fig AF5 – Paragenesis of N00933-1

10.3.3.10. N00933-2 – 508.6 metres (5-Lens)

Lithology – Clean, fossiliferous micrite

Transmitted light – Sample matrix comprises abundant forams, gastropods, shelly bivalve debris and rare coral fragments hosted in a finely-crystalline calcite cement. Groundmass exhibits weak dolomitisation, though fossil debris shows greater dolomitisation. Radiaxial celestites are observed along thin argillite bands separating dolomitised and undolomitised groundmass, and also mantle sulphides.

Reflected light – Minor, euhedral disseminated pyrite is paragenetically earliest and occurs both in dolomitised and undolomitised matrix. Sphalerite and galena are paragenetically later. Sphalerite may be either weakly layered, or occur as a very finely-crystalline dissemination in groundmass (preferentially where the matrix is non-dolomitised). Galenas are subhedral-euhedral and are observed to either co-precipitate with sphalerite, or more commonly mutually replace sphalerite (Fig AG1-AG4).

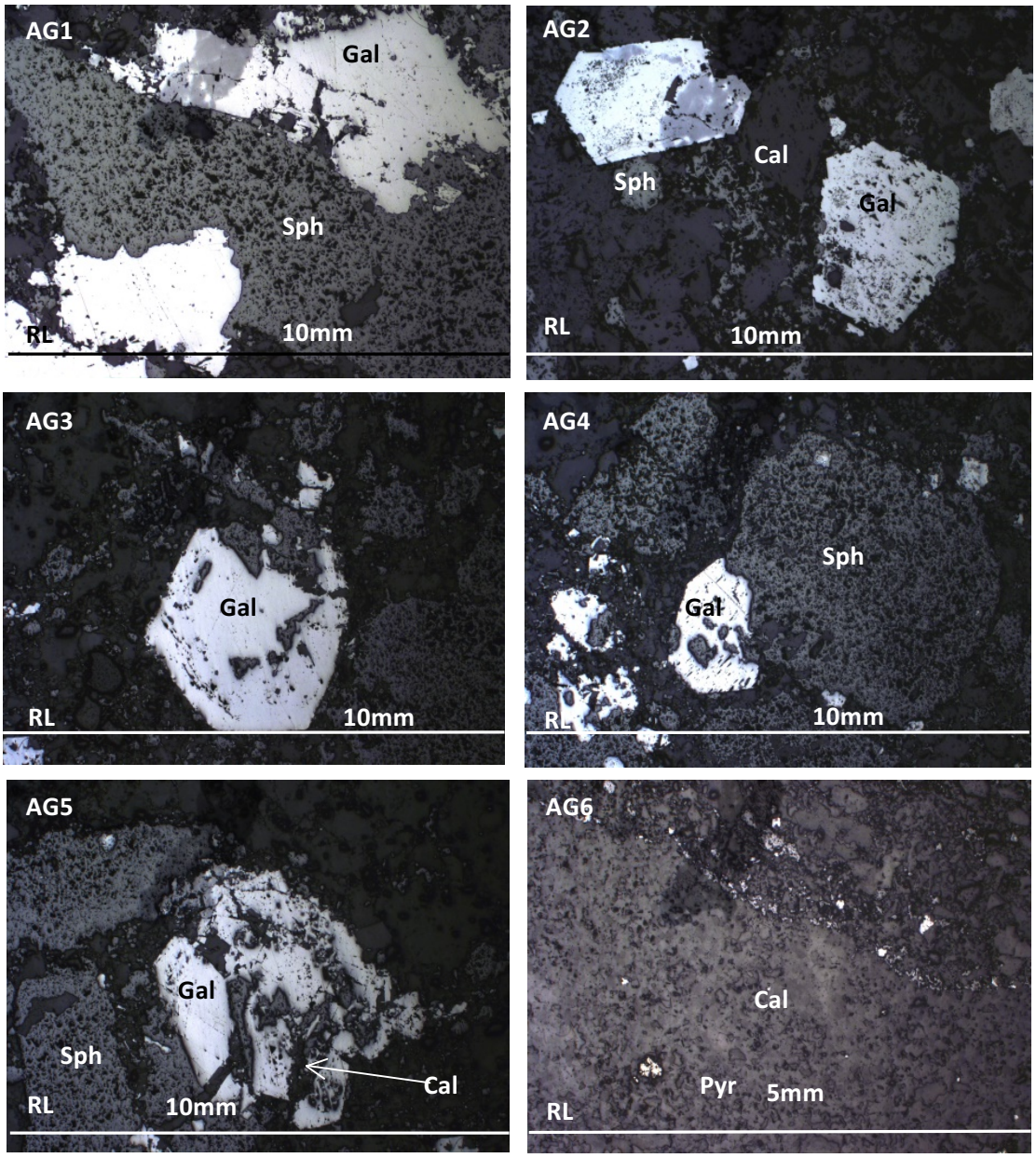

Fig AG1 – Subhedral galenas mantling and partially replacing sphalerite

Fig AG2 – Euhedral galenas.

Fig AG3 – Subhedral galena mantle coarsely-crystalline sphalerite

Fig AG4 – Euhedral galena exhibiting minor sphalerite replacement

Fig AG5 – Cross-cutting calcite in galena

Fig AG6 – Framboidal pyrite in matrix

Mineral	Pre-mineralisation	Main-stage mineralisation	Post-mineralisation
Calcite	———		
Framboidal pyrite		—	
Sphalerite		———	
Galena		———	
Chalcopyrite		—	
Celestite			—
Calcite (vein)			—

Fig AG7 – Paragenesis of N00933-2

10.3.3.11. N00933-3 – 506.8 metres (5-Lens)

Lithology – 5-Lens Dolomite

Transmitted light – Sample matrix comprises finely-crystalline dolomite, fine-grained sub-angular to sub-rounded quartz grains, finely-crystalline calcite and very finely-crystalline opaques, at respective abundances of approximately 60, 30, 8 and 2%. One generation of calcite-sphalerite veining is observed.

Reflected light – Sulphides comprise finely-crystalline, matrix-disseminated euhedral galena, and minor vein sphalerite-calcite (Fig AH1-AH2)

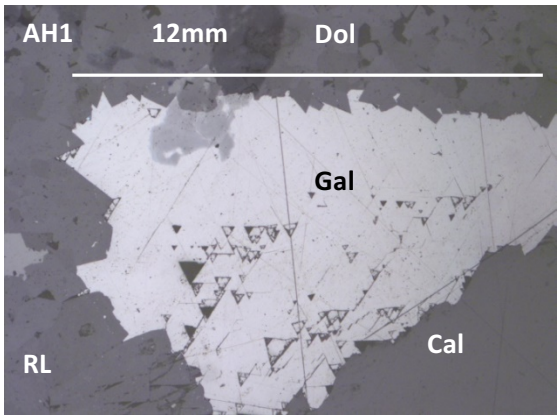

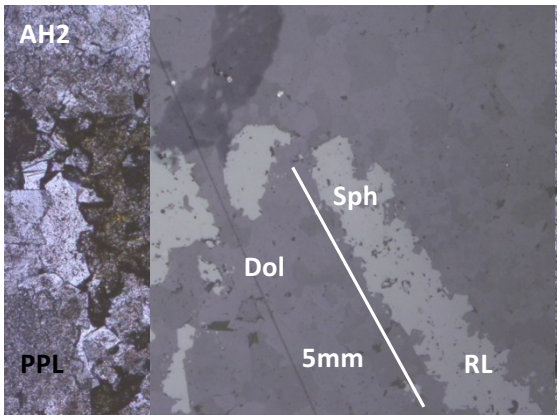

Fig AH1 – Subhedral, coarsely-crystalline galena

Fig AH2 – Finely-crystalline sphalerite-calcite veinlet

Mineral	Pre-mineralisation	Main-stage mineralisation	Post-mineralisation
Calcite Dolomite (planar/non-planar) Framboidal pyrite Sphalerite Galena Calcite (vein)	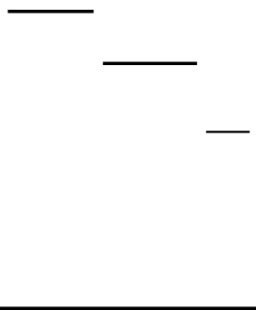	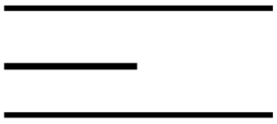	

Fig AH3 – Paragenesis of N00933-3

10.3.3.12. N00849-1 – 484.4 metres (5-Lens)

Lithology – Banded sphalerite, galena and pyrite

Transmitted light: Minor matrix is observed, comprising abundant forams, shelly debris and rare gastropod fragments hosted in a finely-crystalline calcite cement. Rare, blocky calcite vugs are observed.

Reflected light: Mineralisation consists of banded sphalerite, pyrite and galena. Pyrite is paragenetically earliest, and is either irregularly banding, or occurs as a common dissemination stage. Sphalerite and galena are paragenetically later and co-precipitate, comprising regular/irregular banding. Sphalerite and galena often mantle pyrite banding, though may also replace minor pyrite (Fig AI1-AI4), though minor pyrite post-dating sphalerite and galena may also be observed (Fig AI5). Galena and tennantite are often intergrown (Fig AI6-AI7).

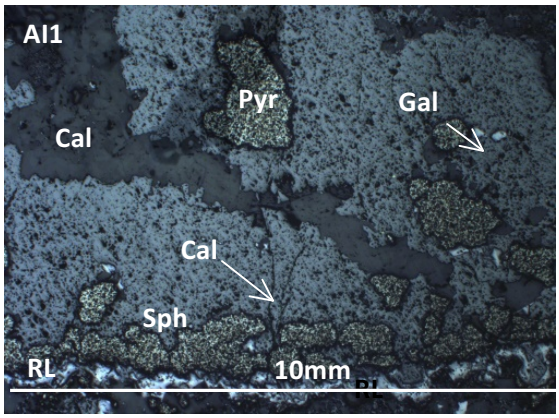

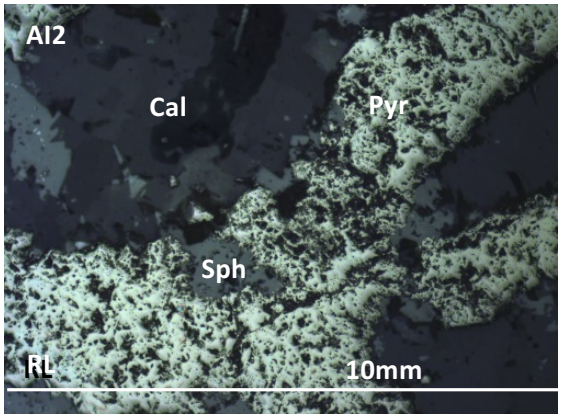

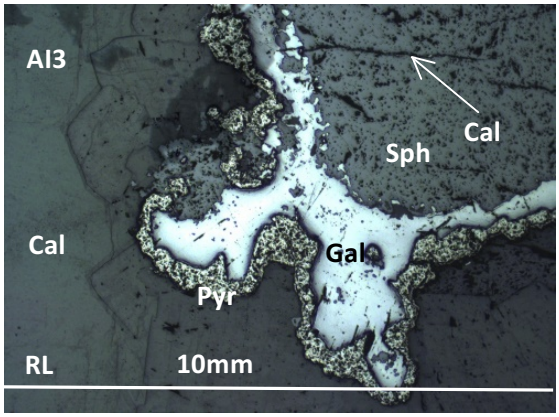

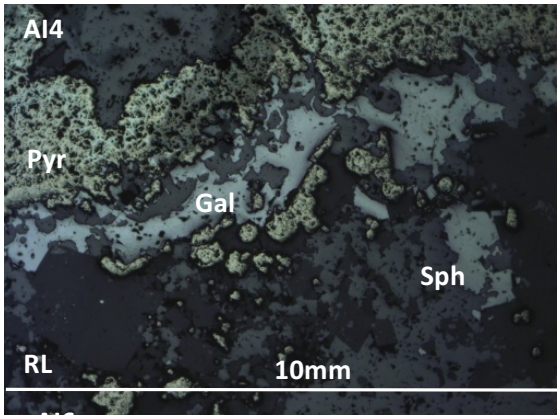

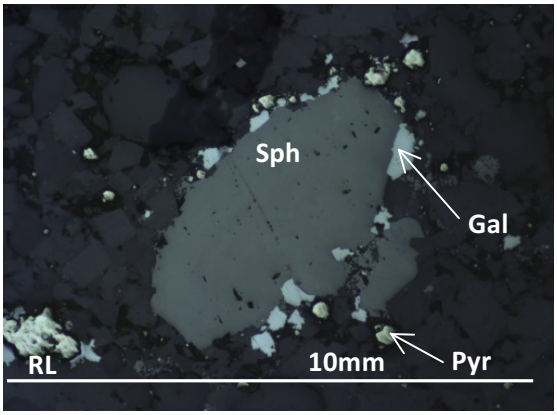

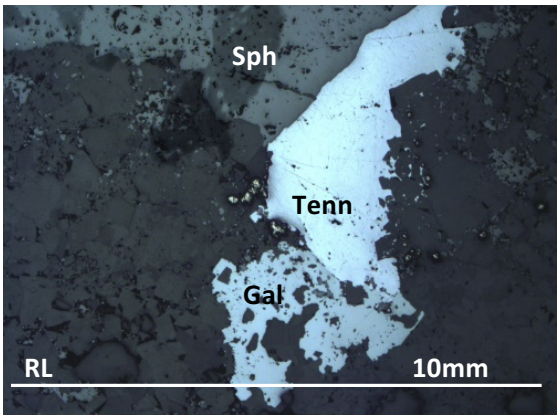

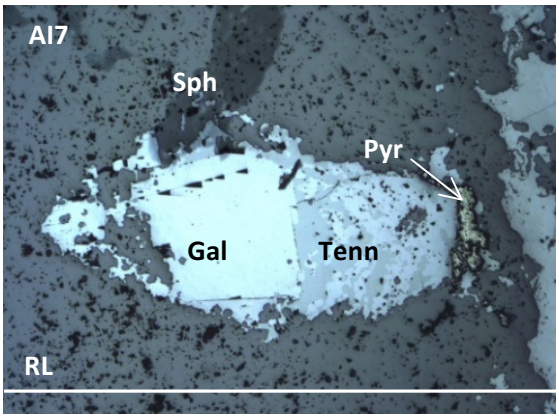

Fig AI1 – Thick sphalerite band rimmed by minor galena and mutually intergrown with anhedral pyrite

Fig AI2 – Anhedral pyrite replaced by minor sphalerite

Fig AI3 – Well-developed sphalerite and galena-pyrite banding

Fig AI4 – Prominent pyrite-sphalerite and galena banding

Fig AI5 – Euhedral sphalerite exhibiting minor galena rim mantling and replacement

Fig AI6 – Sharp, planar contact between co-precipitated galena, sphalerite and tennantite

Fig AI7 – Galena-tennantite intergrowth hosted in sphalerite

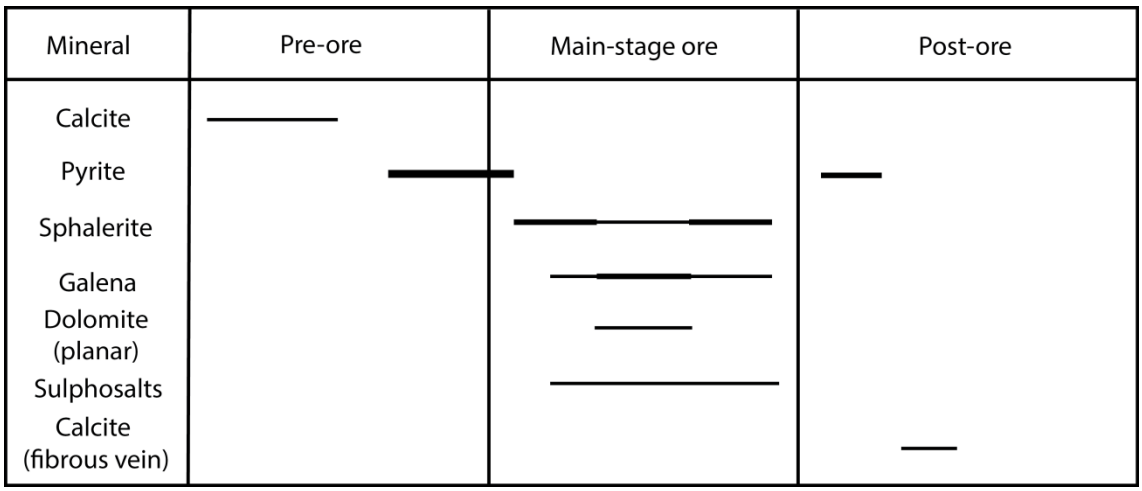

Fig AI10 - Paragenesis of N00849-1

10.3.3.13. N00849-3 – 490.6 metres (5-Lens)

Lithology – Banded sulphide

Transmitted light – Sample comprises banded opaques (sphalerite-galena), minor calcite and radiaxial celestites

Reflected light – Sulphide assemblage dominantly consists of medium-crystalline banded sphalerite and medium-crystalline, anhedral- euhedral individual galena crystals (Fig AJ1-AJ3). Galenas develop preferentially along sphalerite banding planes. Galena morphology varies from anhedral (near perfectly circular), “blebby” bands (open cavity fill? – Fig AJ2), near-cubic or as a fine dissemination throughout sphalerite (co-precipitation), and rarely exhibit relict ooid textures. Pyrite is common and observed to be a replacive phase around galena rims (Fig AJ4). Pyrite is also observed to replace the margins of sphalerite along co-precipitated calcites (Fig AJ5). Rare tennantite is observed in solid state with galena.

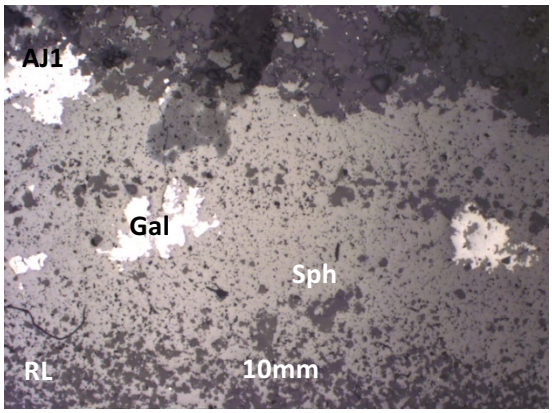

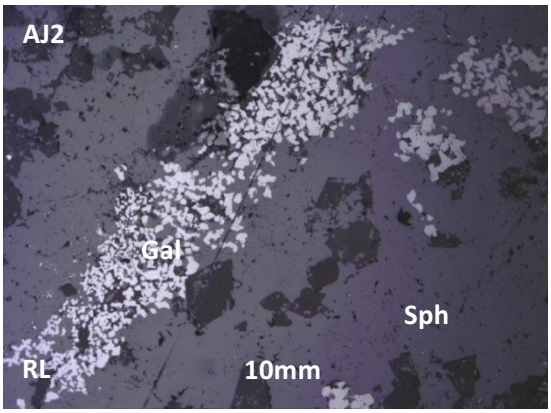

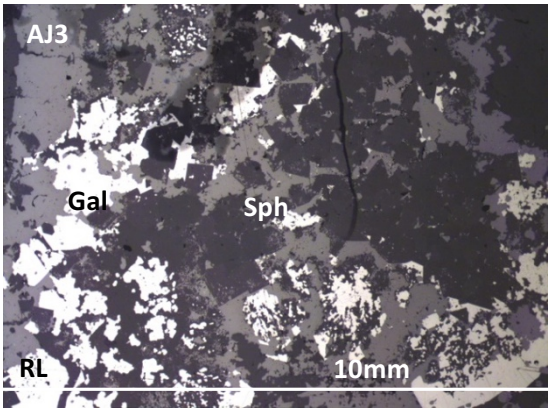

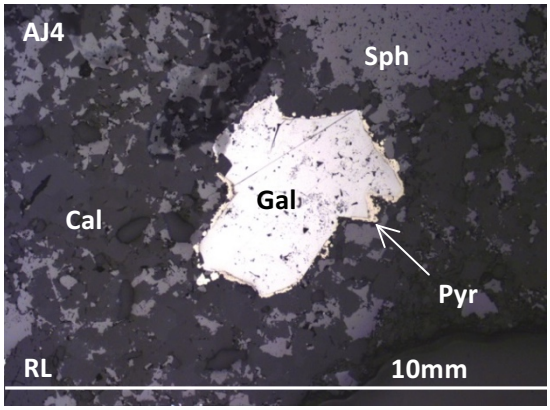

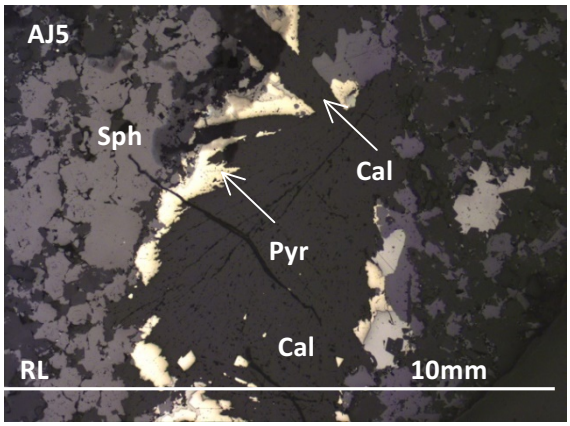

Fig AJ1 – Medium-crystalline, subhedral galenas developed along banded sphalerite plane

Fig AJ2 – "Blebby", finely-crystalline galenas, possibly developed as a cavity fill

Fig AJ3 – Mutually intergrown sphalerite and galena exhibiting minor pyrite replacement

Fig AJ4 – Relict ooid textures visible in subhedral galenas

Fig AJ5 – Pyrite preferentially developing along sphalerite-calcite contact

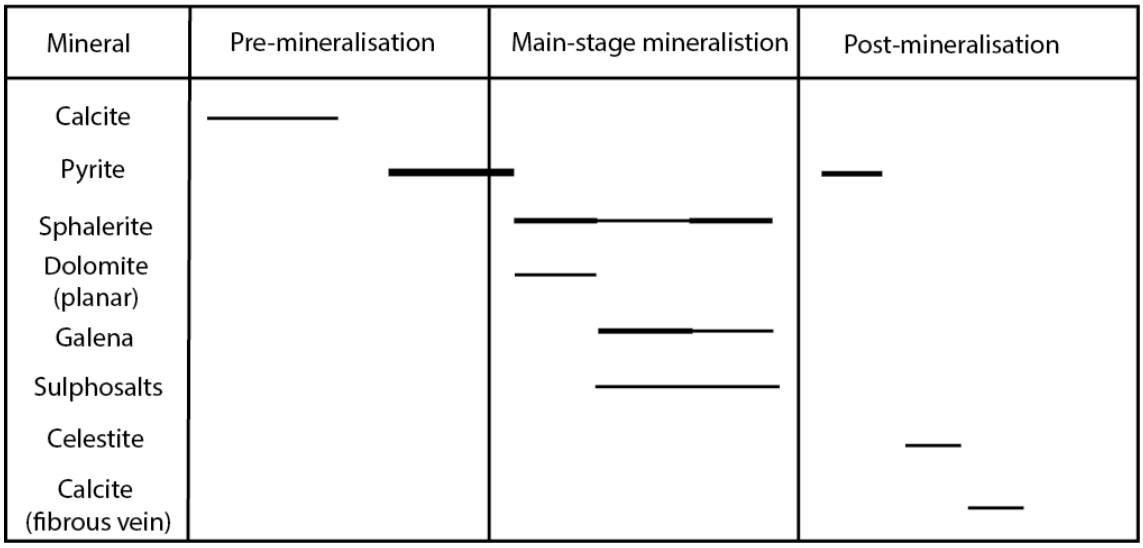

Fig AJ6 Paragenesis of N00849-3

10.3.3.14. N00849-4 – 482.4 metres (5-Lens)

Lithology – 5-Lens Dolomite

Transmitted light – Sample matrix comprises finely-crystalline mosaic dolomite-calcite, very fine-grained, sub-rounded quartz grains and opaques at modal abundances of approximately 75, 15, 5 and 5%, respectively (Fig AK1). Dolomites are typically planar

Reflected light – Sparse matrix-disseminated pyrite observed.

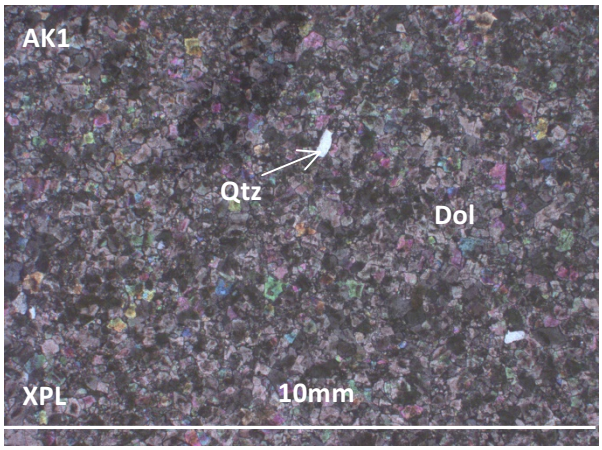

Fig AK1 – XPL: Matrix texture of N00849-4

Mineral	Pre-mineralisation	Mainstage mineralisation	Post-mineralisation
Calcite	———		
Dolomite (planar/non-planar)	———		
Pyrite		———	

Fig AK2 - Paragenesis of N00849-4

10.3.3.15. N00849-5 – 484.4 metres (5-Lens)

Lithology – Fossiliferous micrite

Transmitted light – Groundmass comprises fine-medium crystalline calcite, abundant shelly debris and rare celestite. Groundmass is variably dolomitised and cross-cut by finely-crystalline calcite veins containing minor sulphides, developing along the vein – wallrock contact.

Reflected light – Pyrite is paragenetically earliest, followed by later-stage sphalerite and galena. Sphalerites are crypto-crystalline and intergrown with very finely-crystalline galenas, while galenas often occur as finely-crystalline subhedral-euhedral crystals (Fig AL1-AL5). Notable pyrite overprints both galena and sphalerite (Fig AL6) Galenas often contain small sulfosalt inclusions.

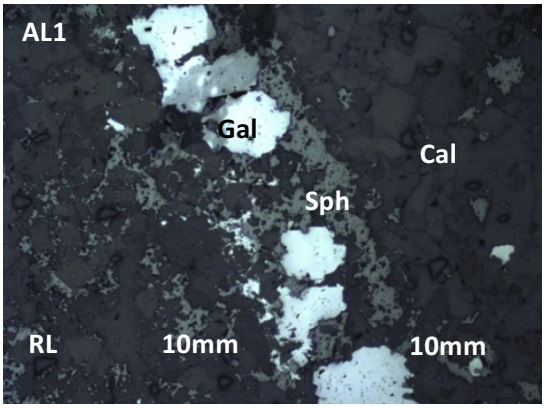

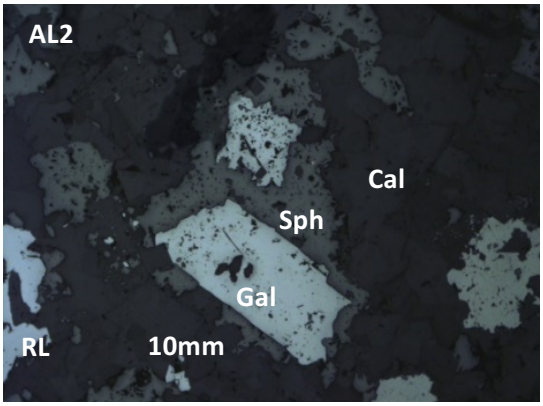

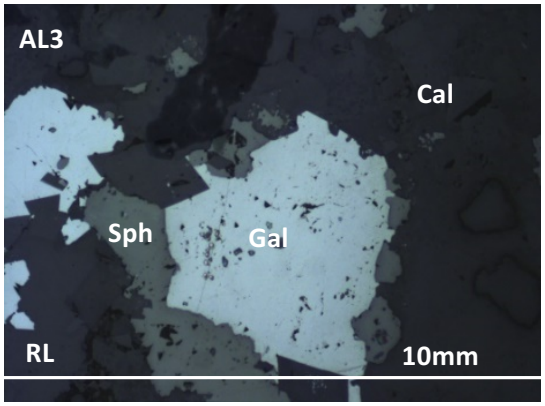

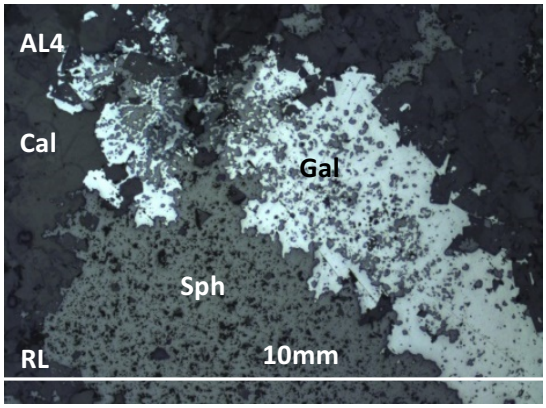

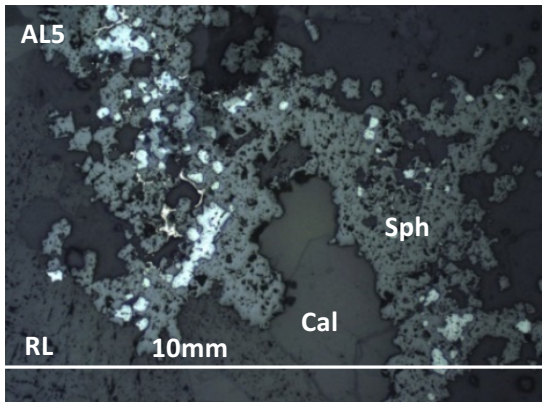

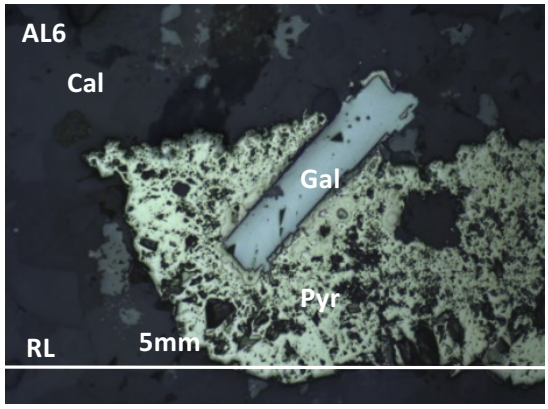

Fig AL1 – Coarsely-crystalline galena rimmed by cryptocrystalline sphalerite

Fig Al2 – Mutually intergrown, cryptocrystalline sphalerite and galena

Fig Al3 – Coarsely crystalline galena mutually intergrown with and marginally replaced by sphalerite

Fig AL4 – Mutually intergrown sphalerite and galena

Fig AL5 – Euhedral galena rimmed by sphalerite

Fig AL6 – Euhedral galena extensively overprinted by pyrite

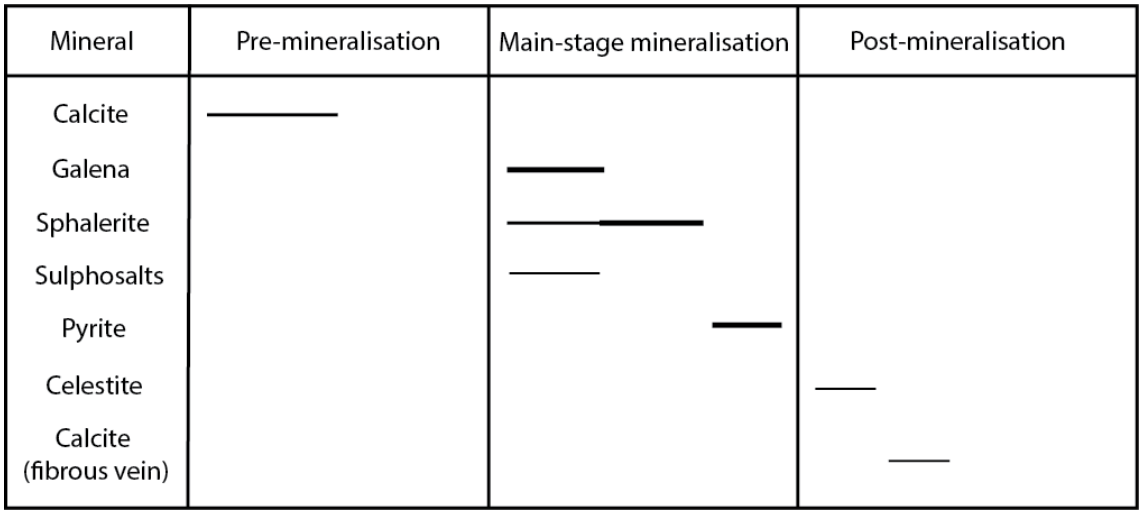

Fig AL8 – Paragenesis of N00849-5

10.4. $\delta^{34}S$ values

Sample	Description	Gal ($\delta^{34}S$‰)	Sph ($\delta^{34}S$‰)	Cpy ($\delta^{34}S$‰)	Py ($\delta^{34}S$‰)
A1 Transect					
N02230-1	Euhedral galena in shaley fault gouge	-6.5			
N02230-4	Cu-Qz(-barite) vein	_	_	3.3	
N02230-5	Cu-Qz(-barite) vein	_	_	2.9	
N02230-7	Calcite vein in stratal dolomite. Contains allochtonous cpy	_	_	0.8	
N02045-3	Gal-cal vein following styolite	6.7	_	_	
N01022-1	Sph replacement	_	-1.5	_	
N01022-2	Galena veinlets	4.1	_	_	
N01972-1	Gal-cal vein	11.2		_	
N01972-2	Gal-sph-cal vein	12.5	5.4	_	
N01628-1	Blocky sph-gal	-0.3	6.3	_	
N01628-2	Sph(-gal) vein	_	9.2	_	
N01628-3	Sph-gal veinlets in 5-Lens Dolomite	6.9	6.7	_	
A2 Transect					
N01579-1	Sph-pink cal vein	_	-6.5		
N01579-2	Pbs-bearing dolomite	-5.5	-4.7		
N00996-2	Sph replacement	_	-8.1		
N00996-3	Gal vein	10.3	9.9		
N01117-1	Sph-gal replacement	-2.1	5.3		
N01117-3	Gal-cal vein	4.9	-5.8		
N01117-4	Galena vein	5.1	_		
N01117-5	Gal-cal vein	10.3	_		
N01269-1	Sph replacement	_	6.4		
N01073-1	Sph replacement	_	-2		
N01073-2	sph-cal-gal nodule	2.5	-18.2		
N01073-3	Sph-gal breccia	5.6	-13.7		
B Transect					
N00862-1	Banded sph-cal(-gal)	_	1		
N00862-2	Pbs-bearing dolomite	5.2	_		
N00862-3	Sph-cal-dolomite vein	_	-15.1		
N00853-1	Sph replacement	3.4	4.4		
N00853-2			2.8		
N00853-3	Sph-gal banding	-13.9	6.4		
N00853-4	Sph-gal banding	-17.3	-7.6		
N00853-5	Sph(-Gal)-cal vein	_	1.4		
N00980-1	Gal(-sph) replacement	5.9	_		
N00980-2	Gal-sph-cal nodule	0.9	7		

N00980-4	Gal vein following styolite	1.1	_	_	_
N01033-1	ZnS-cal vein	_	8.1		
N01033-2	Gal-sph vein	4.4	-7.3		
N01033-3	Sph-gal vein	7.6	5.8		
N01033-4	Galena vein (weak brecciation)	-13.7	_		
C Transect					
N01001-1	Sph(-gal)-cal replacement	_	-6	_	
N01001-2	Dolomite cross-cut by gal-cal vein	3.2		_	
N01001-3	5-Lens Dolomite containing sphalerite and rare galena	2.3	2.3	_	
N01001-4	Gal-cal veining	6.6		_	
N01093-1	Sph-gal banding	2.7	-18	_	
N01093-2	Gal vein with disseminated sph	2.7	1.2	_	
N01056-1	Gal-cal vein	10.5	6.4	_	
N01056-2	Sph-gal replacement	3.2	-16.3	_	
N01056-4	5-Lens Dolomite	_	2.5	_	
N00933-1	Sph-gal-cal banding	2.3	0	_	_
N00933-2	Gal-sph-cal vein in micrite	-1.2	-6	_	
N00933-4			0.2		
N00933-4	Sph-pyr banding in oncholitic micrite	_	0.2	_	-18.4
N00849-1	Layered galena-sphalerite	-3.9	-22	_	-32.7
N00849-3	Galena-sphalerite vein	-19.4	-18.1	_	

Table 10.3 – A-C Transect $\delta^{34}S$ values for sulphides (‰)

10.5. Fluid inclusion homogenisation temperature and salinity values

Sample	Mineral	T_H	Margin of error	Salinity	T_{FREEZE}	T_E	Margin of error	T_{M-ICE}
A1 Transect – Drillhole N02230								
N02230 -4	Quartz	N/A		21.2	-52.9	-48.5	1.0	-17.0
		N/A		20.3	-50.5	-48.5	0.5	-15.5
		N/A		21.2	-54.0	-48.5	1.0	-17.0
		N/A		14.2	-54.0	-48.0	1.0	-7.7
		N/A		21.7	-73.3	N/A		-18.4
		N/A		21.7	-73.4	N/A		-18.4
		N/A		21.8	-73.7	N/A		-18.6
		N/A		20.1	-66.7	N/A		-14.7
		N/A		21.4	-71.7	N/A		-17.5
		N/A		21.3	-71.3	N/A		-17.3
		N/A		17.5	-59.8	N/A		-10.9
		N/A		21.6	-72.4	N/A		-17.9
		N/A		21.6	-72.2	N/A		-17.8
		N/A		20.3	-68.1	N/A		-15.5
		N/A		20.8	-70.1	N/A		-16.6
N02230-5	Quartz	223.0	2.0	22.0	-76.5	54.0	1.0	-18.0
		191.0	1.5	19.7	-70.5	53.0	0.5	-15.5
N02230-6	Calcite	103.0	0.5	20.8	-72.0	-67.0	0.5	-16.0
		116.5	0.5	22.5	-69.2	-64.0	0.5	18.5
		107.0	0.5	16.9	-64.1	-59.5	1.0	-9.9
		105.0	1.0	20.2	-65.2	-58.0	1.0	-14.4
		108.5	0.5	16.7	-65.0	-57.0	1.0	-8.5
		165.0	1.5	17.3	-68.5	-57.5	1.0	-10.5
		101.0	1.0	21.0	-70.9	-59.5	1.0	-16.3
N02230-7	Calcite	102.5	1.0	14.8	-61.7	-52.0	1.0	-7.7
		110.0	1.0	21.5	-65.2	-54.0	1.0	-17.4
		114.0	1.0	17.3	-64.4	-54.6	1.0	-10.5
		111.5	0.5	14.0	-65.3	-54.0	0.5	-7.5
		106.5	0.5	16.0	-55.5	-48.0	0.5	-9.3
		119.5	1.0	22.5	-61.5	-56.0	0.5	-18.5
		110.0	0.5	14.4	-66.0	-55.0	2.0	-7.2
		107.0	1.0	19.0	-65.5	-51.5	1.0	-13.8
		104.0	0.5	18.5	-72.0	-55.0	0.5	-12.5
		108.5	0.5	22.8	-56.0	-48.5	1.0	-19.3
		102.0	0.5	18.7	-64.5	-47.0	1.0	-13.3
		108.5	0.5	20.3	-68.0	-51.0	1.0	-15.3
		113.0	0.5	20.1	-68.9	-53.0	1.0	-14.2
		102.5	1.5	20.2	-71.7	52.0	1.5	-14.6
		120.0	0.5	18.4	-60.0	-52.5	1.0	-13.0
		136.0	1.0	18.4	-68.0	-52.5	1.0	-12.3
		115.0	2.0	17.7	-43.7	N/A		-11.9
		106.0	2.0	17.8	-69.0	-50.0	1.0	-12.0
	Quartz	N/A		10.2	-48.0	N/A		-4.2
		N/A		15.0	-51.4	N/A		-6.1
N02230-7	Saddle dolomite	106.5	0.5	22.2	-63.7	-57.5	1.0	-18.2

		107.0	0.5	22.3	-73.8	-66.0	2.0	-18.8
		104.5	0.5	22.4	-76.4	-70.0	2.0	-19.2
		117.5	0.5	22.5	-61.5	-55.0	1.0	-19.5
		110.0	0.5	22.2	-62.2	-56.0	1.0	-18.3
		118.0	1.0	22.6	-77.1	-68.0	1.0	20.2
		124.5	0.5	22.5	-78.0	-67.0	1.5	-19.5
A1 Transect								
N02045-3	Calcite	82.0	1.0	16.5	-64.5	-59.0	0.5	-12.5
		69.5	1.0	14.2	-61.2	-59.0	0.5	-11.4
		136.5	1.0	14.2	-61.6	-56.0	1.0	-11.3
		85.5	0.5	10.8	-59.2	-55.0	1.0	-10.5
		145.0	1.0	10.6	-51.4	-49.0	1.0	-4.9
		109.5	1.0	13.0	-48.6	-45.0	1.0	-8.1
		94.0	1.0	7.2	-47.4	N/A		-3.9
		110.0	1.0	10.3	-48.3	-43.5	1.0	-4.4
N01972-3	Calcite	85.0	1.0	17.8	-66.2	-52.0	1.0	-11.4
		97.0	1.0	18.0	-63.2	53.0	0.5	12.0
		79.0	1.0	18.0	-77.2	68.0	1.0	12.0
		94.5	1.0	16.5	-64.3	68.0	1.5	11.0
		79.0	1.0	13.5	-77.2	68.0	1.5	8.5
		98.5	0.5	21.5	-67.4	62.0	-1.0	-18.3
		120.5	1.0	21.0	-66.8	-60.0	0.5	-16.3
		100.0	0.5	21.0	-62.5	-52.5	1.0	-16.6
		116.0	1.0	22.7	-68.7	-62.0	1.0	-19.9
		91.5	1.0	10.1	-74.0	-69.0	1.0	-4.0
		98.5	1.0	17.2	-71.7	-69.5	1.0	-12.6
		125.5	1.0	20.8	-63.8	-59.0	1.0	-17.7
		98.0	1.0	21.0	-67.1	-58.0	0.5	-16.5
N01628-1	Calcite	110.0	1.0	12.6	-35.5	N/A		-7.6
		96.5	1.0	8.1	-45.4	41.5	1.0	2.9
		85.5	1.0	11.2	-40.8	N/A		-6.7
		87.0	1.0	11.0	-45.7	-39.5	N/A	-6.4
		107.5	0.5	19.7	-68.5	62.0	1.0	-14.2
		102.5	1.0	19.4	-48.4	-48.5	1.5	-11.7
		125.5	0.5	15.4	-71.7	-69.5	0.5	-10.4
		123.5	1.0	10.6	-49.1	-44.5	1.0	-4.8
		126.0	1.0	17.5	-57.3	-49.5	1.5	-11.2
		123.5	1.0	6.8	-52.8	-47.0	1.5	-2.3
		123.0	1.0	16.8	-59.2	-53.0	1.0	-10.6
A2 Transect								
N00996-1	Calcite	144.0	0.5	7.1	-49.5	N/A		-2.5
		113.0	0.5	10.3	-48.9	N/A		-4.9
N01579-2	Calcite	77.5	0.5	20.4	-71.0	N/A		-17.1
		77.5	1.0	20.3	-70.7	N/A		-16.9
		79.5	0.5	19.1	-65.1	N/A		-13.8
		100.0	1.0	19.3	-65.7	-58.5	1.5	-14.2
		117.0	1.5	19.3	-67.1	-63.0	0.5	-14.1
N01117-5	Calcite	187.0	1.0	7.4	-46.9	-42.5	1.0	-2.8
		166.0	0.5	13.6	-56.8	-37.2	N/A	-8.3
		164.5	1.0	20.2	-56.8	-59.2	N/A	-14.7
		223.5	1.0	7.1	-61.3	-55.0	1.0	-2.5
		162.0	1.0	7.1	-47.1	-42.0	0.5	-2.5

N01093-2	Calcite	104.5	1.0	12.9	-54.6	-50.5	0.5	-8.0
		121.5	0.5	22.0	-72.4	-60.0	1.5	-19.3
		124.5	1.0	17.8	-61.8	N/A		-11.3
C-C' Transect								
N01056-1		107.5	0.5	15.4	-64.1	-54.1	0.5	-10.1
		104.3	0.5	15.1	-40.1	N/A		-9.9
		103.5	0.5	11.9	-51.3	N/A		-6.3
		134.5	0.5	19.7	-68.9	-61.0	0.5	-15.7
		164.0	1.0	19.9	-69.8	-59.0	1.5	-16.1
		135.0	0.5	11.9	-64.9	-53.5	1.5	-5.8
		124.5	0.5	7.3	-52.7	N/A		-2.7
N01001-4		141.0	1.0	18.7	-59.8	-51.0	1.0	-12.8
		111.5	1.0	22.0	-81.3	-74.0	1.0	-18.1
		110.5	0.5	21.9	-81.0	-74.0	1.0	17.9
		121.5	0.5	22.1	-83.3	-72.5	1.0	-19.7
		131.5	0.5	22.2	-82.4	-77.2	2.0	-19.9
		115.5	1.0	22.2	-77.0	-71.0	0.5	-19.8
		154.0	0.5	20.1	-69.6	N/A		-16.6
		115.5	1.0	19.6	-66.4	N/A		-15.6
N00933-1	Calcite	142.5	0.5	12.2	-54.6	-44.5	1.0	-7.0
		124.5	0.5	21.9	-75.2	-68.0	2.0	-18.3
		123.0	1.0	21.7	-74.0	-68.5	0.5	-17.4
		124.5	0.5	21.7	-69.5	-63.5	1.0	-17.4
		124.0	1.0	21.5	-74.5	-64.0	1.0	-17.1
		123.0	0.5	12.1	-54.4	N/A		-6.9
		95.5	1.0	14.9	-65.8	-59.0	1.0	-9.4
		108.5	0.5	18.9	-61.6	-54.5	0.5	-11.9
		109.5	0.5	19.8	-67.2	N/A		-13.1
N00849-3	Calcite	170.0	0.5	17.5	-57.8	-53.0	0.5	-10.7
		204.5	0.5	12.9	-45.5	-37.5	1.0	8.0
		182.5	0.5	15.2	-62.7	-54.5	1.0	-9.6
		204.5	0.5	13.5	-57.9	-54.0	0.5	-8.5
		176.0	0.5	12.7	-53.4	-47.0	1.0	-7.3
		164.5	1.0	12.7	-59.4	N/A		-7.3
		120.0	0.5	11.8	-33.0	N/A		-6.0
		154.0	1.5	18.5	-55.6	N/A		-12.6
		201.0	1.0	11.8	-50.9	N/A		-6.0
		144.0	2.0	12.5	-58.8	-50.5	1.0	-7.5

Table 10.4 – Fluid inclusion values

10.6. C-O isotope values

Sample	Mineral	$^{13}C_{V\text{-}PDB}$ (‰)	$^{18}O_{V\text{-}SMOW}$ (‰)	$^{18}O_{V\text{-}PDB}$ (‰)
A1 Transect				
N02230-5	Vein calcite	-2.2	12.7	-17.6
N02230-6	Stratal dolomite	0.7	19.9	-10.7
N02230-6 2nd generation	Vein calcite	0.15	16	-14.5
N02230-6 1st generation	Vein calcite	-2.1	13.8	-16.6
N02230-7	Saddle dolomite	0.6	20.8	-9.8
N02045-3	5-Lens Dolomite	0.9	21.2	-9.4
N01628-3	5-Lens Dolomite	2.8	25.1	-5.6
A2 Transect				
N01579-2	5-Lens Dolomite	-0.04	21.6	-9.1
N00996-3	5-Lens Dolomite	2.7	19.9	-10.6
N01017-3	5-Lens Dolomite	2.4	18.8	-11.8
N01117-6	5-Lens Dolomite	2.6	19.2	-11.3
N01269-2	5-Lens Dolomite	2.8	20.5	-10.1
N01073	5-Lens Dolomite	2.3	21.7	-8.9
N01155-1	5-Lens Dolomite	4.4	23.8	-6.8
B Transect				
N00853-2	5-Lens Dolomite	2.3	22	-8.7

N00862-4	5-Lens Dolomite	2.6	19.9	-10.7
N01033-1	5-Lens Dolomite	2.0	19.6	-10.9
N00980-3	5-Lens Dolomite	2.4	18.8	-11.8
C Transect				
N01001-3	5-Lens Dolomite	2.4	22.1	-8.6
N01093-3	5-Lens Dolomite	2.5	19.6	-10.9
N01056-3	5-Lens Dolomite	1.7	21.6	-9
N00933-3	5-Lens Dolomite	2.1	22.2	-8.4
N00849-2	5-Lens Dolomite	1.3	16.0	-14.4